Heavy ion physics programme in CMS

G. Baur[1], M. Bedjidian[2,a], B. E.Bonner[3], S. Chatrchyan[4,b], J. Damgov[5], A. De Min[6], D. Denegri[7], O. Drapier[2], G. Eppley[3], A. Galoyan[4], W. Geist[8], V. Genchev[5], F. Geurts[3], I.A. Golutvin[4], R. Haroutunian[2], M. Hayrapetyan[9,c], K. Hencken[10], L. Jenkovszky[11], V. Kartvelishvili[12], Yu. Kharlov[13], O. Kodolova[14], D. Kotliński[15], V.A. Krasnov[4], N. Kruglov[14], R. Kvatadze[12], J. Lamas-Valverde[3], W. Llope[3], I. Lokhtin[14], A.I. Malakhov[4], A. Nikitenko[16], S. Petrouchanko[14], E. Platner[3], A. Racz[6], J. Roberts[3], S. Sadovsky[13], L. Sarycheva[14], M.V. Savina[4], R. Shanidze[12], S.V. Shmatov[4], N.V. Slavin[4], I.V. Slepnev[4], V.A Smirnov[4], A. Snigirev[14], D. Trautmann[10], V.V. Uzhinskii[4], I. Vardanyan[14], Yu.I. Vasilishin[4], R. Vogt[17], G. Wrochna[18], P. Yepes[3] and P.I. Zarubin[4]

Edited by: D. Barney, M. Bedjidian, D. Denegri, O. Drapier, W. Geist, R. Haroutunian and R. Vogt

[1] Institut für Kernphysik, Forschungszentrum Jülich, Postfach 1913, D-52425 Jülich, Germany
[2] Institut de physique nucléaire de Lyon, IN2P3-CNRS et Université Claude Bernard, F-69622 Villeurbanne cedex, France
[3] Rice University, Bonner Nuclear Laboratory MS315, Houston TX 77005-1892, USA
[4] Laboratory of High Energies, Joint Institute for Nuclear Research, 141980 Dubna, Russia
[5] Institute for Nuclear Research and Nuclear Energy (INRNE), 0f Bulgarian Academy of Science , BG-1784 Sofia, Bulgaria
[6] CERN, CH-1211 Genève 23, Switzerland
[7] DSM/DAPNIA, CEA/Saclay, F-91191 Gif-sur-Yvette Cedex, France
[8] Institut de Recherches Subatomiques, IN2P3-CNRS-ULP, LEPSI Strasbourg, F-67037 Strasbourg Cedex, France
[9] Laboratory of Computing Techniques and Automation, Joint Institute for Nuclear Research, 141980 Dubna, Russia
[10] Institut für Physik, Universität Basel, Klingelbergstr. 82, CH-4056 Basel, Switzerland
[11] Bogolyubov Institute for Theoretical Physics, 252143 Kiev, Ukraine
[12] High Energy Physics Institute, Tbilisi State University, Georgia
[13] Institute for High Energy Physics, Protvino, Russia
[14] Moscow State University, Moscow, Russia
[15] Paul Scherrer Institut, Villigen, Switzerland
[16] Institute for Theoretical and Experimental Physics, Moscow, Russia
[17] Nuclear Science Division, Lawrence Berkeley National Laboratory, Berkeley, California 94720, USA and Physics Department, University of California at Davis, Davis, California 95616, USA
[18] Soltan Institute for Nuclear Studies, Warsaw, Poland

General introduction

This report presents the physics capabilities of the CMS detector with heavy ion beams. The primary goal of the heavy ion physics programme is to study the plasma of quarks and gluons (QGP). One of strongest signatures proposed for its evidence is the heavy quark vector mesons suppression. CMS is particularly well suited to study the Υ family and to a lesser extent the J/ψ and ψ'. Detection of

[a] Corresponding author: Marc.Bedjidian@ipnl.in2p3.fr
[b] On leave from Theoretical Physics Division, Yerevan Physics Institute, 375002 Yerevan, Armenia
[c] On leave from Department of Applied Mathematics, Yerevan State University, 375002 Yerevan, Armenia

the $Z^0 \to \mu^+\mu^-$ produced at the same impact parameter will provide a good reference to estimate the suppression as long as the point-like Z^0-boson remains unchanged even at the very high energy densities expected to be reached at the LHC. Hard jet production is another probe of the formation of such a dense state of matter. The energy lost by the parton in traversing dense matter leads to quenching, *i.e.* suppression of high p_T jets. The dijet quenching and enhancement of the monojet/dijet ratio as well as the study of jets in the Z^0+jet and γ+jet channels will be investigated. The centrality of the collision can be determined from the transverse energy production measured over a wide rapidity range, up to $\eta < 5$.

In addition to these signals of dense matter production in central collisions, peripheral collisions can be used to look

for new physics. The coherent photon field surrounding the nucleus leads to high luminosities for $\gamma\gamma$ interaction which can be used to study exotic particles production such like the structure of Pomeron in diffractive processes.

The CMS detector has been designed with the following useful properties. The high magnetic field leads to a compact detector, with the first absorber, the electromagnetic calorimeter, at a distance of 1.3 m from the interaction point, allowing the elimination of a large fraction of the hadronic background. The very powerful tracking system, recently upgraded by the choice of Silicon strip detectors to replace the MSGCs, will provide a good track reconstruction efficiency for dimuons even for the extreme charged particle densities expected ($dN^{\pm}/dy \leq 8000$) and an excellent momentum resolution.

The plasma of quarks and gluons should develop in the mid-rapidity region where baryon number is vanishingly small. At the LHC the rapidity gap will be large even if the stopping power reduces it. CMS can detect muons in the rapidity region $|\eta| < 2.4$. Muons need a transverse momentum $p_{\mathrm{T}} > 3.5$ GeV/c to be detected in the barrel region with $|\eta| < 1.3$. This requirement rejects most of the decay background and results in an appreciable signal/background ratio. However this p_{T} threshold obviously disfavours the observation of low p_{T} J/ψ and ψ' resonances. This is not the case in the endcap region ($1.3 < |\eta| < 2.4$) where muons of $p_{\mathrm{T}} > 2$ GeV/c are accessible. However, the reconstruction performance is not yet studied for this region. In this report, the reconstructed dimuon mass spectra are given for the barrel region only. In this document some calculations were done on the basis of a former geometry in which the barrel covered the region $|\eta| < 1.5$ and the endcaps $|\eta| < 2.6$. In addition, many calculations and simulations were performed with Ca beams. Most probably Ar^{18+} ions will be accelerated instead of Ca^{20+} ions. These changes do not affect significantly the results.

Although CMS has significant capabilities to investigate some heavy ion physics issues, CMS is clearly not a dedicated heavy ion experiment. Many signatures required for a complete QGP study cannot be explored. Therefore CMS can be seen as complementing the general purpose heavy ion detector.

1 The CMS apparatus

The CMS detector, optimized for pp physics, is designed to identify and precisely measure muons, electrons, photons and jets over a large energy range.

A detailed description of the different parts of the detector can be found in the Technical Design Reports [1–4]. An overall view of the apparatus is shown in Fig. 1.1. The central element of CMS is the magnet, a 13 m long, 6 m diameter, high-field solenoid with an internal radius of $\approx$3 m, which will provide a uniform 4 T magnetic field. The tracking system, electromagnetic, and hadronic calorimeters are positioned inside the magnet, whilst the muon detector is outside. The tracker covers the pseudorapidity region $|\eta| < 2.4$, while the electromagnetic and hadronic

calorimeters reach $|\eta| = 3$. A very forward calorimeter, located at ±11 metres from the interaction point, covers the region $3 < |\eta| < 5$ and complements the energy measurement.

The complete geometry of the CMS detector with all detector support structure and services materials, together with the 4 T magnetic field map, is inserted in the CMSIM detailed simulation package [5].

1.1 Tracker description

Starting from the beam axis, the tracker is composed of three different types of detectors: the pixel layers, the silicon strip counters and, finally, the microstrip gas chambers (MSGC). In the new and final tracker design recently adopted by the Collaboration the MSGCs are replaced by silicon strip counters.

The pixel detector is composed of 2 barrel layers which are located at 7.5 cm and 11.5 cm from the beam axis and 2 endcap discs in each of the forward and backward directions. A third layer at 4.5 cm in the barrel will also be present, at least during the initial low luminosity running period.

The barrel layers, covering rapidities up to $\eta = 2.1$, are made of more than 10 million and 16 million pixels for the inner and outer layers respectively, with pixel dimensions of 150×150 μm^2. The migration of the charges and their collection are taken into account in the simulation. The precision for normal (high p_{T}) tracks is around 15-20 μm. The barrel region of the inner Si strip counters consists of 5 cylindrical layers and 6 mini-discs, whilst the endcap regions are each composed of 10 discs. Lying close to the interaction point (210 mm $< R <$ 635 mm in the barrel) with a pitch of 143 μm and Si strip length of 6.4 cm, these counters are copiously illuminated in a central Pb+Pb collision. The occupancy levels are above 30%, forbidding their use in the track reconstruction.

The MSGC tracker is made of 6 layers in the barrel region with radii between 75 and 115 cm, extending up to $|z| = 120$ cm. The sensing electrodes are parallel to the beam. The innermost layer covers a rapidity range up to $|\eta| = 1.3$, the outermost is limited to $|\eta| = 0.8$.

The endcaps are composed of 11 discs, on each side of the barrel, with radii between 70 and 116 cm, extending up to $|z| = 280$ cm. The MSGCs have a 3 mm gas gap and a pitch of 240 μm for non-stereo layers and 400 μm for stereo layers. The strip length is near 10 cm for the forward MSGCs. For barrel cylinders the strip length of the two outermost layers is 25 cm while the remaining 4 layers have a 12.5 cm strip length. Strip noise, the effects of cross-talk and the ballistic deficit in charge collection are taken into account in the simulation.

In the new tracker design, all MSGC layers are replaced with silicon strip detectors. The exact geometry of the outer silicon layers is still being optimized. At this time, instead of 6 outermost layers of MSGCs in $|\eta| < 0.8$ the design proposes five layers of silicon detectors with a strip length of 16 cm and a pitch size of 143 μm.
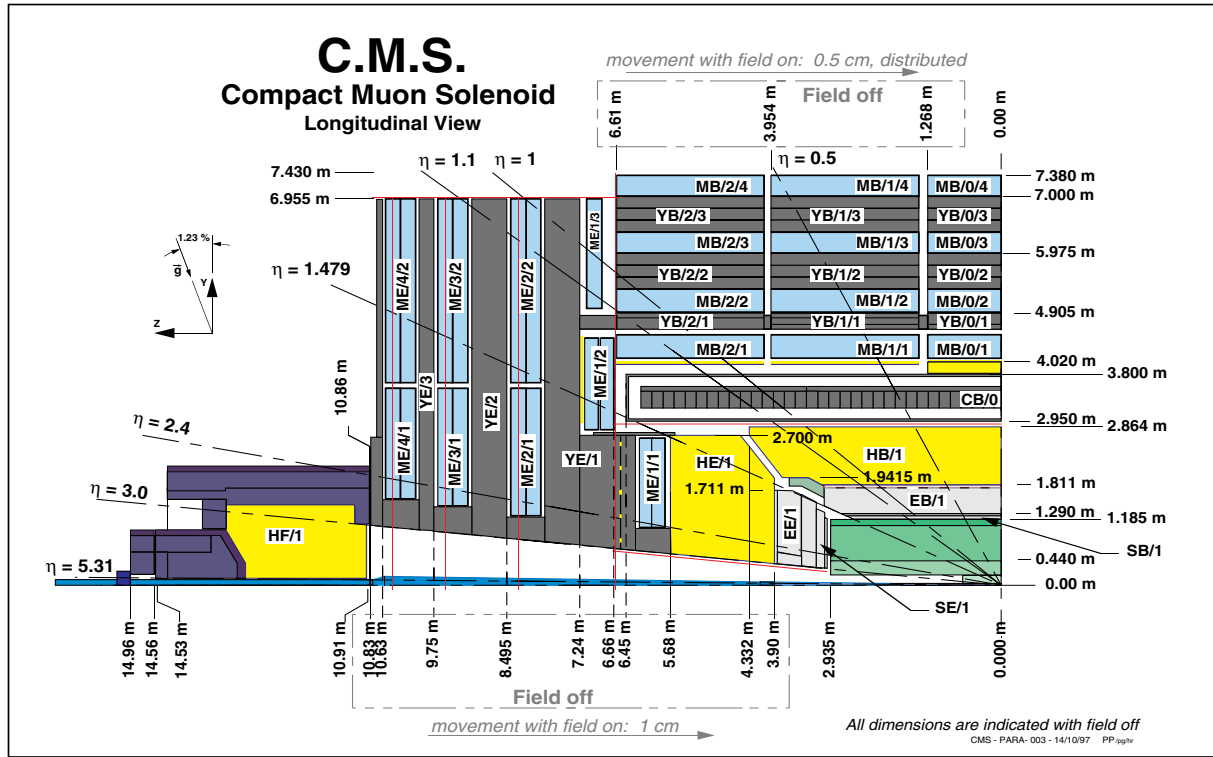
Fig. 1.1. The CMS detector: a longitudinal view

1.2 Electromagnetic calorimeter

The electromagnetic calorimeter (ECAL) is made of almost 83000 scintillating crystals of $PbWO_4$, the light being detected with avalanche photodiodes (APDs) for the barrel and vacuum phototriodes (VPTs) for the endcaps. The barrel part of the ECAL (EB) covers the pseudorapidity range $|\eta| < 1.479$. The front face of the crystals is at a radius of 1.29 m and each crystal has a square cross section of 22×22 mm^2 and a length of 230 mm, corresponding to 25.8 X_0. The truncated-pyramid shaped crystals are mounted in a barrel geometry with a 3^0 shift in ϕ and η with respect to the mean position of the primary vertex. The crystal cross section corresponds to $\Delta\eta \times \Delta\phi = 0.0175 \times 0.0175$ in the barrel region. The endcap crystal calorimeter (EE) covers the pseudorapidity range $1.48 < \eta < 3$. The granularity will increase progressively to a maximum value $\Delta\eta \times \Delta\phi = 0.05 \times 0.05$ though the crystal front section will not change; 25 crystals are organized in one group referred to as a supercrystal. A preshower is located in front of the endcap crystal calorimeter, covering the pseudorapidity range $1.5 < \eta < 2.5$. The preshower comprises two orthogonal planes of silicon strip detectors, placed after 2 X_0 and 1 X_0 of lead radiators respectively.

1.3 Hadronic calorimeter

The hadronic calorimeter is made of two parts: (a) a central calorimeter (HB and HE) covering $|\eta| < 3$, and (b) a forward/backward calorimeter (HF) which covers the

pseudorapidity range from 3 to 5. The forward calorimeter is physically separated from the central calorimeter. Its front face is located 11 m from the interaction point. The central calorimeter consists of the hadron barrel (HB) and hadron endcap (HE) calorimeters, both located inside the CMS magnet cryostat. As both HB and HE are situated inside the 4 T field of the CMS solenoid they are made of non-magnetic material (copper alloy and stainless steel). The central hadronic calorimeter is a sampling calorimeter made of scintillator plates inserted between copper absorber plates. The absorber plates are 5 cm thick in the barrel and 8 cm thick in the endcap. The active elements of the central hadronic calorimeter are 4 mm thick plastic scintillator tiles read out using wavelength-shifting (WLS) plastic fibres. The barrel hadronic calorimeter is about 79 cm deep, which at $\eta = 0$ corresponds to 5.15 nuclear interaction lengths.

To extend the hermeticity of the central hadronic calorimeter system to pseudorapidity of five for a good missing transverse energy measurement in pp collisions and for forward energy flow and impact parameter measurements in heavy ion collisions, a separate forward calorimeter (HF) will be located 6 m downstream from the HE endcaps. The HF calorimeter covers the region $3 < |\eta| < 5$. The active quartz medium is embedded in a copper absorber matrix. The HF will be located in a very high radiation and a very high rate environment. Because of the quartz fibre active element, it is predominantly sensitive to Cerenkov light from neutral pions. This gives it the unique and desirable feature of a very localized response to hadronic showers.

The granularity $\Delta\eta \times \Delta\phi$ will be about 0.087×0.087 for $|\eta| < 2$ to match the electromagnetic calorimeter and the muon chamber structure. This granularity is sufficient for good dijet separation and mass resolution in pp collisions. The calorimeter readout must have a dynamic range from 5 MeV to 3 TeV to allow the observation of single muons in a calorimeter tower for calibration and trigger purposes as well as to measure the highest possible particle jet energies. In heavy ion collisions the dynamic range is shifted to hundreds of TeV.

1.4 Muon system

The muon system uses three different technologies to detect and measure muons: drift tubes (DTs) in the barrel region (MB), cathode strip chambers (CSCs) in the endcap regions (ME) and resistive plate chambers (RPCs) in both barrel and endcap dedicated to triggering. All the muon chambers are positioned roughly perpendicular to the muon trajectories and cover the pseudorapidity range $|\eta| < 2.4$. The barrel drift tubes cover $|\eta| < 1.3$ and cathode strip chambers cover $0.9 < |\eta| < 2.4$. The RPC coverage is $|\eta| < 2.1$.

The barrel muon system consists of four stations integrated in the return yoke of the magnet (YB and YE). Each station is distributed over 5 rings, each 2.5 m long. The 2.5 m long anode wires are parallel to the beam line. There are 60 chambers in each of the inner three barrel stations and 70 chambers in the outer station. The maximum drift time is 400 ns. The twelve planes inside each station are organized in subunits made of 4 planes with parallel wires called superlayers. Two superlayers per station measure the $(r\text{-}\phi)$ coordinate. These two superlayers are separated by 23 cm. Between them there is a superlayer which measures the z coordinate.

Each endcap region of CMS has four muon stations of CSCs. These chambers have a trapezoidal shape and are arranged in rings centred on the beam line. Each CSC has six layers of wires put between cathode panels. The wires have constant spacing. A cathode panel has one plane of strips per gas gap running radially. Each chamber gives 6 measurements of the ϕ-coordinate (strips) and 6 measurements of the r-coordinate (wires).

RPCs will be added in both the barrel and endcaps to provide an additional trigger. Six layers of RPCs will be mounted with the barrel chambers, two layers with each of the inner stations MB1 and MB2 and one in the outer stations MB3 and MB4. In the endcap each of the 4 layers of CSCs will also have a layer of RPC.

The signals from the DTs, CSCs and RPCs will be read out in parallel.

2 Overview of the physics goals

2.1 Introduction

Finite temperature simulations of lattice gauge theory suggest a transition to a new phase of QCD matter—the quark-gluon plasma (QGP). The order of this phase transition depends strongly on the colour and flavour degrees of freedom included in the simulations [6]. In a pure SU(N) gauge theory (gluons only), the phase transition is second order, (*i.e.* continuous), for SU(2) and first order (discontinuous) for SU(3). For the gluon theory, the critical temperature, T_c, is 260 MeV. When light quark degrees of freedom are included, the critical temperature is substantially lower with two light flavours, $T_c \approx 170$ MeV, although in this case the phase transition appears to be continuous. For simulations with more light flavours, $n_f \geq 3$, the transition again appears to be first order. However, this conclusion depends on the relative quark masses. The critical energy density is $\epsilon_c \approx 1-2$ GeV/fm^3, obtained in simulations both with and without quark degrees of freedom. For a QGP to be formed in ultrarelativistic heavy-ion collisions, the initial temperatures and energy densities must be larger than T_c and ϵ_c. The QGP is expected to be produced in high energy heavy-ion collisions. Significant progress in this field has been made in the last decade at the Brookhaven AGS and the CERN SPS [7]. A dedicated heavy ion collider with Au+Au collisions up to $\sqrt{s} = 200$ GeV per nucleon pair, RHIC [8], began operations in June 2000.

Part of the LHC experimental program will be devoted to heavy-ion collisions such as Pb+Pb at $\sqrt{s} = 5.5$ TeV per nucleon pair, the highest energy available for these collisions. This section will focus on possible signatures of quark-gluon plasma formation that can be observed with CMS. Two of the most interesting proposed signatures involving hard processes are quarkonium suppression and manifestations of energy loss of fast partons in the medium. A major advantage of the CMS detector is that it is possible to measure both within the same experiment. The ALICE detector [9], dedicated to heavy-ion running, will be able to measure quarkonium suppression up to the Υ family so that some overlap of results is possible even though the acceptances are different. Such cross checks are desirable.

The probability of QGP production and the resulting strength of its signatures depends strongly on the initial conditions. Therefore the first part of this section describes the initial conditions within the context of minijet production. Quarkonium production and suppression is then described with an emphasis on the family of Υ resonances. Charmonium suppression has already been seen in the CERN fixed target program [10], stimulating considerable interest in this topic. However, at the moment its interpretation remains controversial since it has been shown that interactions with hadrons also cause J/ψ suppression (see [11] for a review), but the anomalous suppression seen in the Pb+Pb data [10] is difficult to explain with hadronic mechanisms alone. Typically, nuclear effects, such as interactions with nucleons and secondary particles which can break up the bound states, are not as strong for Υ production as for the J/ψ [12], perhaps allowing a cleaner interpretation of the Υ data in heavy ion collisions.

The effects of energy loss by fast partons in the medium on heavy quark and jet production is another important signal of dense matter formation that can be measured by CMS. Hard partons interact strongly in the

dense matter formed in heavy-ion collisions. The energy lost by these partons during successive interactions has several observable consequences, some of which are discussed here. First, the dilepton continuum above the Υ resonances has important contributions from $c\bar{c}$ and $b\bar{b}$ decays. The relative decay rates depend on the energy lost by the heavy quarks, influencing the content of the dilepton continuum. In addition, the hard jet spectrum is expected to be modified significantly by reinteractions. Particularly, the dijet rate should be suppressed, resulting in an enhancement of monojet production at large jet transverse energy. Finally, although not of least importance, energy loss will also play a role in redistributing global particle production, affecting global variables such as transverse energy production and total multiplicity.

It is important to note that to complete a systematic study of heavy ion collisions and unambiguously determine QGP effects, the signals proposed here should also be studied in pp and pPb collisions at the same energy. Studies with lighter ions such as Ca are also desirable to understand finite volume and energy density effects.

2.2 Initial conditions

At the Pb+Pb collision energy, perturbative QCD processes are expected to drive the initial conditions. In particular, at early times, $\tau \sim 1/p_{\mathrm{T}} \leq 1/p_0 \sim 0.1$ fm for $p_0 \sim 2$ GeV, semi-hard production of minijets[1] will set the stage for further evolution of the system [15]. The recent work of Eskola and Kajantie is used to determine the initial conditions from minijet production [16].

The calculation of minijet production is based on the jet cross section for $p_{\mathrm{T}} > p_0$. At leading order, LO, the rapidity distribution of a particular parton flavour in AA collisions is

$$\frac{\mathrm{d}\sigma^f}{\mathrm{d}y}(\sqrt{s}, p_0) = K \int \mathrm{d}p_{\mathrm{T}}^2 \mathrm{d}y_2 \sum_{\substack{ij= \\ \langle kl \rangle}} x_1 f_{i/A}(x_1, p_{\mathrm{T}}^2)$$
$$\times x_2 f_{j/A}(x_2, p_{\mathrm{T}}^2)$$
$$\times \left[\delta_{fk} \frac{\mathrm{d}\hat{\sigma}^{ij\to kl}}{\mathrm{d}\hat{t}}(\hat{t}, \hat{u}) + \delta_{fl}\frac{\mathrm{d}\hat{\sigma}^{ij\to kl}}{\mathrm{d}\hat{t}}(\hat{u}, \hat{t}) \right]$$
$$\times \frac{1}{1 + \delta_{kl}} . \tag{2.1}$$

The parton distributions in the nucleus are normalized to the per nucleon distribution. The limits of integration on p_{T}^2 and y_2 are $p_0^2 < p_{\mathrm{T}}^2 < s/(4\cosh^2 y)$ and $\ln(r_{p_{\mathrm{T}}} - e^{-y}) \leq y_2 \leq \ln(r_{p_{\mathrm{T}}} - e^y)$ where $|y| \leq \ln(r_{p_0} + \sqrt{r_{p_0}^2 - 1})$, $r_{p_{\mathrm{T}}} = \sqrt{s}/p_{\mathrm{T}}$ and $r_{p_0} = \sqrt{s}/2p_0$. The sum over initial states includes all combinations of two parton species with three flavours while the final state includes all pairs without a mutual exchange and four flavours (including charm) so that $\alpha_s(p_{\mathrm{T}})$ is calculated at one loop with four flavours.

---

[1] Minijets are jets with $p_{\mathrm{T}} \geq p_0 \sim 1 - 3$ GeV [13], usually not observable as individual jets below $p_{\mathrm{T}} \sim 5$ GeV [14].

The final factor, $1/(1 + \delta_{kl})$, is needed to correctly count identical particles in the final state. The parton densities are evaluated at scale p_{T}, with x values at $y = y_2 = 0$ as low as $x_{1,2} \sim 2p_0/\sqrt{s} \sim 7 \times 10^{-4}$ in Pb+Pb collisions. Thus the small x behaviour of the parton densities strongly influences the initial conditions of the minijet system. While the deep inelastic scattering data from HERA [17] continues to refine the parton densities at small x, uncertainties in the distributions still exist. To account for these, results are presented with two different parton distribution sets, GRV 94 LO [18] and MRST LO [19], both because they have low initial scales and because the LO set is more consistent to use with a LO calculation. The K factor in (2.1) indicates the NLO corrections. Previous analysis showed that $K \approx 1.5$ at LHC energies [20]. Assuming $K = 1$, as done in [16], gives a conservative lower limit.

Other uncertainties are associated with the presence of the nuclear medium. Experiments [21, 22] have shown that the proton and neutron structure functions are modified by a nuclear environment. For momentum fractions $x < 0.1$ and $0.3 < x < 0.7$, a depletion is observed in the nuclear parton distributions. The low x, or shadowing, region and the larger x, or EMC region, is bridged by an enhancement known as antishadowing for $0.1 < x < 0.3$. The entire characteristic modification as a function of x is commonly referred to as shadowing. Therefore to take this effect into account in nucleus-nucleus collisions, the convolution of the parton densities is modified so that

$$f_{i/A}(x_1, p_{\mathrm{T}}^2) f_{j/A}(x_2, p_{\mathrm{T}}^2) \to$$
$$S^i(A, x_1, p_{\mathrm{T}}^2) f_{i/p}(x_1, p_{\mathrm{T}}^2) S^j(A, x_2, p_{\mathrm{T}}^2) f_{j/p}(x_2, p_{\mathrm{T}}^2) . \tag{2.2}$$

When $S(A, x, p_{\mathrm{T}}^2) = 1$, there is no shadowing. The shadowing effect is studied with two parameterizations previously used to estimate the effect on heavy quark production in nucleus-nucleus collisions [23] as well as a third, more recent one [24,25]. All are based on nuclear deep-inelastic scattering data and are averaged over the nuclear volume. The first, $S_1(A, x)$, is based on fits to recent nuclear deep inelastic scattering data [26]. It treats the quark, gluon and antiquark functions equally without Q^2 evolution. The second, $S_2^i(A, x, Q^2)$, separately modifies the valence quark, sea quark and gluon densities and includes Q^2 evolution up to 100 GeV^2 [27] but is based on the Duke-Owens parton distributions [28]. The most recent shadowing parameterization, $S_3^i(A, x, Q^2)$, based on the GRV LO parton distributions [29], evolves each parton distribution separately for $Q^2 \geq 2.25$ GeV^2 [24,25]. Note that the spatial dependence of the parton densities is not considered in these calculations but uses the average results measured in nuclear deep-inelastic scattering. The possible effects of this spatial dependence have been considered for $c\bar{c}$ and $b\bar{b}$ production [30] as well as the application to the initial conditions discussed in this section [31].

The resulting rapidity distributions are shown in Figs. 2.1 and 2.2 for the two sets of parton distributions with and without shadowing. The cross sections are given in units of mb per nucleon pair. Note that the shadowing
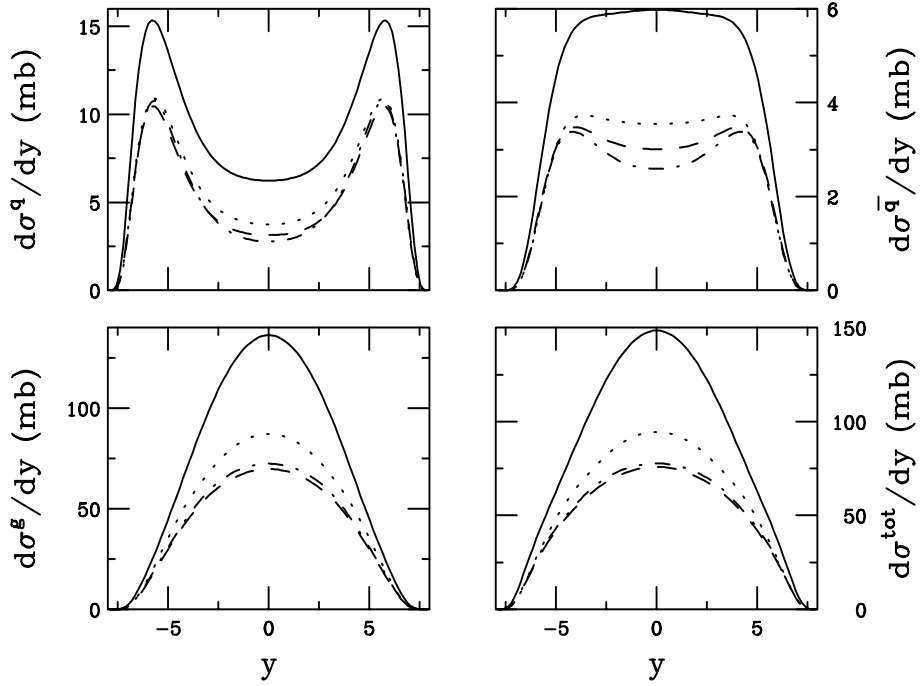
Fig. 2.1. The rapidity distributions of quarks, antiquarks, gluons and the sum of all contributions in Pb+Pb collisions at $\sqrt{s} = 5.5$ TeV in units of mb per nucleon pair calculated with the GRV 94 LO parton distributions. The *solid curve* is with no shadowing, the dashed is with shadowing parameterization S_1, the dot-dashed is with parameterization S_2 and the dotted uses S_3. Taken from [31]
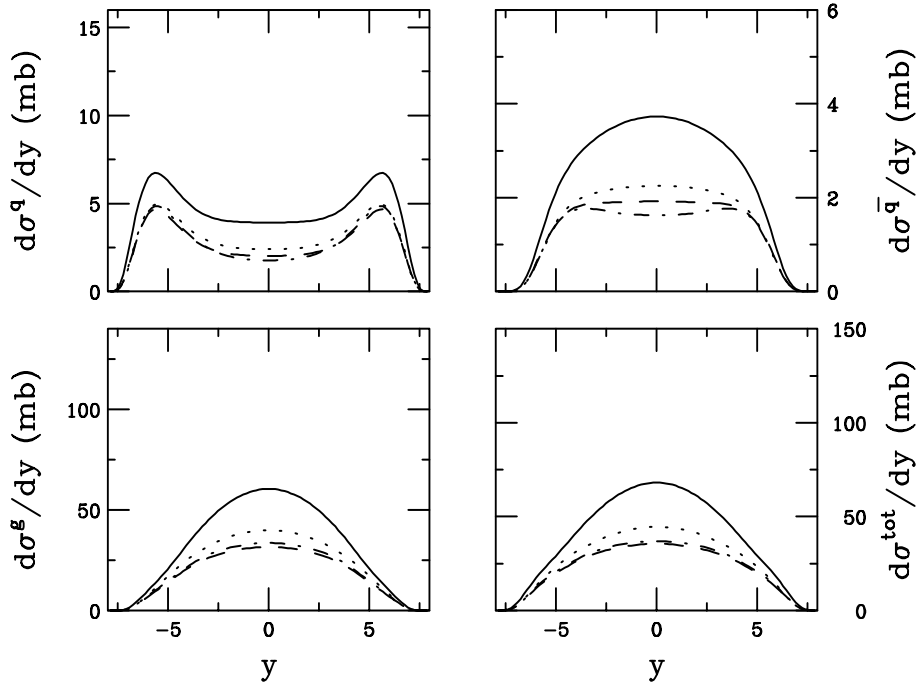

Fig. 2.2. The rapidity distributions of quarks, antiquarks, gluons and the sum of all contributions in Pb+Pb collisions at $\sqrt{s} = 5.5$ TeV in units of mb per nucleon pair calculated with the MRST LO parton distributions. The *solid curve* is with no shadowing, the *dashed* is with shadowing parameterization S_1, the *dot-dashed* is with parameterization S_2 and the *dotted* uses S_3. Taken from [31]

can reduce the number of produced partons by a factor of two or more, depending on the parameterization and the parton type. The smallest shadowing effect is found with the newer S_3 parameterization.

Assuming that the shadowing is independent of impact parameter, the average number of partons produced in a Pb+Pb collision in the CMS acceptance, $|\eta| < 2.4$, can be calculated. In collisions at $b = 0$, the total number of partons of flavour f is then

$$\overline{N}^f_{AA}(b = 0, \sqrt{s}, p_0) = 2T_{AA}(b = 0)\,\sigma^f(\sqrt{s}, p_0) \quad (2.3)$$

where $T_{AA}(b)$ is the nuclear overlap function [32,33],

$$T_{AA}(b) = \int \mathrm{d}^2 s\, T_A(s)\, T_A(|b - s|) . \quad (2.4)$$

The nuclear overlap is the convolution of the two nuclear profile functions, $T_A(b) = \int \mathrm{d}z \rho_A(b, z)$, calculated using measured nuclear density distributions [34]. For estimates of conditions in central, $b = 0$, Pb+Pb collisions, $T_{AA}(0) \approx A^2/(\pi R_A^2) \propto A^{4/3} = 30.4/\mathrm{mb}$ is used. The transverse area of the system and the initial volume in the nuclear rest frame with the lead radius, $R_{\mathrm{Pb}} = 6.62$ fm, are

$$A_T = \pi R_{\mathrm{Pb}}^2 = 137.8 \text{ fm}^2 \quad (2.5)$$
$$V_i = A_T \Delta y/p_0 = 65.28 \text{ fm}^3 , \quad (2.6)$$

where $\tau_i = 1/p_0$ with $p_0 = 2$ GeV is used to calculate the volume. The average number of each type of parton in the CMS acceptance is shown in Table 2.1, with and without shadowing[2].

Parton production saturates when the transverse area occupied by the partons is larger than the total transverse area available. The total number of partons produced in a $b = 0$ collision is the sum over flavours,

$$\overline{N}^H_{AA}(0) = \sum_f \overline{N}^f_{AA}(0, \sqrt{s}, p_0) \quad (2.7)$$

The partons occupy a transverse area $\pi \overline{N}^H_{AA}(0)/p_0^2$. Saturation occurs when the area occupied by partons is equivalent to the transverse area of the target in a symmetric heavy ion collision at $b = 0$, $\overline{N}^H(0) > R_A^2 p_0^2$. In Pb+Pb collisions, saturation occurs if the hard cross section is greater than 74 $(p_0/2 \text{ GeV})^2$ mb. At the LHC, gluons alone are sufficient to saturate the transverse area, even with shadowing.

These conclusions depend on the small x behaviour of the gluon distribution, the factor K_{jet}, the cutoff p_0, and the shadowing parameterization. Transverse saturation does not occur at the LHC when the MRST LO set is used if $K_{\mathrm{jet}} = 1$. An empirical K_{jet} may be obtained by comparing model calculations to data, giving some freedom in the value of K_{jet} for different parton distributions.

However, less variation is allowed in the theoretical values of K_{jet} obtained from the ratio of the NLO and LO cross sections. The theoretical K_{jet} does, however, tend to rise as p_T decreases, rendering calculations with $p_0 < 2$ GeV less reliable.

Transverse saturation at $p_0 = 2$ GeV implies that the minijet cross section exceeds the inelastic pp cross section, violating unitarity. This is especially a problem for the GRV 94 LO distributions because of the high gluon density at low x. At very low x then, the proton is like a black disc and instead of further splitting to increase the density of partons, the partons begin to recombine, acting to lower the density below that without recombination. Therefore at very low x, the density of partons should not increase without bound but begin to saturate. This recombination corresponds to one picture of shadowing in the proton [35]. A recent HERA measurement of the derivative of the structure function F_2 found that at low x and Q^2, $\mathrm{d}F_2/\mathrm{d}\ln Q^2$ no longer increases, in contrast to the GRV 94 parton densities which continue to increase over the range of their validity [36]. The newer MRST distributions have been tuned to fit this behaviour for $Q^2 > 1$ GeV^2. This data implies that the unitarity violation in pp interactions is likely an artifact of the free proton parton densities.

The magnitude of the problem can be gauged by calculating the number of collisions suffered by incoming partons. If, on average, a parton collides more than once while crossing the nucleus, unitarity violation is a serious problem. The higher the incoming parton x_1, the more low x_2 target partons are available for it to interact with, the larger the interaction cross section, and the subsequent number of collisions. The minimum x_2 depends on p_0 and $\sqrt{s}$. Since the gluon interaction cross sections are larger than those of quarks, incoming gluons with $x = 0.1$ are chosen. The average number of collisions experienced by such an initial gluon at the LHC is shown in Figs. 2.3a and b for GRV 94 LO and MRST LO distributions respectively. The scattering cross section has been multiplied by the nuclear profile function $T_A(b)$ to give the number of collisions. A gluon can suffer up to an average of 5 hard scatterings in central collisions with GRV 94 LO and $S = 1$. It experiences less than one collision in the target when $b > 5 - 6$ fm. Shadowing reduces the severity of the problem by decreasing the number of scatterings by $\approx 30\%$. On the other hand, u and $\overline{u}$ quarks with $x = 0.1$ typically scatter once or less in the target, even without shadowing. With the MRST LO distributions, the unitarity violation is less severe, with $1.4 - 2$ scatterings per central collision for gluons and 0.5 u or $\overline{u}$ collisions per central event. Therefore one might expect that to satisfy unitarity, transverse saturation cannot be used as a criteria for determining p_0 and early equilibration by minijet production is unlikely in reality.

To calculate further the initial conditions such as the energy density and the produced particle multiplicity, the transverse energy carried by the partons is needed. Estimates of the initial conditions depend on the first E_T moment of each flavour, $\sigma(\sqrt{s}, p_0)\langle E_T^f \rangle$, calculated within

---

[2] Note that in these and in the following calculations, including the spatial dependence of shadowing increases the effect at small x in central collisions at this energy [30].

Table 2.1. The average number of partons, (2.3), average parton transverse energy, (2.11), and energy density, (2.12), in central Pb+Pb collisions at $\sqrt{s} = 5.5$ TeV/nucleon within the CMS acceptance. Results are given for both sets of parton distributions used and separated into contributions from quarks, antiquarks and gluons as well as the total. The calculations are done without shadowing, $S = 1$, and with shadowing parameterizations S_1, S_2 and S_3

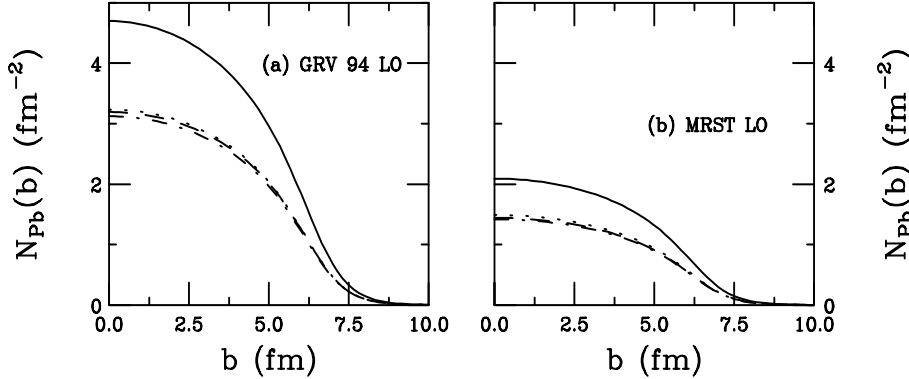|	GRV 94 LO				MRST LO			
S	q	$\bar{q}$	g	total	q	$\bar{q}$	g	total
	$\overline{N}_{\mathrm{Pb+Pb}}(0, \sqrt{s}, p_0)$							
1	928.5	852.9	18384.7	20166.1	576.7	529.7	8327.4	9433.8
S_1	478.2	439.0	9622.2	10539.7	283.6	260.6	4150.6	4694.8
S_2	437.2	384.5	10015.3	10837.0	252.4	219.8	4447.1	4919.4
S_3	568.6	512.5	11948.7	13029.7	342.7	306.9	5344.1	5993.7
	$\overline{E}_{\mathrm{T}}^{f}(0, \sqrt{s}, p_0)$ (GeV)							
1	2888.8	2623.9	54534.6	60046.1	1845.5	1674.3	26348.0	29867.8
S_1	1515.0	1372.6	28892.8	31780.2	924.6	839.0	13329.0	15092.6
S_2	1460.3	1266.6	31695.0	34421.9	879.3	754.5	15169.0	16802.8
S_3	1858.3	1652.2	36957.3	40465.4	1161.5	1024.6	17769.0	19955.1
	$\epsilon^{f}(0, \sqrt{s}, p_0)$ (GeV/fm^3)							
1	44.25	40.19	835.39	919.82	28.27	25.65	403.6	457.5
S_1	23.21	21.03	442.60	486.83	14.16	12.85	204.2	231.2
S_2	22.37	19.40	485.52	527.30	13.47	11.56	232.4	257.4
S_3	28.47	25.31	566.13	619.88	17.79	15.70	272.2	305.7

Fig. 2.3. The number of scatters suffered by an incoming gluon as a function of impact parameter at $x_1 = 0.1$ are shown in **a** and **b** for GRV 94 LO and MRST LO parton densities respectively. The *solid curve* is without shadowing, the *dashed* is with shadowing parameterization S_1, the *dot-dashed* is with S_2 and the *dotted* uses S_3. Adapted from [31]

the CMS acceptance. A crude approximation of the acceptance is

$$\epsilon(y) = \begin{cases} 1 & \text{if } |y| \leq 2.4 \\ 0 & \text{otherwise} \end{cases} . \qquad (2.8)$$

Note that at leading order, the parton pairs are produced back-to-back whilst at next-to-leading order the angular distribution is somewhat smeared, potentially modifying the E_{T} moments. The E_{T} distribution of each flavour is [16]

$$\frac{\mathrm{d}\sigma^f}{\mathrm{d}E_{\mathrm{T}}}(\sqrt{s}, p_0) = \frac{1}{2} \int \mathrm{d}p_{\mathrm{T}}^2 \mathrm{d}y_2 \mathrm{d}y \sum_{\substack{ij= \\ \langle kl \rangle}} x_1 f_{i/A}(x_1, p_{\mathrm{T}}^2) x_2 f_{j/A}$$

$$\times (x_2, p_{\mathrm{T}}^2) \frac{1}{1 + \delta_{kl}} \left\{ \frac{\mathrm{d}\hat{\sigma}^{ij \to kl}}{\mathrm{d}\hat{t}}(\hat{t}, \hat{u})\delta(E_{\mathrm{T}} - [\delta_{fk}\epsilon(y) \right.$$

$$+ \delta_{fl}\epsilon(y_2)]p_{\mathrm{T}}) + \frac{\mathrm{d}\hat{\sigma}^{ij \to kl}}{\mathrm{d}\hat{t}}(\hat{u}, \hat{t})\delta(E_{\mathrm{T}} - [\delta_{fl}\epsilon(y)$$

$$\left. + \delta_{fk}\epsilon(y_2)]p_{\mathrm{T}}) \right\} . \qquad (2.9)$$

The first E_{T} moment is obtained by integrating (2.9) over E_{T} so that

$$\sigma(\sqrt{s}, p_0)\langle E_{\mathrm{T}}^f \rangle = \int \mathrm{d}p_{\mathrm{T}}^2 \mathrm{d}y_2 \mathrm{d}y \sum_{\substack{ij= \\ \langle kl \rangle}} x_1 f_{i/A}$$

$$\times (x_1, p_{\mathrm{T}}^2) \, x_2 f_{j/A}(x_2, p_{\mathrm{T}}^2) \frac{1}{1 + \delta_{kl}}$$

Table 2.2. The total multiplicity, (2.15), and initial temperature, (2.14), within the CMS acceptance. Results for gluons alone as well as for the total are given for both sets of parton distributions. The calculations are done without shadowing, $S = 1$, and with shadowing parameterizations S_1, S_2 and S_3.

S	GRV 94 LO		MRST LO	
	g	total	g	total
		dN/dy		
1	4004.6	5649.3	2319.9	3345.8
S_1	2486.8	3505.5	1391.5	2005.3
S_2	2665.6	3721.7	1533.3	2173.4
S_3	2991.1	4201.9	1726.4	2472.5
		T_i (MeV)		
1	1051	820	876	689
S_1	897	699	739	581
S_2	918	714	763	596
S_3	954	743	794	623

$$\times \left[\delta_{fk} \frac{d\hat{\sigma}^{ij \to kl}}{d\hat{t}}(\hat{t}, \hat{u}) + \delta_{fl} \frac{d\hat{\sigma}^{ij \to kl}}{d\hat{t}}(\hat{u}, \hat{t}) \right] \epsilon(y) p_T \ . \tag{2.10}$$

The E_T moment is given as a function of rapidity in Figs. 2.4 and 2.5 both with and without shadowing for the GRV 94 LO and MRST LO parton densities. The average transverse energy given to a particular parton species in a central Pb+Pb collision within the CMS acceptance is then

$$\overline{E}_T^f(b = 0, \sqrt{s}, p_0) = T_{AA}(b = 0)\, \sigma(\sqrt{s}, p_0)\langle E_T^f \rangle \ , \tag{2.11}$$

where $\sigma(\sqrt{s}, p_0)\langle E_T^f \rangle$ is calculated in (2.10). The energy density of each parton species in a central collision in the CMS acceptance then follows:

$$\epsilon^f = \frac{\overline{E}_T^f(0, \sqrt{s}, p_0)}{V_i} \ . \tag{2.12}$$

The results from (2.11) and (2.12) are given in Table 2.1 both with and without shadowing. Again, shadowing can reduce the average transverse energy and energy density by up to a factor of two.

In an ideal plasma, the evolution of the energy density is governed by [37]

$$\frac{d\epsilon}{d\tau} + \frac{\epsilon + P}{\tau} = 0 \tag{2.13}$$

where P is the pressure and τ denotes time. There are two extreme cases for the evolution: free streaming, $P = 0$, leading to $\epsilon \sim \tau^{-1}$ and ideal hydrodynamics, $P = \epsilon/3$, where $\epsilon \sim \tau^{-4/3}$. The lower limit of multiplicity is obtained from ideal hydrodynamics where the system is assumed to be in thermal equilibrium at $\tau = 1/p_0 = 0.1$ fm and expands adiabatically with τ. Then the initial entropy determines the final-state multiplicity. The energy

and entropy densities are $\epsilon = 3aT^4$ and $s = 4aT^3$ where $a = \gamma_{dof}\pi^2/90$, proportional to the number of degrees of freedom with $\gamma_{dof} = 16$ for a gluon gas and 47.5 for a plasma with gluons and three light quark flavours. The initial temperature can be related to the energy density by

$$T_i = \left(\frac{\epsilon}{3a} \right)^{1/4} \ . \tag{2.14}$$

The final multiplicity in the CMS acceptance is then [38]

$$\frac{dN}{dy} \approx \frac{1}{3.6} \frac{dS}{dy} \approx \frac{1}{3.6} \tau_i \pi R_A^2 4aT_i^3$$
$$= \frac{4}{3.6} \left[\frac{\tau_i \pi R_A^2 a}{27} \left\{ \frac{\overline{E}_T^{PbPb}(|y| \leq 2.4)}{\Delta y} \right\}^3 \right]^{\frac{1}{4}} \ , \tag{2.15}$$

where T_i and $\overline{E}_T$ are related by (2.12) and (2.14). The multiplicities and initial temperatures for a pure gluon plasma and a quark-gluon plasma with three quark flavours, calculated with (2.15), are given in Table 2.2. Note that for the GRV 94 LO distributions, the total multiplicity at $y = 0$ is $\approx 4000 - 6000$ or about 2700-4000 charged particles. Shadowing reduces the number of charged particles to $\approx 1800 - 2600$. Again, as with the average parton number, the gluon E_T moment dominates the total and drives the rapidity distribution, as can be inferred from Figs. 2.4 and 2.5. Note that even though the initial energy density is higher when the quarks are included, the temperature is higher in the gluon plasma since the energy is distributed over fewer degrees of freedom. In either case, T_i is large, nearly 1 GeV for a gluon gas based on the GRV 94 LO parton densities. The initial conditions deduced from minijet production yield significantly larger values of $\epsilon(\tau_i)$ and T_i and, consequently, larger multiplicities than earlier estimates (see e.g. [39]). The reason for this is twofold: the fast gluon equilibration time, $\tau_i \sim 1/p_0 \sim 0.1$ fm, and the increase in the parton density at small x as seen at HERA [17]. These high temperatures have important consequences for QGP signatures. Note also that even though shadowing reduces the number of partons and the energy density by up to a factor of two, the corresponding reduction in the multiplicity is lower and the initial temperature is reduced by only 10-15% when shadowing is included, as can be seen in Table 2.2.

Minijet production thus tends to enhance the probability of QGP production in thermal equilibrium. Effects like shadowing reduce the initial energy density and temperature, taking the system further away from equilibrium. A QGP would still be formed, although not an equilibrated plasma. It is important to determine the effects of minijet production and shadowing on the proposed plasma signatures.

2.3 Quarkonium production and suppression in CMS

One of the proposed signatures of the QCD phase transition is the suppression of quarkonium production [40,
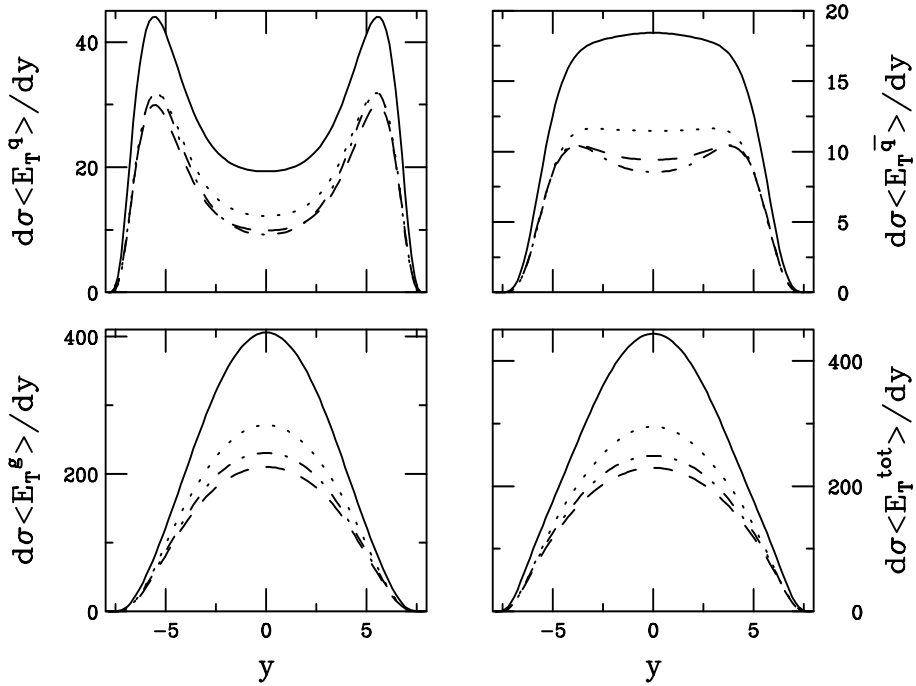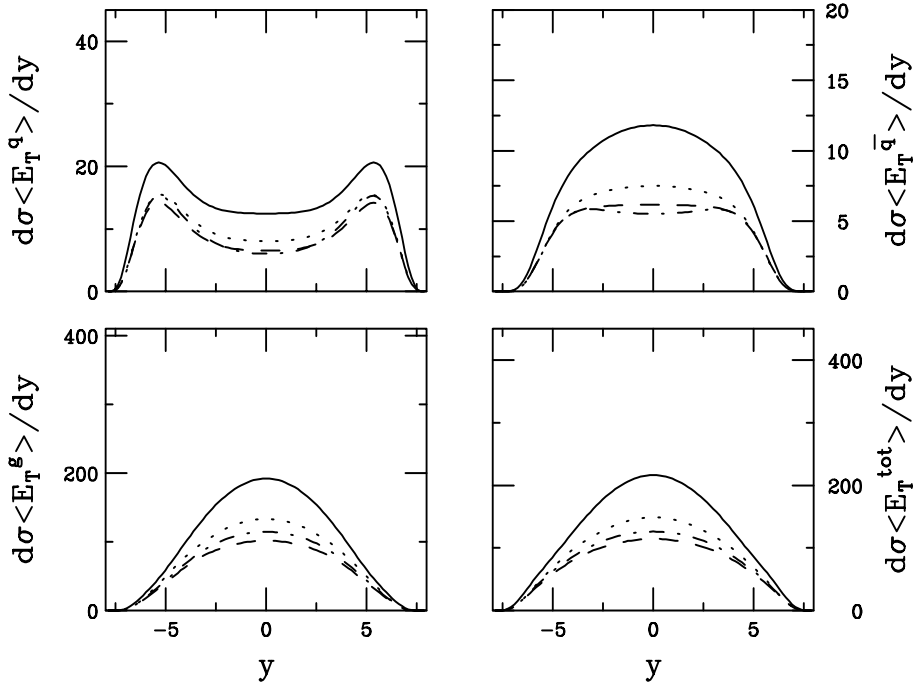
Fig. 2.4. The first E_T moment, $\sigma(\sqrt{s}, p_0)\langle E_T^f \rangle$, as a function of rapidity for quarks, antiquarks, gluons and the sum of all contributions in Pb+Pb collisions at $\sqrt{s} = 5.5$ TeV in units of mb×GeV per nucleon pair calculated with the GRV 94 LO parton distributions. The *solid curve* is with no shadowing, the *dashed* is with shadowing parameterization S_1, the *dot-dashed* is with parameterization S_2 and the *dotted* uses S_3. Taken from [31]

Fig. 2.5. The first E_T moment, $\sigma(\sqrt{s}, p_0)\langle E_T^f \rangle$, as a function of rapidity for quarks, antiquarks, gluons and the sum of all contributions in Pb+Pb collisions at $\sqrt{s} = 5.5$ TeV in units of mb GeV per nucleon pair calculated with the MRST LO parton distributions. The *solid curve* is with no shadowing, the *dashed* is with shadowing parameterization S_1, the *dot-dashed* is with parameterization S_2 and the *dotted* uses S_3. Taken from [31]

Table 2.3. Properties of the quarkonium states both at $T = 0$ and $T = T_D$, taken from [41]. The masses, radii and formation times at $T = 0$ are obtained by solving the Schrödinger equation [41]. The value of T_D is determined by the functional form of $\mu(T)$. The screening mass at breakup, μ_D does not depend on the functional form

	J/ψ	ψ'	$\chi_c(1P)$	Υ	Υ'	$\chi_b(1P)$
M (GeV)	3.07	3.698	3.5	9.445	10.004	9.897
r (fm)	0.453	0.875	0.696	0.226	0.509	0.408
τ_F (fm)	0.89	1.5	2.0	0.76	1.9	2.6
μ_D (GeV)	0.699	0.357	0.342	1.565	0.671	0.558

Table 2.4. The values of T_D for the two choices of $\mu(T)$, (2.16) from perturbative estimates assuming the high-temperature limit and the pure gluon SU(N) case with $n_f = 0$, (2.19)

T_D (MeV)					
	$n_f = 2$	$n_f = 3$	$n_f = 4$	$n_f = 0$	Eq. (2.19)
J/ψ	451	406	366	541	260
ψ'	211	189	170	260	260
χ_c	185	178	170	260	260
Υ	1105	994	901	1326	391
Υ'	434	386	352	512	260
χ_b	350	314	282	416	260

41]. Suppression of the J/ψ and ψ' has been observed in nucleus-nucleus collisions at the CERN SPS [10]. In a QGP, the suppression occurs due to the shielding of the $c\bar{c}$ binding potential by colour screening, leading to the breakup of the resonance. The $c\bar{c}$ and $b\bar{b}$ resonances have smaller radii than light-quark hadrons and therefore need higher temperatures for the quarkonium states to break up. At current energies, the situation for the J/ψ is rather ambiguous because the bound state can also break up through interactions with nucleons and comoving hadrons—QGP production has not been proved to be the unique explanation of J/ψ suppression even though an increased density of secondary production is needed, see [11]. Because the Υ is much smaller than the $c\bar{c}$ and other $b\bar{b}$ resonances, a much higher temperature is needed to dissociate the Υ [41]. Therefore it was previously assumed that the Υ would not be suppressed by QGP production [41, 42]. However, in view of the high initial temperature of a gluon plasma, $T \sim 0.9 - 1$ GeV, as shown in Table 2.2, it was recently shown that, depending upon the properties of the plasma, the Υ could be suppressed, providing a valuable tool to determine the initial state of the system and the characteristics of the plasma [43].

At zero temperature, the massive $Q\bar{Q}$ bound states of charmonium and bottomonium can be described by a nonrelativistic potential model with a linear confining term and a Coulomb-like one gluon exchange term. The quarkonium mass, radius and formation time at $T = 0$ are given in Table 2.3.

In a high temperature environment, the quarkonium binding energy may be reduced due to colour screening where the screening mass, $\mu(T)$, is a function of temperature [41]. Minimizing the quarkonium energy at each temperature gives the radius of the bound state as a function of T. For $\mu(T)$ above the critical value, μ_D, there is no longer a minimum and the screening has become strong enough to prevent the formation of the resonance at temperature T_D where $\mu(T_D) = \mu_D$. The values of μ_D for the quarkonium states are also given in Table 2.3. The actual values of T_D depend upon the functional form of $\mu(T)$.

Perturbative estimates of the screening suggest that $\mu(T) \propto gT$ [44],

$$\frac{\mu(T)}{T_c} = \sqrt{1 + \frac{n_f}{6}}\, g\left(\frac{T}{T_c}\right)\frac{T}{T_c}\,, \qquad (2.16)$$

where the temperature-dependent running coupling constant is

$$g^2\left(\frac{T}{T_c}\right) = \frac{48\pi^2}{(33 - 2n_f)\ln F^2}\,, \qquad (2.17)$$

with $F = K(T/T_c)(T_c/\Lambda_{\overline{MS}})$ and K is also in principle temperature dependent [45]. In SU(3) gauge theory, $T_c = 260$ MeV [46] and $T_c/\Lambda_{\overline{MS}} = 1.03 \pm 0.19$ [47]. A fit to the heavy quark potential in the high temperature limit, $T \gg T_c$, yields the constant $K \approx 33.8$ [45]. Lattice results with $n_f = 2$ and 4 suggest $T_c = 170$ MeV and $T_c/\Lambda_{\overline{MS}} = 1.05$ [47]. Realistically, the high temperature limit is probably invalid for $T/T_c \leq 3.5$ [48]. Then fitting K to lattice results for $T \geq T_c$ yields [45],

$$K(T/T_c) = \frac{18}{18.4e^{-0.5(T/T_c)^2} + 1}\,. \qquad (2.18)$$

The lower values of $K(T/T_c)$ near T_c result in larger values of $\mu(T)$, suggesting $T_D = T_c$ for all states except the Υ. As shown in Fig. 2.6 for $n_f = 3$, the two different limiting assumptions of K produce similar results for $\mu(T)$ when $T/T_c \geq 3$ even though below this ratio, they are quite different.

In their prediction of J/ψ suppression, Matsui and Satz [40] used a parameterization based on SU(N) lattice simulations [49],

$$\frac{\mu(T)}{T_c} \simeq 4\frac{T}{T_c}\,, \qquad (2.19)$$

which produces values of T_D similar to the results with (2.18) except for the Υ. This parameterization is also shown in Fig. 2.6 for $T_c = 260$ MeV.

Due to the uncertain behaviour of $\mu(T)$ above T_c, the suppression hierarchy of the quarkonium states in several possible scenarios, described below, is given. The values obtained for T_D in each case are shown in Table 2.4.

Two cases are chosen for further illustration: i) $n_f = 3$ in the high-temperature limit and ii) $T_D = T_c = 260$ MeV ($n_f = 0$ and SU(3)), (2.19).

As a first step toward studying colour screening with the Υ family, it must be determined if the Υ production rate is large enough for the suppression measurement to
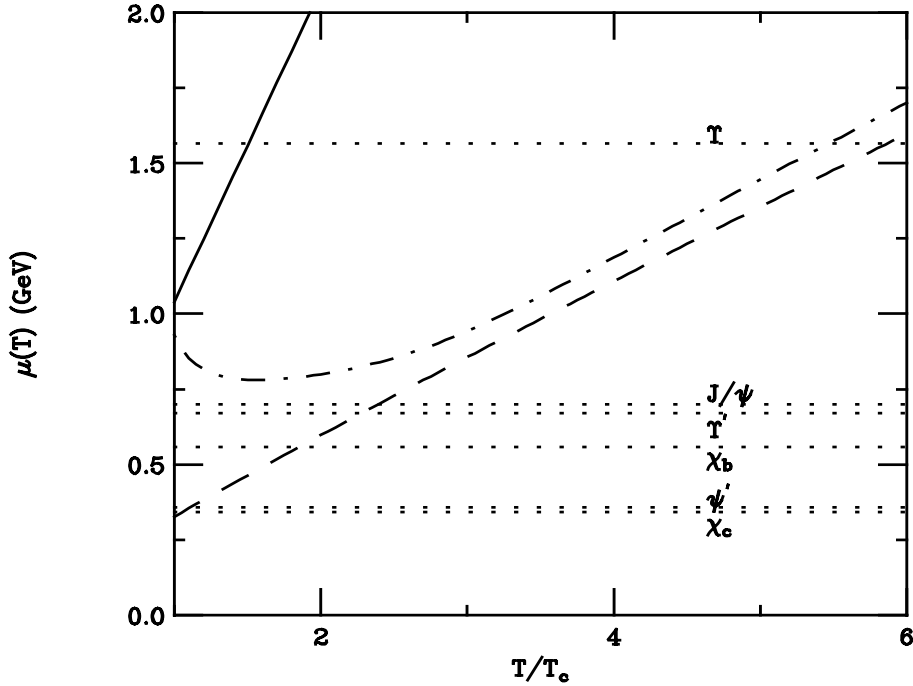
Fig. 2.6. The screening mass as a function of temperature for (2.19) with $T_c = 260$ MeV (*solid*). The *dashed* and *dot-dashed* curves take $\mu \propto gT$, (2.16), with $n_f = 3$ in the high temperature limit and the low T fit, (2.18) respectively. The values of μ_D for the quarkonium states are indicated by the *dotted lines*. From [11]

be feasible. To do this, the phenomenologically successful colour evaporation model [50] is used. In this model, the $Q\overline{Q}$ pair neutralizes its colour by interaction with the collision-induced colour field—"colour evaporation". The Q and the $\overline{Q}$ either combine with light quarks to produce heavy-flavoured hadrons or bind with each other in a quarkonium state. The additional energy needed to produce heavy-flavoured hadrons is obtained nonperturbatively from the colour field in the interaction region. Depending on m_b, the yield of all bottomonium states may be only a small fraction of the total $b\bar{b}$ cross section below the $\sqrt{\hat{s}} = 2m_B$ threshold. At leading order,

$$\tilde{\sigma}(s) = \sum_{i,j} \int_{4m_b^2}^{4m_B^2} d\hat{s} \int dx_1 dx_2 \; f_{i/p}(x_1) \; f_{j/p}(x_2)$$
$$\times \sigma_{ij}(\hat{s}) \; \delta(\hat{s} - x_1 x_2 s) \;, \qquad (2.20)$$

where $ij = q\bar{q}$ or gg and $\sigma_{ij}(\hat{s})$ is the $ij \to b\bar{b}$ subprocess cross section. The colour evaporation model was taken to next-to-leading order (NLO) using exclusive $Q\overline{Q}$ hadroproduction [51] to obtain the energy, x_F, and p_T-dependence of quarkonium production [52,53]. In the colour evaporation picture, gg scattering followed by the splitting $g \to b\bar{b}$ incorporated at NLO is similar to models of $g \to \Upsilon$ fragmentation [54]. By including this splitting, the colour evaporation model provides a good description of the quarkonium p_T distributions.

The division of $\tilde{\sigma}$ into heavy-flavoured hadrons and quarkonium as well as the relative quarkonium production rates are parameters in the colour evaporation model. Once these parameters have been determined for a sys-

tem, the model has significant predictive power if the relative quarkonium production rates are independent of projectile, target, and energy. This appears to be true for the charmonium ratios χ_c/ψ and ψ'/ψ over a broad energy range [55, 56, 57, 58]. The available bottomonium data also follow this trend: $\Upsilon'/\Upsilon = 0.53 \pm 0.13$ and $\Upsilon''/\Upsilon = 0.17 \pm 0.06$ for pp interactions at 400 [59] and 800 GeV [60,61] and in $p\bar{p}$ collisions at the Tevatron, $\sqrt{s} = 1.8$ TeV [62]. The colour evaporation model also reproduces the energy dependence of charmonium and bottomonium production as well as most of the x_F dependence of the charmonium states[3]. The Tevatron charmonium and bottomonium p_T data are also in good agreement with the model at NLO [53].

Using the measured Υ'/Υ and Υ''/Υ ratios, the normalization of each quarkonium state can be fixed empirically from data, allowing predictions of the production cross sections at LHC energies.

First, the model is compared with existing $pp/p\bar{p}$ data. Fixed target Υ data have generally given the sum of Υ, Υ', and Υ'' production, especially if the mass resolution is not good enough to clearly separate the peaks. From the cross section at $y = 0$, $B(d\sigma/dy)_{y=0}$, where B is an effective dilepton branching ratio from all states, a good fit to the data [59–61,64,65] is obtained with

$$B\left(\frac{d\sigma(s)}{dy}\right)_{y=0} = 1.33 \; \times 10^{-3} \; \left(\frac{d\tilde{\sigma}(s)}{dy}\right)_{y=0} \;. \; (2.21)$$

---

[3] At high x_F, other production mechanisms such as intrinsic heavy quarks [63] may be important. Additionally, the x_F dependence in nuclear targets is non-trivial.

The cross section $d\tilde{\sigma}/dy$ is computed using the GRV 94 LO [18] and MRS G [66] parton densities with $m_b = 4.75$ GeV and the renormalization and factorization scales set to $\mu = m_{\mathrm{T},b\bar{b}} = \sqrt{m_b^2 + (p_{\mathrm{T},b}^2 + p_{\mathrm{T},\bar{b}}^2)/2}$ reflecting the production yield through the Υ, Υ', and Υ'' resonances. As shown in Fig. 2.7, from [52] with updated parton densities, the high energy data from UA1 [67] and CDF [62] also agree with the energy dependence of the colour evaporation model, as obtained from (2.20). The MRS G distributions produce a better fit to the data than the GRV 94 LO densities, as may be expected since the NLO parton density is more compatible with the NLO calculation. The GRV 94 LO densities are included since they were used to determine the initial conditions. However, the predictions of the Υ yield will be given with the MRS G densities.

The indirect Υ, Υ' and Υ'' components are extracted separately using the Υ'/Υ and Υ''/Υ ratios, and the known branching ratios $B_{\Upsilon_i} \equiv B(\Upsilon_i \to \mu^+\mu^-)$ where Υ_i represents the individual Υ states. If $d\sigma_{\Upsilon_i}/dy|_{y=0} \equiv f_{\Upsilon_i}^{\mathrm{in}} d\tilde{\sigma}/dy|_{y=0}$ for the Υ_i cross sections, then from (2.21),

$$f_\Upsilon^{\mathrm{in}} B_\Upsilon + f_{\Upsilon'}^{\mathrm{in}} B_{\Upsilon'} + f_{\Upsilon''}^{\mathrm{in}} B_{\Upsilon''} = B = 0.00133 \,. \quad (2.22)$$

Using $f_{\Upsilon'}^{\mathrm{in}}/f_\Upsilon^{\mathrm{in}} = \Upsilon'/\Upsilon = 0.53$ and $f_{\Upsilon''}^{\mathrm{in}}/f_\Upsilon^{\mathrm{in}} = \Upsilon''/\Upsilon = 0.17$ [59–62] and B_{Υ_i} [68],

$$f_\Upsilon^{\mathrm{in}} = 0.038 \,, \quad f_{\Upsilon'}^{\mathrm{in}} = 0.02 \,, \quad f_{\Upsilon''}^{\mathrm{in}} = 0.0065 \,, \quad (2.23)$$

which are slightly smaller than found in [53], perhaps due to the difference in the small x behaviour of the parton densities.

Finally, direct and indirect production are separated. The measured Υ_i production cross sections, or equivalently $f_{\Upsilon_i}^{\mathrm{in}}$, are only effective values which reflect both direct production and chain decays of higher mass states. For each i, it is assumed that

$$f_{\chi_{bi}(1P)}^{\mathrm{d}} = f_{\Upsilon'}^{\mathrm{in}} \,; \quad f_{\chi_{bi}(2P)}^{\mathrm{d}} = f_{\Upsilon''}^{\mathrm{in}} \,, \quad (2.24)$$

where $i = 0, 1, 2$ labels the χ_b states in Particle Data Group notation [68], and $f_{\Upsilon_i}^{\mathrm{d}}$ indicates the fraction of $\tilde{\sigma}$ from *direct* production. With this and the summed branching ratios [68]

$$\sum_{i=0,1,2} B(\chi_{bi}(1P) \to \Upsilon\gamma) \sim 0.63 \,,$$

$$\sum_{i=0,1,2} B(\chi_{bi}(2P) \to \Upsilon\gamma) \sim 0.16 \,,$$

$$\sum_{i=0,1,2} B(\chi_{bi}(2P) \to \Upsilon'\gamma) \sim 0.42 \,,$$

along with $B(\Upsilon' \to \Upsilon X) \sim 0.27$ and Υ'' decays to Υ', Υ and $\chi_{bi}(2P)$, the $f_{\Upsilon_i}^{\mathrm{d}}$'s for direct production can be found for all the Υ_i. About 0.013 of the total $f^{\mathrm{in}} = 0.038$ is due to $\chi_{bi}(1P)$ decays, similar to the analogous ψ and χ_c fractions. Similarly, ~ 0.001 of f_Υ^{in} and ~ 0.0027 of $f_{\Upsilon'}^{\mathrm{in}}$ would be due to $\chi_{bi}(2P)$ decays. Also important are $\Upsilon' \to \Upsilon X$ decays; from (2.23), $f_{\Upsilon'}^{\mathrm{in}}$ implies that an additional 0.0054

of f_Υ^{in} would be indirect. The contributions from chain decays of the Υ'' are small. Also, there are no contributions to the Υ'' rate coming from higher states that are known to be significant. Altogether:

$$f_\Upsilon^{\mathrm{d}} \sim 0.019 \,, \ f_{\Upsilon'}^{\mathrm{d}} \sim 0.017 \,, \ f_{\Upsilon''}^{\mathrm{d}} \sim 0.0065 \,,$$
$$f_{\chi_{bi}(1P)}^{\mathrm{d}} \sim 0.020 \,, \ f_{\chi_{bi}(2P)}^{\mathrm{d}} \sim 0.0065 \,, \quad (2.25)$$

where $i = 0, 1, 2$ labels the different $\chi_{bi}(1P, 2P)$ states. Note that only about half of f_Υ^{in} is due to direct Υ production.

In Table 2.5, the corresponding normalized direct production cross sections in pp collisions, $f^{\mathrm{d}}\tilde{\sigma}_{pp}$, are given for each state with f^{d} from (2.25) and $\tilde{\sigma}_{pp}$ computed using the MRS G parton densities at $\sqrt{s} = 5.5$ TeV/nucleon. The cross sections in Table 2.5 are integrated over all rapidity. When shadowing is included, the rate per nucleon pair decreases by 55% with the S_1 parameterization, 30% with $S = S_2$ and 26% with S_3.

The results for $f^{\mathrm{d}}\tilde{\sigma}_{pp}$ given in Table 2.5 in pp collisions can be employed to predict the rates for direct production of bottomonium states in Pb+Pb collisions at the LHC. For central collisions, the expected rates are given by

$$N^{\mathrm{d}}(\text{central}) = \sigma_{NN} T_{\mathrm{PbPb}}(0) f^{\mathrm{d}}\tilde{\sigma}_{pp} \mathcal{L}_{\mathrm{int}}^{\mathrm{PbPb}} \,, \quad (2.26)$$

where $\sigma_{NN} T_{\mathrm{PbPb}}(0) = 1824$ is the number of central Pb+Pb collisions[4]. The number of Υ states produced in minimum bias collisions (all impact parameters) is

$$N^{\mathrm{d}}(\text{min bias}) = A^{2\alpha} f^{\mathrm{d}}\tilde{\sigma}_{pp} \mathcal{L}_{\mathrm{int}}^{\mathrm{PbPb}} \,, \quad (2.27)$$

where $\alpha \approx 0.95$ for Υ production at fixed-target energies [12]. In one month (30 days) of running the integrated luminosity for lead beams is expected to be $\mathcal{L}_{\mathrm{int}}^{\mathrm{PbPb}} = 2.59$/nb assuming that $\mathcal{L}^{\mathrm{PbPb}} = 1 \times 10^{27}$ cm^{-2}s^{-1}. Typical rates are on the order of 10^6 for Υ and Υ'. Approximately 10-15% of the cross section is within $|\eta| \leq 1$. The number of muon pairs from the Υ, Υ' and Υ'' decays, found by multiplying the total number of Υ_i directly produced in central or minimum bias collisions, N^{d}, by the appropriate branching ratio, is also given in Table 2.5. These rates suggest that production and suppression of these states should be measurable by CMS in the very clean $\mu^+\mu^-$ final state decay mode.

Since the expected rate is large enough to be measurable before colour screening is taken into account, predictions of how the Υ rate would be modified by QGP production at the LHC are given. With the high temperatures in Table 2.2, strong suppression due to QGP formation might be expected. Unfortunately the short equilibration time of the minijet system correspondingly reduces the plasma lifetime in the scaling expansion, causing the minijet plasma to be too short-lived to produce quarkonium suppression in some cases.

Alternatively, the initial conditions could be dominated by kinetic equilibration processes [69] with a correspondingly longer equilibration time, $t_0 \sim 0.5 - 0.7$ fm.

---

[4] Assuming that σ_{NN} rises as $\sigma_{p\bar{p}}$ at high energies, $\sigma_{NN} \approx 60$ mb.
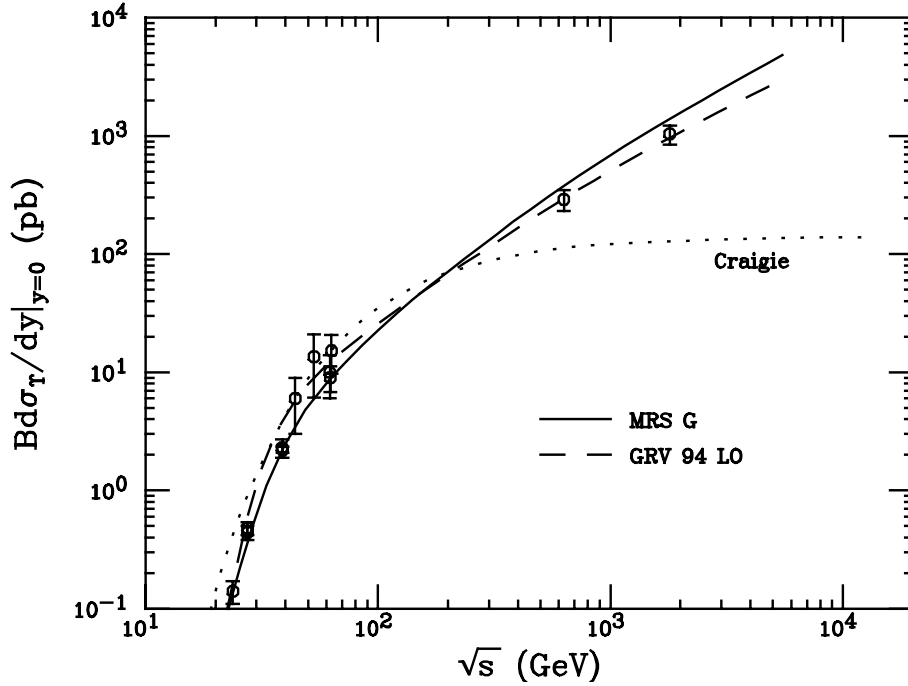
Fig. 2.7. $Bd\sigma/dy|_{y=0}$ is shown for $\Upsilon + \Upsilon' + \Upsilon''$ in pp collisions, as indicated in (2.21), for the MRS G [66] (*solid*) and GRV 94 LO [18] (*dashed*) parton densities. The data are taken from [59,60,62,64,65,67]. This figure is updated from [52]

Table 2.5. The normalized cross sections, $f^{\mathrm{d}}\tilde{\sigma}_{pp}$, for directly produced bottomonium states in pp collisions at $\sqrt{s} = 5.5$ TeV/nucleon, using the direct fractions f^{d} from (2.25) and the prediction of (2.20), $\tilde{\sigma}_{pp} = 15.84$ μb, with the MRS G parton densities, $m_b = 4.75$ GeV and $\mu = m_{\mathrm{T},b\bar{b}}$. Also given is the number, N^{d}, of each type of bottomonium state directly produced in central, (2.26), and minimum bias, (2.27), Pb+Pb collisions. For Υ, Υ' and Υ'' the corresponding number of $\mu^+\mu^-$ pairs from decays of directly produced states, $N^{\mathrm{d}}_{\mu\mu}$, is also given for central and minimum bias collisions. Modified from [43]

	Υ	Υ'	Υ''	$\chi_b(1P)$	$\chi_b(2P)$
$f^{\mathrm{d}}\tilde{\sigma}_{pp}$ (nb)	301	269	103	316	103
N^{d}(central)	1.42×10^6	1.27×10^6	4.87×10^5	1.49×10^6	4.87×10^5
$N^{\mathrm{d}}_{\mu\mu}$(central)	3.52×10^4	1.66×10^4	8.81×10^3	-	-
N^{d}(min bias)	7.64×10^6	6.28×10^6	2.61×10^6	8.02×10^6	2.61×10^6
$N^{\mathrm{d}}_{\mu\mu}$(min bias)	1.89×10^5	8.91×10^4	4.72×10^4	-	-

This time is reached when the momentum distributions are locally isotropic due to elastic scatterings and the expansion of the system. Chemical equilibrium is generally not assumed but the system moves toward equilibrium as a function of time. Then the cooling of the plasma is more rapid than the simple scaling [37] adopted here, producing incomplete suppression at low p_{T}. Because the equilibration time of the parton gas is longer than that obtained from the minijet initial conditions, the time the system spends above the breakup temperature is also longer, leading to stronger suppression even though T_0 is lower.

The time at which the temperature drops below T_D and the state can no longer be suppressed, $t_D = t_0(T_0/T_D)^3$, and the maximum quarkonium p_{T} for which the resonance is suppressed, $p_{\mathrm{Tm}} = M\sqrt{(t_D/\tau_F)^2 - 1}$, are given in Table 2.6 for cases i ($\mu(T) \propto gT$ with $n_f = 3$ in the high temperature limit since $T_0 > 3T_c$) and ii ($\mu(T) = 4T$, SU(3) plasma with $T_c = 260$ MeV) with both

the parton gas and minijet, Table 2.2, initial conditions. Results for the minijet initial conditions are given for the GRV 94 LO parton densities for both $S = 1$ and the lowest temperatures obtained with shadowing when $S = S_1$. Note that the reduction of the initial temperature due to shadowing significantly reduces the p_{T} range of the suppression. However, this result can be distinguished from a case with no significant shadowing and a plasma with a smaller spatial extent [43].

A high statistics study of quarkonium production ratios such as ψ'/ψ and Υ'/Υ as a function of p_{T} may provide a conclusive test of plasma production at high energies. However, before the efficiency of the measurement as a test of QGP formation is proven, the relative importance of other effects must be established. Although shadowing is important, the effects should be cancelled in ratios of quarkonium states with very similar masses, as can be checked by pA studies. Nuclear absorption would

Table 2.6. LHC values of t_D, and p_{Tm} with cases i and ii for $\mu(T)$ with a parton gas and a minijet plasma with $S = 1$ and S_1 from the GRV 94 LO calculation, adapted from [43]

	case i, $n_f = 3$		case ii, $T_c = 260$ MeV	
	parton gas			
	$T_0 = 820$ MeV, $t_0 = 0.5$ fm			
	t_D (fm)	p_{Tm} (GeV)	t_D (fm)	p_{Tm} (GeV)
ψ	4.12	13.96	15.69	54.0
ψ'	40.8	100.6	15.69	38.5
χ_c	48.9	85.47	15.69	27.2
Υ	-	0	4.6	56.53
Υ'	4.79	23.16	15.69	81.98
χ_b	8.90	32.42	15.69	58.9
	minijet plasma, $S = 1$			
	$T_0 = 820$ MeV, $t_0 = 0.1$ fm		$T_0 = 1.05$ GeV, $t_0 = 0.1$ fm	
	t_D (fm)	p_{Tm} (GeV)	t_D (fm)	p_{Tm} (GeV)
ψ	-	0	6.59	22.7
ψ'	8.17	19.8	6.59	15.8
χ_c	9.78	16.75	6.59	11.0
Υ	-	0	1.94	22.2
Υ'	-	0	6.59	33.2
χ_b	-	0	6.59	23.05
	minijet plasma, $S = S_1$			
	$T_0 = 699$ MeV, $t_0 = 0.1$ fm		$T_0 = 897$ MeV, $t_0 = 0.1$ fm	
	t_D (fm)	p_{Tm} (GeV)	t_D (fm)	p_{Tm} (GeV)
ψ	-	0	4.11	13.8
ψ'	5.06	11.9	4.11	9.4
χ_c	6.06	10.0	4.11	6.3
Υ	-	0	1.21	11.7
Υ'	-	0	4.11	19.2
χ_b	-	0	4.11	12.1

also cancel in the ratios if the quarkonium state interacts with nucleons while still in a preresonance colour octet state, as already proposed at fixed-target energies [70]. To complicate matters, the resonances can interact with comoving secondaries. However, even though these cross sections can differ for individual resonances, the p_{T} dependence of these comover interactions is already weak at CERN SPS energies [71] and are expected to be weaker at the LHC [43].

If the ratios exhibit a significant p_{T}-dependence at large p_{T} in AB collisions, it will be virtually certain that a quark gluon plasma was formed. The precise behaviour of the ψ'/ψ and Υ'/Υ ratios can then be used to constrain strongly the QGP model parameters. In particular, the ratios will be very different if only the Υ' or ψ' is suppressed relative to the case where all quarkonium states are suppressed.

In Fig. 2.8, the ratio of the ψ' and ψ cross sections are shown for several sets of initial conditions. Since it has been demonstrated that the χ_c and ψ' contributions to large p_{T} J/ψ production can be subtracted at $p\bar{p}$ colliders [55], the direct or 'prompt' ratio is displayed. The parton gas produces suppression over nearly twice the p_{T} range as the minijet initial conditions, as shown in Ta-

ble 2.6. In case ii, the ψ is more suppressed than the ψ' for a large range of p_{T}, up to 54 GeV for the parton gas. In case i, the ψ' is more suppressed than the ψ except when $p_{\mathrm{T}} < 9$ GeV in the parton gas. The kink in the dashed curve appears when the ψ is no longer suppressed. In each case, the p_{T} signature obvious in the ψ'/ψ production ratios is unique if the full p_{T} range can be measured. Otherwise it may be difficult to distinguish between the parton gas and minijet plasma initial conditions for $p_{\mathrm{T}} < 20$ GeV at the LHC unless the measurement is made with sufficiently high statistics. Note that even though the decreased initial temperature of the minijet gas when shadowing is included reduces the p_{T} range of the suppression, the shape of the ratio remains similar.

It is doubtful that the prompt Υ rate can be successfully extracted because the feeding from χ_b states will be difficult to disentangle [72]. The Υ family is also more complex, including feeddown to the Υ from Υ', Υ'' and two sets of χ_b states and feeddown to the Υ' from the Υ'' and $\chi_b(2P)$ states. Thus in the Υ'/Υ ratio, all sources of Υ' and Υ, each associated with a different suppression factor, must be considered [43]:

$$\frac{\Upsilon'}{\Upsilon}\bigg|_{\mathrm{indirect}} \equiv \frac{\Upsilon' + \chi_b(2P)(\to \Upsilon') + \Upsilon''(\to \Upsilon')}{\Upsilon + \chi_b(1P, 2P)(\to \Upsilon) + \Upsilon'(\to \Upsilon) + \Upsilon''(\to \Upsilon)}. \quad (2.28)$$

In computing this 'indirect' Υ'/Υ ratio it is assumed that the suppression factor is the same for the $\chi_b(2P)$ and $\chi_b(1P)$ states and that identical suppression factors can be used for the Υ' and Υ''. The relative production and suppression rates in the colour evaporation model, including the χ_b states, can be found in [43].

Figure 2.9 gives the indirect results. In a parton gas assuming a plasma like case ii, all the Υ states can be suppressed for $p_{\mathrm{T}} > 50$ GeV, producing the rather flat ratio given in the solid curve. A measurement at the 20% level is thus needed to distinguish between the pp value of the ratio and the QGP prediction. Substantial systematic errors in the ratio could make the detection of a deviation quite difficult due to the slow variation with p_{T}. This is a disadvantage of the indirect ratio: the prompt ψ'/ψ ratio is enhanced by nearly a factor of two over the pp value, making detection easier. With the slowly growing screening mass of case i, the direct Υ rate is not suppressed while the Υ' and χ_b states are suppressed. Under these conditions, the indirect ratio is less than the pp value until the Υ' is no longer suppressed and then is slightly enhanced by the χ_b decays until they also no longer suffer from plasma effects. Thus although the indirect ratio is less sensitive to the plasma, the Υ'/Υ and ψ'/ψ ratios together can significantly constrain plasma models, especially if the quarkonium states can be measured with sufficient accuracy up to high p_{T}. Again, the shape of the ratio is similar when the effect of shadowing on the initial conditions is included although the range of the suppression is reduced.

2.4 Using the Z^0 as a baseline

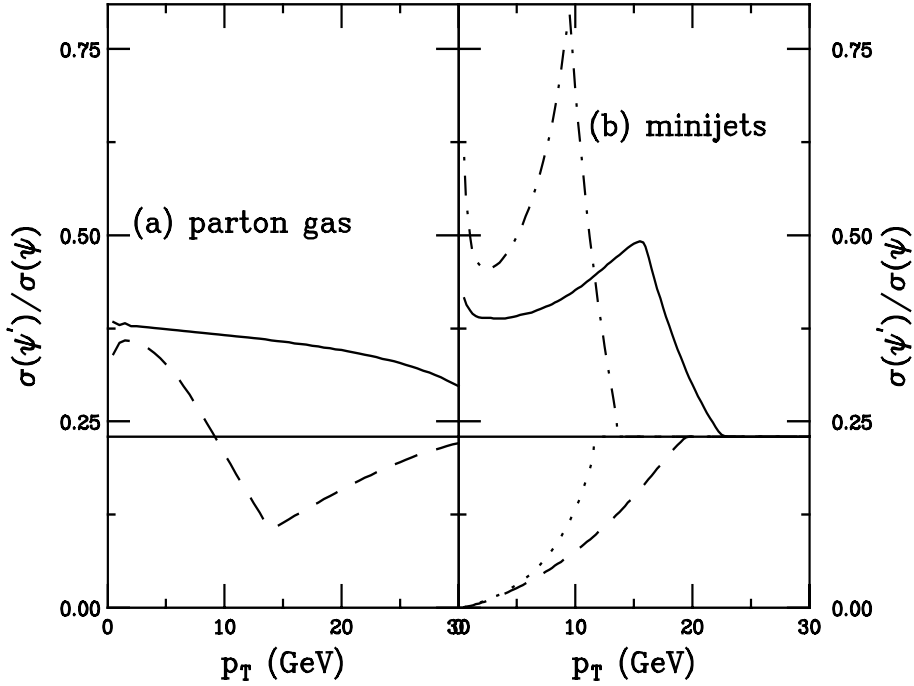In the current experiments at the CERN SPS, J/ψ production is compared to the dilepton continuum [10,73].

Fig. 2.8. The direct or prompt ψ'/ψ ratio as a function of p_T is shown for several choices of initial conditions and $R = R_{\mathrm{Pb}}$. In **a)**, **parton gas results are shown for case i** (***dashed*** and case ii (*solid*). In **b** minijet results are given for both cases without shadowing, case i (*dashed*) and case ii (*solid*), and with $S = S_1$, case i (*dotted*) and case ii (*dot-dashed*). The horizontal curve represents the pp ratio. Modified from [11]
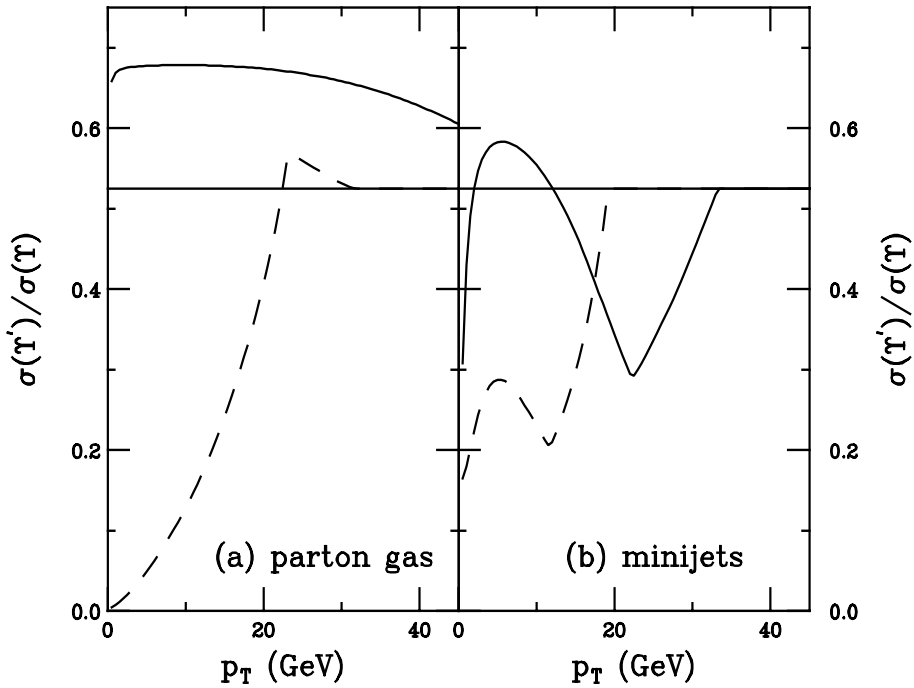

Fig. 2.9. The Υ'/Υ ratio computed from (2.28) is shown for several initial conditions and $R = R_{\mathrm{Pb}}$. In **a)**, **parton gas results are shown for case i** (***dashed*** and case ii (*solid*). In **b** minijet results are given for case ii without shadowing (*solid*) and with $S = S_1$ (*dashed*). The horizontal curve represents the pp ratio. Modified from [11,43]

The continuum is assumed to be produced via the Drell-Yan ($\gamma^\star$, $Z^{0\star}$-exchange) process and is, in fact, Drell-Yan-like. At the LHC, the continuum will be more difficult to understand because of the important contribution from semileptonic $c\bar{c}$ and $b\bar{b}$ decays. Not only are there uncertainties in the total $c\bar{c}$ cross section, but the heavy quark decays are also subject to nuclear effects. The relatively small Drell-Yan contribution is also subject to shadowing effects in the mass range between the J/ψ and the Υ. Another choice is needed. One possibility is Z^0 production. Because the Z^0 is produced in point-like fashion, the difference between the Z^0 p_T-dependence in pp and Pb+Pb collisions will not be influenced by the quark-gluon plasma.

Figure 2.10 illustrates the cross section for Z^0 production as a function of p_T at $\sqrt{s} = 5.5$ TeV assuming no shadowing. The p_T distribution, $d\sigma/dp_T$, is given for $pp \rightarrow Z^0 X$ including the individual contributions from $q\bar{q}$ and $qg + \bar{q}g$ collisions. One-loop corrections to the $Z^0 +$ jet cross section are included[5] but resummation effects are not. To obtain the number of events per month per GeV in central collisions, multiply by $\sigma_{NN} T_{\mathrm{PbPb}}(0)\mathcal{L}_{\mathrm{int}}^{\mathrm{PbPb}} = 4.973 \times 10^3$ nb^{-1}. At $p_T = 50$ GeV, the cross section is of order 10^{-3} nb/GeV, implying about 2 events per GeV for 40% acceptance and detection efficiency. Thus, for a 5 GeV bin, about 10 events are found in this bin per month of running. After a year of running, this would yield a statistical accuracy of order 9%. At low p_T, event rates are a factor of ~ 10 larger, yielding correspondingly greater accuracy. The predicted effects of the QGP typically imply survival probabilities that differ by much larger percentages compared to unity. In any case, as estimated earlier, the errors in the measurements of the Υ spectra will be larger. Thus, production rates in the $p_T \lesssim 50$ GeV domain are high enough that $Z^0 \rightarrow l^+l^-$ can provide a standard of comparison. It is necessary to also measure Z^0 production in pp collisions at $\sqrt{s} = 5.5$ TeV to determine if shadowing and other nuclear effects influence the Pb+Pb spectra. Good statistical accuracy for up to $p_T = 50$ GeV requires an integrated luminosity for pp collisions of order $\mathcal{L} = 0.01$ fb^{-1}, which should be easily achieved in a few weeks of running.

The two difficulties with using Z^0 production as a benchmark are: $m_{Z^0} \gg m_{\Upsilon_i}$ and the difference in the production mechanisms, $q\bar{q}$ and $qg + \bar{q}g$ for the Z^0 and gg for $b\bar{b}$ production. The large m_{Z^0} reduces the value of Z^0 production as a benchmark for two reasons. First, shadowing and related nuclear effects may be dependent upon Q^2, as in S_2 and S_3 [24,25,27]. Thus, it is possible that the shadowing at $Q^2 = m_{\Upsilon_i}^2$ will differ substantially from that at $Q^2 = m_{Z^0}^2$. Second, the x values probed ($x \sim m_{Z^0}/\sqrt{s} \sim 0.016$ at $y = 0$) are much larger than in Υ production at the same energy. In Fig. 2.10, one sees that $q\bar{q}$ collisions are dominant for $p_T \lesssim 15$ GeV while at higher p_T values $qg + \bar{q}g$ collisions dominate. Thus, to probe nuclear effects on the g distribution at $Q^2 = m_{Z^0}^2$, these effects on the q and $\bar{q}$ distributions at the same values of x and Q^2 must be understood. There is no direct measurement of q and $\bar{q}$ shadowing at small x with Q^2 values as high as $m_{Z^0}^2$. However, if nuclear beams become available at HERA, such measurements would be possible.

Given these issues, it would be advantageous if lepton pair production at $m_{\mu^+\mu^-} \approx m_{\Upsilon_i}$ could be used to constrain shadowing and nuclear effects at parton x and Q^2 values closer to those of direct relevance. As already noted, a large background from $c\bar{c}$ and $b\bar{b}$ production processes is expected for $m_{\mu^+\mu^-} \leq m_{\Upsilon_i}$. At these low masses, this background will be very difficult to veto by requiring that the leptons be isolated because of the high density of soft tracks in the Pb+Pb collision environment. In the mass region above about 15 GeV the dilepton rate from $c\bar{c}$ ($b\bar{b}$) pair production is predicted to be smaller than (comparable to) that from $\gamma^\star$, $Z^{0\star}$-exchange [74]. Further, in this higher mass range, vetoing the $b\bar{b}$ component using isolation requirements on the leptons might prove feasible at a level adequate to extract the pure DY dilepton spectrum. In Fig. 2.10, $d\sigma/dp_T$ is given for production of muon pairs with 15 GeV $\leq M_{\mu^+\mu^-} \leq 20$ GeV coming from $\gamma^\star$, $Z^{0\star}$-exchange. In this case the $qg + \bar{q}g$ collision component is always dominant, as would be desirable for learning as much about gluon shadowing as possible. However, the cross section is nearly a factor of 100 below that for production at the Z^0 resonance, implying that statistics would be a factor of 10 worse. Even a year of running will not provide enough Pb+Pb luminosity to yield measurements that are sufficiently accurate to constrain the shadowing and nuclear effects at the needed level of $\lesssim 5 - 10\%$. Thus, the low rate and uncertainty regarding the ability to veto the $b\bar{b}$ background implies that it may not be possible to use lepton pairs below the Z^0 mass to improve the understanding of nuclear effects on the gluon distribution. Nonetheless, the possibility of doing so should not be ignored and appropriate data, including event characteristics that might allow vetoing, should be collected.

2.5 Energy loss

A dense parton system is expected to be formed in the early stage of relativistic heavy-ion collisions due to the onset of hard and semihard parton scatterings. Interactions among the produced partons in this dense medium will most likely lead to partial thermalization and formation of a quark-gluon plasma. It is thus important to study phenomenological signals of the early parton dynamics, a crucial step towards establishing the evidence of a strongly interacting initial system and its approach to thermal equilibrium. Therefore the energy loss of fast partons is a good probe of dense matter [75]. Three signals of this energy loss, dE/dx, are discussed: the effect on heavy quark decays and consequently, on the shape of the dilepton continuum, jet quenching and rapidity shifts in global event characteristics.

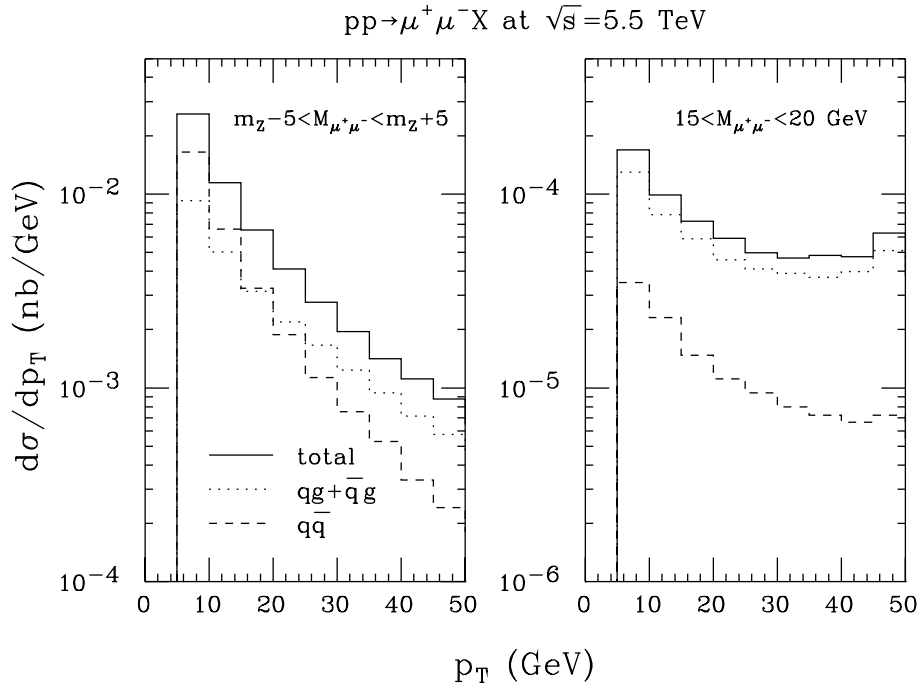[5] Thanks to U. Baur for providing a program against which to check these calculations.

$$pp \rightarrow \mu^+\mu^- X \text{ at } \sqrt{s} = 5.5 \text{ TeV}$$

Fig. 2.10. In (a), $d\sigma/dp_T$ is shown for $pp \rightarrow \mu^+\mu^- X$ at $\sqrt{s} = 5.5\,\text{TeV}$ as a function of p_T for Z^0 production (defined by $m_{Z^0} - 5\,\text{GeV} \leq M_{\mu^+\mu^-} \leq m_{Z^0} + 5\,\text{GeV}$). In (b), the same cross section is plotted for $15\,\text{GeV} \leq M_{\mu^+\mu^-} \leq 20\,\text{GeV}$. The separate contributions from $q\bar{q}$ and $qg + \bar{q}g$ collisions are indicated by dashed and dotted histograms, respectively. From [43]

2.5.1 Heavy quarks and the dilepton continuum

Since heavy-flavoured mesons carry most of the heavy quark energy after hadronization, the energy lost by heavy quarks travelling through the quark-gluon plasma is directly reflected in the suppression of large p_T heavy-flavoured mesons. Previous work suggested that since the charm production cross section is large, charm decays would dominate the dilepton continuum for $2 < M < 10$ GeV [23] after random π and K decays had been subtracted. Therefore the dilepton yields could be used as an indirect measurement of the charm spectrum. However, this conclusion depends crucially on the hadronization mechanism, the acceptance of a real detector and the energy loss in the medium. Large invariant mass heavy quark pairs are suppressed by the energy loss. Thus dileptons from their decays are also suppressed [76,77]. The treatment of the energy loss in the model is described here [76,77] followed by a discussion of how the $c\bar{c}$ and $b\bar{b}$ pairs are generated, hadronized and decayed. The effect observable by CMS is finally examined.

First, the phase space distribution of the heavy quarks and the space-time evolution of the dense matter must be specified. The matter has a longitudinal fluid velocity $v_z^F = z/t$ in the local frame [37], essentially the fluid velocity of free-streaming particles produced at $z = 0$ and $t = 0$. Transverse flow, which sets in later, is neglected and both the medium and the heavy quarks are assumed to be produced at $z = 0$, the same point at which expansion begins. Then, for any space-time point, (z, t), a heavy quark is in a fluid with the same longitudinal velocity. In the fluid rest frame, the heavy quark thus has

momentum $(0, \boldsymbol{p}_T)$. Energy loss reduces the heavy quark momentum to $(0, \boldsymbol{p_T}')$ in the rest frame so that the momentum of the heavy quark changes from $(m_T \sinh y, \boldsymbol{p}_T)$ to $(m_T' \sinh y, \boldsymbol{p}_T')$ in the lab frame. Thus the heavy quark loses its transverse momentum but retains its rapidity because it follows the longitudinal flow.

To simplify the calculations, spherical nuclei of radius $R_A = 1.2A^{1/3}$ are assumed so that in central collisions, the transverse area of the system is the area of the nucleus. For a heavy quark with a transverse path, l_T, and mean-free path, λ, in the medium, $\mu = l_{rmT}/\lambda$ gives the average number of scatterings. The actual number of scatterings, n, is generated from the Poisson distribution, $P(n, \mu) = e^{-\mu}\mu^n/(n!)$. This corona effect is particularly important for heavy quarks produced at the edge of the transverse plane of the collision. In the rest frame of the medium, the heavy quark then experiences a momentum loss $\Delta p = n\lambda\, dE/dx$.

When a heavy quark loses most of its momentum in the fluid rest frame, it begins to thermalize with the dense medium. The heavy quark is considered to be thermalized if its final transverse momentum after energy loss, p_T', is smaller than the average transverse momentum of thermalized heavy quarks with a temperature T. These thermalized heavy quarks are then given a random thermal momentum in the rest frame of the fluid generated from the distribution $dN/d^3p \propto \exp(-E/T)$. The final momentum of the thermalized heavy quark is obtained by transforming back from the local fluid frame to the centre-of-mass frame of the collision. The parameters used in the calculation are $dE/dx = -1$ GeV/fm, $\lambda = 1$ fm and $T = 150$ MeV. Note that larger values of dE/dx, both

collisional and radiative have been recently suggested for heavy quarks in the high temperature environment of the LHC [78]. However, simulations at RHIC energies [76] suggest that once the heavy quarks are assumed to lose energy, the suppression of the heavy quark spectra appears as long as $|dE/dx| \geq \langle p_T \rangle / R_A$ where $\langle p_T \rangle$ is the average transverse momentum of the heavy quark which produces leptons inside the detector acceptance. At central rapidities with Pb beams and $\langle p_T \rangle = 3$ GeV, $\langle p_T \rangle / R_A \sim 0.4$ GeV/fm.

The momentum distribution of the $Q\overline{Q}$ pairs is generated with PYTHIA 6.115 [79]. Initial and final state radiation effectively simulates higher-order contributions to heavy quark production so that the pair is no longer azimuthally back-to-back as at leading order[6]. The MRS D−′ [80] parton distribution functions are used to normalize the charm pair production cross section to 17.7 mb in pp collisions at $\sqrt{s} = 5.5$ GeV [23]. The number of $Q\overline{Q}$ pairs in a Pb+Pb collision at impact parameter $b = 0$ is obtained by multiplying the pp production cross section by the nuclear overlap,

$$N_{Q\overline{Q}} = \sigma_{Q\overline{Q}}^{pp} T_{\text{PbPb}}(0) \qquad (2.29)$$

where $T_{\text{PbPb}}(0) = 30.4$/mb. This scaling results in 540 charm pairs in a central Pb+Pb event[7]. The $b\overline{b}$ production cross section is 224 μb in $\sqrt{s} = 5.5$ TeV pp collisions, extrapolating to 6.8 $b\overline{b}$ pairs in an average central Pb+Pb event[8]. Although the energy loss experienced by bottom quarks may be different from that of charm quarks [78], the same parameters are used.

Only dileptons from correlated $Q\overline{Q}$ pair decays, $N_{ll}^{\text{corr}} = N_{Q\overline{Q}} B^2 (Q/\overline{Q} \to l^\pm X)$ are considered, i.e., a single $Q\overline{Q}$ pair produces the dilepton. Dileptons from uncorrelated $Q\overline{Q}$ decays, which appear at higher invariant mass than the correlated decays due to their larger rapidity gap, will be particularly abundant for charm decays since $N_{ll}^{\text{uncorr}} = N_{Q\overline{Q}} (N_{Q\overline{Q}} - 1) B^2 (Q/\overline{Q} \to l^\pm X)$. In principle, the finite detector acceptance significantly reduces the uncorrelated rate and like-sign subtraction should remove most of the remainder. In practice however, full subtraction will be difficult. Another problem arises from uncorrelated lepton pairs from a heavy quark and a background π or K decay. Treatment of this background could be a problem, especially since high p_T pions and kaons are also expected to experience energy loss.

In order to obtain the final meson distributions, the heavy quark distributions are convoluted with a fragmentation function. While a delta-function type of fragmenta-

tion is sufficient for low p_T hadroproduction [81,82], high p_T heavy quarks should fragment according to the Peterson function [83], $D(z) \propto [z(1 - 1/z - \epsilon/(1 - z))^2]^{-1}$ where $z = p_Q / p_H$ and $\epsilon_c = 0.06$ and $\epsilon_b = 0.006$ [84]. Note that the heavy quark quantities are denoted by Q while the heavy hadron formed from the fragmentation of the quark is denoted with H. A corresponding intrinsic k_T kick of 1 GeV for the partons in the proton is also included. In a high-energy collision, $\sqrt{s}/m \gg 1$, the heavy quark rapidity distribution is essentially flat. However, the hadronization of the heavy quark enhances the rapidity distribution at central rapidities. If the delta-function type of fragmentation is assumed, the momentum does not change but the rapidity shifts so that

$$dn \propto dy_Q = \frac{dp_{zQ}}{E_Q} = \frac{dp_{zH}}{E_Q} = \frac{\cosh y_H \, dy_H}{\sqrt{\cosh^2 y_H - \alpha^2}} \quad (2.30)$$

where

$$\alpha^2 = \frac{m_H^2 - m_Q^2}{m_{\text{T},H}^2} \; . \qquad (2.31)$$

For $m_c = 1.3$ GeV, $m_D = 1.87$ GeV and $m_{\text{T},D} \approx \sqrt{2} m_D$, $\alpha^2 = 0.25$, enhancing the D distribution at $y = 0$ by $\approx 15\%$. When $m_b = 4.75$ GeV, $m_B = 5.27$ GeV and $m_{\text{T},B} = \sqrt{2} m_B$, $\alpha^2 = 0.09$, enhancing the B distribution by $\approx 5\%$. The range of the enhancement is $|y_H| < 2.5$. If the Peterson function is used instead, α^2 increases,

$$\alpha^2 = \frac{m_H^2 - z^2 m_Q^2}{m_{\text{T},H}^2} \; , \qquad (2.32)$$

increasing the D enhancement at $y = 0$ to $\approx 30\%$ for $\langle z \rangle \approx 0.7$ and the B enhancement to $\approx 15\%$ for $\langle z \rangle \approx 0.85$. These $\langle z \rangle$ are typical for the Peterson function with the ϵ values given above. The fragmentation then tends to pile up heavy hadrons at central rapidities.

Since the CMS detector is sensitive to decays of charm quarks with $p_T > 20$ GeV, the charm spectrum was generated in two steps to obtain a sufficient number of high p_T charm quarks. First 10^5 normal $c\overline{c}$ pairs were generated followed by an equal number of $c\overline{c}$ pairs with a high p_T trigger such that the $c\overline{c}$ pair spectrum contains pairs with $p_{\text{T},c} > 5$ GeV and $p_{\text{T},\overline{c}} > 5$ GeV only. These high p_T $c\overline{c}$ pairs were then removed from the normal spectrum so that the resulting soft $c\overline{c}$ spectrum contains those pairs with $p_{\text{T},c} < 5$ GeV or $p_{\text{T},\overline{c}} < 5$ GeV. The relative weight of the high p_T spectrum is obtained from the ratio of the high p_T events to the total distribution. Because the b quarks have a harder p_T spectrum than charm quarks, such a procedure is unnecessary for $b\overline{b}$ pairs.

The average branching ratios of $\overline{D} \to \mu X$ are $\approx 12\%$. The lepton energy spectrum from D meson semileptonic decays in PYTHIA 6.115 is consistent with the measurement of the MARK-III collaboration [85]. The b quarks are assumed to fragment into B^-, $\overline{B}^0$, $\overline{B}_s^0$ and Λ_b^0 with production percentages 38%, 38%, 11% and 13%, respectively. Single leptons from bottom decays can be categorized as primary and secondary leptons. Muons directly produced

---

[6] No shadowing has been included in these calculations.

[7] When the MRST HO [19] parton distribution functions are used, the $c\overline{c}$ pair production cross section decreases to 5.5 mb in pp collisions, reducing the number of charm pairs in Pb+Pb collisions to 167, substantially reducing the charm contribution, particularly from uncorrelated pairs.

[8] If the MRST HO parton distribution functions are used to calculate $b\overline{b}$ production, the cross section is not substantially changed. It is reduced to 193 μb, leading to 5.9 $b\overline{b}$ pairs per event.

in the decay $B \to lX$ are primary while those indirectly produced, $B \to DX \to lY$, are secondary. Primary leptons have a harder energy spectrum than secondary leptons. A decaying b hadron mainly produces primary μ^- and secondary μ^+ although it can also produce a smaller number of primary μ^+ due to $B^0 - \overline{B}^0$ mixing. The branching ratios of the necessary B hadron decays are 9.30% to primary μ^-, 2.07% to secondary μ^-, 1.25% to primary μ^+, and 7.36% to secondary μ^+. The total number of dimuons from a $B\overline{B}$ decay can be readily estimated to be 0.020. Another important source of dimuons from bottom decays is the decay of a single bottom, $B \to Dl_1X \to l_1l_2Y$. The branching ratio for a single B meson to a dimuon is 0.906%, therefore this source gives 0.018 dimuons, comparable to the yield from a $b\overline{b}$ pair decay. These branching ratios [68] and energy spectra from PYTHIA 6.115 are consistent with measurements [86].

In Fig. 2.11 the single charm p_T distribution and the resulting dilepton invariant mass spectrum from correlated $D\overline{D}$ decays are shown without any phase space cuts. The spectra in Fig. 2.11 are normalized, as are all figures in this section, to a single central Pb+Pb event. The dashed curves are the generated spectra without energy loss while the solid curves are the distributions after energy loss. Thermalization of charm quarks that have lost most of their momentum causes the build-up at low p_T, as seen in Fig. 2.11a. At higher values, a shift in p_T occurs but these quarks are sufficiently energetic to escape the dense medium without being thermalized. A comparison of the dilepton spectra before and after energy loss, Fig. 2.11b, would naively suggest that the overall effect is small. However, this impression is misleading because the spectrum is integrated over the entire phase space. Heavy quarks and antiquarks in a pair tend to be separated by a significant rapidity gap. This gap can cause the invariant mass of the subsequent lepton pair to be also large. However, once the finite detector geometries are included, the effect of energy loss becomes more dramatic.

Figure 2.12 shows the corresponding single bottom p_T distribution and the integrated invariant mass spectra from correlated $B\overline{B}$ and single B decays. The dotted curve is the result of the decays of a single B to lepton pairs. When $M < 3$ GeV, this contribution is larger than the dilepton yield from $B\overline{B}$ decays, shown in the dot-dashed curve. Both include energy loss. The solid curve is the sum of the two contributions while the dashed curve is the sum of single and pair decays to dileptons without energy loss. The same trends are seen for bottom as well as charm except that the suppression of the spectrum due to energy loss begins at larger invariant mass. Note that the mass distribution in Fig. 2.12b is truncated to show more clearly the contribution from single B decay.

The CMS muon acceptance is in the range $|\eta| \leq 2.4$ with a lepton p_T cut of 3 GeV. After these simple cuts are applied, the results are shown in Fig. 2.13 for both $D\overline{D}$ and $B\overline{B}$ decays. Whereas for $M \leq 15$ GeV, the $D\overline{D}$ decays would dominate those of $B\overline{B}$ before the cuts, the measured $B\overline{B}$ decays are everywhere larger than those from charm mesons both before and after energy loss. The generally larger momentum of muons from B decays and the rather high momentum cut result in less acceptance loss for $B\overline{B}$ decays. No $D\overline{D}$ decay pairs with $M \leq 5$ GeV survive the momentum cut. A factor of 50 reduction in rate at $M \sim 10$ GeV is found before energy loss when comparing Figs. 2.13 and 2.11b. A decrease in rate by a factor of 100 is obtained when energy loss is included. The corresponding loss of acceptance from $B\overline{B}$ decays is significantly less, a factor of ≈ 8 before energy loss and ≈ 15 when energy loss is included. Interestingly, the leptons in the decay chain of a single B meson are energetic enough for both to pass the momentum cut, causing the peak at $M \sim 2 - 3$ GeV. These results suggest that rather than providing an indirect measurement of the charm cross section, as postulated in [23], the dilepton continuum above the Υ family could instead measure the $b\overline{b}$ production cross section indirectly. A comparison with the spectrum from pp interactions at the same energy would then be sensitive to the amount of energy loss, dE/dx, of the medium.

A comparison of the p_T distributions of single muons in the CMS acceptance from the decays of D and B mesons can also provide a measure of the b cross section, shown in Fig. 2.14. When $p_T > 10 - 15$ GeV, the muon p_T distribution is clearly dominated by B decays. This method of studying heavy quark production with single high p_T leptons was proposed as a measure of the charm rate at RHIC [87]. However, for this method to be viable, the background from random π and K decays must be well understood.

There are a number of uncertainties in the model. Although the relative formation times are neglected, the longitudinal velocity of heavy quarks and the fluid could be mismatched. The rapidity distribution of the heavy quarks is very sensitive to the flow pattern. The energy loss is assumed to be constant during the expansion of the system and the subsequent drop in the energy density. This need not necessarily be the case. Transverse flow, which could quantitatively change the low invariant mass dilepton yields, is also not included. However, the qualitative features of the results, such as the clear dominance of $b\overline{b}$ decays and the effect of energy loss when $|dE/dx| \geq \langle p_T \rangle / R_A$, are not likely to change.

2.5.2 Jet quenching: the monojet to dijet ratio

Jet quenching is a very good candidate for measuring energy loss since a fast parton traversing dense matter must experience multiple scatterings, or collisional energy loss, and also suffer radiative energy loss [88, 89, 90, 91]. Two signatures of this energy loss in hard jet production addressed in this section are dijet quenching, a suppression of pairs of high p_T jets [92], and an enhancement of monojet production relative to the dijet rate [93]. The sensitivity of CMS to these signals for jets with transverse energy greater than 100 GeV was recently considered [94]. Other possible signatures that could directly measure the energy loss involve tagging the hard jet opposite a particle that does not interact strongly such as a Z^0 boson [95] or a photon [96].
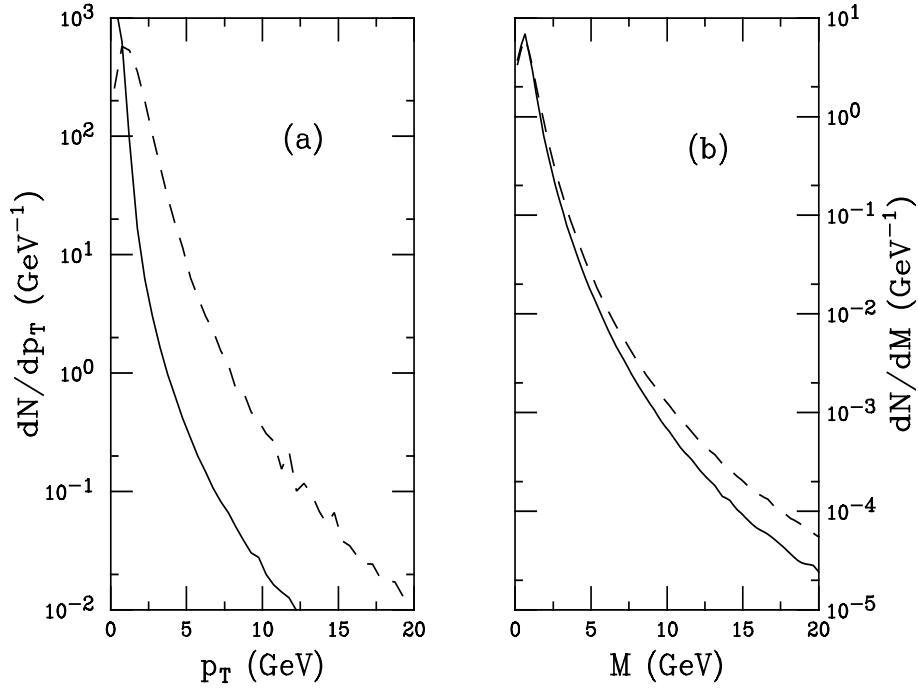
Fig. 2.11. a The p_T distribution of single D mesons. **b** The invariant mass distribution of lepton pairs from correlated $D\overline{D}$ decays. Both distributions are integrated over all phase space. The *dashed curves* are results without energy loss, the *solid curves* include energy loss with $dE/dx = -1$ GeV/fm. From [77]
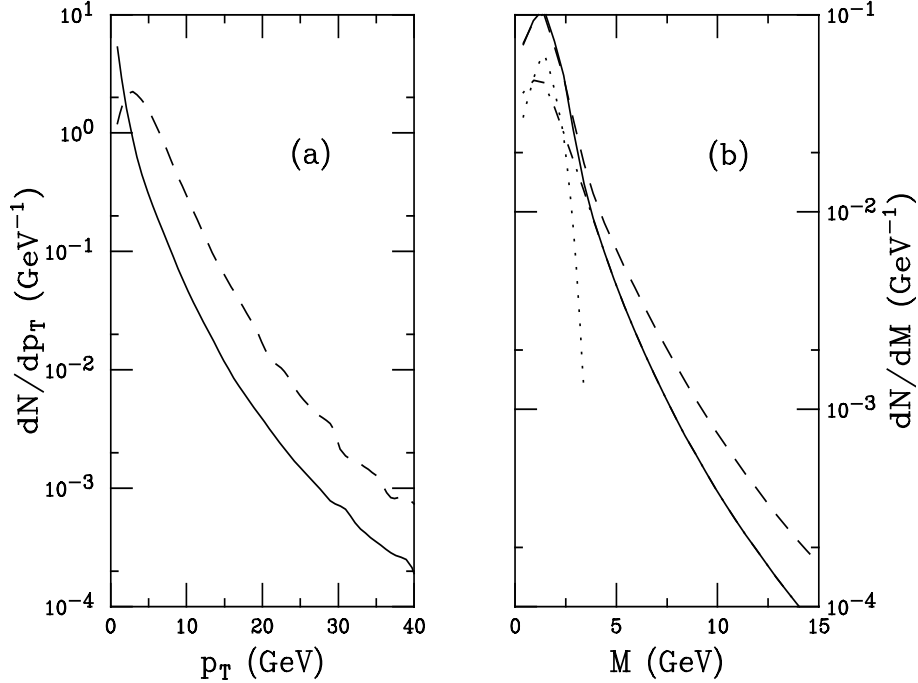

Fig. 2.12. a The p_T distribution of single B mesons. **b** The invariant mass distribution of lepton pairs from correlated $B\overline{B}$ decays and single B decays. Both distributions are integrated over all phase space. The *dotted curve* is the contribution from semileptonic decay chains of single B mesons while the *dot-dashed* curve is from correlated $B\overline{B}$ decays. Both include energy loss. The *dashed curves* are results without energy loss, the *solid curves* include energy loss with $dE/dx = -1$ GeV/fm. Note that in **b**, the *dashed* and *solid curves* include all single B and $B\overline{B}$ pair decays. From [77]
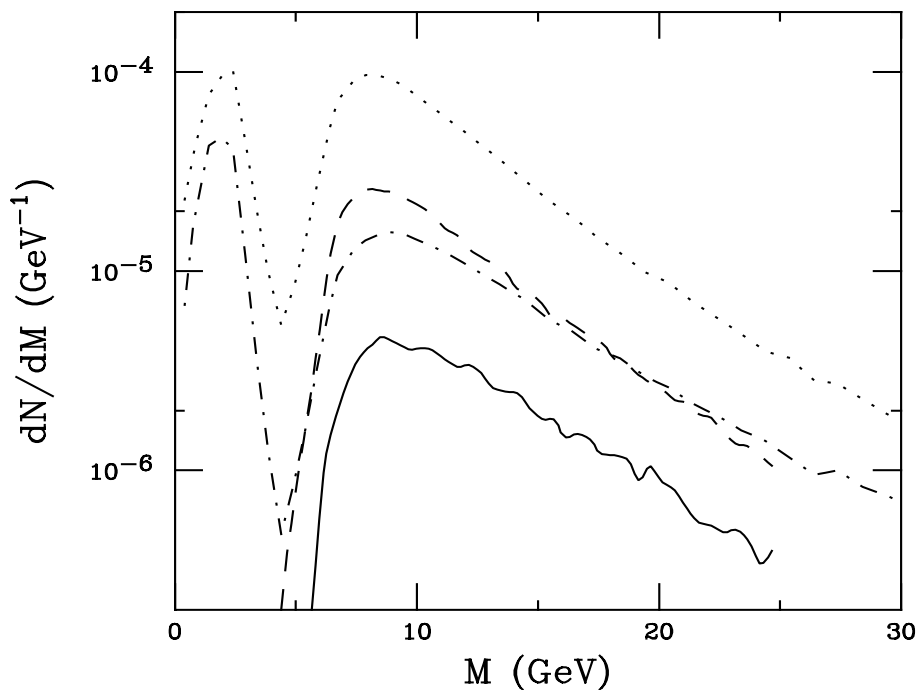
Fig. 2.13. The dilepton invariant mass distribution in the CMS acceptance. The *dashed* and *dotted curves* are the $D\overline{D}$ and summed single B and $B\overline{B}$ decays respectively without energy loss. The *solid* and *dot-dashed curves* are the corresponding results with $\mathrm{d}E/\mathrm{d}x = -1$ GeV/fm. From [77]
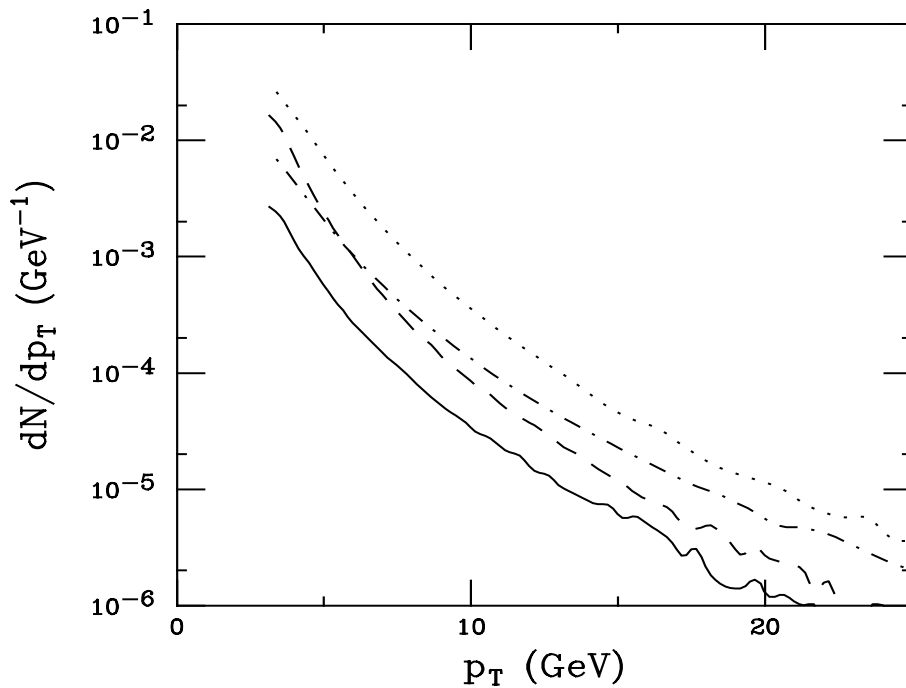
Fig. 2.14. The single muon p_T distributions in the CMS acceptance. The *dashed* and *dotted curves* are the D and B meson decays respectively without energy loss. The *solid* and *dot-dashed curves* are the corresponding results with $\mathrm{d}E/\mathrm{d}x = -1$ GeV/fm. From [77]

The total energy lost by a hard parton due to multiple scattering, ΔE_{tot}, is obtained by averaging over dijet production vertices (R, φ), the Q^2 of the rescattering, and the space-time evolution of the medium [97,98]:

$$\Delta E_{\text{tot}} = \frac{1}{\sin\theta} \int\limits_0^{2\pi} \frac{\mathrm{d}\varphi}{2\pi} \int\limits_0^{R_A} \mathrm{d}R\, P_A(R)$$

$$\int\limits_{\tau_0}^{\tau_L} \mathrm{d}\tau \left(\frac{\mathrm{d}E^{\text{rad}}}{\mathrm{d}x}(\tau) + \frac{\mathrm{d}E^{\text{coll}}}{\mathrm{d}x}(\tau) \right) \quad (2.33)$$

where τ_0 and $\tau_L = \sqrt{R_A^2 - R^2\sin^2\varphi} - R\cos\varphi$ are the QGP formation time and the time the jet escapes the plasma, respectively. Assuming a spherical nucleus, $P_A(R)$ is the distribution of distances R from the nuclear collision axis to the dijet production vertex, $P_A(R) \approx 3(R_A^2 - R^2)/2R_A^3$ for $R \leq R_A$, and θ is the polar angle of the jet relative to the collision axis.

There are two contributions to the energy loss: $\mathrm{d}E^{\text{rad}}/\mathrm{d}x$ is the radiative loss and $\mathrm{d}E^{\text{coll}}/\mathrm{d}x$ is the collisional loss. The discussion here is restricted to the collisional loss, as in [97,98]. Although the radiative energy loss is expected to dominate the collisional loss by up to an order of magnitude [88], there is no direct experimental verification of this loss. It was recently shown [89, 90, 91] that the radiation of energetic gluons in a QCD medium is essentially different from the Bethe-Heitler independent radiation pattern since the formation time of such gluons exceeds their mean free path in the medium. Then coherent effects play a crucial role, leading to a strong suppression of medium-induced gluon radiation. This suppression is the QCD analogue of the Landau-Pomeranchuk-Migdal (LPM) effect in QED. The coherent LPM radiation induces a significant dependence of the jet energy on the jet cone size θ_0. Including radiative loss would increase ΔE_{tot} and thus enhance the proposed dijet quenching effect.

The collisional loss represents an incoherent sum over all rescatterings and is almost independent of the initial parton energy. Additionally, the angular distribution of the collisional energy loss is essentially different from that of the radiative loss. The majority of particles knocked out of the dense matter by elastic scatterings fly off transverse to the hard jet axis. As a result, the collisional energy loss is practically independent of θ_0. The contribution from the collisional loss could become significant for jets with finite cone size propagating through the plasma predicted in central heavy ion collisions.

The dijet production rate for jet pairs with individual jet transverse momenta p_{T_1} and p_{T_2} produced in the initial hard scatterings in central AA collisions is the result of averaging the total energy loss of each jet, (2.33), over all dijet production vertices (R, φ),

$$\frac{\mathrm{d}N_{ij}^{\text{dijet}}}{\mathrm{d}y_1\mathrm{d}y_2\mathrm{d}p_{T_1}\mathrm{d}p_{T_2}} =$$

$$T_{AA}(0) \int\limits_0^{2\pi} \frac{\mathrm{d}\varphi}{2\pi} \int\limits_0^{R_A} \mathrm{d}R P_A(R) \int \mathrm{d}p_T^2 \frac{\mathrm{d}\sigma_{ij}}{\mathrm{d}p_T^2}\, \delta(p_{T_1} - p_T$$

$$+ \Delta E_{\text{tot}}^i(\varphi, R))\, \delta(p_{T_2} - p_T + \Delta E_{\text{tot}}^j(\pi - \varphi, R))\,. \quad (2.34)$$

The jet cross section, $\mathrm{d}\sigma_{ij}/\mathrm{d}p_T^2$, is calculated in pp collisions using PYTHIA [79]

$$\frac{\mathrm{d}\sigma_{ij}}{\mathrm{d}p_T^2} = k \int \mathrm{d}x_1 \int \mathrm{d}x_2 \int \mathrm{d}\hat{t}\, f_{i/p}(x_1, p_T^2) f_{j/p}(x_2, p_T^2)$$

$$\frac{\mathrm{d}\hat{\sigma}_{ij}}{\mathrm{d}\hat{t}} \delta(p_T^2 - \frac{\hat{t}\hat{u}}{\hat{s}}), \quad (2.35)$$

where $\mathrm{d}\hat{\sigma}_{ij}/\mathrm{d}\hat{t}$ is parton-parton scattering cross section and $K \sim 2$ was used to account for higher order contributions. Shadowing is not included since it is not expected to be a strong effect in the x range of high E_T jets [94].

At leading order, hard jets are produced with $p_{T_1} = p_{T_2}$. A monojet is created from a dijet if one of the two hard jets loses so much energy that only a single jet is observable. This monojet rate is obtained by integrating the dijet rate over the transverse momentum p_{T_2} of the second (unobserved) jet for p_{T_2} smaller than the threshold value p_{cut}. Then the dijet rate, R^{dijet}, with p_{T_1}, $p_{T_2} > p_{\text{cut}}$, and the corresponding monojet rate, R^{mono}, with $p_{T_1} > p_{\text{cut}}$ and $p_{T_2} < p_{\text{cut}}$, in central AA collisions at $y = 0$ is

$$R_{AA}^{\text{dijet}}(p_{T_1}, p_{T_2} > p_{\text{cut}}) = \int\limits_{p_{\text{cut}}} \mathrm{d}p_{T_1} \int\limits_{p_{\text{cut}}} \mathrm{d}p_{T_2} \int \mathrm{d}y_1 \mathrm{d}y_2$$

$$\sum_{i,j} \frac{\mathrm{d}N_{ij}^{\text{dijet}}}{\mathrm{d}y_1\mathrm{d}y_2\mathrm{d}p_{T_1}\mathrm{d}p_{T_2}}\,, \quad (2.36)$$

$$R_{AA}^{\text{mono}}(p_{T_1} > p_{\text{cut}}, p_{T_2} < p_{\text{cut}}) =$$

$$\int\limits_{p_{\text{cut}}} \mathrm{d}p_{T_1} \int\limits^{p_{\text{cut}}} \mathrm{d}p_{T_2} \int \mathrm{d}y_1 \mathrm{d}y_2 \sum_{i,j} \frac{\mathrm{d}N_{ij}^{\text{dijet}}}{\mathrm{d}y_1\mathrm{d}y_2\mathrm{d}p_{T_1}\mathrm{d}p_{T_2}}\,. \quad (2.37)$$

The dijet rate in AA relative to pp collisions can be studied by introducing a reference process, unaffected by energy loss and with a rate proportional to the number of nucleon-nucleon collisions, such as Drell-Yan production,

$$\frac{R_{AA}^{\text{dijet}}}{R_{pp}^{\text{dijet}}} = \frac{\sigma_{AA}^{\text{dijet}}/\sigma_{pp}^{\text{dijet}}}{\sigma_{AA}^{\text{DY}}/\sigma_{pp}^{\text{DY}}}\,, \quad (2.38)$$

or Z^0 production. This normalization is necessary to remove systematic errors in the luminosity. However, the ratio $R^{\text{mono}}/R^{\text{dijet}}$ does not need any external normalization since both rates can be measured simultaneously in AA collisions, making such a study possible during a single run. A measurement relative to a reference process, as in (2.38), requires pp and Pb+Pb runs at the same energy.

Three different assumptions of the collisional energy loss were studied in [98]: (i) no quenching; (ii) jet quenching in an ideal plasma where $\langle \Delta E_g \rangle \simeq 9$ GeV at $y = 0$ is obtained from (2.33); (iii) jet quenching in a maximally viscous plasma with $C_\eta = 0.34$, resulting in $\langle \Delta E_g \rangle \simeq 18$ GeV at $y = 0$ [97]. The quark loss can be determined from the gluon loss by the ratio of colour factors such that $\langle \Delta E_q \rangle = 4/9 \langle \Delta E_g \rangle$. A parton with energy E loses on average $\nu = \langle Q^2/2m_0 \rangle$ in a single elastic scattering with a parton of energy m_0 in the medium and also gets a transverse momentum kick $k_T = Q\sqrt{1 - \nu/E}$. The initial conditions for a gluon plasma in central Pb+Pb collisions were taken from [38], without shadowing.

The hard jet background is principally lower energy jets from secondary parton scatterings after the system has thermalized. This false jet background was simulated with a hydrodynamical model assuming $dN^\pm/dy|_{y=0} = 8000$ in the central unit of rapidity with $\langle p_T^\pi \rangle = 0.5$ GeV and $\langle p_T^K \rangle = 0.7$ GeV [98,99]. Central Pb+Pb events are constructed from a superposition of the hydrodynamical model with the hard jet generated by PYTHIA in pp collisions [79].

To assess the CMS calorimeter response, some simplifying assumptions were made [98,100]. Only the barrel calorimeter, $|\eta| < 1.5$, is included with a 4 T uniform magnetic field. The calorimeter cell size is 0.1×0.1 in $\eta - \phi$ with hadronic calorimeter resolution $\sigma/E = 70\%/\sqrt{E/\text{GeV}} \oplus 1\%$ and electromagnetic calorimeter resolution $\sigma/E = 2\%/\sqrt{E/\text{GeV}} \oplus 0.5\%$. The modified UA1 jet finding algorithm was used and only jets with $\langle R \rangle/R_{\text{jet}} < 0.5$ were accepted, where $R_{\text{jet}} = \sqrt{\Delta\eta^2 + \Delta\phi^2} = 0.5$ is the jet radius in $\eta - \phi$ space. The average jet radius is

$$\langle R \rangle = \sum_i R_{i_0}(E_i - \overline{E}_i)/E^{\text{jet}}, \quad E^{\text{jet}} = \sum_i (E_i - \overline{E}_i),$$

(2.39)

where R_{i_0} is the distance between cell i of the jet and the centre of the jet, E_i and E^{jet} are the transverse energy in the cell and in the complete jet respectively, and $\overline{E}_i$ is the average cell transverse energy. A dijet is extracted from n-jet events by selecting the jet with the maximum transverse energy and because of the strong correlation, essentially back-to-back in azimuth, between the initial jet pair momenta, the jet opposite the first jet with the largest transverse energy was also selected:

$$E^1_{\text{T,jet}} = \max_{i=1,n} E_{\text{T}_i},$$
$$E^2_{\text{T,jet}} = \max_{i=2,n} E_{\text{T}_i} \cos(\varphi_1 - \varphi_i - \pi). \quad (2.40)$$

Figure 2.15 shows R^{dijet} as a function of the threshold jet energy E_T in central Pb+Pb collisions. An average jet radius $\langle R \rangle/R_{\text{jet}} < 1$ is assumed in (a) while $\langle R \rangle/R_{\text{jet}} < 0.5$ is used in (b). The probability of false dijet detection for $E^{1,2}_{\text{jet}} \geq E_T = 100$ GeV decreases by 2 orders of magnitude when the UA1 criteria is used. The contamination from false dijets, produced in secondary collisions, at threshold $E_T = 100$ GeV is about 25% in (a) and only $\sim 0.5\%$ in (b), decreasing rapidly with increasing threshold E_T. Thus

the selection criterion on jet internal structure maximizes suppression of the false jet background. The hard dijet yield can be suppressed by up to a factor of ~ 7 due to collisional loss alone and could be even larger when radiative loss is included. The quenching is nearly independent of jet energy if the loss depends only weakly on the energy of the initial hard parton.

At luminosity $\mathcal{L}_{\text{PbPb}} \simeq 1 \times 10^{27}$ cm^{-2}s^{-1} with $\sigma^{\text{in}}_{\text{PbPb}} \simeq 8$ b and a 3%-centrality trigger, there are $I^{\text{central}}_{\text{PbPb}} = 3\% \mathcal{L}_{\text{PbPb}} \sigma^{\text{in}}_{\text{PbPb}} = 240$ events per second. Table 2.7 shows the hard dijet detection rates $H^{\text{dijet}}_{\text{PbPb}} = R^{\text{dijet}}_{\text{PbPb}} I^{\text{central}}_{\text{PbPb}}$, monojets $H^{\text{mono}}_{\text{PbPb}} = R^{\text{mono}}_{\text{PbPb}} I^{\text{central}}_{\text{PbPb}}$ and the monojet to dijet ratio $H^{\text{mono}}/H^{\text{dijet}}$ in the CMS barrel. The expected statistics should be sufficient to study high E_T jet production.

On the other hand, monojet detection and resolution are far from ideal. Initial state gluon radiation, finite calorimeter energy resolution, peculiarities of the jet finding algorithm, in addition to the background smears the observed hadronic jet characteristics relative to the initial partonic jet. In particular, there is a finite probability to register a jet with energy higher or lower than the initial jet, i.e. $p_{T_1} \neq p_{T_2}$, in contrast to the simple QCD picture of a single hard parton-parton scattering. As a consequence, $R^{\text{mono}}/R^{\text{dijet}} > 1$ even when no plasma is produced (see the lower solid line in Fig. 2.16) because of the smearing in $p_{T_1} - p_{T_2}$ at the parton level. Dijets with energy lower than the threshold energy E_T are partly transformed into monojets with energy higher than E_T while the reverse process is suppressed due to the sharp decrease of the initial dijet spectrum with energy, $\propto E_T^{-5}$. When energy loss in the plasma is included, $R^{\text{mono}}/R^{\text{dijet}}$ increases up to a factor of $1.5 - 2$ at $E_T \geq 100$ GeV over the rate in a plasma without energy loss, a factor of $3 - 6$ above the baseline scaled PYTHIA result without plasma production, as also shown in Fig. 2.16.

Dijet production is more sensitive to the multiple scattering of jet partons in dense matter than the monojet yield which suffers from finite resolution and background effects. Studies of $R^{\text{mono}}/R^{\text{dijet}}$ can also provide additional information on the energy loss. Using the selection criteria $\langle R \rangle/R_{\text{jet}} < 0.5$ maximizes the efficiency of true hard jet recognition while suppressing the false jet background.

2.5.3 Jet quenching: effects on initial conditions

CMS can also measure global event characteristics such as total transverse energy in the event, E_T, and the neutral and charged particle multiplicities, N_0 and N_{ch} [72]. These measurements would allow the correlation of plasma signals with event centrality in a meaningful way. The pseudorapidity coverage of the calorimeters, $-5 < \eta < 5$, will cover $\approx 80\%$ of $dE_T/d\eta$, providing a good measure of the global transverse energy. The energy loss by fast partons in matter, already discussed for heavy quarks [76,77] and high transverse energy jets [94], would also modify global characteristics such as $dE_T/d\eta$. Studies [101] of radiative energy loss effects, proportional to the transverse
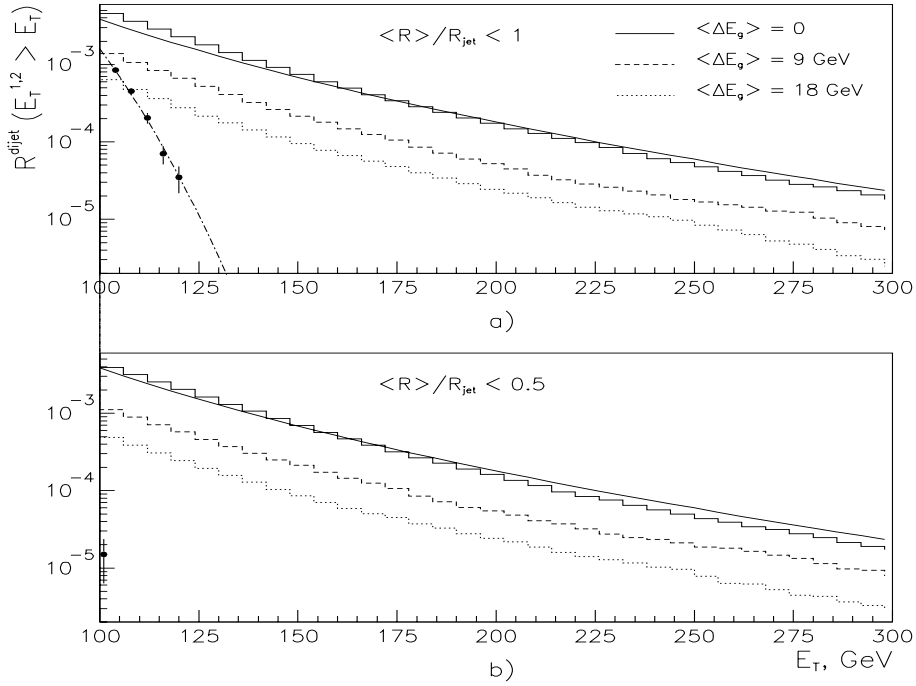
Fig. 2.15. The dijet rate $R^{\rm dijet}$ with transverse energy $E_{\rm T}^{1,2} > E_{\rm T}$ in central Pb+Pb collisions for different quenching scenarios with true hard jets (histograms) compared to false jets (points with Gaussian fit, *dot-dashed curve*) from the hydrodynamic calculation with $dN^{\pm}/dy(y=0) = 8000$. The histograms represent $\langle \Delta E_g \rangle = 0$ (solid), 9 GeV (*dashed*), and 18 GeV (*dotted*). In **a** $\langle R \rangle / R_{\rm jet} < 1$ is used while $\langle R \rangle / R_{\rm jet} < 0.5$ is assumed in **b**. The scaled PYTHIA result for the dijet spectrum is shown in the *solid curve*
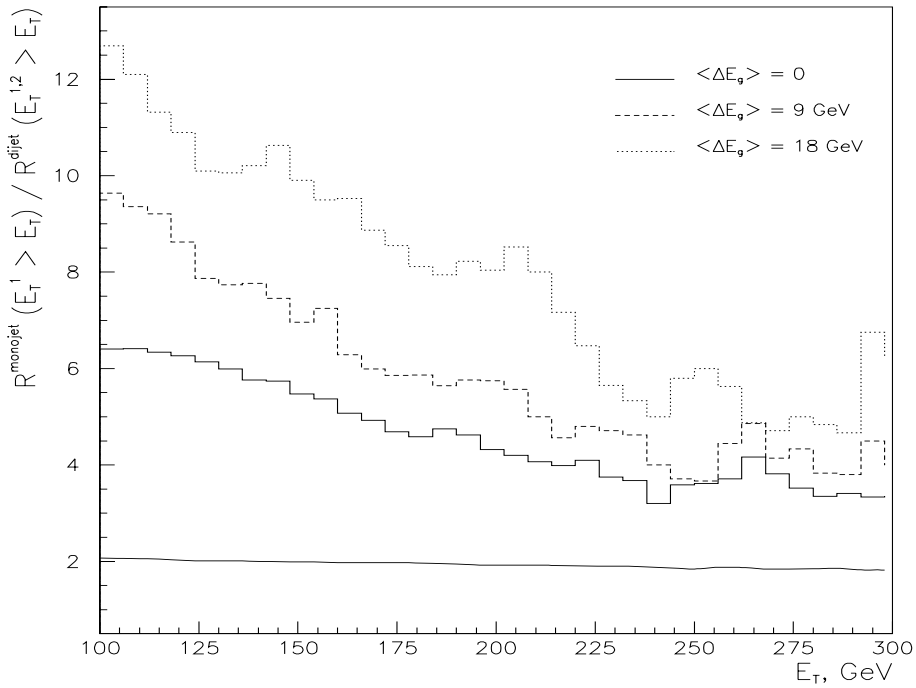
Fig. 2.16. The monojet/dijet ratio as a function of the threshold jet energy $E_{\rm T}$ in central Pb+Pb collisions for different quenching scenarios and $\langle R \rangle / R_{\rm jet} < 0.5$. The histograms represent $\langle \Delta E_g \rangle = 0$ (*solid*), 9 GeV (*dashed*), and 18 GeV (*dotted*). The scaled PYTHIA result for the dijet spectrum in shown in the *solid curve*

Table 2.7. The dijet ($E_{\mathrm{T}}^{1,2} > E_{\mathrm{T}}$) and monojet ($E_{\mathrm{T}}^1 > E_{\mathrm{T}}$) rates in central Pb+Pb collisions for $|\eta| < 1.5$

E_{T} (GeV)	100	150	200	250	300
no loss, $\langle \Delta E_g \rangle = 0$					
H^{dijet} (Hz)	1.0	1.5×10^{-1}	3.3×10^{-2}	1.0×10^{-2}	4.1×10^{-3}
H^{mono} (Hz)	6.3	8.0×10^{-1}	1.4×10^{-1}	3.6×10^{-2}	1.4×10^{-2}
$H^{\mathrm{mono}}/H^{\mathrm{dijet}}$	6.3	5.3	4.2	3.6	3.4
jet quenching in ideal QGP, $\langle \Delta E_g \rangle = 9$ GeV					
H^{dijet} (Hz)	3.1×10^{-1}	4.7×10^{-2}	1.2×10^{-2}	3.0×10^{-3}	1.0×10^{-3}
H^{mono} (Hz)	3.0	3.3×10^{-1}	6.9×10^{-2}	1.3×10^{-2}	5.2×10^{-3}
$H^{\mathrm{mono}}/H^{\mathrm{dijet}}$	9.7	7.0	5.7	4.2	5.2
jet quenching in viscous QGP, $\langle \Delta E_g \rangle = 18$ GeV					
H^{dijet} (Hz)	1.3×10^{-1}	2.1×10^{-2}	5.4×10^{-3}	1.8×10^{-3}	8.0×10^{-4}
H^{mono} (Hz)	1.7	2.1×10^{-1}	4.3×10^{-2}	1.1×10^{-2}	5.0×10^{-3}
$H^{\mathrm{mono}}/H^{\mathrm{dijet}}$	12.7	10.0	8.0	6.1	6.2

distance traveled by a jet in the medium, using the HIJING event generator [102] indicate an enhancement in the range $|\eta| < 2$.

Figure 2.17 shows $\mathrm{d}E_{\mathrm{T}}/\mathrm{d}\eta$ for ~ 1000 minimum bias Pb+Pb collisions at $\sqrt{s} = 5.5$ TeV/nucleon generated by HIJING in four different scenarios: no energy loss or nuclear shadowing; energy loss only; shadowing only; and the combined effect of shadowing and energy loss. A significant enhancement appears in the pseudorapidity range $|\eta| < 2$ when energy loss is included. Even peripheral Pb+Pb collisions show the effects of energy loss with the central enhancement still evident at impact parameters up to 12 fm [101]. Note that the shadowing parameterization used in HIJING reduces $\mathrm{d}E_{\mathrm{T}}/\mathrm{d}\eta$ in the central region by a factor of ~ 1.8, similar to the decrease in $\overline{E}_{\mathrm{T}}$ expected with more recent shadowing parameterizations and parton densities, as shown in Table 2.1. This is rather remarkable because HIJING uses a simplified model of shadowing [102] along with the Duke-Owens parton densities [28]. Shadowing is included in all further HIJING simulations shown here.

The energy dependence of the enhancement in $\mathrm{d}E_{\mathrm{T}}/\mathrm{d}\eta$ at central η is studied in Fig. 2.18. The results are given for Pb+Pb collisions at $\sqrt{s} = 5.5$, 3, 1, 0.5, and 0.2 TeV/nucleon. The enhancement is observable above a central plateau when $\sqrt{s} > 0.5$ TeV/nucleon. At lower energies the effect is less pronounced because the rapidity gap between the projectile and target fragmentation regions is decreased. A study of the energy dependence thus requires a scan of $\sqrt{s}$ from a few hundred GeV/nucleon to several TeV/nucleon to survey the onset of the enhancement.

Since the LHC heavy ion injection system can provide sufficient luminosity for a variety of fully stripped nuclei with a short transition time between the injection of different ion types [103], it is possible to study the nuclear dependence of the energy loss. Because smaller nuclei require a shorter transverse distance for the partons to traverse before escaping the system, the effect must depend on system size. A scan of collisions of different nuclear systems provides an additional test of jet quenching. Thus

HIJING was also used to simulate up to 10000 minimum bias Nb+Nb, Ca+Ca, and O+O interactions at $\sqrt{s} = 5.5$ TeV. These results are compared to the Pb+Pb results in Fig. 2.19. The central enhancement due to energy loss decreases with system size as obvious from the comparisons with and without energy loss.

The effect has only been shown for the global E_{T} distributions, $\mathrm{d}E_{\mathrm{T}}/\mathrm{d}\eta$. However, qualitatively the same picture is seen when charged or neutral particle production is studied instead of E_{T}.

The greater the energy loss, the more transverse energy is piled up at central η values, leading to an increase in energy density or 'stopping' in the central region, as has been seen at lower energies [104], in contradiction to the assumption of nuclear transparency [37]. Preliminary results indicate that the qualitively same results shown in Figs. 2.17–2.19 can be obtained using VENUS [105] with nucleon rescattering included. It is interesting to note that even though the physics of the VENUS rescattering mode is very different than that of the energy loss mechanism in HIJING, the end result is similar. This may be due to the fact that nucleon rescattering is also an effective form of nuclear 'stopping' [104]. The measurement of global characteristics can also provide an important correlation with collision centrality for signatures such as jet [94] and lepton pair production [43,76,77] as well as studies of the spatial dependence of the nuclear parton distributions [30].

This study demands a brief run with the solenoid switched off and variations in collision energy and system size. The availabilty of heavy ion beams when the CMS solenoid is not yet on is necessary to obtain undistorted distributions of total energy and charged multiplicity with η. Otherwise, distortions in the electromagnetic calorimeter due to charged hadron contamination must be shown to be small. In nucleus-nucleus collisions, normalization to pp collisionsat the same energy would eliminate these systematic uncertainties. Only a relatively small sample of events is then needed to observe the enhancement, e.g. 100 Pb+Pb events was shown to be sufficient for observation of this central enhancement [106].
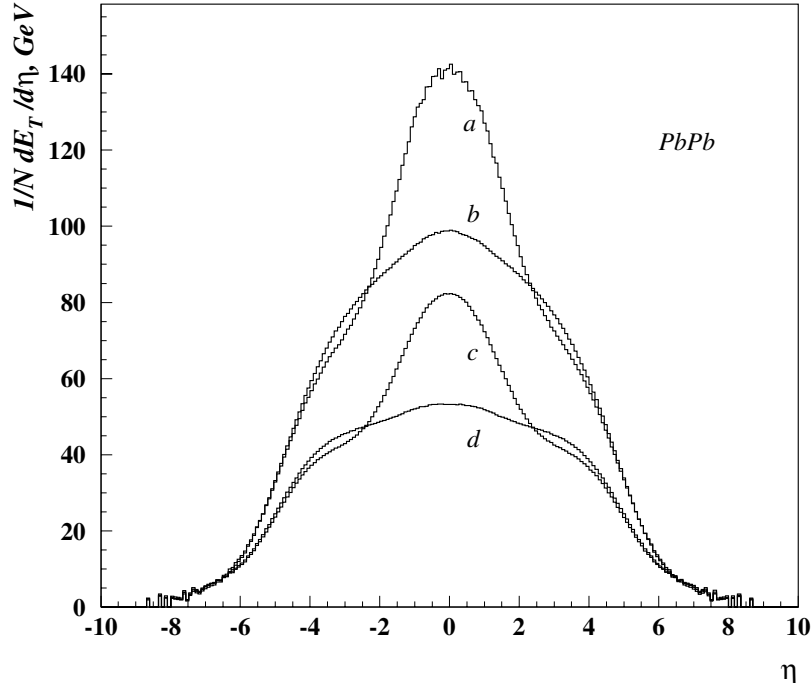
Fig. 2.17. Modification of $dE_T/d\eta$ (GeV) as a function of η for 1000 Pb+Pb collisions at $\sqrt{s} = 5.5$ TeV/nucleon normalized to the number of events with $d\eta = 0.087$ from the HIJING model. From top to bottom at $\eta = 0$ the curves are: **a** energy loss only, no shadowing; **b** no energy loss or shadowing; **c** energy loss and shadowing; **d** no energy loss, shadowing only
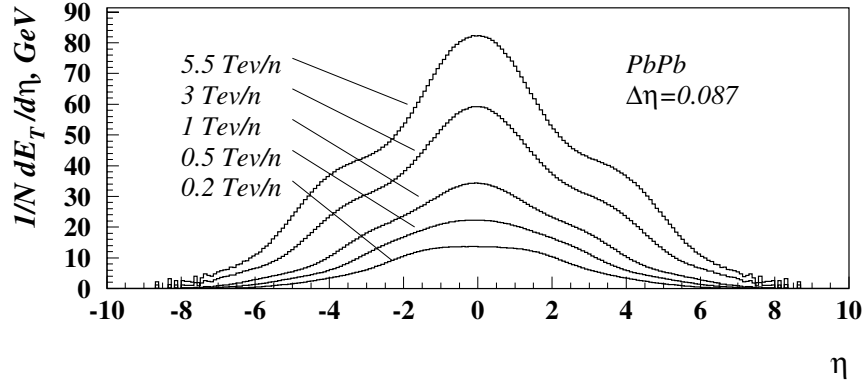

Fig. 2.18. Total transverse energy as a function of η, $dE_T/d\eta$ (GeV), for Pb+Pb collisions at (from top to bottom) $\sqrt{s} = 5.5$, 3, 1, 0.5, and 0.2 TeV/nucleon normalized to the number of events with $d\eta = 0.087$. The HIJING simulation includes both energy loss and shadowing

2.6 Summary

Some of the most prominent quark-gluon plasma signatures that could be studied with the CMS detector have been discussed here. Since the relative importance of these signatures depend on the initial conditions of the system, the role of minijet production in determining the initial conditions was described. Parton shadowing, which influences the initial temperature and the final multiplicity in an ideal quark-gluon plasma, was included. It was found that shadowing could reduce the initial temperature by decreasing the initial parton production. This reduction in the multiplicity would have the effect of making the environment easier to handle experimentally since the number of particles to be tracked would be reduced.

Quarkonium suppression through the Υ family is a promising signature, as already known from fixed-target experiments at the CERN SPS [10]. The p_T dependence of the Υ'/Υ ratio, as measured by CMS, could provide valuable information on the initial conditions of the plasma. As was shown, the initial conditions and the subsequent expansion of the system strongly influence the Υ'/Υ ratio. The Υ production rate is large enough for such measurements to be feasible. The ψ'/ψ ratio as a function of p_T can provide additional important information on the plasma even at high p_T.

Energy loss effects such as the modification of the dilepton continuum through heavy quark decays and jet quenching will provide complementary information on the density of the mediumtraversed by the hard partons as
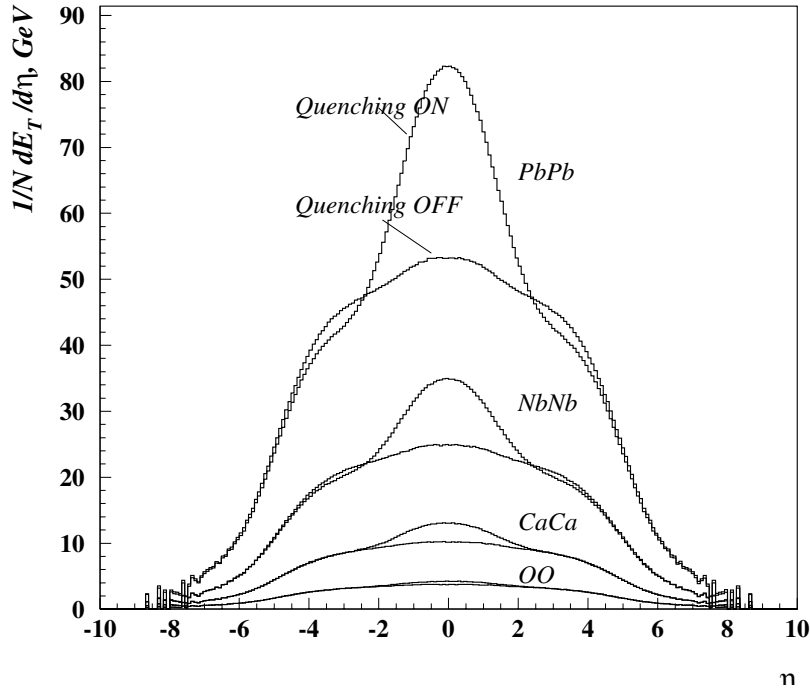
Fig. 2.19. Total transverse energy as a function of η, $dE_T/d\eta$ (GeV) for (from top to bottom) Pb+Pb, Nb+Nb, Ca+Ca, and O+O collisions at $\sqrt{s} = 5.5$ TeV/nucleon with and without energy loss normalized to the number of events with $d\eta = 0.087$ from the HIJING model. All simulations include shadowing

well as the influence of energy loss on global variables. The size of the energy loss influences the relative charm and bottom contribution to the dilepton continuum and the monojet to dijet ratio at high E_T. Both effects are observable by CMS. The CMS detector is particularly well suited for measuring high E_T jets.

Finally, it is important to note that any conclusions regarding quark-gluon plasma production depend on correlating as many signatures as possible. To understand the systematics of plasma production, studies of other systems at more than one energy will be crucial. To establish a baseline, pp and pPb collisions at the same energy as the Pb+Pb collisions are strongly advised. Going down in energy to *e.g.* the Tevatron energy of 1.8 TeV could provide an important cross check. Comparison of the Pb+Pb results with other nuclear systems such as Ca+Ca will also be important for a study of finite volume effects. Another necessary cross check for CMS will be comparison with results from the dedicated heavy-ion detector ALICE whenever possible since controversial results require confirmation, as already evident from the fixed-target heavy-ion program. Lessons learned from the CERN SPS heavy-ion program and the lower energy collider studies at RHIC should be put to good use as well.

3 Options for pA physics

3.1 Introduction

Why would one bother to investigate p-nucleus (pA) collisions at very high energies, while the simpler pp inter-

actions are either not understood sufficiently in the non-perturbative regime, or well matched by QCD predictions at large momentum transfer ?

The most naive reason is that – apart from limited experimental efforts with heavy targets and beam momenta $p_{lab} = 800$ GeV/c [107,108], and with deuterons and alphas at a centre-of-mass (c.m.s.) energy $\sqrt{s} = 63$ GeV [109] – most measurements have been performed at $p_{lab} \leq 200$ GeV/c [110,111]. Hence, pA collisions at the LHC near $\sqrt{s} = 9$ TeV [112] per nucleon would increase the energy scale for these interactions by more than a factor 230, a rather unprecedented jump indeed. Extrapolations will become easier when based upon future pA experiments at RHIC ($\sqrt{s} \simeq 350$ GeV) [8].

Many of the following arguments for investigating pA collisions at the LHC depend on the fact that nuclei serve both as targets and detectors since they are collections of nucleons separated by typical distances of the order of 1 fm in the nuclear rest frame, equivalent to a typical timescale of about 3×10^{-22} sec. Very soft partons from all nucleons overlap, however, in Lorentz contracted nuclei. Novel QCD effects caused by the large density may replace the free proton parton evolution scheme.

So far, the prominent features of pA interactions, such as total cross sections, elastic scattering, average multiplicities, and distributions of charged secondaries are conveniently described in the framework of Glauber theory. This hadronic multiple scattering scheme [113] is sketched in Section 3.2.

Predictions for collisions of heavy ions at, *e.g.*, the LHC are often made in this framework [113,114], which is also used in the interpretation of cosmic ray data [115].

It may, however, turn out that the basic assumptions of this multiple scattering approach breaks down at very high energies. Therefore, basic features of pA collisions have to be determined experimentally in order to establish an improved theoretical framework. These questions, as well as the production of B mesons and of top quarks, Pomeron interactions, and the concept of "formation time" are addressed in Section 3.3.

The characteristics of rare "perturbative" processes in collisions involving hadrons depend on the structure functions of the colliding objects which are, so far, not well understood theoretically. A wealth of data from deep inelastic lepton-nucleus scattering has revealed subtle nuclear effects [22]. Structure functions of nuclei can be derived at the LHC most directly from the yields of γ, J/ψ, Υ, $W^\pm$ and Z^0. Measurements of multiple production of heavy objects may give access to parton-parton correlations in nuclei. These aspects of the structure of bound nucleons and of nuclei are discussed in Section 3.4.

Partons emerging from hard processes in pA collisions traverse the surrounding cold nuclear matter. The so-called "Cronin-effect", measured for single hadrons [116] and jets [117] at $p_{\text{lab}} \leq 800$ GeV/c, signals multiple scattering of the initial parton [118] in the target nucleus. Systematic studies of these features at much higher energies should improve its theoretical understanding. This is particularly relevant since QCD suggests the energy loss of partons in cold hadronic matter and in a hot, deconfined quark-gluon plasma (QGP) should be different [91, 92]. Section 3.5 is concerned with these topics.

Data from pA collisions at LHC energies are not only interesting on their own but also improve event generators for pA and heavy ion collisions. They are therefore crucial for calibrating quark-gluon plasma (QGP) searches at the LHC as well as cosmic ray data at similar collision energies. In this context one may also envisage, as mentioned in Section 3.6, dedicated measurements with the CMS detector of μ fluxes from cosmic air showers.

More speculative ideas, including those suggested by cosmic ray data, may be found in [119]. They are usually based upon very good acceptance in the fragmentation regions and/or at rather small transverse momenta, kinematic regions not optimally covered by CMS.

3.2 Current understanding of pA data

3.2.1 Integrated cross sections and elastic scattering

Scattering of hadrons off nuclear targets at energies $\sqrt{s} \leq 63$ GeV is usually well described in the framework of multiple interactions [113], if one assumes independent small angle scatterings of the projectile hadron off individual target nucleons at frozen positions. This yields good agreement between data and predictions [120], as illustrated in Fig. 3.1(right) which shows measured and calculated differential cross sections for pd elastic coherent scattering at $\sqrt{s} = 63$ GeV. The individual contributions from single and double scattering, as well as from the deuteron s-wave (form factor S_s) and d-wave (form factor S_Q) are
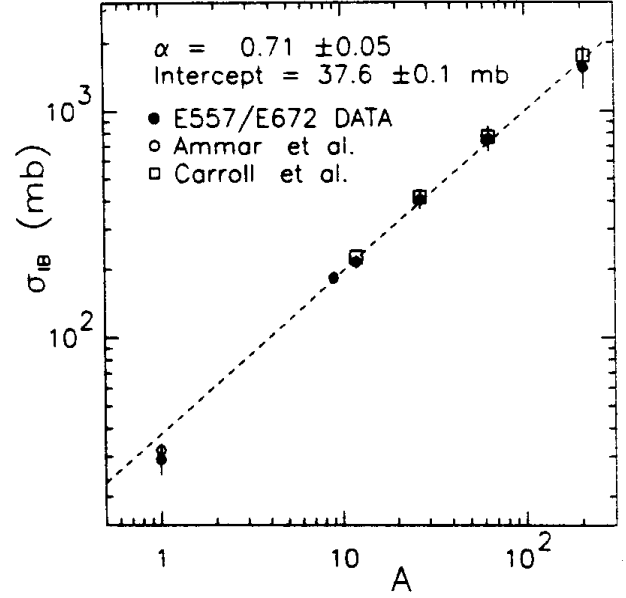
Fig. 3.2. Production cross sections from p-nucleus interactions at $p_{\text{lab}} = 800$ GeV/c as function of A with a fit from A^α. From [107]

shown in Fig. 3.1(left). Applying the optical theorem leads to the total cross section σ_{pd}^{tot}:

$$\sigma_{pd}^{\text{tot}} = \sigma_{pn}^{\text{tot}} + \sigma_{pp}^{\text{tot}} - \delta\sigma \tag{3.1}$$

Originally, $\delta\sigma$ was assumed to be a consequence of elastic double scattering of the incident hadron [113]. More detailed theoretical work indicated, however, that there is a non-negligible contribution from inelastic intermediate states where the object propagating from the first to the second target nucleon is not a hadron in its ground state. This demonstrates rather directly that nuclei may be used to analyse objects immediately after emerging from a first interaction. The inelastic contribution grows with $\sqrt{s}$ [120].

One of the key assumptions of Glauber theory is that a proton incident on a nuclear target scatters with only one nucleon at a time. In this "large A" approximation, the total cross section in pA collisions is

$$\sigma_{pA}^{\text{tot}} = \sigma_{pp}^{\text{tot}} A^{2/3} \tag{3.2}$$

and the nucleus absorbs the incident proton proportional to the surface area of the target. The absorption cross section is half the total cross section, $\sigma_{pA}^{\text{abs}} = 1/2\sigma_{pA}^{\text{tot}}$. Available data show [107] that

$$\sigma_{pA}^{\text{abs}} \propto A^{0.71}$$

(see Fig. 3.2), close to the value of 2/3. In fact, for small inelastic cross sections or lighter nuclei, exponents greater than 2/3 are predicted in Glauber theory.
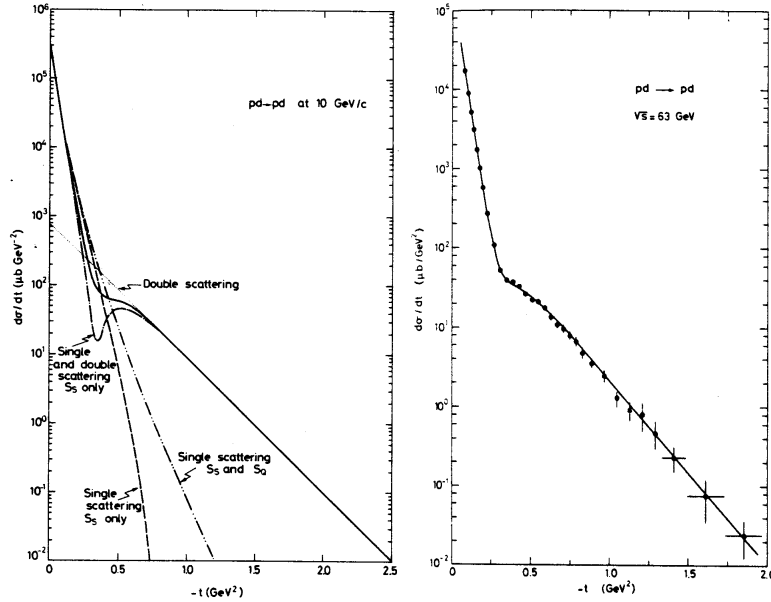
Fig. 3.1. *Left:* calculation of the individual contributions to elastic coherent *pd* scattering at $p_{\text{lab}} = 10$ GeV/c. *Right:* differential cross section for elastic coherent pd scattering at $\sqrt{s} = 63$ GeV and a prediction from the extended Glauber model. From [120]

The *pp* total cross section can be related to the opacity of the proton, $\Gamma_0(\sqrt{s})$, and the proton radius, $R_p(\sqrt{s})$, by [122]

$$\sigma^{\text{tot}}(pp) = 2\pi R_p^2(\sqrt{s})\Gamma_0(\sqrt{s}). \qquad (3.3)$$

It has been shown to increase with the center of mass energy as

$$\sigma_{pp}^{\text{tot}}(\sqrt{s}) = 21.70\, s^{0.0806} + 56.08\, s^{-0.4525}, \qquad (3.4)$$

shown in Fig. 3.3 up to Tevatron enegies. If the target is "black", or $\Gamma_0(\sqrt{s}) = 1$, then the growth of the total cross section implies that the effective proton radius is increasing, perhaps as much as ~ 1.5 between $\sqrt{s} = 20$ GeV and 2 TeV. An effectively larger proton could therefore conceivably interact with more than one nucleon simultaneously, leading to a breakdown of the Glauber model at high energies. Measurable consequences of such a breakdown will be discussed in Section 3.3.2. Neither systematic measurements of the dependence of σ_{pA}^{abs} on both A and $\sqrt{s}$, nor a precise comparison to σ_{pp}^{tot} or $\sigma_{pp}^{\text{inel}}$ have been made so far at high energies.

3.2.2 Average multiplicities

Intuitively one would guess that the multiplicity $\langle n(pA)\rangle$, *i.e.* the average number of secondary particles in *pA* collisions, is given by the average number of collisions of the projectile in the nucleus, $\overline{\nu}_{pA}$, and by the multiplicity of nucleon-nucleon collisions, approximated by $\langle n(pp)\rangle$:

$$\langle n(pA)\rangle = \overline{\nu}_{pA}\langle n(pp)\rangle \qquad (3.5)$$

This relation is actually quite well borne out by the data taken at p_{lab} between 50 and 200 GeV/c [123]. However,

$\overline{\nu}_{pA} \simeq A^{0.27}$, a weaker A dependence than the Glauber prediction [124]

$$\overline{\nu}_{pA} = \frac{A\sigma^{\text{tot}}(pp)}{\sigma^{\text{tot}}(pA)} \sim A^{1/3}. \qquad (3.6)$$

For AA collisions one has, also in the Glauber framework [124],

$$\overline{\nu}_{AA} = \frac{A^2\sigma(pp)}{\sigma^{\text{tot}}(AA)} \sim A^{4/3}. \qquad (3.7)$$

Nucleons are ejected from the target nucleus due to interactions of the projectile. Some of them can be detected as so-called "grey protons", *i.e.* recoiling protons with lab momenta above about 300 MeV/c. Thus the number n_p of grey protons per event is correlated with the number $\nu(n_p)$ of projectile interactions in the event. Figure 3.4 [125] shows the multiplicity of pions, $\langle n_\pi\rangle$, as a function of $\nu(n_p)$ for various target nuclei and a proton beam of 200 GeV/c. One finds that, independent of A, the quantity $\nu(n_p)$ determines the final state multiplicity and is therefore something like a measure of the "centrality" of the collision. Of course, events with many projectile interactions are very rare, as illustrated by the data displayed in Fig. 3.5 [126].

Most recently, experiment NA49 at CERN has installed an electronic detector for measuring grey particles [127]. The relative yields of strange and non-strange hadrons were then determined as a function of n_p in *p*Pb collisions at 158 GeV/c. One of the surprising and little understood findings is that the fraction of strange particles among the final state hadrons increases substantially with n_p [128]. This does not seem to be compatible with a simple Glauber scheme.
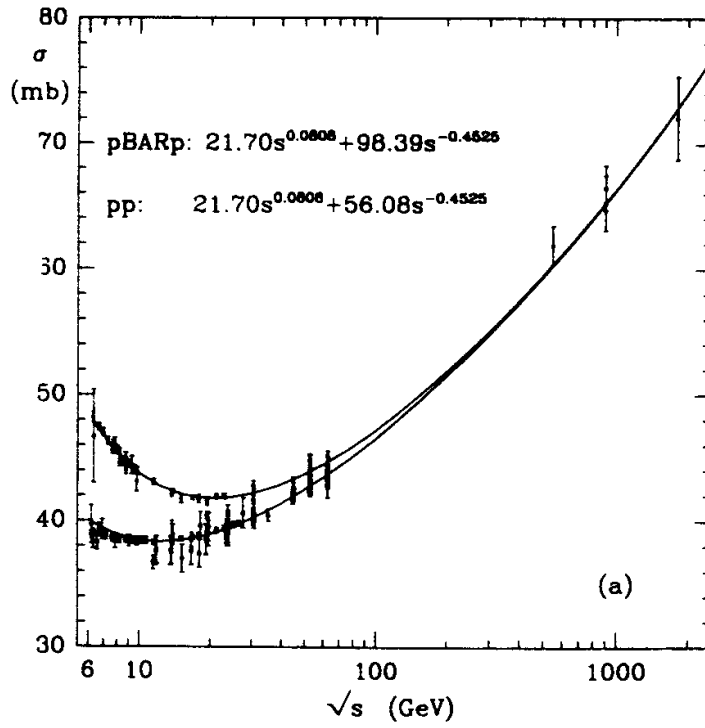
Fig. 3.3. Measured total cross sections for pp and $\overline{p}p$ interactions as function of $\sqrt{s}$ with fits based upon Regge theory. From [121]
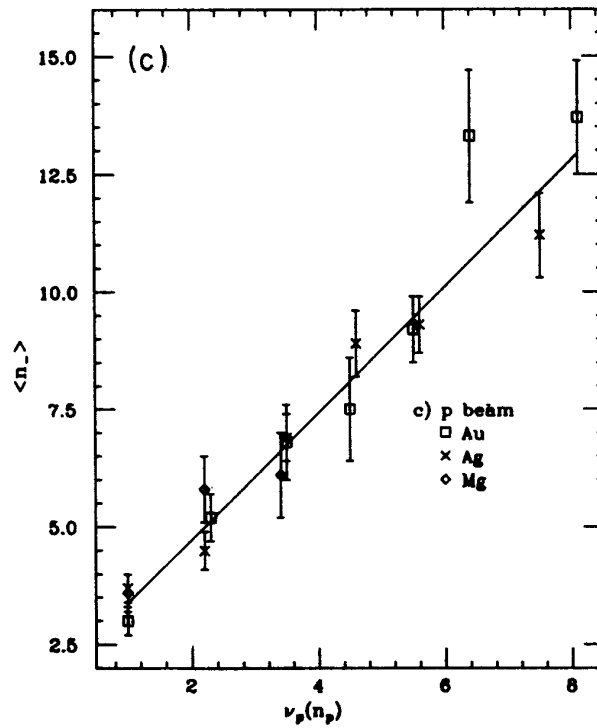

Fig. 3.4. Average multiplicity of negative particles from p-nucleus collisions at $p_{\text{lab}} = 200$ GeV/c and theoretical predictions. From [125]
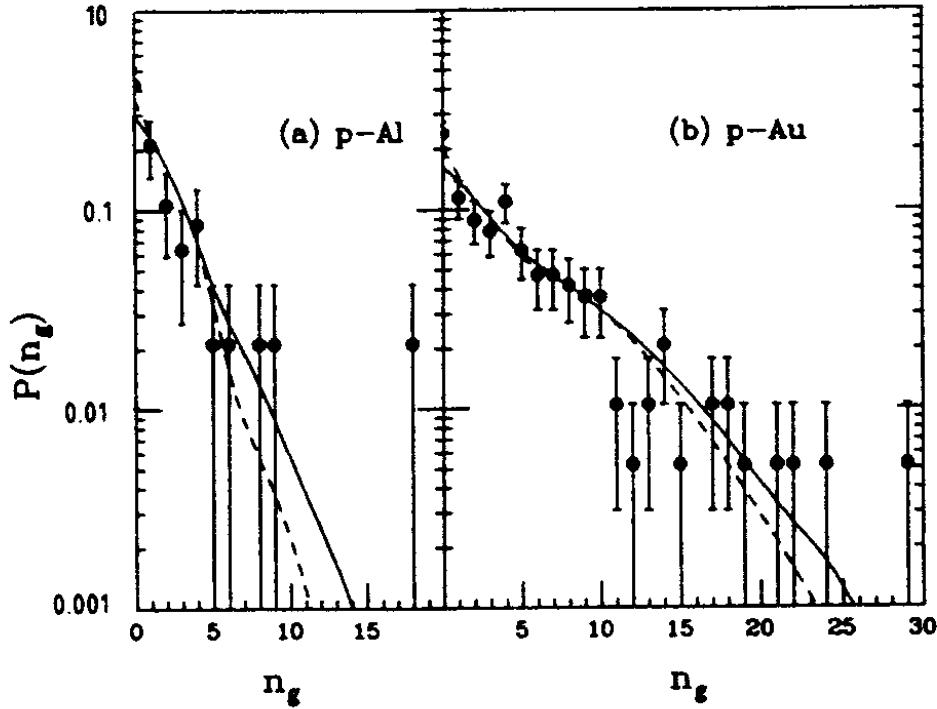
Fig. 3.5. Distributions of the number of grey tracks from pAl and pAu collisions at $p_{lab} = 200$ GeV/c and theoretical predictions. From [126]

3.2.3 Inclusive spectra

A more detailed understanding of these multiple collision processes may be gained from inclusive differential cross sections; normalized to pp collisions, rapidity distributions of charged secondaries are displayed in Fig. 3.6 as a function of lab rapidity y for A=Xe and a 200 GeV/c proton beam [129]. At the c.m.s. rapidity $y_{c.m.s.} = 0$, *i.e.* $y_{lab} \approx 3$, the ratio is close to $\bar{\nu}_{pA}$ as expected. There is a depletion beyond $y_{lab} \approx 6$, probably related to the energy loss of the projectile [130]. The very strong enhancement of particle production in pA collisions at $y_{lab} \leq 2$ is nevertheless surprising. Note, however, that the absolute number of secondaries in the range $y_{lab} < 2$ is rather small in case of pp collisions.

In order to find a simple qualitative explanation of the measurements at $y_{lab} < 2$, one may assume that the final state emerging from a hadron-hadron collision needs a certain formation time [131] to turn into hadrons. The minimum c.m.s. momentum (or the maximum rapidity y) at which hadrons begin to exist inside the nucleus is given by the condition that the formation time in the lab, t_F, is smaller than the time needed to traverse the diameter, $2R_A$, of the target nucleus:

$$t_F = \gamma t_0 \leq 2R_A, \qquad (3.8)$$

from which follows that $y < 2$ for a formation time $t_0 = 1$ fm/c in the frame comoving with the hadronizing object. If the quanta of this early final state are less efficient than hadrons in creating hadrons in subsequent collisions, it is only in this restricted kinematical range that many further hadrons are produced by reinteractions of secondary hadrons in the nucleus, a process often called "cascading".

An interesting aspect of cascading is that the formation times, $t_F(Q)$, of heavy quarks Q with mass m_Q may be shorter [131] than those of light quarks q for a given energy:

$$t_F(Q)/t_F(q) \approx \gamma_q/\gamma_Q \approx \frac{1}{m_Q}. \qquad (3.9)$$

The role of hadron formation time has also been addressed experimentally in deep inelastic scattering: the number of hadrons carrying a fraction z_h of the momentum of the struck quark has been measured as a function of the energy ν transferred [132]. As one may infer from Fig. 3.7, hadrons with $z_h \geq 0.2$ from energetic quarks are nearly unaffected by the target nuclei − copper and deuterium in this case − as the quarks traverse the nucleus before hadronization sets in. Leading hadrons from slower quarks are partially "absorbed" in the heavier nucleus.

One is thus lead to conclude that nuclei provide a testing ground for ideas on hadronization.
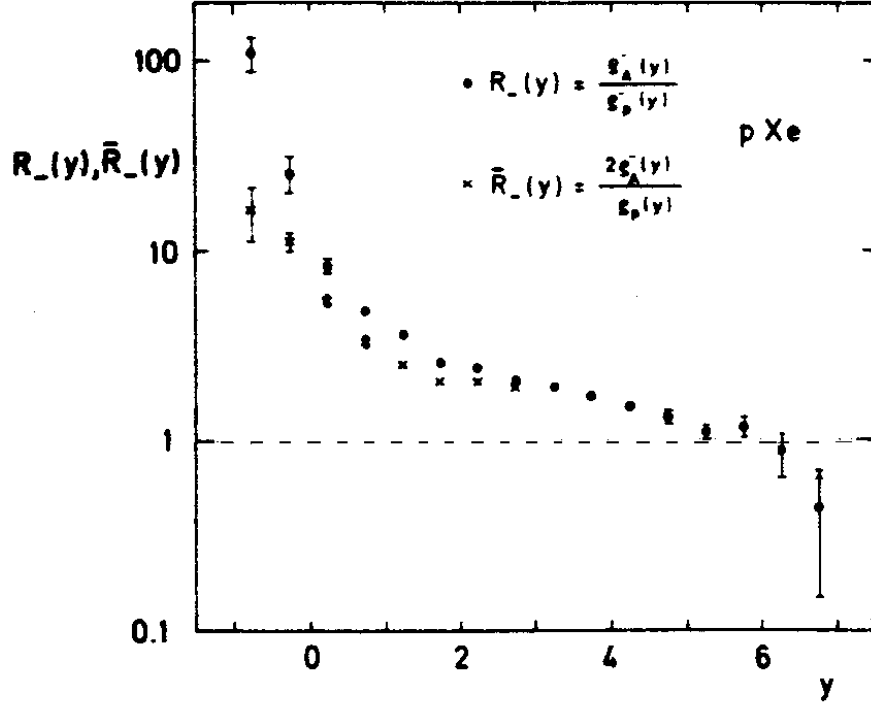
Fig. 3.6. Ratio $R(y)$ of track density $\rho^{\text{Xe}}(y)$ from pXe collisions and from pp collisions as functions of y_{lab} for $p_{\text{lab}} = 200$ GeV/c. From [129]
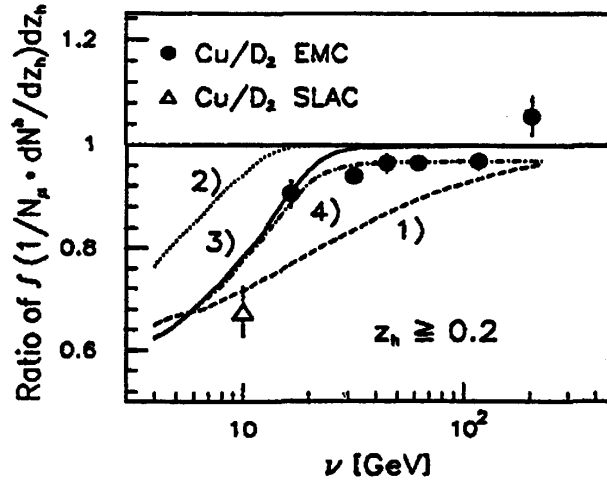

Fig. 3.7. Ratio of track density $\mathrm{d}N/\mathrm{d}z_h(z_h \geq 0.2)$ from μCu interactions and from μD$_2$ interactions as function of ν. From [132]

3.3 Measurement of characteristic features of pA interactions

3.3.1 Estimation of event rates, inclusive rates and event sizes

Extrapolating the pp total cross sections in (3.4) to 5.5, 9 and 14 TeV suggests $\sigma_{pp}^{\text{tot}} \approx 90$, 95 and 100 mb respectively. Note that the lower energies are the pPb and PbPb energies, rescaled from 14 TeV by $(Z_1 Z_2/A_1 A_2)^{1/2}$ where

Z and A are the proton number and nuclear mass number. Assuming $\sigma_{pA}^{\text{tot}} = \sigma_{pp}^{\text{tot}} A^{2/3}$ as in (3.2) and $\sigma_{AA}^{\text{tot}} = 4A^{2/3}\sigma_{pp}^{\text{tot}}$ [124,133], one finds at 9 TeV $\sigma_{p\text{Pb}}^{\text{tot}} \approx 3.3$ b and $\sigma_{p\text{Ca}}^{\text{tot}} \approx 1.1$ b while $\sigma_{\text{PbPb}}^{\text{tot}} \approx 12.6$ b at $\sqrt{s} = 5.5$ TeV. Given these total cross sections, the event rates, R, may be calculated from the luminosity,

$$R(A_1 A_2, \sqrt{s}) = \mathcal{L}\sigma_{A_1 A_2}^{\text{tot}}(\sqrt{s})$$

Using the luminosities given in Table 3.2, one finds $R(p\text{Pb}, 9\text{TeV}) \approx 3 \times 10^6 \text{s}^{-1}$ and $R(p\text{Ca}, 9\text{TeV}) \approx 3 \times$

Table 3.1. Luminosities of ion collisions. From [112]. Due to different bunch spacing, slightly different luminosities have been reported recently [134]

Collision	Luminosity $(\mathrm{cm^{-2}s^{-1}})$	Run time $(\mathrm{s/year})$	CM Energy (TeV)
pp	10^{29} - 10^{31}	10^7	14
Pb+Pb	10^{26}	10^6	1148
Ca+Ca	4×10^{30}	10^5 - 10^6	280
pPb	10^{30}	10^5	126
pCa	10^{31}	10^5	63

Table 3.2. Various parameters characterizing pA and AB collisions at the LHC. From [112,119]

System	$\sqrt{s}$(TeV)	Central y	Multiplicity $|\eta| < 0.9$	σ^{inel}(b)
PbPb	5.5	0.00	11000	7.60
pp	14.0	0.00	11	0.07
pO	9.9	0.35	21	0.40
pCa	9.9	0.35	26	0.73
pPb	8.8	0.46	36	1.94
dO	7.0	0.00	29	0.68
dCa	7.0	0.00	36	1.10
dPb	6.2	0.12	50	2.62

$10^7 \mathrm{s}^{-1}$. Assuming $\mathcal{L}_{pp} = 10^{34}$ cm^{-2} s^{-1}, $R(pp, 14\mathrm{TeV}) = 10^9 \mathrm{s}^{-1}$, leading to the following relative event rates:

$$\frac{R(p\mathrm{Pb}/9\mathrm{TeV})}{R(pp/14\mathrm{TeV})} \approx 3 \times 10^{-3},$$

$$\frac{R(p\mathrm{Ca}/9\mathrm{TeV})}{R(pp/14\ \mathrm{TeV})} \approx 10^{-2},$$

$$\frac{R(p\mathrm{Pb}/9\mathrm{TeV})}{R(\mathrm{PbPb}/5.5\ \mathrm{TeV})} \approx 25.$$

Besides the event rate, another important experimental quantity is the occupancy, essentially proportional to the event size or multiplicity. To a good approximation the multiplicity at $y = 0$ in the center of mass, $(\mathrm{d}N/\mathrm{d}y)_{y=0}$ is proportional to $\overline{\nu}_{pA} \approx A^{1/3}$, (3.6), and to $\ln(\sqrt{s})$. Therefore, using (3.5) we find

$$\langle n(pA, \sqrt{s}) \rangle = \overline{\nu}_{pA} \langle n(pp, 14\mathrm{TeV}) \rangle \frac{\ln \sqrt{s}}{\ln 14}. \qquad (3.10)$$

Thus $\langle n(p\mathrm{Pb}, 9\mathrm{TeV}) \rangle \sim 5 \langle n(pp, 14\mathrm{TeV}) \rangle$ and $\langle n(p\mathrm{Ca}, 9\mathrm{TeV}) \rangle \sim 3 \langle n(pp, 14\mathrm{TeV}) \rangle$. These results are in qualitative agreement with simulations based on Glauber scattering, given in Table 3.1 for the pseudorapidity interval $|\eta| < 0.9$ (see also [112]). Note that, in asymmetric systems, the center of mass rapidity shifts relative to the pp rapidity by the factor

$$\Delta y = \frac{1}{2} \ln Z_1 A_2 / Z_2 A_1,$$

also given in Table 3.1. In pPb collisions, $\Delta y \sim 0.5$, a rather large shift. There is no shift for dO and dCa because both have $Z/A = 1/2$.

3.3.2 Experimental tests of Glauber theory

If the effective proton radius is increasing with energy as suggested by Fig. 3.3 and (3.4) and (3.3), then a proton incident on a target nucleus interacts simultaneously with many nucleons. Thus, one of the key assumptions of Glauber multiple scattering theory no longer holds. As a

consequence, measurements of the differential cross section for elastic pA scattering, of the total cross section $\sigma^{\mathrm{tot}}(pA)$, of the absorption cross section $\sigma^{\mathrm{abs}}(pA)$, and also of global features of invariant inclusive cross sections may hint at improvements of this theory (see *e.g.* [135]).

Elastic pA scattering and total cross sections

Predictions for the differential cross sections for elastic and quasi-elastic pPb scattering (break up of the nucleus without production of secondaries) are given in Fig. 3.8 for $\sqrt{s} = 9$ TeV in the "large A" approximation [119]. For an optimal test of the theory, one should both cover the t-range down to $|t| \geq 5 \times 10^{-3} \mathrm{GeV}/c^2$ and be able to measure elastic and quasielastic collisions separately. At lower energies and/or for lighter nuclei the width of $\mathrm{d}\sigma/\mathrm{d}t$ increases due to smaller geometrical sizes of the scattering objects, such that it is easier to cover the necessary t-range experimentally. Extrapolation of the elastic differential cross sections to $t = 0$ then yields the total cross sections $\sigma^{\mathrm{tot}}(pA)$ as functions of $\sqrt{s}$ and A, allowing further tests of the theory. The large A approximation to Glauber theory is very general and does not depend critically on its specific assumptions. Measurements with lighter nuclei, such as $A = $ O, Ca, Ag in addition to Pb and p are therefore mandatory for a thorough study. In order to obtain a good overall picture, measurements with these nuclei should be performed at various energies, *e.g.* at $\sqrt{s} = 2$ ($p\bar{p}$ at the Tevatron), 5.5 (PbPb collisions at the LHC), and 9 TeV (pp at the LHC).

An optimized detector is needed for a dedicated investigation of elastic and total cross sections for pA collisions with a geometrical acceptance for the elastically scattered proton down to very small angles. Very good coverage for secondary hadrons ensures a precise measurement of the cross section for inelastic processes, as required for the determination of total cross sections independent of the knowledge of luminosity. It is therefore a fortunate coincidence that the TOTEM experiment [136] would like to
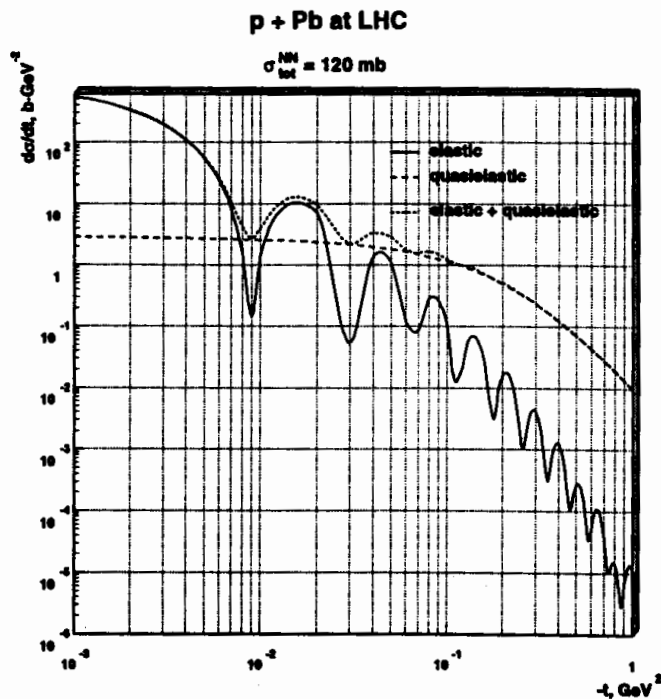
Fig. 3.8. Predicted differential cross sections for elastic coherent and elastic incoherent (quasielastic) pPb scattering as function of t at the LHC. From [119]

share the CMS site; its main goal is a precise measurement of the elastic differential cross section, and therefore of the total cross section in pp collisions. At present it is not clear whether the kinematical range $|t| < 10^{-2}$ GeV/c^2 can be reached [136]; a measurement of $\sigma^{\rm abs}$ (pA) is then even more important (Section 3.2). TOTEM also foresees an in-depth study of diffractive phenomena. As emphasized in [119] an investigation of diffraction in pA collisions is very desireable.

For the separation of elastic coherent ($pA \to pA$) and quasi-elastic contributions to elastic pA scattering one should be able to detect single nucleons ejected from the circulating nuclei. It is conceivable to use a "zero degree calorimeter" of the type envisaged by ALICE [9] for this purpose (see Section 3.3.5).

Integrated cross section for the production of secondaries

There are no measurements of $\sigma^{\rm abs}(pA)$ for inelastic pA collisions at $p_{\rm lab} > 800$ GeV/c. Theoretical predictions can be derived in the Glauber framework as a function of A. The expected energy dependence is related to that of the elementary nucleon-nucleon interactions.

A measurement at LHC energies would require a rather complete geometrical acceptance up to very large c.m.s. rapidities. Again, use should be made of the TOTEM detector which covers rapidities $|y_{\rm c.m.s.}| \leq 7$ in order to determine $\sigma^{\rm tot}(pp)$ via the "luminosity independent" method [137], *i.e.* by recording the rate of inelastic pp collisions.

The choice of collision energies and of nuclei should be compatible with the one for elastic scattering. In particular, the usefulness of pN or pO collisions should be emphasized. These interactions at LHC energies are an important fraction of cosmic air showers at energies beyond the "knee" shown in Fig. 3.9 [138]. Their relative contribution may change with energy. Thus, LHC data taken at well defined $\sqrt{s}$ and fixed A would be very welcome to "calibrate" cosmic ray data.

An alternative method to determine $\sigma^{\rm abs}(pA)$ depends on measurements of the inclusive differential cross section $\mathrm{d}\sigma/\mathrm{d}t$ for protons at $|t| \geq 0.1$ GeV/c^2, where inelastic production dominates elastic contributions [139].

Inclusive rapidity spectra

Typical inclusive rapidity distributions of negative particles from pAr and pXe collisions at $p_{\rm lab} = 200$ GeV/c are displayed in Fig. 3.10 [105]. There are no data for heavy nuclei at higher energies. One concludes from Fig. 3.10 that these measurements of non-identified secondaries are of rather modest precision and that theoretical calculations, based upon a string model and including multiple interactions in the Glauber framework, are close to the data. It is, however, interesting to note that two-particle correlations in pBe interactions at $p_{\rm lab} = 200$ GeV/c are, so far, not matched by any model [140]. The experimental situation may soon improve substantially since experiment NA49 is expected to provide precise differential cross sections from pp and pPb interactions at

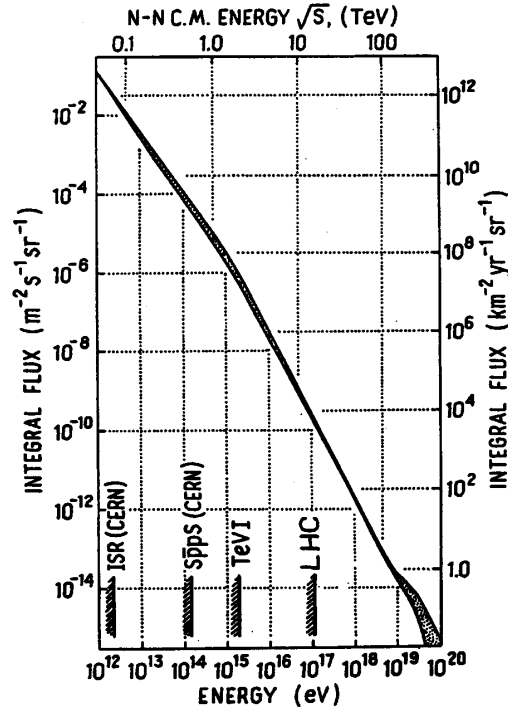**Fig. 3.9.** Integral flux of cosmic rays as function of $\sqrt{s}$. From [138]

158 GeV/c [128], including a "centrality" dependence in the case of $p\overline{p}$ interactions. Nonetheless, the large energy gap up to LHC energies remains. At increasing energies, simple versions of string models may run into trouble as strings may start overlapping. On the other hand, more and more partons would interact at rather large momentum transfer, giving rise to calculable perturbative parton cascades. Rather recent theoretical calculations of inclusive rapidity distributions for Pb+Pb collisions at the LHC in the Glauber framework and from the Parton Cascade Model are shown in Fig. 3.11 [141]. Both predictions differ significantly. In the rapidity range $|y_{\text{c.m.s.}}| \geq 5$ relevant data can be obtained by CMS; for $7 \geq |y_{\text{c.m.s.}}| \geq 5$ the "inelastic" detector of TOTEM would be useful. For $|y_{\text{c.m.s.}}| \approx 7$ evidence for "nuclear" cascading may be found. A substantial reduction of particle production in the central region relative to Glauber predictions is also expected from Reggeon calculus [135]. In this theoretical framework the influence of nuclei on rapidity spectra and structure functions (see Section 3.4) is closely related to diffraction and properties of the Pomeron (see Section 3.3.4).

To be more specific, what should be measured are the inclusive distribution dN/dy of charged secondaries, and the inclusive energy distribution dE/dy – including both the hadronic and electromagnetic components – with the nominal CMS magnetic field. As a non-negligible fraction of charged particles escape detection, a measurement of the inclusive pseudo-rapidity (η) distributions, $dN/d\eta$, for charged particles and of $dE/d\eta$ should also be envisaged without magnetic field. The non-optimal position of tracking chambers in the case of no magnetic field might be (partially) compensated by the fact that one is dealing exclusively with straight tracks. A comparison of both data sets using event generators may improve the understanding of the underlying dynamics substantially.

In addition, the feasibility of measurements of inclusive production of strange particles at a reduced magnetic field of *e.g.* 1 T, should be investigated. Unexpected trends have been observed in pPb collisions at 158 GeV/c [128]. Production of strange hadrons may also signal the formation of a QGP [9] in Pb+Pb collisions.

As stated in previous sections, data should be taken at $\sqrt{s} = 2$, 5.5 and 9 TeV, as well as for various nuclei, and, if possible, as a function of the number of interacting nucleons determined by a 0° calorimeter (see Section 3.3.5). This program would be close to what is currently being studied in considerable detail by NA49 [128].

As in the case of integrated cross sections, these measurements are relevant for understanding multiple production processes. An improved knowledge of pA production mechanisms is also essential for the interpretation of heavy ion collisions when searching for the QGP [142]. Last, but not least, these measurements serve again for calibrating cosmic ray data, even if the latter come predominantly – due to experimental procedures – from the fragmentation region.

3.3.3 Inclusive production of heavy quarks

Cosmic ray data indicate the existence of a threshold of heavy flavor production at very high energies [143]. It is in-
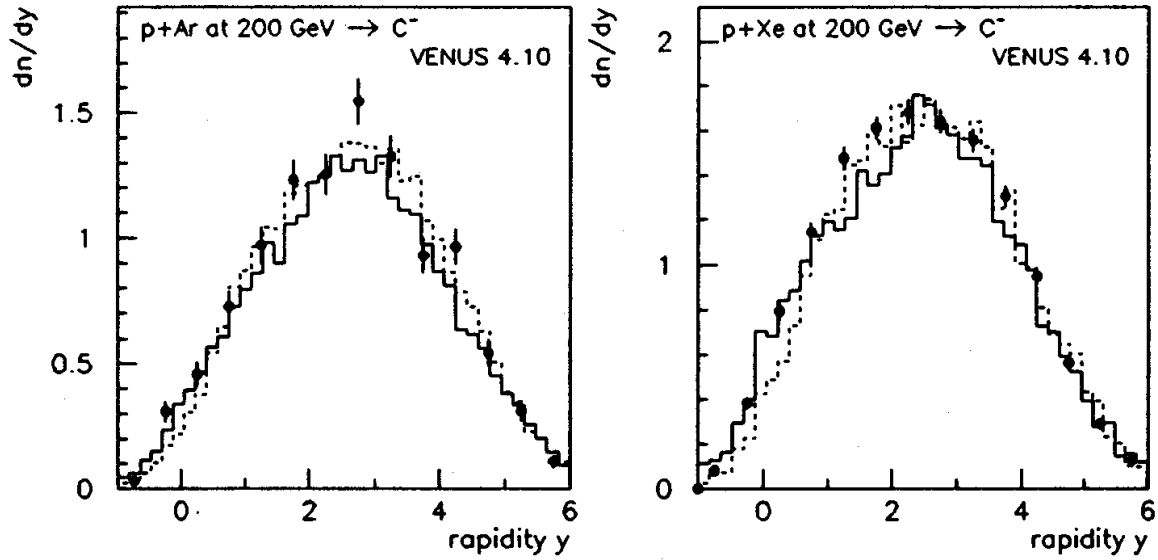
Fig. 3.10. Rapidity distributions of negative particles from pAr and pXe interactions at $p_{\text{lab}} = 200$ GeV/c and theoretical predictions. From [105]
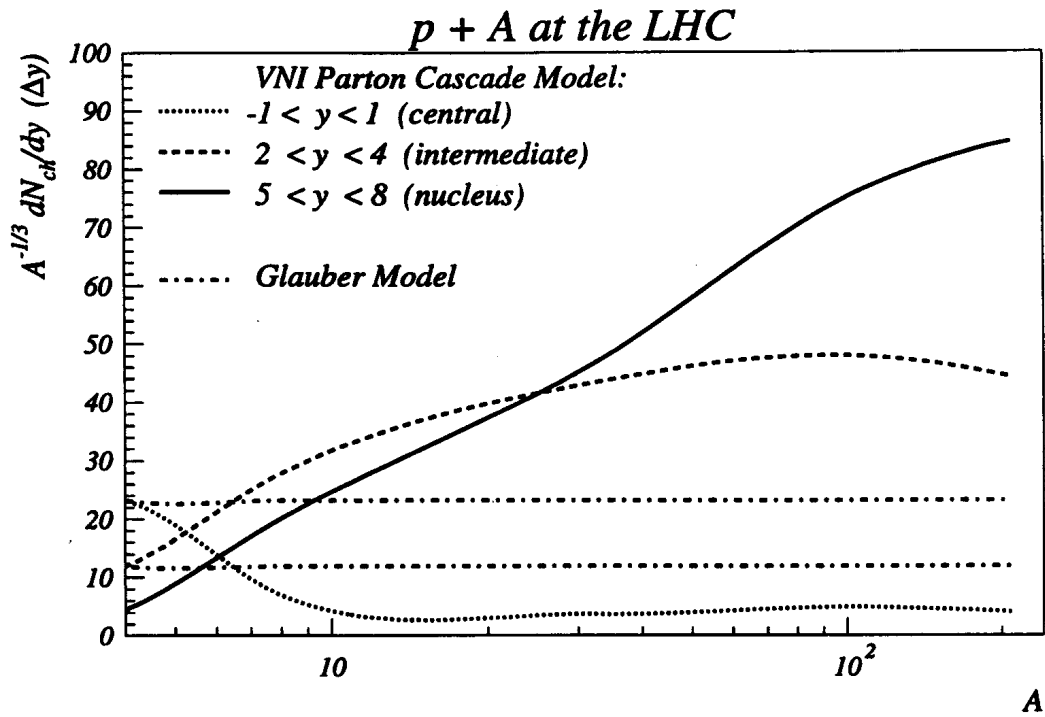

Fig. 3.11. Scaled particle density at the LHC for 3 intervals of $y = y_{\text{c.m.s.}}$ as function of A from Glauber and Parton Cascade Models. From [141]

triguing to speculate that this might be a reflection of large densities of soft partons in high energy pA collisions (see Section 3.4) which can be investigated at the LHC. The inclusive rate of reconstructed B-mesons, or top-quarks, from pA collisions relative to that in pp collisions is estimated on the basis of the formulae of Section 3.3.1. There may be a further enhancement factor (see Section 3.5) due to the "Cronin-effect" [116,144]. Differential cross sections from about 10^4 reconstructed B-decays ($B^0 \to J/\psi$, K_s^0) and t-decays [145] per month can be obtained from pPb or pCa interactions at 9 TeV. We have assumed $\sigma_{b\bar{b}} = 500\mu$b and $\sigma_{t\bar{t}} = 1$nb for pp collisions. Much larger statistics can be obtained from semi-leptonic decays of b-quarks. Searching for a threshold implies an energy scan, $e.g.$ measurements at $\sqrt{s} = 2$, 5.5 and 9 TeV. Further interest in measuring b-quark yields in pA collisions is presented in Section 3.5.

Proton-Calcium collisions at 9 TeV are equivalent to pp collisions at $\sqrt{s} = 14$ TeV and $\mathcal{L}_{pp} \geq 10^{32}$ cm^{-2} s^{-1} as far as rates are concerned.

3.3.4 Photon-Pomeron interactions

Even though the concept of the Pomeron was introduced long ago, a profound interpretation of this object is still missing. This is why the Pomeron is currently being studied intensively in deep inelastic lepton-proton interactions [146]. At the HERA ep collider one relevant process is emission, by the incoming charged lepton, of a photon that interacts with a Pomeron coupled to the proton. In proton-proton collisions at $\sqrt{s} = 63$ GeV double Pomeron cross sections have been determined [147]. This process dominates over two-photon mechanisms due to the small electromagnetic coupling constant. In heavy ion collisions at very high energies $\gamma\gamma$ processes are expected to occur much more frequently than double Pomeron interactions due to the factor Z^2 at each vertex instead of $A^{2/3}$ for each Pomeron [148,149].

One may therefore anticipate a relatively comfortable rate of γ-Pomeron interactions in pA collisions at the LHC, where the Pomeron is preferentially emitted by the proton while the nucleus is the photon source. Hopefully, competing mechanisms are negligible. Such a reaction is characterized kinematically by rather small momentum transfers between initial state and final state protons and nuclei, respectively, as well as by two large raidity gaps next to the outgoing fast hadrons. The γ-Pomeron interaction gives rise to particles or clusters of particles with limited invariant masses, produced close to $y_{\text{c.m.s.}} = 0$ but shifted systematically towards the rapidity of the nucleus. This feature is a consequence of the spectrum of emitted photons which is inversely proportional to the photon energy [148,149]. A non-Pomeron background to the γ-Pomeron process may be suppressed experimentally in collisions of heavy nuclei with deuterons acting as isospin filters.

Once theoretical predictions of cross sections and kinematics for these processes are available, an experimental feasibility study for CMS should be undertaken.

3.3.5 Calorimetry at 0°

In the case of inelastic pA collisions it is important to determine the number, Π, of target nucleons involved, which are therefore recoiling with non-negligible transverse momentum. Equivalently, one can measure the number F of "spectator" nucleons which do not interact and therefore retain their incoming Fermi momenta. If $F = A - \Pi$ nucleons recombine their Fermi-momenta in the final state to emerge as a nuclear fragment, A_F, the standard deviation $\sigma_\perp$ of the distribution of the momenta of A_F, transverse to the direction of the incoming beam, is given by [150]:

$$\sigma_\perp \approx \frac{P_F}{\sqrt{5}} \sqrt{\frac{A_F(A - A_F)}{A - 1}} \approx 0 \ (100\text{MeV}/c) \quad (3.11)$$

where P_F is the average Fermi momentum in a nucleus.

In coherent processes the outgoing nuclei stay in the beam pipe, as do nuclear fragments with $Z/A \approx 1/2$. Non-interacting protons or neutrons leave the beam pipe as $Z/A = 1$, or 0, respectively. Calorimeters measuring the total energy E^0 in a cone with an opening angle of the order of $\sigma_\perp/(\sqrt{s}/2)$ about the proton and neutron trajectories, yield therefore, to a good approximation, the number of spectator nucleons provided that not many nuclear fragments A_F with $Z_F/A_F \approx 1/2$ are produced.

This method of determining the centrality, or impact parameter, of a collision is particulary important for selecting candidate events for QGP searches in heavy ion collisions. In this context, ALICE [9] has studied the feasibility of detecting the spectator energy in two small cones using 2 appropriate calorimeters near each outgoing beam. They are placed at about 92 m from the interaction point and have rather small transverse dimensions ($\leq 16 \times 16$ cm ^{2}), see Fig. 3.12).

It needs to be investigated whether one system of 2 radiation-hard calorimeters of this type can be integrated into the accelerator lattice at the "nucleus" side of CMS. Its use for tagging quasielastic pA scattering, for the suppression of eventual background to γ-Pomeron events, and for selecting central pA collisions (see also Sections 3.4 and 3.5) must be assessed.

3.4 Nuclear structure functions

Experiment shows that structure functions of bound nucleons differ from those of free nucleons [22]. At Bjorken-$x \leq 0.1$ a relative depletion has been established relative to that of free nucleons. There is abundant literature on the theoretical interpretation of this so-called "EMC-effect" [22]. A very simple argument emphasizes the main interest in this phenomenon in the framework of QCD: a nucleus A at high momentum p_A is Lorentz-contracted to a disc of thickness $\Delta z_A \approx 2R_A m_A/p_A$, where $R_A(m_A)$ is the radius (mass) of A. Soft partons are confined to a longitudinal dimension $\Delta z_S \approx (x(p_A/A))^{-1}$ by the uncertainty relation. For $\Delta z_s \leq \Delta z_A$, $i.e.$ for $x \leq (2R_A m_A)^{-1} \approx 0.01$, all partons from all nucleons
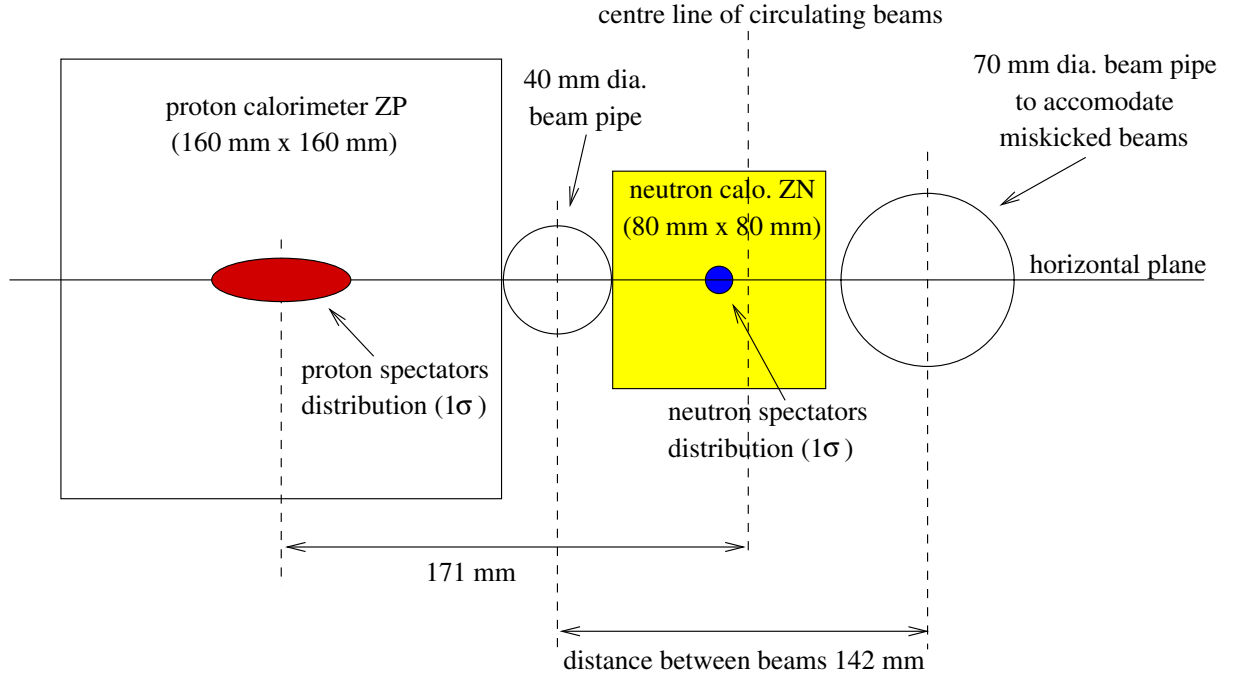
Fig. 3.12. Layout of the ALICE $0°$ calorimeter. From [9]

overlap in longitudinal space, with an individual transverse size of about 1 fm, or of the order of $1/\sqrt{Q^2}$ for momentum transfers $Q \geq Q_0$.

The number of partons, n^{part}, with $x \leq 0.01$ per cross sectional area of the nucleus A is given by $dn^{part} \approx A^{1/3}$ independent of $\sqrt{s}$. One may therefore anticipate a fast approach to saturation in pA collisions [151]. At this point, parton recombination processes may set in – a topical subject of current research at HERA [152]. This corresponds to novel QCD equations superseeding the known parton evolution, with non-negligible effects $e.g.$ on inclusive spectra (Sections 3.3.2 and 3.3.3).

The A-dependence of structure functions is measurable, $e.g.$ in the gluon mediated processes $pp \rightarrow gg \rightarrow J/\psi$ (Υ) or via $q\bar{q} \rightarrow Z^0$ and $q\bar{q} \rightarrow W^\pm$. Typical examples of measurements from J/ψ production in pA collisions at various energies and from lepton-antilepton pairs $(\ell\bar{\ell})$ in the Drell-Yan process $pp \rightarrow q\bar{q} \rightarrow \ell\bar{\ell}$ are shown in Figs. 3.13 and 3.14 [116,22]. The relative yields from heavy nuclei signal directly a modification of the relevant structure frunctions by the nuclear environment. At $y_{c.m.s.} = 0$ there is the kinematical relation between x and the mass, M, of the produced particle: $x \approx M/\sqrt{s}$. The respective structure functions can therefore be investigated at $\sqrt{s} = 9$ TeV in the range $x \approx 10^{-2}(Z^0, W^\pm)$, $x \approx 10^{-3}(\Upsilon)$, $x \approx 3 \times 10^{-4}$ (J/ψ). In a similar way, direct photons at large p_T and $y_{c.m.s.} \approx 0$, produced by quark-gluon fusion, probe structure functions at $x \approx 2p_T/\sqrt{s}$. To reach the range $x \ll 10^{-4}$, good acceptance at very large rapidities would be needed [119].

Approximate event samples for 1 month of data taking at $\sqrt{s} = 9$ TeV and a luminosity of 10^{30} cm^{-2} s^{-1} can be scaled from calculated yields from Pb+Pb collisions at $\sqrt{s} = 5.5$ TeV [141]. We find the following production rates

in pPb collisions:

$$pPb \rightarrow J/\psi > 13000$$
$$\rightarrow \Upsilon \quad > 28000$$
$$\rightarrow Z^0 \quad > 13000 \ .$$

These numbers must be multiplied by 2 for pCa collisions at a luminosity of 10^{31} cm^{-2} s^{-1}.

Triggering on the centrality of these interactions may enhance states of even larger parton densities such that surprises are not excluded. This has not been attempted so far.

Differential cross sections for the above processes do not only depend on structure functions but may also reveal details on multiple scattering of partons in the initial state [153], $i.e.$ before parton fusion. The outgoing vector-meson resonances may furthermore be absorbed to some degree by the surrounding nuclear matter [11]; this should not be the case for production of dileptons from Z^0 decays nor for photons due to the weakness of electromagnetic forces.

Dedicated measurements along these lines should help interpreting data on parton-propagation both in cold hadronic matter (see Section 3.5), and in a hot, deconfined plasma [91,92].

One may anticipate that in pA collisions two partons of the incident proton undergo hard interactions with two partons from two nucleons of the nucleus. The signature is multiple production of energetic objects such as jets [154], γ, J/ψ, Υ, Z^0, or W, eventually compensating their transverse momenta pairwise :

$$pA \rightarrow J/\psi + J/\psi \ (+2 \text{ jets})$$
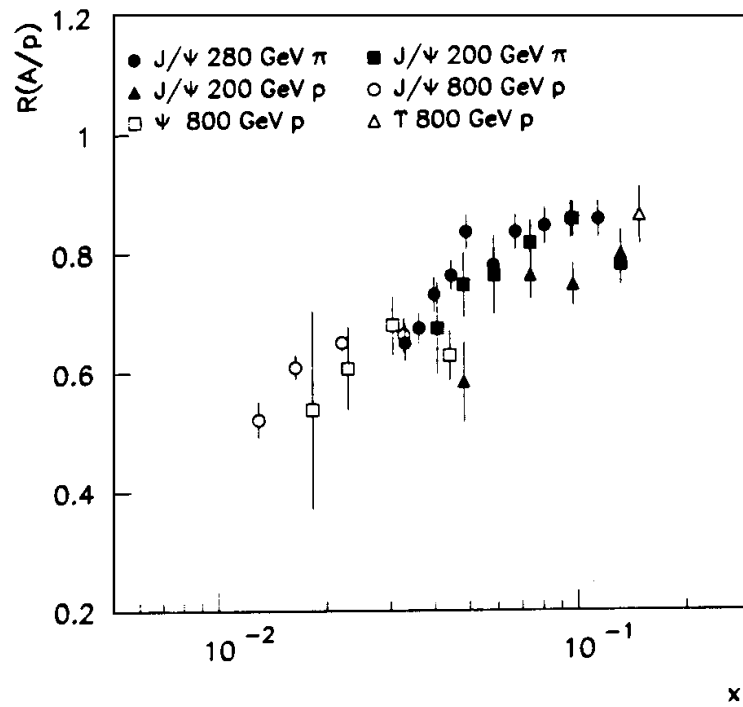$$\rightarrow \Upsilon + \Upsilon \ (+2 \text{ jets})$$

Fig. 3.13. Ratio of the number of vector mesons produced in πPt, πW, pPt, and pW interactions to interactions with proton targets. From [116]
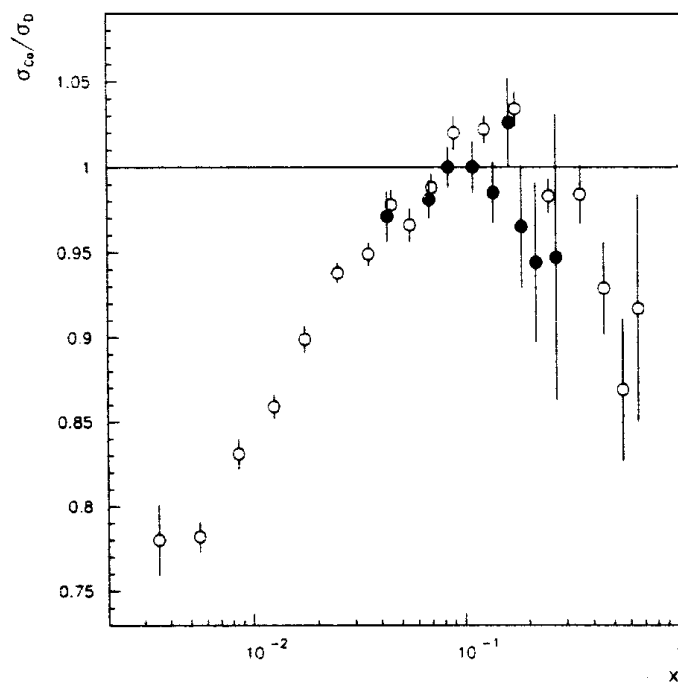

Fig. 3.14. Ratio of the yields of Drell-Yan pairs from pCa and pd collisions as function of Bjorken x. From [22]

$$\to Z^0/W + Z^0/WQ \quad (+2 \text{ jets})$$

$$\vdots$$

$$\to \gamma + 3 \text{ jets}$$

$$\vdots$$

$$\to 4 \text{ jets}$$

A measurement of rates as a function of A and of correlations among the final states may reflect correlations of partons inside nuclei. So far, no experiment has been able to address this phenomenon. Processes of this type should be more easily detectable at the LHC energies.

3.5 Parton propagation in cold hadronic matter

3.5.1 Inclusive spectra

It came as a surprise that in pA collisions at 200 GeV/c the differential cross section $E d\sigma/dp(pA \to \text{hadrons})$ was proportional to $A^{\alpha(p_{\mathrm{T}})}$ where $\alpha(p_{\mathrm{T}}) > 1$ at $p_{\mathrm{T}} \geq 2$ GeV/c. Typical measurements of $\alpha(p_{\mathrm{T}})$ are shown in Fig. 3.15 [116]. This so-called "Cronin-effect" found its likely explanation in terms of multiple parton scattering in the target nucleus [118] where the high p_{T} hadron is the leading fragment of a scattered parton [155]. One would expect that – in analogy to Glauber multiple scattering – the shape of the differential cross section of pA interactions depends on the differential cross section for pp collisions and therefore on $\sqrt{s}$. However, an energy dependence of the Cronin-effect has so far not been measured with sufficient precision.

The theoretical interpretation of the Cronin-effect would imply that the differential cross section $E d\sigma/dp(pA \to \text{jet})$ was also proportional to $A^{\alpha(p_{\mathrm{T}})}$, with $\alpha(p_{\mathrm{T}}) > 1$ for large transverse momenta p_{T} of hadron jets from scattered partons. Figure 3.16 shows measurements of $\alpha(p_{\mathrm{T}})$ in pA collisions at 800 GeV/c [117]. The difference between the two sets depends on the experimental definition of jets in pA collisions. One may conclude that the subject of parton propagation in cold nuclear matter is by far not exhausted, neither experimentally nor theoretically.

Comparisons of single pion and/or jet yields at rather large p_{T} from pA collisions at the LHC with measured yields of J/ψ, Υ and $W^{\pm}$, as well as of $\gamma^{\star}/Z^0 \to \ell\bar{\ell}$ should enable us to separate effects of structure functions and initial state multiple scattering from final state rescattering, especially due to gluons which dominate inclusive single pion and jets rates for $x \geq 0.1$. The QCD mechanisms of energy loss of partons in nuclear matter are currently of considerable interest. A method to study energy loss in AA collisions is described in Chapter 6.

Another tool for the investigation of parton multiple scattering may turn out to be a measurement of Z^0 production with subsequent decay into a $q\bar{q}$ pair, background permitting. As the Z^0 lifetime is extremely short, i.e. about 10^{-25} s [156], the decay q or $\bar{q}$ will reinteract in the nucleus after evolving from a small colour dipole for
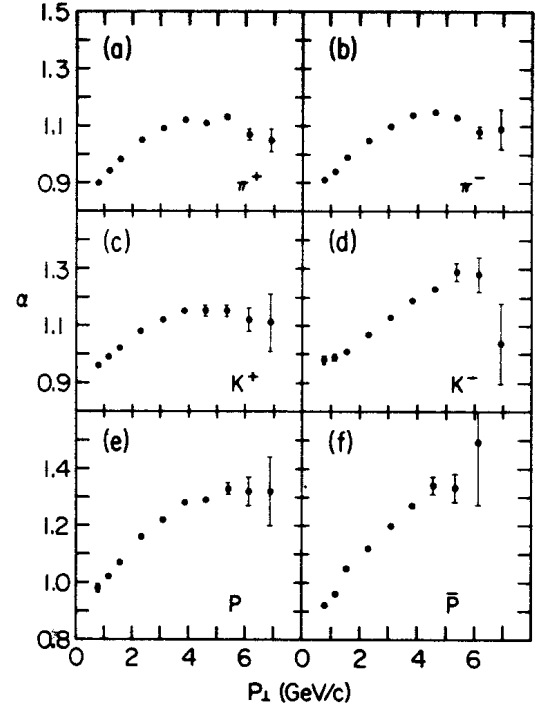

Fig. 3.15. The power α of the A dependence of the invariant differential cross section as function of transverse momentum for pA collisions at $p_{\mathrm{lab}} = 400$ GeV/c. From [116]

which the nucleus is supposed to be transparent. In case of reinteractions the ratio of the numbers of the decays $Z^0 \to q\bar{q} \to \text{jet}+\text{jet}$ and $Z^0 \to \ell\bar{\ell}$ may depend on the measured value of $p_{\mathrm{T}}(Z^0)$. Due to the same reason the width of Z^0-bosons reconstructed from two jets may depend on A and $p_{\mathrm{T}}(Z^0)$ beyond instrumental effects.

For formation times, t_F, shorter than the time needed by a parton to traverse the nucleus, the internal structure of jets of hadrons from parton fragmentation could depend on A, a consequence of reinteracting hadrons. So far there are not sufficiently precise data on this subject.

Finally, it may be amusing to find an unusual trend of the relative yield of B-mesons to, e.g., pions as a function of p_{T} and A. Pions at $p_{\mathrm{T}} \gg \langle p_{\mathrm{T}} \rangle$ are predominantly fragments of light quarks and gluons [155] with a rather long formation time while the time to form B-mesons from b-quarks is expected to be very short (see Section 3.2.3). Thus B-mesons may have more time than pions to reinteract in the nucleus, giving rise to a stronger Cronin-effect.

All these parton processes in cold hadronic matter should be understood before interpreting corresponding spectra from AA collisions in terms of "jet quenching" in a QGP [124,157].

3.5.2 Correlations

Measurements of correlations between two jets, j_1 and j_2, provide more detailed insight into the dynamics of final state partons in nuclear matter. Partons emerge from a
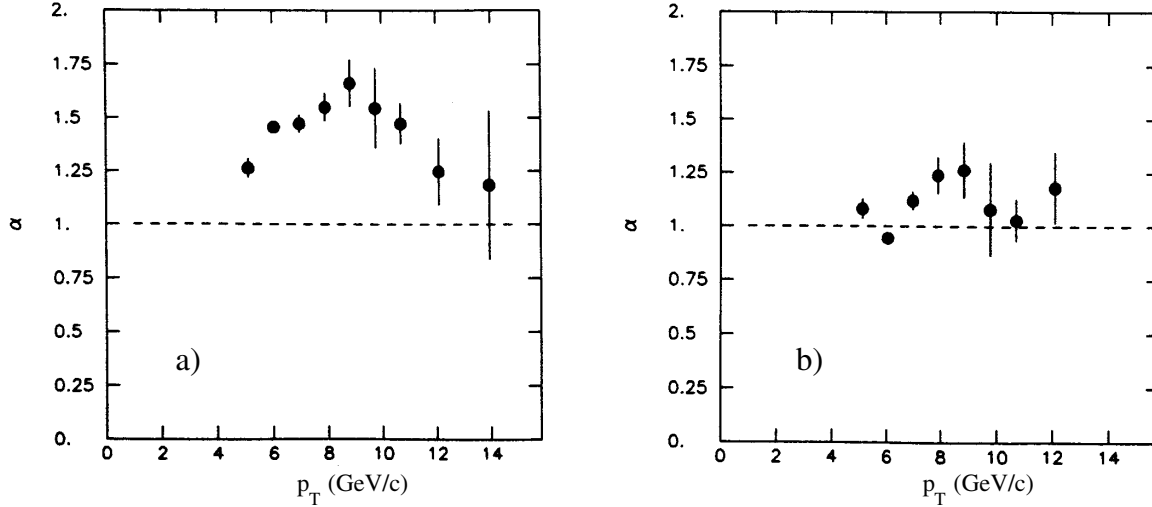
Fig. 3.16. The power α of the A dependence of jet yields as function of their transverse momenta from pA collisions at $p_{\mathrm{lab}} = 800$ GeV/c with **b** and without **a** subtracting the estimated non-jet background. From [117]

hard interaction back-to-back in the plane transverse to the pA collision axis, *i.e.* with an azimuthal separation $\Delta\phi \approx 180°$. Small initial state transverse momenta are neglected here. Both partons may reinteract or emit gluons subsequently such that the dispersion $\sigma(\Delta\phi)$ grows with increasing A. Experimentally, the azimuthal angles $\phi(j)$ of both jets are taken for the azimuthal angles of both partons. The difference $\phi(j_1) - \phi(j_2)$ then approximates $\Delta\phi$. At $p_{\mathrm{lab}} = 800$ GeV/c this has been done as shown in Fig. 3.17 [117]. One observes a widening of the measured distribution of $\Delta\phi$ with increasing A.

A quantitative analysis may become simpler if one of the two jets was replaced by a photon or a Z^0 decaying into $\ell\bar{\ell}$, neither of which are affected by reinteractions in the nucleus. Replacing one of two jets by a Z^0 decaying into 2 jets tends to enhance the effect of final state interactions. Note that while 2-jet events are dominated by gluons in a large kinematic range of small to moderate transverse momenta/energies, quark jets will dominate recoils against high p_T photons.

A substantial improvement of the experimental situation should be attempted at LHC energies.

3.6 Cosmic rays

Interactions of protons with nuclei at $\sqrt{s} = 9$ TeV correspond to beam momenta of nearly 100 PeV/c incident on target nuclei at rest. This energy range is very important to cosmic ray physics (Fig. 3.9) [138]. Extensive air showers (EAS) are predominantly induced by cosmic p, He and Fe (with energy dependent fractions) colliding with N and O in the atmosphere. As repeatedly stated in previous sections, these interactions should be studied for calibration purposes under the controlled conditions at the LHC. The well-known ambiguity [158] between the chemical composition (*i.e.* A) of cosmic rays and the average inelasticity of their interactions in the atmosphere may thus be re-

solved. For experimental reasons, EAS experiments are particularly sensitive at very large rapidities. Therefore, any detector (*e.g.* TOTEM) completing the forward acceptance of CMS would be useful. Measurements of total or inelastic cross sections, of inclusive fluxes of secondary particles and of transverse energy, even at more central rapidities , as well as of inclusive yields of open heavy flavors for pO or pN collisions at $\sqrt{s} = 2$, 5.5, and 9 TeV are badly needed (Fe+O or Fe+N interactions at $\sqrt{s} \leq 5.5$ TeV would be useful).

Such a contribution of CMS to cosmic ray physics can be complemented by measurements of the μ component of EAS. Cosmo-ALEPH [159] with a sensitive area of about 16 m^2 (the TPC area) has given some characteristic numbers for μ with momenta above 70 GeV/c. The rate of μ from EAS is close to 0.4 $\mu(m^2 \text{ s})^{-1}$ with $\approx 1\mu/\mathrm{m}^2$ for a typical shower. Two μ-showers are displayed in Figs. 3.18 and 3.19 [159]. Using the whole CMS detector these numbers would translate into rates of more than to 80 μ/sec and showers containing perhaps more than 4000 μ ! CMS provides good μ momentum measurement, μ identification and $\mu - \mu$ separation. The feasibility of an independent trigger should be investigated. A time stamp from the Global Positioning System (GPS) would be valuable, in particular for correlation measurements with other (LHC) detectors. The total data taking time would easily exceed 10 years.

The CMS detector might be surrounded, up to a distance of about 1 km, by simple μ-stations of an area of 4 m^2, each consisting of 2 layers of segmented scintillators. Thus, the centers of EAS can be determined more precisely. Coincidences over large distances have been found already, see [159,160]. Data from these stations can also be, due to their simplicity, made accessible via Internet, for example to highschools in the framework of an outreach project.
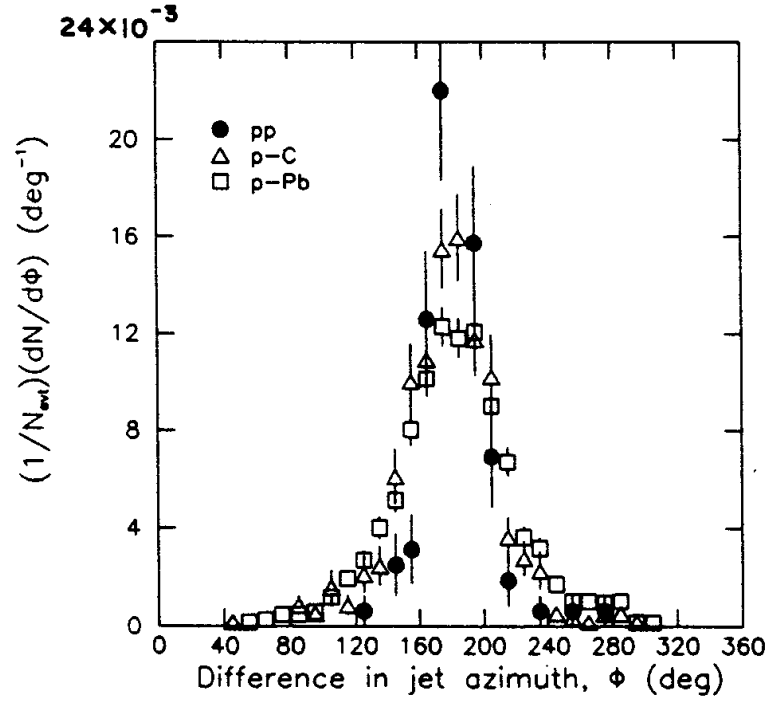
Fig. 3.17. The number of pairs of jets as function of the difference $\Delta\phi$ in jet azimuth for pA collisions at $\mathrm{p}_{lab} = 800$ GeV/c. From [117]
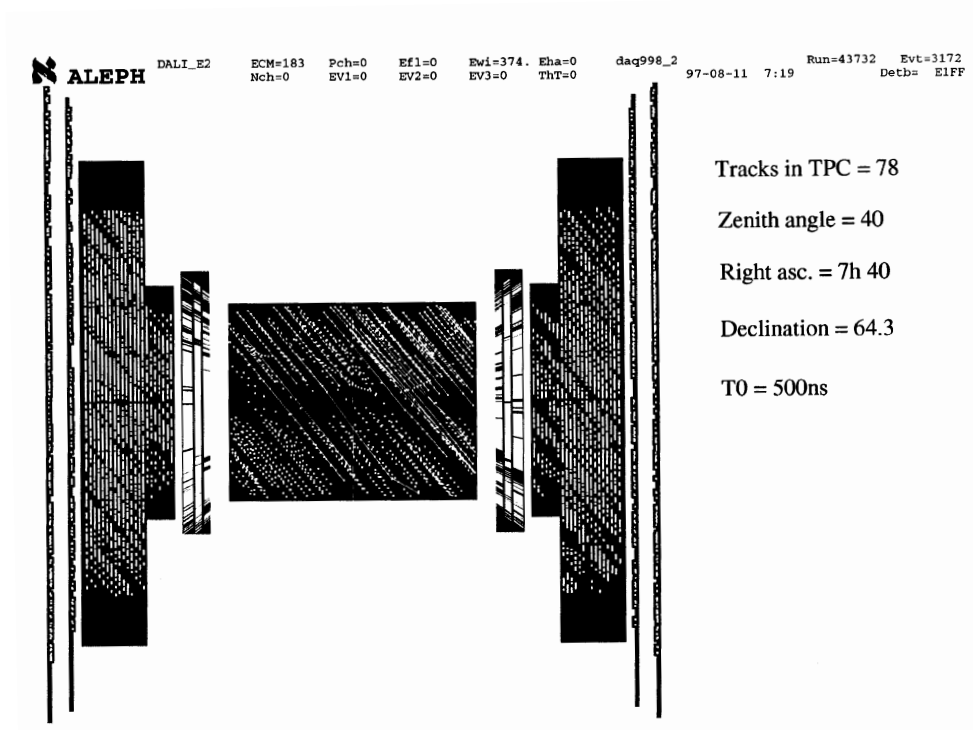

Fig. 3.18. Displays of μ-showers in the ALEPH detector. From [159]
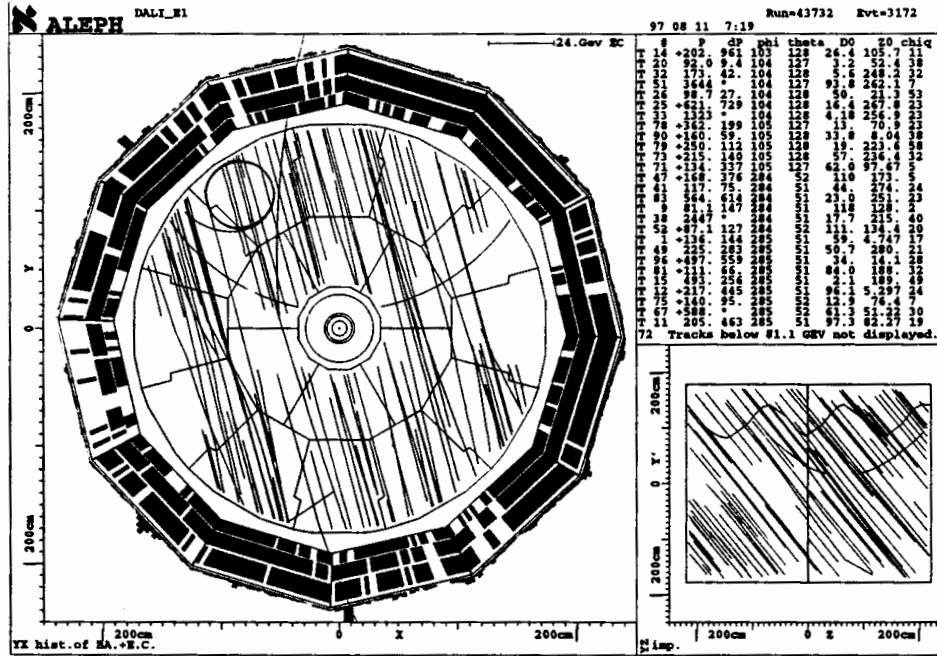
Fig. 3.19. Displays of μ-showers in the ALEPH detector. From [159]

3.7 Summary

Nuclei are attractive for at least two reasons: the internucleon distances of about 1 fm correspond to a timescale of about 3×10^{-22} s , typical for strong interactions. They are also supposed to provide very high densities of soft partons. From pA interactions at high energies one may therefore gain insight into many facets of the strong interaction in the framework of, or related to, QCD. Even if this theory is unchallenged, it needs a more profound and complete understanding. The topics in the preceding sections have all been presented in this perspective: multiple scattering in the Glauber approach or its generalization, hadronisation, γ-Pomeron interactions, and, in particular, propagation of partons in extended nuclear matter and the structure of bound nucleons. Very soft partons may overlap strongly in Lorentz-contracted nuclei such that non linear phenomena may occur which can no longer be described by current parton evolution schemes. CMS is able to contribute to an investigation of all of these topics. A compilation of desirable measurements is given in Table 3.3 as a function of $\sqrt{s}$ with typical values of A. Some remarks concerning experimental aspects are added. The interest in the setup of TOTEM with its Roman pots and geometrical acceptance beyond $|y| = 5$ and in a dedicated small calorimeter ("ZDC") to determine the "centrality" of pA collisions is highlighted. Except for γ-Pomeron interactions and multiple hard parton collisions, for which cross sections are presently not known, typical time scales for data taking per $\sqrt{s}$–A combination are up to one day for the rather global measurements [136]. They

are below one month depending on the selected final state for more differential cross sections of rarer processes. It is clear that much more detailed feasibility studies have to be performed in order to better assess experimental requirements and to establish a well understood order of priorities.

Most of the relevant data are also badly needed for predictions of "standard" nuclear effects in high energy heavy-ion collisions. Deviations from those extrapolations can then be taken as evidence for QGP formation.

Proton-nucleus collisions studied under the controlled conditions of accelerator experiments serve as a yard-stick for interpreting data from cosmic rays experiments, often at similar collision energies. The muon flux generated by cosmic rays in the atmosphere is also measurable with the CMS detector.

Detailed experimental problems have not been addressed. They are reserved for a future progress report.

4 Generalities of AA collisions

4.1 Luminosity

At the LHC heavy ions will be accelerated up to the energies $E = E_p(2Z/A)$ per nucleon pair where $E_p = 7$ TeV is the proton beam energy for the LHC. The energy per nucleon pair will be 5.5 TeV and 7 TeV for Pb+Pb and Ca+Ca beams respectively. For a single Pb+Pb experiment, the expected nominal luminosity ranges between 0.85 and 1.8×10^{27} cm^{-2} s^{-1}, depending on the luminos-

Table 3.3. p-A collisions, selection of physics opportunities (HI = Heavy Ions; CR = Cosmic rays)

Measurements	Physics topic	Related	$\sqrt{s}$(TeV)	A (suggested)	Additional experimental requirements
$\frac{\mathrm{d}\sigma}{\mathrm{d}t}, \sigma^{\mathrm{el}}, \sigma^{\mathrm{tot}}$	"Glauber"		0.2 /5.5/9	Pb, Ag, Ca, O/N	TOTEM
σ^{abs}	"Glauber"	HI, CR	0.2/5.5/9	Pb, Ag, Ca, O/N	TOTEM, $|\overline{B}| = 0$?
$\frac{\mathrm{d}\sigma}{\mathrm{d}y}(h^{\pm}), \frac{\mathrm{d}E}{\mathrm{d}y}$,	"Glauber",	HI, CR	0.2 /5.5/9	Pb, Ag, Ca, O/N	TOTEM and/or ZDC beneficial
$\frac{\mathrm{d}\sigma}{\mathrm{d}\eta}(h^{\pm}), \frac{\mathrm{d}E}{\mathrm{d}\eta}$	hadronization				TOTEM and/or ZDC beneficial; $|\overline{B}| = 0$?
$\frac{\mathrm{d}\sigma}{\mathrm{d}y}(V^0)$	hadronization	HI	0.2/5.5/9	Pb, Ag, Ca	TOTEM and ZDC beneficial; $|\overline{B}| = 1$T ?
$E\frac{\mathrm{d}\sigma}{\mathrm{d}p}(B, t)$	prod. mech.	CR	5.5 /9	Pb, Ag, Ca, O/N	ZDC ?
$\sigma(pA \rightarrow \gamma P \rightarrow \text{hadrons})$	Pomeron		9	Pb, Ca	TOTEM and ZDC ?
$E\frac{\mathrm{d}\sigma}{\mathrm{d}p}(J/\psi, \Upsilon, W, Z, \gamma)$	structure functions	HI	5.5 /9	Pb,Ag, Ca	ZDC beneficial
σ (double coll.)	parton corr.		9	Pb, Ca	ZDC ?
$E\frac{\mathrm{d}\sigma}{\mathrm{d}p}(h^{\pm}, \text{jet}, Z^0 \rightarrow q\bar{q})$, $E\frac{\mathrm{d}\sigma}{\mathrm{d}p}(2 \text{ jets, jet} + \gamma/Z^0)$	parton propagation	HI	5.5 /9	Pb, Ag, Ca	ZDC ?
Cosmic μ-fluxes	CR				μ-stations at large distances, GPS

ity lifetime [161]. The integrated luminosity per experiment will be reduced by a factor 3-4 for two experiments running at high luminosity [134]. In the following we shall often use the luminosity value of 10^{27} cm^{-2} s^{-1}. The interaction cross section for Pb+Pb collisions is about 7.6 b, leading to an event rate of 7.6 kHz. The bunch spacing for Pb+Pb interactions will be ~125 ns, compared to 25 ns for pp case. For lighter ion beams much higher luminosities can be achieved, e.g.$\mathcal{L}_{\mathrm{Ca}}/\mathcal{L}_{\mathrm{Pb}} = 2500$ [103]. Whereas the pile-up effect will be almost non-existent with Pb+Pb it cannot be neglected for Ca beams. To limit it at a low level ($\approx 3\%$) we shall probably have to reduce the Ca beam luminosity by one order of magnitude, and not exceed 2.5×10^{29} cm^{-2} s^{-1}. Scanning from $pp$to Pb+Pb collisions leads to strongly different experimental conditions. Some of them are summarized in Table 4.1 for the Pb and Ca beams. The luminosity values quoted in the table are those used in this study.

4.2 Nucleon-nucleon collisions and π/K multiplicity

The characteristics of a given AA collision (impact parameter, b, number of nucleon-nucleon collisions or hadronic multiplicity $\mathrm{d}N/\mathrm{d}y$) are determined using HIJING [102] as a model. We did not use the CMS simulation package coupled with the HIJING generator for our studies mainly because of CPU constraints. We have therefore developed a separate program using the HIJING results as an input. First, the impact parameter b is randomly chosen according to a fit of the distribution given by HIJING. The choice of b governs several important characteristics of an AA collison.

For a given b we can deduce the number of nucleon-nucleon collisions, N_{col}. It is given by the following parameterized function:

$$N_{\mathrm{col}} = N_0 \exp\left(-\left(\frac{b}{b_0}\right)^2\right) - a_0 \, b$$

where $N_0 = 1550$, $b_0 = 7$ fm and $a_0 = 0.5$ for Pb+Pb collisions (see Fig. 4.1) and $N_0 = 180$, $b_0 = 4.5$ fm and $a_0 = 0$ for Ca+Ca. Resonance production cross sections as well as the contribution to the dimuon background from open b and c production are estimated from N_{col}.

The most important variable in ion-ion collisions from the point of view of dimuon detection is the multiplicity of secondary charged hadrons for $b=0$, $(\mathrm{d}N^{\pm}/\mathrm{d}y)_{y=0}$. It is presently difficult to give a precise value for this variable at LHC energies. Several event generators like VENUS, HIJING, the DPM and FRITIOF predict a multiplicity ranging from 3000 to 8000 in the case of very central Pb+Pb collisions [162]. Obviously, the lower the multiplicity, the easier the dimuon reconstruction and the lower the associated dimuon background will be. As we cannot reject the eventuality of a high multiplicity we used the most pessimistic assumption.

The multiplicity for a given impact parameter is calculated using the following functions for Pb+Pb collisions:

$$\left(\frac{\mathrm{d}N^{\pm}}{\mathrm{d}y}\right)_{y=0} = 1.18\left(1 - \frac{b}{11.5}\right)\left(\frac{\mathrm{d}N^{\pm}}{\mathrm{d}y}\right)_{y=0}^{b=0}$$

if $b < 10$ fm

$$\left(\frac{\mathrm{d}N^{\pm}}{\mathrm{d}y}\right)_{y=0} = 5.9 \exp(2 - 0.56463 \, b)\left(\frac{\mathrm{d}N^{\pm}}{\mathrm{d}y}\right)_{y=0}^{b=0}$$
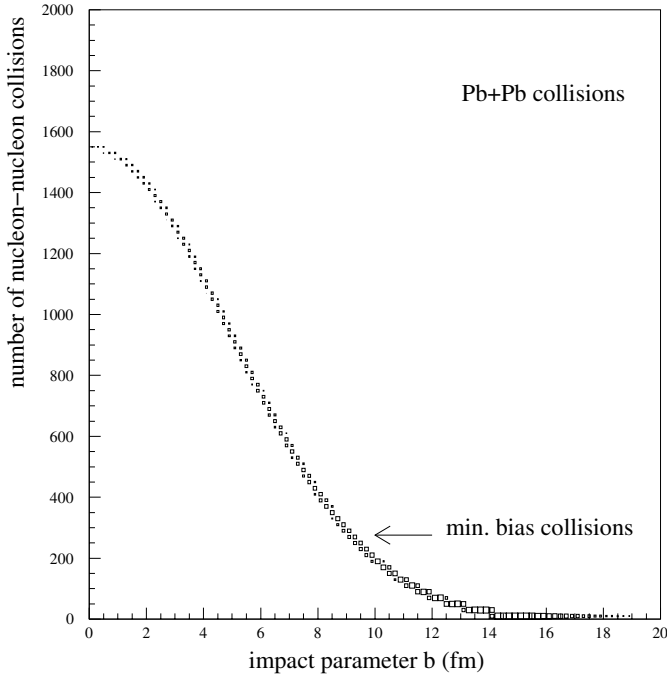
if $b > 10$ fm

Fig. 4.1. Number of nucleon-nucleon collisions in Pb+Pb collisions as a function of the impact parameter

Table 4.1. General parameters for Pb and Ca beams used in the present study

	Pb+Pb	Ca+Ca
$\sqrt{s}_{NN}$ (TeV)	5.5	7.0
$\mathcal{L}_{AA}$ (cm^{-2}s^{-1})	10^{27}	2.5×10^{29}
$\sigma(AA)$ (b)	7.6	2.1
$(\mathrm{d}N^{\pm}/\mathrm{d}y)^{b=0}_{y=0}$	8000	900

A similar function is used for Ca+Ca collisions. This parameterization leads to a maximum charged particle multiplicity at $b=0$ of 9440 for Pb+Pb and 1417 for Ca+Ca, significantly higher than the upper limit given by the event generators. Figure 4.2 displays the event distribution as a function of the multiplicity. It shows that in our simulations an average Pb+Pb collision would emit 1620 charged pions and kaons in one unit of rapidity in the central region in agreement with the HIJING predictions. Some numbers characterizing the 5% most central and the minimum bias collisions (*i.e.* averaged over all impact parameters) in the case of Pb and Ca beams are given in Table 4.2 .

To take an even more pessimistic view we have considered that all of these charged particles consist of pions and kaons only. In fact, this is true for $\approx$80% of the total. The relative π/K proportion 5:1 is assumed to be independent of the impact parameter.
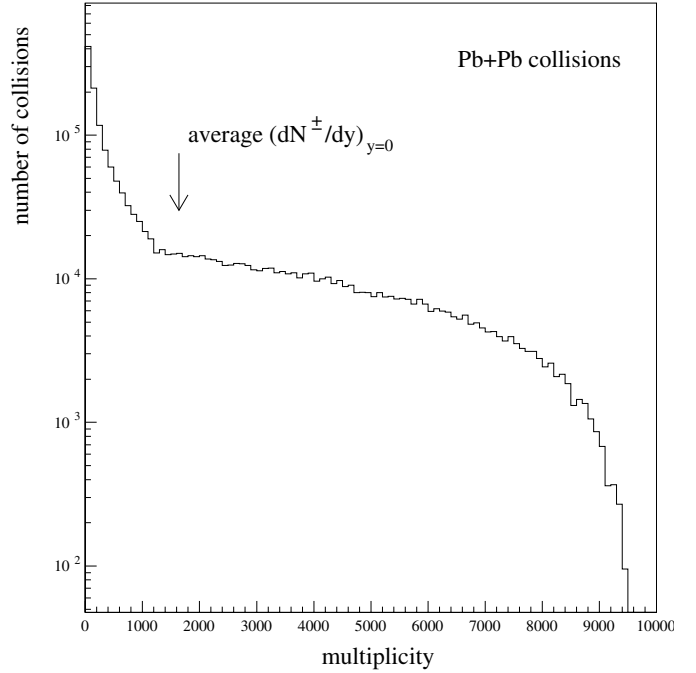
Fig. 4.2. Number of Pb+Pb collisions as a function of the multiplicity of charged particles per unit of rapidity at $y=0$

Table 4.2. Mean values for minimum bias and for the 5% most central collisions

	Pb		Ca	
	min. bias	central	min. bias	central
$\langle b \rangle$ (fm)	11	2.4	6.7	1.5
$\langle N_{\mathrm{col}} \rangle$	272	1360	37	160
$\langle \mathrm{d}N^{\pi,K}/\mathrm{d}\,y \rangle$	1620	7460	260	1110

4.3 Transverse energy measurement

The CMS detector with its large-acceptance muon system, fine granularity, large geometrical coverage of calorimeters and its high quality central tracker can explore several promising measurable effects of QGP formation:

- suppression of heavy quark ($c\bar{c}$ and $b\bar{b}$) resonance states through their muon decay channels;
- energy loss of hard partons (jets) detected in calorimeters;
- energy loss of heavy quarks through their muon decays;
- Z^0, Z^0+jet and γ+jet production.

For each of these studies, it is extremely important to perform measurements for different event centralities, from peripheral to central nucleus-nucleus collisions. In these interactions, the transverse energy of the event is related to the impact parameter of the collision. Hence, the measurement of E_{T} is mandatory for all experiments studying heavy ion collisions.

In the following, we present results from simulations of the capabilities of the CMS detector to perform transverse energy measurements in Pb+Pb and Ca+Ca collisions.

4.3.1 Simulations

For this specific study, Pb+Pb and Ca+Ca collisions were simulated using the HIJING Monte Carlo program [102]. The important parameters for the transverse energy measurement are the multiplicities of charged and neutral particles and their transverse momenta. They are presented in Table 4.3 for minimum bias Pb+Pb and Ca+Ca collisions.

Detector response is modelled using the CMSJET program [163] where the description of the electromagnetic calorimeter (ECAL) corresponds to the CMS technical design report [3] while the hadron calorimeter (HCAL) is represented by the TP7 design [164]. A recent design [165] is used for the very forward calorimeter (VF). Details on shower simulation in the calorimeters can be found in [163]. The thresholds on cell energies for ECAL, HCAL and VF are 5, 10 and 50 MeV respectively. Figure 4.3 presents the expected distribution of the detected energy in cells of the barrel, endcap and very forward calorimeters for the most central Pb+Pb collisions (those with impact parameter $b = 0$). The averaged values of cell energy obtained for 100 central Pb+Pb collisions are: 0.5 GeV and 1.1 GeV for the barrel part of ECAL and HCAL, 2.9 GeV and 10.6 GeV for the endcap part of ECAL and HCAL, and 280 GeV for the very forward calorimeter. The two-dip structure of the energy distribution in the endcap part of the hadron calorimeter is due to 3 different cell sizes in this region. The simulations show that even in this extreme case of purely central collisions, the energies deposited in cells of all calorimeters are well below the maximum values allowed by the dynamic ranges of the electronic readout systems (2 TeV for the ECAL [3] and 3 TeV for HCAL and VF [1]).

4.3.2 Transverse energy-impact parameter correlation

We have studied the possibility of measuring the transverse energy in Pb+Pb and Ca+Ca collisions for different intervals of the impact parameter. For this purpose 100 Pb+Pb and 500 Ca+Ca interactions were generated in each impact parameter interval. Figure 4.4 presents the dependence of the detected transverse energy on the impact parameter for the barrel, endcap and very forward parts of the CMS calorimeters. The detected transverse energy strongly decreases with increasing impact parameter, thus allowing the measurement of the centrality of the collisions and the selection of central events using the E_T trigger. For central collisions, the transverse energy measured in the endcap part appears to be slightly greater (by about 10%) than in the barrel and very forward calorimeters. However, for the most peripheral events, the E_T detected in the barrel part is about 1.6 times smaller than in the endcap calorimeters. Note that the same type of

Table 4.3. General parameters of Pb+Pb and Ca+Ca collisions used for the study of the transverse energy measurement

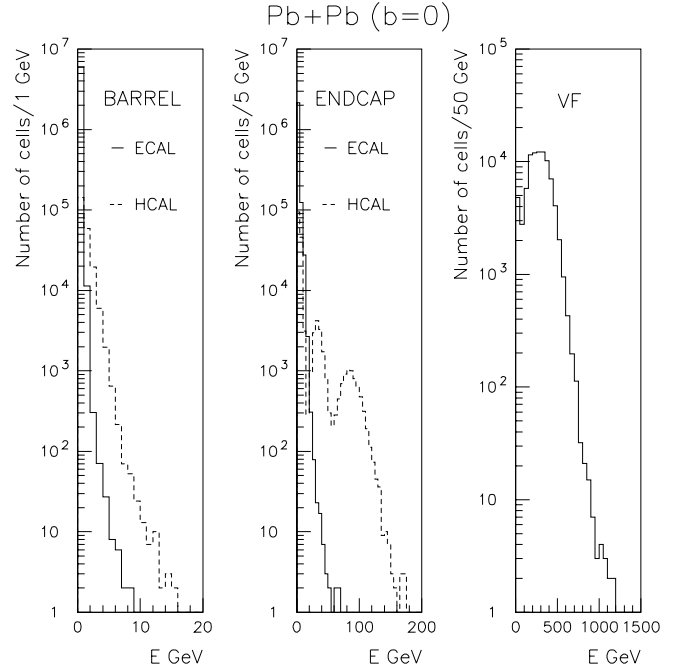|	Pb+Pb	Ca+Ca
$(dN_{ch}/dy)_{0<y<1}$	1620	260
$(dN_\gamma/dy)_{0<y<1}$	1550	250
p_T^{ch} (GeV/c)	0.42	0.44
p_T^γ (GeV/c)	0.21	0.22

Fig. 4.3. Distribution of detected energy in cells of the barrel, endcap, and very forward calorimeters

dependence of the measured E_T on the impact parameter was obtained with the HOLIAF event generator [106] and SHAKER parameterization for the transverse momentum distributions of the secondary particles [166].

Figure 4.5a shows the relative difference between the generated and the detected transverse energy, $R(b) = (E_T^G - E_T^D) / E_T^G$, for different values of the impact parameter b in Pb+Pb and Ca+Ca collisions. For Pb+Pb collisions, $R(b)$ is approximately constant, about 0.14 for impact parameters $b \leq 12$ fm, and increases up to 0.18 for peripheral interactions. For Ca+Ca collisions this ratio is 0.13 for central interaction events and increases up to 0.24 for $b = 12$ fm. In both nucleus-nucleus collisions the major fraction of the generated transverse energy (typically more than 80%) will be detected by the CMS calorimeters.

Naturally, the value of $R(b)$ varies from one event to another. The approximation of this distribution for each impact parameter interval with a gaussian function gives the values of the "resolution" σ presented in Fig. 4.5b. This resolution increases with increasing impact parame-
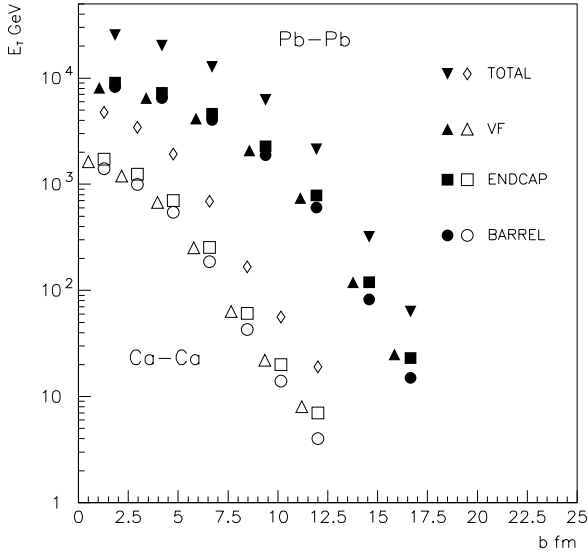
Fig. 4.4. Dependence of the measured transverse energy on the impact parameter of the collisions
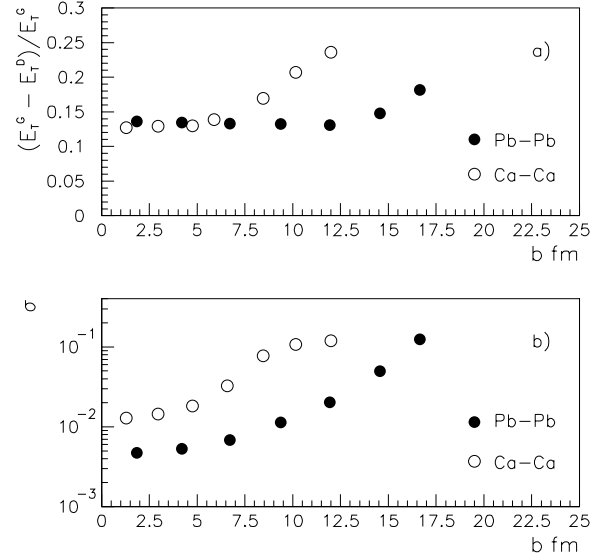

Fig. 4.5. Relative difference between generated and detected transverse energy (**a**) and the width of a gaussian approximation (**b**)

ter, and is significantly smaller for Pb+Pb collisions compared to the Ca+Ca case.

The expected dependence of the measured transverse energy on the impact parameter of Pb+Pb collisions is presented in Fig. 4.6 for the electromagnetic and hadron calorimeters. In the barrel part, the detected transverse energy in the electromagnetic calorimeter is 3.5 - 4.0 times larger compared to the hadron calorimeter. The barrel and endcap electromagnetic calorimeters detect a major fraction of the transverse energy generated in this rapidity range. This is due to the fact that most of the secondary particles produced at central rapidities in heavy ion collisions are soft and lose a significant portion of their energy inside the electromagnetic calorimeter before hitting the hadron calorimeter. The difference between the detected E_T within the barrel and the endcap parts of the hadron calorimeter is related to the momentum difference between the charged particles emitted in the corresponding rapidity ranges.

4.3.3 Summary

The CMS detector is well adapted for the transverse energy measurement in heavy ion collisions. This will allow the study of the dependence of many processes, e.g., suppression of the J/ψ and Υ and energy loss of light and heavy partons, on impact parameter.
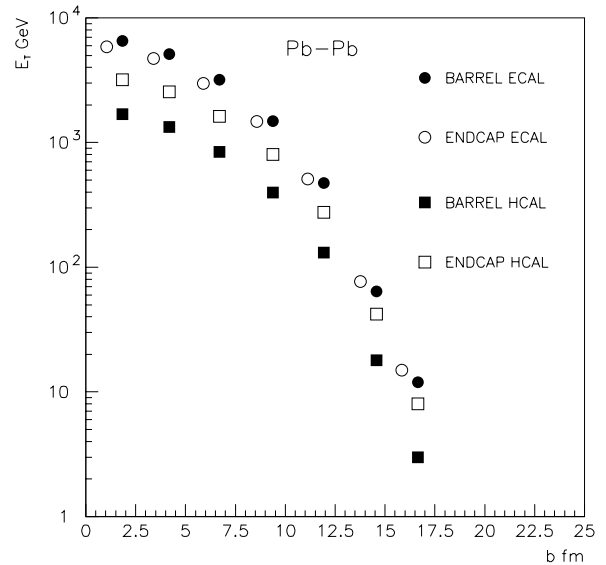

Fig. 4.6. Dependence of detected transverse energy on impact parameter in barrel and endcap sections of the calorimeters

5 Quarkonia production and dimuon reconstruction

The dissociation of heavy vector mesons such as J/ψ, ψ' and Υs is one of the most promising signatures of QGP formation [40]. Such suppression has been observed at SPS energies by the NA50 Collaboration [10], and its interpretation is a much debated question. At $\sqrt{s}_{NN} \approx 17$ GeV, the J/ψ, and to a lesser extent the ψ', can be studied. At the LHC the Υ family is accessible. One of the main goals of the CMS heavy ion program is to measure the production of quarkonia, via their decay to dimuons, scanning from pp to Pb+Pb collisions. In the pp case, although the energy density can locally reach high values, the interaction volume is too small to create a plasma. In Pb+Pb interactions, which involve much greater number of nucleons, the colour screening effect should lead to the suppression of heavy quark bound state production in the most central collisions where all the conditions for QGP formation should be achieved.

Muons are detected in CMS over a wide range of pseudorapidity, $|\eta| < 2.4$. However, the study is often limited to the barrel part of the detector ($|\eta| < 1.3$). In this chapter, the Υ and J/ψ production rates and their geometrical acceptance in the CMS detector are studied. Pattern recognition and track reconstruction of Υ decays are then presented. This study requires a specific track reconstruction algorithm to cope with the huge number of charged particles detected in the inner tracker. The reconstruction efficiency and the mass resolution of signal and background muon pairs are calculated. The different background sources are studied, together with their contributions to the expected dimuon mass spectrum.

In addition, the possibility of detecting muon pairs from Z^0 decays is investigated. As this signal is unaffected by the evolution of the matter created in the interaction, it could be used as a reference process for other signals.

5.1 Quarkonium production rates and acceptances

5.1.1 Cross sections

In $p\bar{p}$ reactions at $\sqrt{s} = 1.8$ TeV the production cross section $B_r \, \mathrm{d}\sigma/\mathrm{d}y \, (p\bar{p} \rightarrow \Upsilon + \Upsilon' + \Upsilon'')$ has been measured to be approximately 1 nb in the central rapidity region [62] where B_r is the branching ratio for $\mu^+\mu^-$ decay. Extrapolating linearly to $\sqrt{s} = 5.5$ TeV gives an expected cross section of 3 nb for the combined Υ S-states. The relative fractions taken in our simulations are $\Upsilon{:}\Upsilon'{:}\Upsilon'' = 1 : 0.3 : 0.1$.

The J/ψ integrated cross section was measured by the CDF Collaboration [167] for $p_T^{J/\psi} \geq 4$ GeV/c and $|\eta| < 0.6$ is 29.1 nb. Using PYTHIA 5.7 [79] to correct for the p_T cut and extrapolating to LHC energies leads to an expected cross section of ≈ 400 nb.

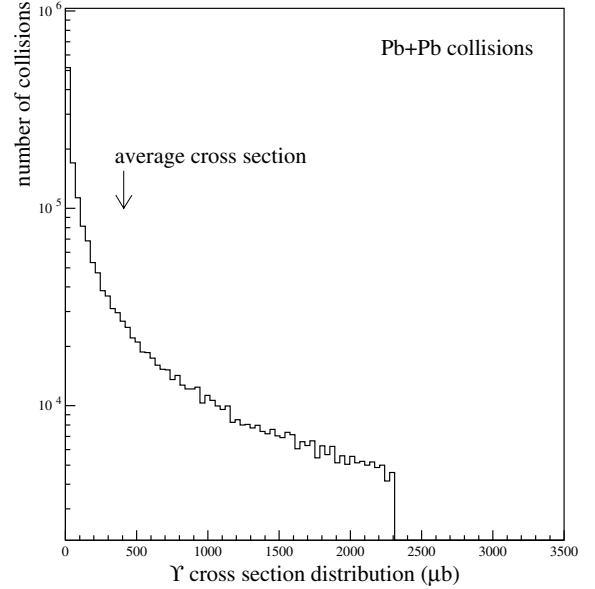In AA collisions the production cross sections of the charmonium and bottomonium are deduced from $p\bar{p}$ col-

Fig. 5.1. Number of collisions versus Υ production cross section

lisions according to the following A-scaling law

$$B_r \left[\frac{\mathrm{d}\sigma(AA)}{\mathrm{d}y} \right]_{y=0} = A^{2\alpha} B_r \left[\frac{\mathrm{d}\sigma(p\bar{p})}{\mathrm{d}y} \right]_{y=0}$$

with $\alpha = 0.9$ for the charmonium states and $\alpha = 0.95$ for the bottomonium states [168,169]. In our study no p_T dependence of α was considered. The cross sections are increased by 20% from Pb+Pb to Ca+Ca to take into account the difference in $\sqrt{s}$. Table 5.1 summarizes the total cross sections for the production of quarkonia.

These cross sections correspond to minimum bias AA collisions. We have introduced a simple linear dependence on the number of nucleon-nucleon collisions, N_{col}. Figure 5.1 shows the case of Pb+Pb collisions. From very peripheral to the most central collisions with $N_{\mathrm{col}} > 1500$, the Υ cross section ranges from 2 μb to a maximum of 2300 μb. The parameters are tuned to give a mean value of 410 μb as given by A-scaling. This cross section parameterization enables us to study separately central collisions for which the Υ production cross section is ≈ 2000 μb for Pb+Pb collisions, and 90 μb for Ca+Ca collisions.

5.1.2 Acceptances

The resonances are generated in p_T and y space according to functions fitting the distributions obtained either from experiment for the p_T of Υs, extracted from CDF, or from PYTHIA. The same functions have been used for J/ψ and ψ' on one hand, and Υ, Υ' and Υ'' on the other. The p_T functions are:

$$\frac{\mathrm{d}N_\Upsilon}{\mathrm{d}p_T} = \frac{p_T}{\left[1 + \left(\frac{p_T}{7.5}\right)^2\right]^{3.5}} \qquad \text{with } \langle p_T \rangle = 4.9 \text{ GeV}/c$$

Table 5.1. Production cross sections $B_r\sigma(AA \rightarrow q\bar{q})$ of quarkonium states in AA collisions

	Pb+Pb	Ca+Ca
J/ψ(mb)	58.0	3.6
ψ' (mb)	1.4	0.09
Υ (μb)	410	21
Υ' (μb)	120	6.4
Υ'' (μb)	41	2.1

$$\frac{\mathrm{d}N_{J/\psi}}{\mathrm{d}p_T} = p_T \exp\left[-\left(\frac{p_T}{1.75}\right)^{1.33}\right] \text{ with } \langle p_T\rangle = 2.2 \text{ GeV}/c$$

The primary vertex is assumed to be the geometrical centre of the detector. Each muon from a resonance decay is then tracked in a 4 T magnetic field by GEANT [170] using the CMSIM package [5]. The dimuon is accepted when both decay muons pass through at least one muon chamber. Additionally, we have introduced a cut of $p_T^\mu > 3.5$ GeV/c for each muon, just above the minimum p_T^μ needed to reach the first muon chambers in the barrel. The muons from J/ψ decays have an average p_T of 1.7 GeV/c so that only 0.8% of the J/ψ are above the p_T threshold. On the other hand, the Υ have an average p_T of 4.6 GeV/c allowing 40% to survive the p_T threshold. The p_T, y and η distributions of the Υ(1S) are drawn in Fig. 5.2 for three cases: i) at generation, ii) when both muons are accepted without p_T cut, iii) after the $p_T^\mu > 3.5$ GeV/c cut on each muon

The same acceptance plots are shown for the J/ψ in Fig. 5.3. In this case, the accepted distributions have been magnified to make them visible.

Table 5.2 gives the integrated acceptances for Υ and J/ψ in the barrel and endcaps, and for the barrel alone, $|\eta| < 1.3$. These acceptances are geometrical and take into account neither the dimuon reconstruction efficiencies nor the trigger efficiency. In the full rapidity range of the CMS detector the global acceptance amounts to 27% and is reduced to 16% once the p_T^μ cut is applied. Limiting the detector to the barrel, the acceptance finally drops to 9.5%. The p_T dependence of the accepted Υ in Fig. 5.4 does not indicate a specific difference between what is found in the full detector and in the barrel. An interesting point is that the p_T distribution starts from zero and is only statistic limited in the high p_T region. This allows a comparison between high and low p_T events.

The situation is different for the J/ψ. As indicated in Table 5.2, the integrated J/ψ acceptance is about ten times lower than for the Υ. The acceptance is reduced by an additional factor of 10 when it is limited to the barrel. This drop is related to the natural p_T cut on the individual muons due to the material located in front of the muon chambers. Increasing the cut to $p_T = 3.5$ GeV/c diminishes the acceptance very strongly. Only muons from high p_T J/ψ can reach the muon chambers, as clearly shown in Fig. 5.3.

A full p_T analysis is possible only in the forward and backward directions. Nevertheless, the cross section for J/ψ production is 150 times greater than for the Υ. In one month, 1.3×10^6 seconds, about 10000 high p_T J/ψ will be detected in the barrel at a Pb beam luminosity of 10^{27} cm^{-2}s^{-1}. The study described here is limited to the barrel part of CMS since the dimuon reconstruction efficiencies in the forward and backward directions have not yet been estimated.

5.2 Muon pair reconstruction

Pattern recognition and track reconstruction determine, to a large extent, the feasibility of heavy ion physics studies with CMS. In this section we describe an algorithm for the reconstruction of tracks from the decay $\Upsilon \rightarrow \mu^+\mu^-$ and its performance over a broad range of charged particles multiplicities up to the most difficult situation, *i.e.* of central Pb+Pb collisions at $\sqrt{s} = 5.5$ TeV. Central collisions are difficult because of the large number of background tracks leading to very high occupancies in most of the tracker detectors.

The multiplicity of charged particles per unit rapidity at $y = 0$ in central Pb+Pb collision ranges from 3000 to 8000, depending on the model [9,162]. In the latter case, the occupancy level in the inner tracker reaches 10% to 30% for the last four MSGC layers (located beyond 80 cm from the beam) and may exceed 50% for the innermost MSGC and Si-strip detectors. Occupancies of 2-4% [171] are expected for the pixel layers thanks to their very high granularity.

Therefore a useful algorithm must be able to reconstruct muon tracks with about half of the number of measured coordinates available in pp collisions. In fact, only the four outermost MSGC layers and the pixel detectors can be used in this extreme situation. In peripheral Pb+Pb collisions or in collisions of lighter ions, the use of inner MSGC layers may be possible due to lower multiplicities. On the other hand, not all tracks need to be reconstructed but only those which reach the μ-stations. This limits the track momenta to $p > 3.5$ GeV/c. For the barrel tracker this translates to a transverse momentum limit $p_T > 3.5$ GeV/c, close to the mean p_T for muons from Υ decay. Muons with $p > 3.5$ GeV/c lose almost 2 GeV in the calorimeters and the magnetic coil (with an uncertainty of 300-500 MeV/c). This is approximately half of the total momentum in the pseudorapidity region covered by the barrel tracker. Therefore the matching of tracks in the muon chambers and in the tracker detectors is very difficult since a rather large number of ghost tracks may be associated with each track segment in a muon chamber.

In the following we consider only muon tracks in muon chambers which originate from Υ, π/K and b decays. The goal of this study is to find criteria yielding the optimal ratio between efficiency and purity of reconstructed Υ decays into dimuons for various occupancy levels and to reject at the same time most of the dimuons from uncorrelated backgrounds. The algorithm presented here is split into
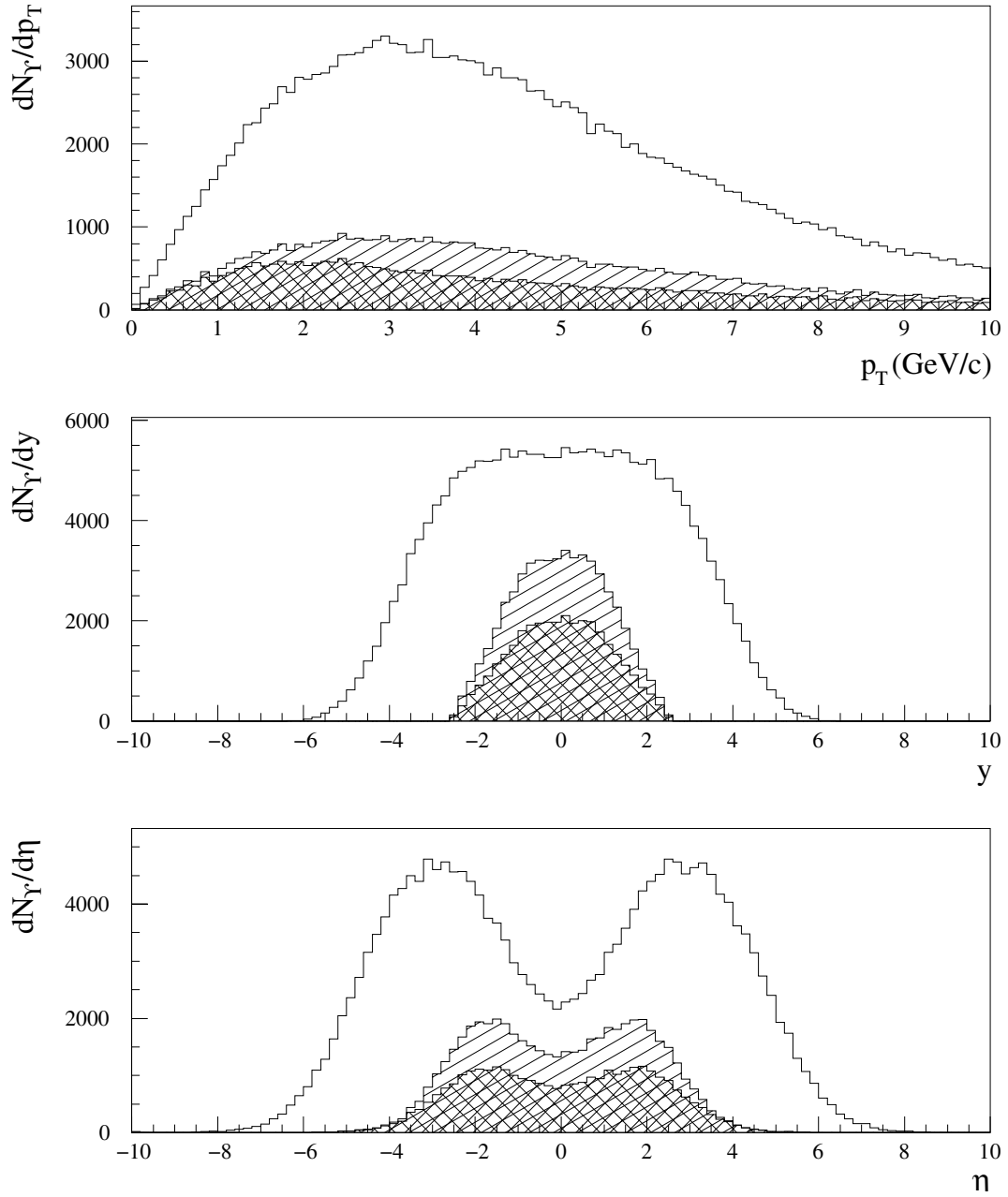
Fig. 5.2. Υ (1S): distributions of p_T (*top*), y (*middle*) and η (*bottom*). The solid lines correspond to the generated events, the hatched areas stand for accepted ones and the cross hatched areas correspond to $p_T^\mu > 3.5$ GeV/c for each muon

Table 5.2. Integrated acceptances and p_T cut effect for J/ψ and Υ resonances

	J/ψ		Υ	
	barrel	barrel+endcaps	barrel	barrel+endcaps
accepted (%)	0.2	2.8	12.7	26.7
$p_T^\mu > 3.5$ GeV/c(%)	0.01	0.03	9.5	16.3
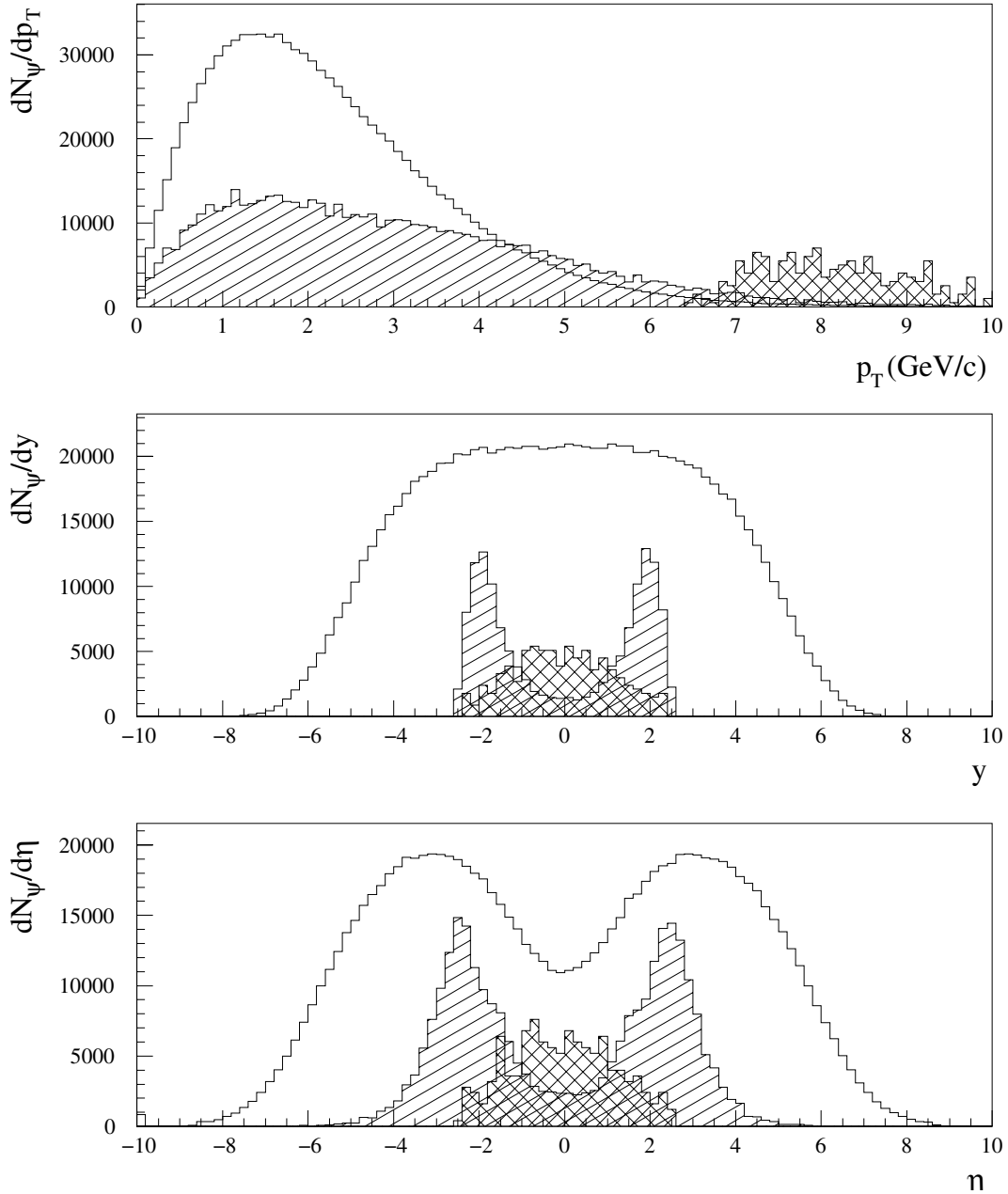
Fig. 5.3. J/ψ: same distributions as in Fig. 5.2. Due to the very low acceptances, the accepted distributions (*hatched* and *cross hatched areas*) have been magnified to make them visible

four steps: vertex finding, preselection, fitting procedure and χ^2 selection.

In the fall of 1999, the MSGC technology was given up in favour of silicon strip counters. Therefore, we complete our study with a comparison of both set-ups.

5.2.1 Simulations

The complete geometry of the CMS detector, together with the 4T magnetic field map, is inserted in the CM-SIM simulation package [5]. A detailed description of the different parts of the tracker detector can be found in the Technical Design Report [4]. A short description of the

tracker was presented in Chapter 1. In this section only the barrel region with $|\eta| < 1.3$ is studied. A schematic view of this region is shown in Fig. 5.5. Starting from the beam axis, the tracker is composed of three different type of counters: pixel, silicon strips, and micro strip gas chambers (MSGC). Charged particles with $p_T > 0.8$ GeV/c can escape the tracker. Between the tracker and the muon chambers (located 4 m from the beam), the tracks have to cross the calorimeter system and the magnet coil (hatched region in Fig. 5.5). In order to hit the first muon station, the tracks must be produced with $p_T \geq 3.5$ GeV/c at $\eta = 0$. Two rapidity regions are distinguished in the barrel: the central barrel with $|\eta| \leq 0.8$ where the muon
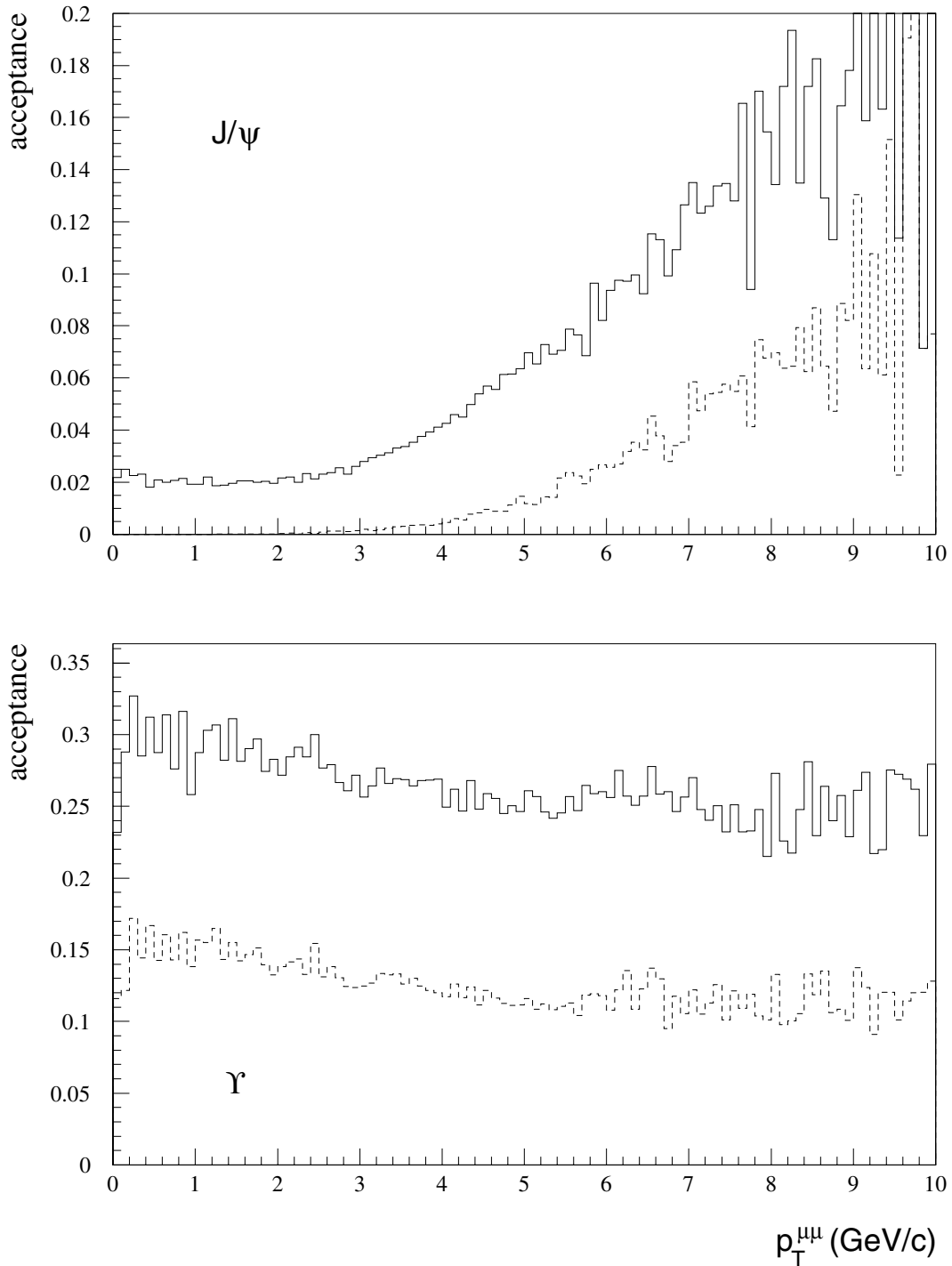
Fig. 5.4. p_T dependence of the dimuon acceptance for J/ψ (*upper*) and Υ (*lower*) resonances. In each case the full CMS detector (*solid line*) and the barrel only (*dashed line*) have been considered

track crosses only barrel layers and the forward barrel with $0.8 \leq |\eta| \leq 1.3$ where the muon track intersects some forward MSGC discs.

In the central barrel, the 4 outermost MSGC layers (non-stereo) and the 2 pixel planes were used for reconstruction purposes as well as up to 5 forward MSGC discs in the forward tracker. For tracks intersecting forward MSGC discs the number of hits varies from 5 to 8. The total number of hits in the central barrel amounts therefore to 6 per track and rises up to 10 in the forward barrel region.

The alternative tracker design, where all MSGC layers are replaced by strip silicon detectors, comprises five detector layers with a strip length of 16 cm and a pitch size of 147 μm. In this new design, we also use only the 4 outermost silicon layers.

R (m)
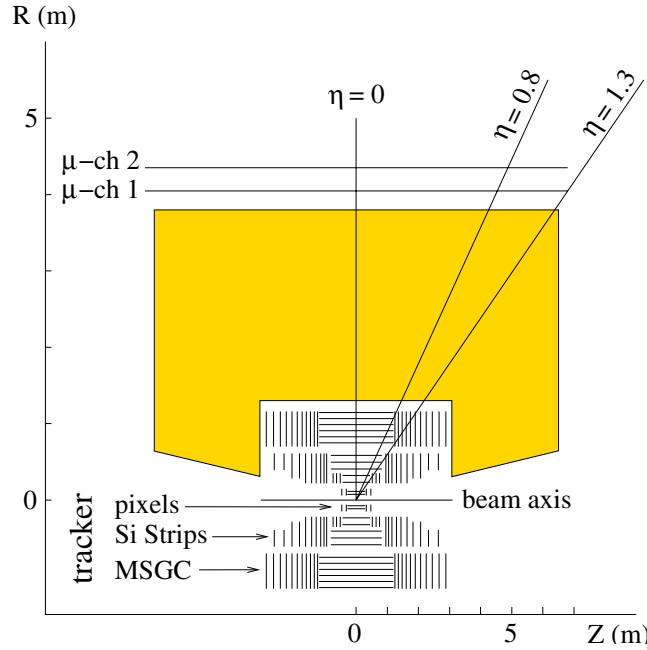
Fig. 5.5. Detector layers used for reconstruction

5.2.2 Tracks from hadrons

As explained in Section 4.2, for each central Pb+Pb collision the 8000 charged secondary hadrons are taken to be pions and kaons [172] with a ratio $K/\pi = 0.2$, and neutral particles (only π^0) are added so that

$$\left(\frac{\mathrm{d}N}{\mathrm{d}y}\right)^{b=0}_{y=0} = 8000(\pi^{\pm} + K^{\pm}) + 4000(\pi^0). \qquad (5.1)$$

The shape of the secondary kaons and pions pseudorapidity distributions were given by the HIJING-model [102]. The transverse momenta are distributed according to the SHAKER parameterization. This parameterization yields the largest number of particles at high p_T of all the Monte Carlo models. With these assumptions 60,000 particles are generated in $|\eta| < 5$. Close to 1/3 of them are in the barrel region of CMS. The collision point is arbitrarily chosen at $x = 5$ μm, $y = 5$ μm and $z = 5$ cm. These values are in agreement with the beam parameters [161].

The particles were tracked through the detector using GEANT 3.21 [170] including all secondary processes. The default GEANT cuts for particle energy were decreased to 100 keV for gammas and electrons and to 1 MeV for hadrons. The GEANT energy thresholds CUTGAM, CUTELE, BCUTE, DCUTM, DCUTE and DCUTM defining the minimum energy for electrons, gammas, muons and δ-rays [170] are changed from 1 MeV to 100 keV.

5.2.3 Analysed tracks

Two samples of muon tracks are superimposed on the hadronic background event:

- The first sample of tracks consists of muons from the Υ(1S) decay. Among all the Υs generated in the (p_T, η) phase space only those leading to muons which cross at least 2 chambers in the first barrel μ-station are selected.
- The second sample comprises high p_T muon tracks coming from π/K decays. The muon pairs formed by these tracks are one of the main sources of dimuon background [172,173]. Here, too, the muon track is required to give 2 hits in the first barrel μ-station.

5.2.4 Clusterization

a) MSGC's

The method of signal generation, digitization and clusterization was presented in the Tracker Technical Design Report [4].

- Signal generation: For each track crossing the sensitive volume of an MSGC layer, the simulation package CMSIM returns the entry and exit points. This information is used to simulate primary and secondary ionization, diffusion, drift and avalanche multiplication in the gas mixture Ne(30%)-DME(70%). During extrapolation through the gas the generation of δ-rays by GEANT is suppressed to avoid double counting. The other processes are generated by GEANT. The MSGC simulation model includes generation of ionization clusters from primary and secondary electrons along the track path and the number of electrons per cluster. Each electron then drifts towards an anode. The effect of the solenoidal magnetic field is taken into account by a deviation of the drift direction with respect to the electric field. At the end of the drift region

Table 5.3. Number of clusters in the MSGC layers (barrel) for one central Pb+Pb event

Layer	#3	#4	#5	#6
Number	15000	14500	8700	7500

the avalanche starts and the resulting signal is added to the corresponding channel. All parameters of the simulation of track propagation of minimum ionizing particles are tuned according to results obtained from beam tests.

– Digitization and cluster reconstruction: The charge deposited on each anode strip is analysed by the cluster finding algorithm which retains all strips with a signal exceeding the noise (σ=1875 electrons per strip) by a factor of 1.8. Adjacent strips are then gathered into candidate clusters for which a second selection criterion requires at least one strip with a significance of $3.5\ \sigma$.

For Pb+Pb collisions a clusterization procedure differing from the *pp* procedure is applied. In ion collisions, the aim is to favour clusters from muon tracks over those from background tracks. For this purpose, an additional third threshold concerns the charge of the strip giving the largest signal. This latter threshold depends on the cluster size, *i.e.*on the number of strips per cluster. The threshold value is fixed at 19000 e^- for clusters composed of one strip or more than three strips (see Fig. 5.6a,b). Clusters with one strip are often a part of bigger clusters with one missing strip or single noisy strips surviving the two threshold algorithm selections.

Applying the thresholds to the muon tracks leads to a loss of $\approx$16% of all Υ events as 4% of all muon tracks will have at least 5 of 6 possible hits in the barrel tracker. The number of background clusters, however, decreases approximately by a factor of 2.

The requirements for a muon cluster are: a signal larger than 3400 e^- for all strips, the cluster is made only of adjacent strips, and the threshold on the largest signal in the cluster depends on the total number of strips in the cluster.

The above procedure is applied for the MSGC counters. In the case of the new tracker design, the same standard digitization and clusterization procedures are used as in *pp* collisions.

The occupancies obtained after noise suppression are given in Fig. 5.7 for the MSGC design (with two different pitch sizes) and for the new design where silicon strips replace the MSGCs.

The numbers of clusters obtained in each MSGC layer are given in Table 5.3. For our track finding algorithm the number of clusters per elementary detector (512 strips for an MSGC module) is more important than the strip occupancy. The number of clusters per detector for both tracker designs is shown in Fig. 5.8.

The distribution of distances between neighbouring clusters inside the same ring (see Chapter 1 for definitions) is presented in Figs. 5.9a,b for MSGC layers 6 and

3 respectively. The mean value varies from 0.6 to 0.4 cm depending on cluster density.

b) Pixels

For the pixel detector, the digitization and clusterization procedures are the same as in the *pp* case, described in detail in [4].

– Signal Simulation.
  The entrance and exit points in the pixel sensitive volume together with the energy deposition are recorded during GEANT track propagation. The track path inside the volume is divided into 10 μm segments and the corresponding energy loss is parameterized with a distribution taking into account Landau fluctuations in thin material layers. The charge of each track segment drifts to the detector surface and diffusion is taken into account with a Gaussian distribution in the plane perpendicular to the electric field. The Lorentz angle in the 4T solenoidal magnetic field is included. The two dimensional charge distribution is mapped onto the pixel geometry and the charge detected by each pixel is determined.

– Digitization and cluster reconstruction.
  To digitize the signal collected in a pixel, the charge is multiplied by a gain factor and the ADC digitization is simulated by converting the signal into an integer, including saturation. All pixels with signals below 1080 electrons (4σ in units of noise) are rejected. Pixels above threshold are analysed with the cluster finding algorithm. For each cluster its width in two dimensions and its charge are calculated. Clusters with charge below a threshold fixed at 2160 electrons ($8\ \sigma$ in units of noise) are rejected.

In the case of a central Pb+Pb collision, this procedure leads to 36000 and 33000 clusters in the first and second layers respectively .

5.2.5 Track finding and roads

The goal of the track finding algorithm is to select pairs of muon tracks. One needs, first, to reconstruct tracks from cluster positions. The reconstructed tracks are then combined in pairs, each pair being submitted to a vertex condition. The "best quality dimuon" is finally accepted.

The tracking algorithm presented makes use of cylindrical coordinates (r, ϕ, z) with the centre of the detector at (0,0,0).

a) Vertex determination

The knowledge of the z-coordinate of the collision point is of key importance for an optimal reconstruction efficiency and purity as has been shown in earlier studies [174]. This is due to a wide distribution ($\pm$10 cm) of ghost tracks
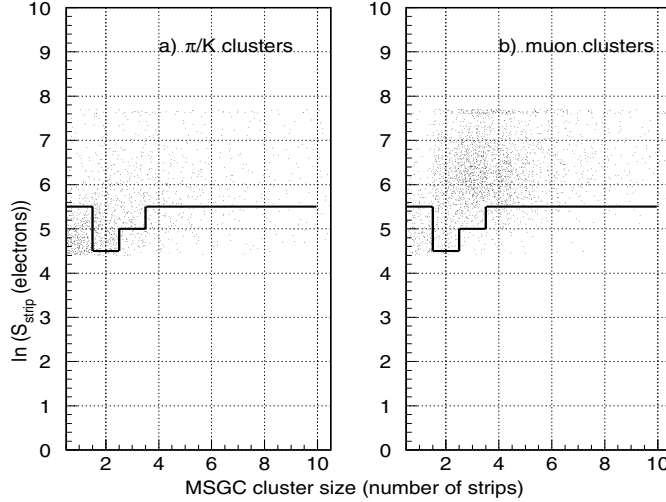
Fig. 5.6. Correlation between cluster size and the number of electrons in the strip with the largest signal. The *line* shows the third threshold

along the z-axis whereas muon tracks from Υ decays intersect the beam line at a distance of less than a few hundred μm from the collision point, as indicated in Fig. 5.10.

In the following, the pixel detector is used to determine the z-coordinate of the interaction point [175]. The clusters obtained in the two pixel layers are combined to form track candidates, the transverse momentum of which are calculated assuming that the primary vertex transverse coordinates are $(0,0)$. In order to increase the proportion of real tracks in the candidate sample only pairs with 0.5 GeV/c< p_T< 5 GeV/c are selected. For each pair the z - coordinate is estimated by extrapolating a straight line in the (r,z) plane to the beam axis. The distributions of z - coordinate are presented in Fig. 5.11 for two different particle multiplicities. The maximum due to real tracks can easily be distinguished from the uniform background originating from fake pairs. We use the vertex z-coordinate found from the method described above. A fit of the vertex distributions using the following Gaussian:

$$F = \exp((z - z_0)/(2\ \sigma^2)) + \text{const.} \quad (5.2)$$

gives $z_0 = 5$ cm and $\sigma_{z_0} = 140\ \mu$m.

b) Track parameterization

Due to the high occupancy only non-stereo MSGC detectors have been used in this study. In the barrel part of the tracker a cluster's r and ϕ coordinates are well determined whereas the $z-$ coordinate is rather imprecise due to the length of the strips. In the forward discs the measured positions ϕ and z are accurate and r is not very well determined. Therefore, we consider two different types of

trajectories in the following: the ones intersecting only the barrel tracker and those going from the barrel cylinders into forward discs. The track parameterization involves two tracker geometry descriptions: an averaged geometry where detector layers are cylinders in the central barrel and discs in the forward barrel, and a detailed geometry with detailed description of all detector elements.

c) Preselection step

i) Barrel tracker

A muon track passing through barrel cylinders on two different layers (averaged geometry) is presented schematically in Fig. 5.12. The difference, $\delta\phi(i,j)$, between the azimuthal angles of the two clusters (i,j) is calculated from

$$\delta\phi(i,j) = \sin^{-1}(r_i/2R) - \sin^{-1}(r_j/2R) \sim K\frac{\delta r_{ij}}{P_T} \quad (5.3)$$

where R is the radius of the muon trajectory, r_i the radius of a detector layer, and $\delta r_{ij} = |r_i - r_j|$ is the difference of the radii. For high energy tracks, one has $\delta r_{ij} << R$ and therefore a simple p_T dependence. For the averaged geometry, the expression becomes even simpler since $\delta r_{ij} =$ constant for all pairs of clusters from the two layers.

This parameterization suggests a simple selection criteria in the $\delta\phi(i,j)$-p_T plane obtained by simulating prompt muon tracks and the geometry of the CMS detector. An example of roads created for the barrel tracker is shown in Fig. 5.13. For the 8 points (2 pixels + 4 MSGCs + 2 μ-chambers) defining a track we get 28 $\delta\phi$-p_T roads. Let
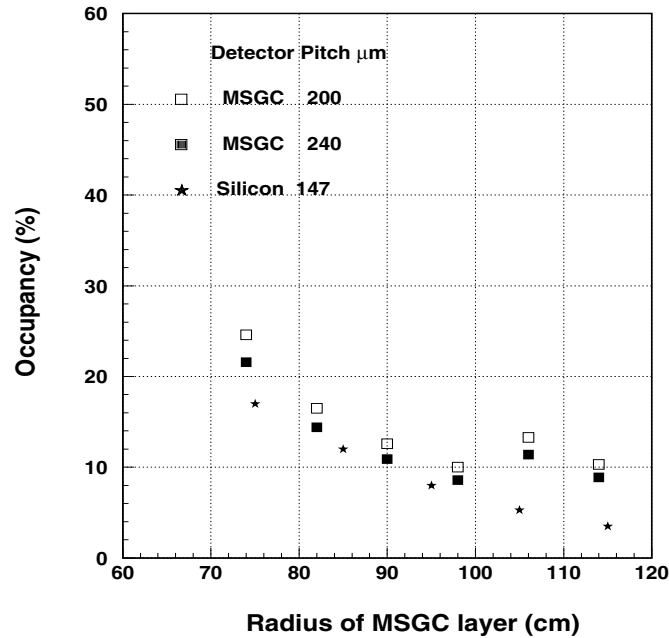
Fig. 5.7. Occupancy in outermost detectors for $\mathrm{d}N^{\pm}/\mathrm{d}y = 8000$
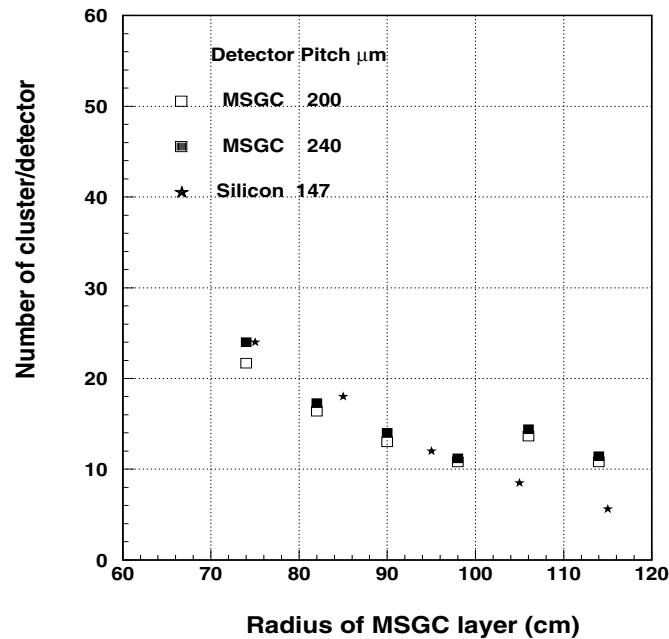

Fig. 5.8. Number of clusters per detector for $\mathrm{d}N^{\pm}/\mathrm{d}y = 8000$ (detector: 512 strips for MSGC design)

us remark that we compute these roads for muon chambers as well, although 5.3 does not strictly hold for these detectors since the magnetic field is not constant outside the coil.

Because the muons have to traverse all the material inside the coil, these roads (look-up tables) must take into account multiple scattering and energy loss. Practically, this means that propagation of errors of a track trajec-

tory from layer to layer are tabulated before any track finding procedure (this would be different for a Kalman filter, where error propagation is calculated either analytically or using GEANE [176] during track extrapolation).

In the detailed geometry MSGCs are boxes whose centres are positioned on a cylindrical surface (see Fig. 5.14). In this case δr depends on the cluster position inside these boxes such that roads can be used only to predict the
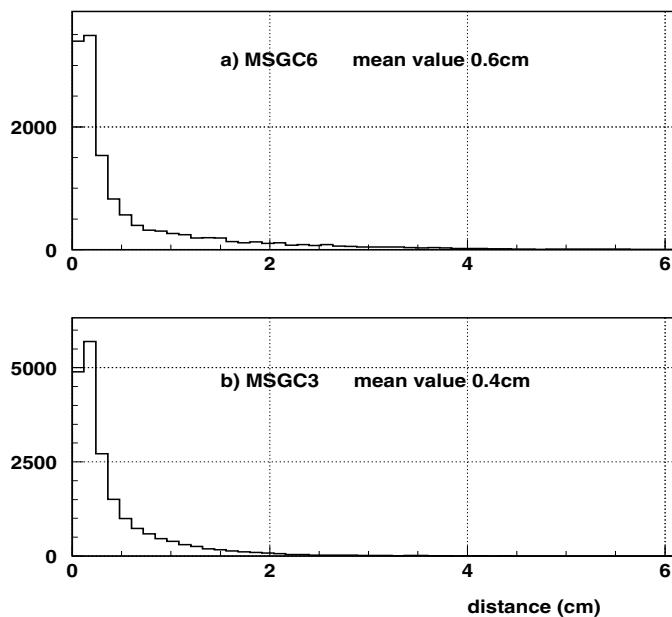
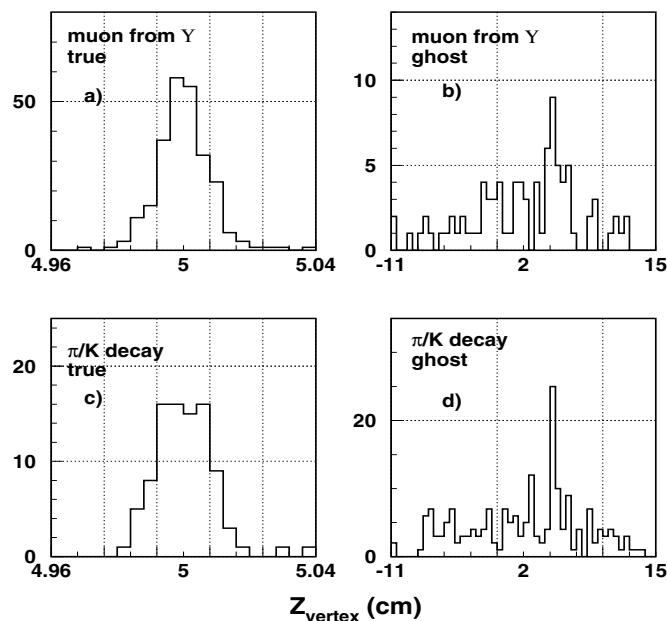**Fig. 5.9.** Distribution of cluster distance in MSGC layers 6 and 3

Fig. 5.10. Distribution of expected (z) coordinates for true and ghost muons from Υ and π/K decays, generated at $z = 5$ cm

chamber in which a cluster is located. It is also necessary to take into account that the barrel wheels (9 or 18 depending on the tracker layer) have different mean radii. To determine the wheel number within ± 1 traversed by a track, a linear fit in the (r, z) plane is performed.

The track finding algorithm starts from the muon chambers as they are the less populated planes. Particle hits are smeared according to gaussian distributions with

$\sigma = 200$ μm in the x, y and z coordinates. The ϕ coordinates are calculated assuming that the collision occurred at (0,0,0). In our GEANT simulation the collision point is at (5 μm, 5 μm, 5 cm). Using the road defined for both planes (Fig. 5.13a) the quantity $\delta\phi_{\mathrm{meas}} = \phi_{\mathrm{MC2}} - \phi_{\mathrm{MC1}}$ corresponds to an interval p_{T1} whose centre gives the first estimate for the p_{T} of the track.
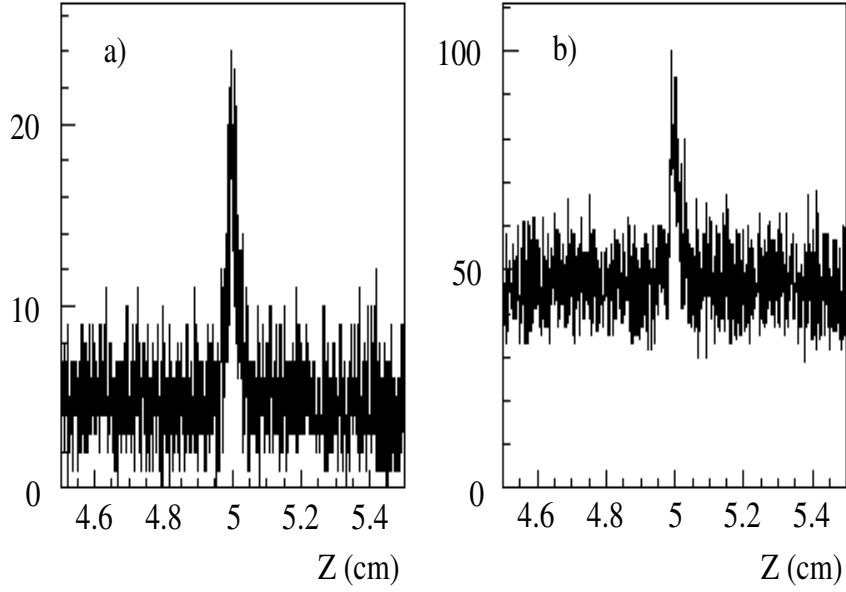
Fig. 5.11. Distribution of the z-position of the primary vertex for **a** $dN^{\pm}/dy = 2500$, and **b** $dN^{\pm}/dy = 8000$
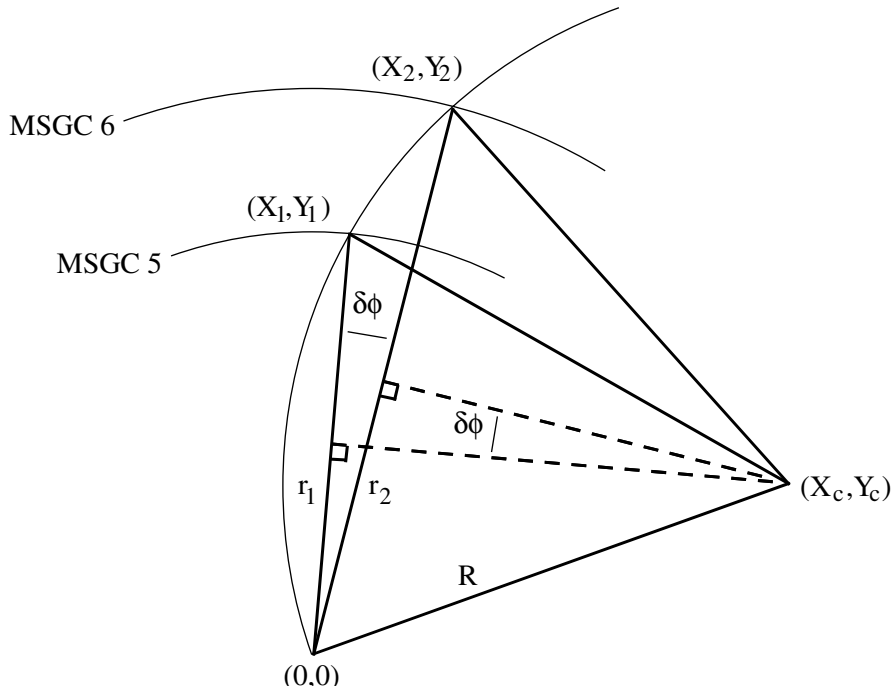

Fig. 5.12. Muon trajectory parametrisation in tracker barrel for averaged geometry
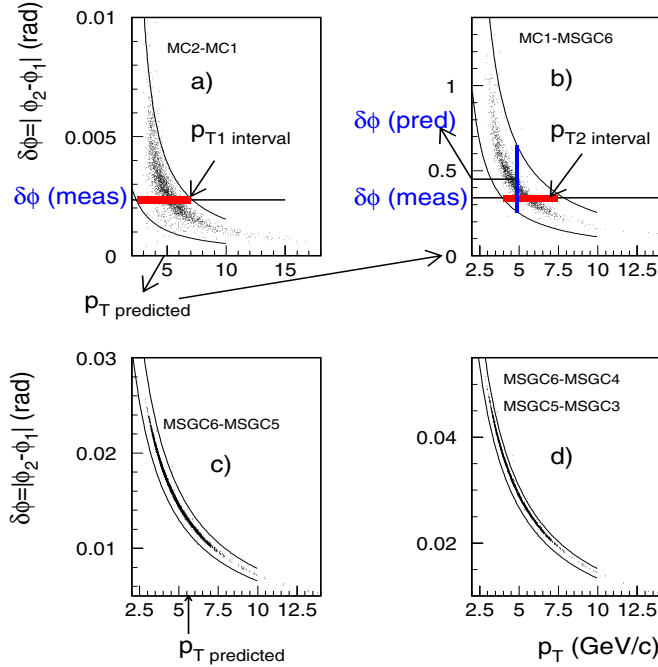
Fig. 5.13. Correlation in azimuth between clusters from two layers and the p_T of a muon track from Υ decay. The lines are analytical curves defining the roads

Using the road between MC1 and the outermost MSGC layer #6 (Fig. 5.13b), we determine the expected interval $\delta\phi_{\mathrm{predicted}} = (\phi_{\mathrm{MC1}} - \phi_{\mathrm{MSGC\#6}})$ corresponding to this predicted p_T. The centre of this $\delta\phi$ interval gives the predicted ϕ coordinate on the MSGC #6. The distribution of the difference between the predicted and measured $\phi_{MSGC\#6}$ is shown in Fig. 5.15a. with a σ of ± 0.1 radian. From $\delta r_{\mathrm{MC1,MSGC\#6}} = 3$ m and $\delta\phi = 0.5$ rad a predicted hit in MSGC#6 has an uncertainty of $\pm$ 0.5 m in the transverse plane. This reflects multiple scattering in the calorimeters and in the coil. This area is the minimal zone for a search for hits. We used an iterative procedure to find hits in the transverse plane. A given layer is divided into cells of $\delta\phi=0.5$ rad and for a predicted ϕ coordinate in cell i we look for all clusters belonging to cells $i-1$, i, $i+1$. Each cluster found implies, via a road, (Fig. 5.13b) a new interval, p_{T2}, which differs slightly from p_{T1}. A new estimate for the p_T of the track is obtained by taking the centre of the interval of overlap to be

$$P_T \ (\mathrm{predicted}) = \frac{\min(p_{T1}^{up}, p_{T2}^{up}) + \max(p_{T1}^{low}, p_{T2}^{low})}{2} \quad (5.4)$$

where $p_{T1}^{up}, p_{T2}^{up}, p_{T1}^{low}, p_{T2}^{low}$ are the upper and lower boundaries of the p_{T1} and p_{T2} intervals, respectively.

This new value of the predicted p_T corresponds to a new predicted ϕ coordinate in MSGC #6 closer to the found cluster. Thus some clusters can be rejected before extrapolating the track to MSGC #5. This procedure is identical for the averaged and detailed geometries as shown in Figs. 5.15a and 5.16a since the uncertainty of $\delta\phi$ due to multiple scattering is much larger than due to the deviation from an ideal cylindrical shape. The iter-

ative procedure is then repeated between MSGC#6 and MSGC#5 (Fig. 5.15b).

For the detailed geometry of all layers (except MSGC #6), the roads are used to predict the exact MSGC module in which the search for a cluster has to be done. The intersection of the trajectory with the real detector plane is then deduced from the (r, ϕ) coordinates and the p_T prediction assuming the transverse coordinates (0,0) as the origin of the track (Fig. 5.14).

Starting from MSGC#5 the ϕ window is about $\delta\phi = \pm$ 3 mrad due to the good resolution of the MS-GCs and to the absence of material between layers which gives a search area of 300 μm^2 at a distance of about 10 cm (Figs. 5.15b and 5.16b) between MSGC planes. This dimension is much smaller than the average distance (<1 cm) between clusters in any MSGC layer as shown in Fig. 5.9a,b for MSGC#6 and MSGC#3. This procedure is repeated for all successive planes including the pixel detectors. However, we also used the roads for non successive planes for control purposes, e.g. between MSGC#6 and MSGC#4 (Fig. 5.13d).

At each step the estimated value p_T^{est} gets closer to the generated p_T^{gen}. The distribution of the quantity $(\Delta p_T / p_T^{\mathrm{gen}})$, with $\Delta p_T = p_T^{\mathrm{est}} - p_T^{\mathrm{gen}}$ is shown in Fig. 5.17a–d for p_T^{gen} between 3.5 GeV/c and 15 GeV/c. The dispersion of Δp_T approaches 40 MeV/c when reaching the inner pixel layer.

The z-coordinate is predicted by roads defined by differences of polar angles, $\theta_i - \theta_j$, for MSGC#6 and MSGC#5 and by a linear fit in the $(r$-$z)$ plane for the other tracker layers (MSGC#4, MSGC#3, PIX#2, PIX#1). For the detailed geometry, the z-coordinate is
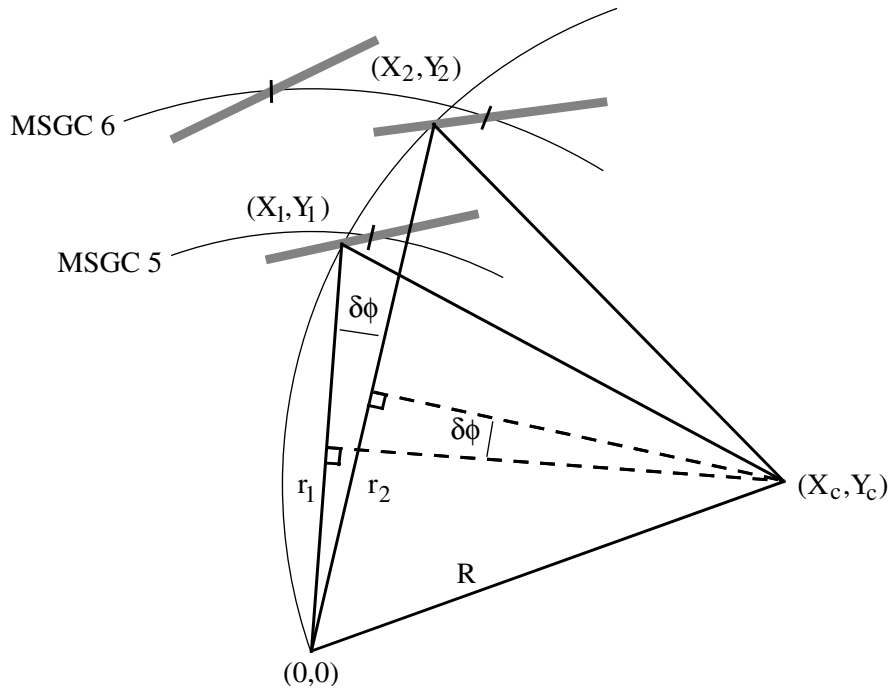
Fig. 5.14. Muon trajectory parameterization in tracker barrel for detailed geometry
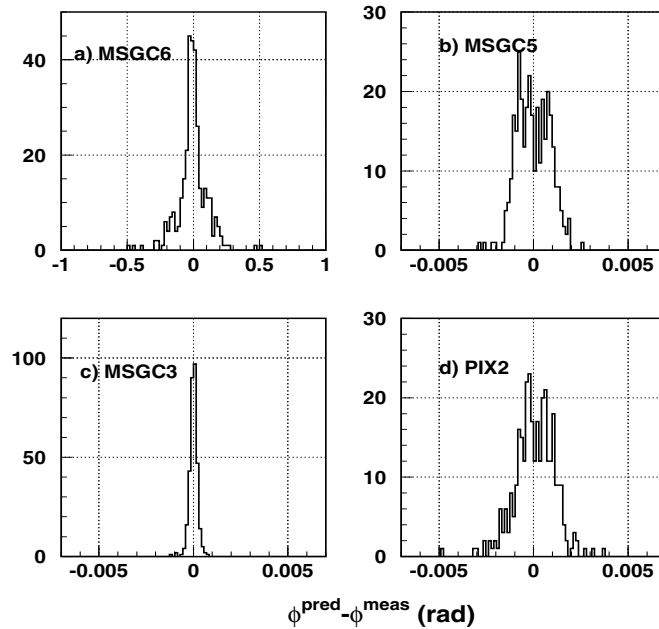

Fig. 5.15. Distribution of $\delta\phi$ from successive MSGC layers for muons from Υ decay (averaged geometry)

used to determine the barrel wheel to be considered because the wheels have slightly different mean radii.

The number of clusters found in the (ϕ-z) cells of various layers is shown in Fig. 5.18a–d as well as the size of the corresponding cells. For MSGC#6 (Fig. 5.18a) the spot size is so large that for each track in the muon chambers there are a few dozen clusters. This is the main source of fake tracks. The next layer improves the situation (see

Fig. 5.18b). Only 10% of cells have one cluster and the number of cells with 2 or more clusters is negligible. For the outermost pixel layer the mean number of candidates in the cell is 2-3.

ii) Forward tracker

In the forward tracker ϕ and z are well measured and the $\delta\phi(i, j)$ of a muon track can be parameterized (Fig. 5.19)
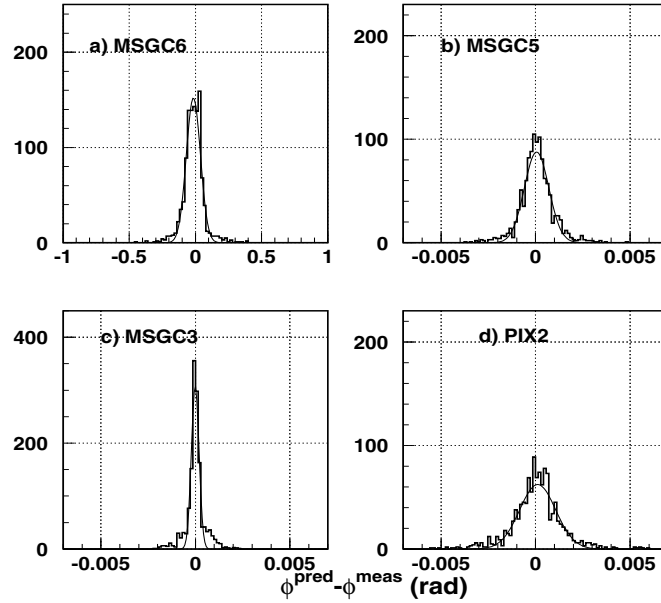
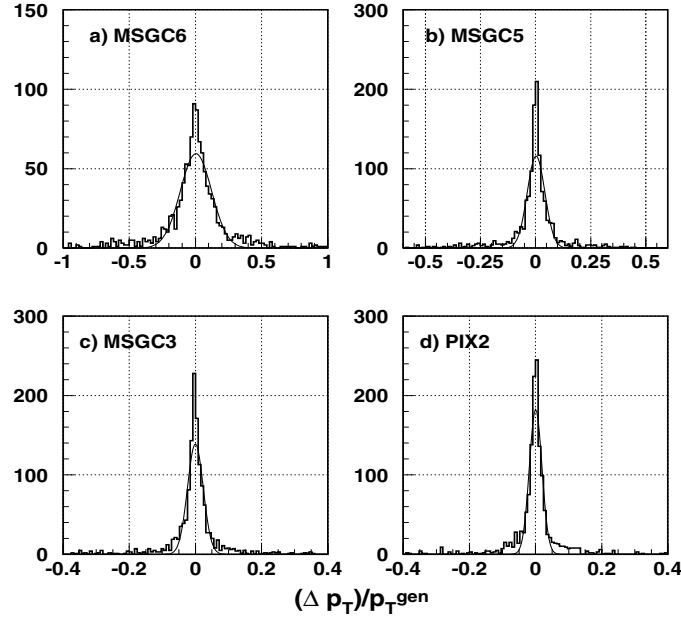**Fig. 5.16.** Distribution of $\delta\phi$ from successive MSGC layers for muons from Υ decay (detailed geometry)

Fig. 5.17. p_{T} matching from step-to-step for muons from Υ decay

as:

$$\delta\phi(i,j) = \frac{0.0015\ B\ \delta z_{i,j}}{p_{\mathrm{L}}} \qquad (5.5)$$

This parameterization is used for the detailed geometry of the forward discs as well as for the averaged geometry. The azimuthal correlation as a function of the longitudinal momentum of the muon track is shown in Fig. 5.20 where the dashed line represents (5.5). For the averaged geometry, (5.5) can be used independently of a linear (r-z) fit. For the detailed geometry one takes into account the fact that different rings on a given disc have different z-coordinates. The propagation to a mean z-coordinate determines the ring in which a cluster has to be searched for.

In the interval $0.8{<}\eta{<}1.3$, the muon tracks detected in the barrel muon chambers may intersect one or several for-
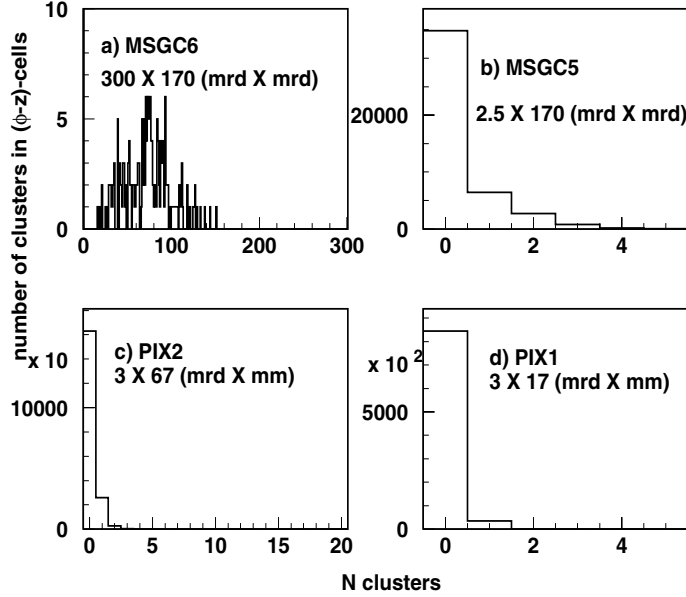
Fig. 5.18. Cluster multiplicity distribution in (θ-ϕ) window in (mrad)^2 for MSGC#6 (**a**), MSGC#5 (**b**) and ($\phi - z$) window in (mrad×mm) for PIX#2 (**c**), PIX#1 (**d**)

ward tracker discs. The road between MC1 and the radial position of MSGC #6 (Fig. 5.13b) is used to determine the ϕ window and the forward discs this muon track intersects. As the radial length of the modules (about 12 cm) is negligible with respect to its distance from the muon chambers (400 cm), the size of the (ϕ,θ)-window is the same (± 0.3 rad, ± 0.17 rad) as for the tracker barrel (see Fig. 5.21a).

For each track candidate from the muon station a first approximation to p_L (Fig. 5.22a) is derived from a p_T estimate obtained from a (MC2-MC1) road (see Fig. 5.13a) and from the θ coordinate of the track segment in the first muon station. Equation (5.5) is then used for the following steps of the track finding algorithm, since the r-coordinate is poorly determined in this region. Distributions of $\Delta p_L/p_L^{\mathrm{gen}}$ are shown for each step in Fig. 5.22b,c. Arriving on the fourth forward MSGC disc one has an rms deviation of $\Delta p_L/p_L^{\mathrm{gen}}$ of 1.3%, as for the p_T in the barrel.

Distributions of $\delta\phi = \phi^{\mathrm{gen}} - \phi^{\mathrm{meas}}$ from the forward layers are presented in Fig. 5.21a–d. One sees that the distributions are close to those obtained from the barrel detector (Fig. 5.16a–d).

Depending on η, each track can intersect different forward discs when emerging from the barrel tracker. Furthermore, it can either come from a barrel MSGC layer or from the pixel detector. When tracking from the forward discs into the barrel tracker, it is necessary to change the parameterization from p_L to p_T (Fig. 5.22d) using the p_L prediction and θ coordinate of the cluster. The width of the predicted ϕ window in the barrel MSGC layer reached first is approximately 10 mrad (Fig. 5.23a). This holds also for the pixel layer if the track does not intersect any barrel MSGC (Fig. 5.21d). The width of the distribution of $\delta\phi$

between forward and barrel layers is five times larger than that from two forward layers at the same z-coordinate. The distributions of $\delta\phi$ for the last barrel windows are shown in Fig. 5.23.

d) χ^2 selection

Once the final value of p_T is determined, the new value of ϕ is recalculated in all layers. The resulting $\delta\phi$ distributions are shown in Fig. 5.24a–d for all barrel tracker layers used. One can now define updated smaller windows. Similar distributions are obtained for the forward layers. With the dispersions σ_{layer} of these distributions, a χ^2-like quality parameter X^2 is introduced:

$$X^2 = \sum_{\mathrm{layer}} \frac{(\delta\phi_{\mathrm{layer}} \ (\mathrm{predicted}) - \delta\phi_{\mathrm{layer}} \ (\mathrm{measured}))^2}{\sigma_{\mathrm{layer}}^2}$$

(5.6)

where $\sum$ runs over all barrel and forward tracker layers.

Applying this procedure to muon tracks from π/K-decay, the resulting $\delta\phi$ distributions for all layers (Figs. 5.25a–d and 5.26a–d) are much wider than those obtained from Υ decay muons (Fig. 5.24). Each deviation of the track greater than 0.5 mm (on crossing the MSGC radii) forces it to leave the roads. The X^2 parameter constructed for π/K decay muons using the value of σ_{layer} determined for the true muon sample has large values. The main reason for such a different trend of the muons from π/K decays is decay kinematics.

The difference between the direction of the primary π track and that of the muon track at the decay point (Fig. 5.27) in the transverse plane is ± 10 mrad for π
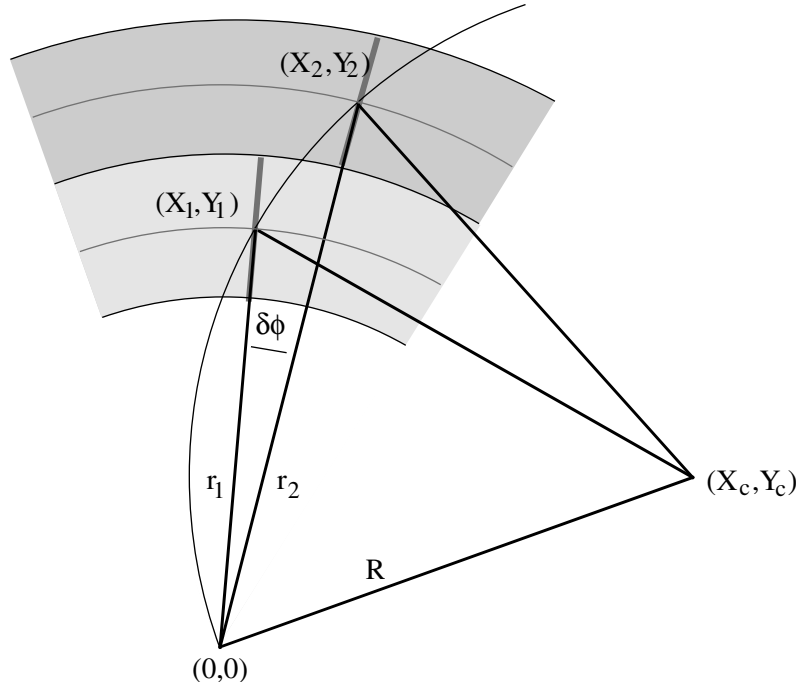
Fig. 5.19. Parameterization of a muon trajectory in the forward tracker for the averaged geometry

decays (Fig. 5.28a) and about ±150 mrad for K decays (Fig. 5.28b). Typical values of $\delta\phi$ for neighbouring detector layers are close to a few mrad depending on the layer. If a K decays between the pixel detectors and the MSGC layers, the emerging muon track has no chance to be accepted.

The preselected tracks are fitted to a circle in the transverse plane and a linear (S,z) dependence, where S is the length of the track segment in the transverse plane (helix fit [177,178]). The fit uses the 6 inner tracker hits (MSGC+pixels) and assumes the vertex point to be at (0,0,5 cm) with $\sigma_x = \sigma_y$ =20 μm, and σ_z=200 μm. An additional linear fit in the (r,z) plane is performed with the 2 μ-chamber hits. This second step reduces the sample of the track candidates by a factor 2. Momentum and dimuon mass resolution of true muon tracks (detailed geometry) are presented in Fig. 5.29a–d.

In the forward part, since only non-stereo MSGC are used, the same circle fit in the transverse plane does not yield acceptable results and is therefore replaced by a linear fit: $\phi_i - \phi_1 = A\ (z_i - z_1)$, where ϕ_i and z_i are the coordinates on the forward disc i while ϕ_1 and z_1 stand for the coordinates on the first pixel layer. Momentum components p_x and p_y are then calculated using the two pixel detectors. Figure 5.30a–d shows the momentum and dimuon mass resolution for the forward barrel.

e) dimuon charges

The next step consists of classifying the dimuons according to their charge combination, i.e. into opposite-sign ($\mu^+\mu^-$) or like-sign ($\mu^+\mu^+$ or $\mu^-\mu^-$) dimuons, and to reject any like-sign combination. Furthermore, the like-sign

sample can be used to estimate the number of opposite sign pairs due to uncorrelated decays of π and K.

f) track quality

Each track in the central barrel is characterized by four different quantities: the X^2 parameter (5.6) and 3 values of χ^2 from the above 3 fits. We define a track quality parameter R as

$$R = \frac{1}{P_1 P_2 P_3 P_4} \qquad (5.7)$$

with:

$$P_i = \int_{\chi_i^2}^{\infty} P(\chi^2)\mathrm{d}\chi^2 \qquad (5.8)$$

where P_i is the probability that the hypothesis i is wrong. This global parameter R takes into account the different numbers of degrees of freedom of our estimates. For the forward barrel there are only two values of χ^2 obtained with linear fits and X^2 obtained with (5.6).

g) vertex constraints

The last adjustable parameter is the distance between the two fitted trajectories at the interaction point. As shown in Fig. 5.10a,b for the Υ decay tracks and in Fig. 5.10c,d for the π/K decays, the z coordinate of the primary vertex for the true tracks is found within a ± 200 μm interval, centred on the generated value: $z = 5$ cm. For ghost tracks the distribution of the z coordinate is very wide (±10 cm).
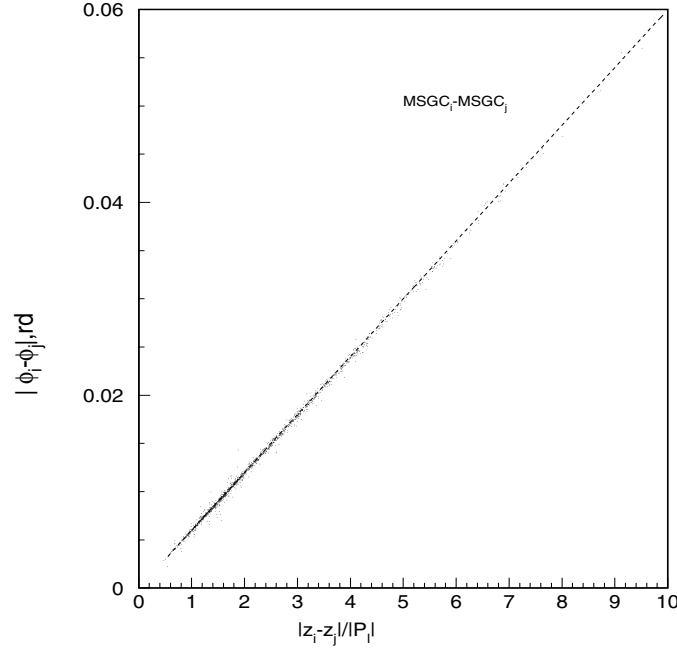
Fig. 5.20. Correlation in azimuth between two layers and of muon tracks from Υ decay. The *dashed line* shows the analytical prediction

A vertex constraint is defined by the following restrictions:

$$\left(\frac{\mathrm{d}z}{\sigma_z}\right)^2 < 6 \qquad (5.9)$$

$$\left(\frac{\mathrm{d}r}{\sigma_r}\right)^2 < 14 \qquad (5.10)$$

where the rms deviations $\sigma_z = 50~\mu$m and $\sigma_r = 20~\mu$m are determined from dimuons from Υ decay. The deviation σ_z characterizes the distance between intersection points on the beam line for both tracks and σ_r the distance in the x-y plane between the vertex points predicted by the helix fit. Practically, this vertex constraint selects those dimuon candidates for which both muons come from the same initial point within 3 or 4 σ in each direction. These vertex constraints are imposed at the level of track propagation.

h) vertex quality

Finally a quality selection enables us to conserve only one candidate which has the best quality factor K given by:

$$K = \left(\left(\frac{\mathrm{d}z}{\sigma_z}\right)^2 + \left(\frac{\mathrm{d}r}{\sigma_r}\right)^2\right)\frac{1}{(P_1 P_2 P_3 P_4)_{\mu_1}}\frac{1}{(P_1 P_2 P_3 P_4)_{\mu_2}}$$
$$(5.11)$$

i) treatment of lost clusters

As the MSGC cluster efficiency is approximately equal to 93%, only 75% of all muon tracks are found with all hits after the clusterization process. For high multiplicity events, a background cluster may be accepted by the track finding algorithm and replace a missing hit. Nevertheless, this leads generally to a bad χ^2, as background clusters are distributed uniformly inside the ϕ, z interval about the expected hit. In order to recover tracks with a missing cluster, we apply the following procedure: each track from the vertex that does not satisfy the vertex constraint is propagated again, considering any combination of 3 out of the 4 MSGC layers. Special roads have been designed for this purpose. Finally, the χ^2 and vertex selection are applied to the resulting candidates.

5.3 Υ and π/K reconstruction, efficiencies and purities

The algorithm for the central barrel is based upon a vertex determination using tracks in the two pixel detectors, including treatment of lost clusters. About 1600 Υs plus 470 π/K tracks (giving 110215 $\mu^+\mu^-$ and LS pairs) in the central barrel and 800 Υs with at least one muon in forward barrel were generated. For efficiency calculations in the forward barrel 510 π/K decays in the central barrel and 212 π/K in the forward barrel have been generated. This yields 108000 pairs with at least one of the tracks in the range $0.8 < |\eta| < 1.3$. Almost 800 $b\bar{b}$ decays into muons have also been generated using PYTHIA.

For the all-silicon tracker design almost 500 Υs were generated in the central barrel. Efficiencies are given in Table 5.4 for the central barrel with MSGC counters and in Table 5.5 for the new all-silicon tracker. Table 5.6 gives the efficiencies and purities for the forward barrel with
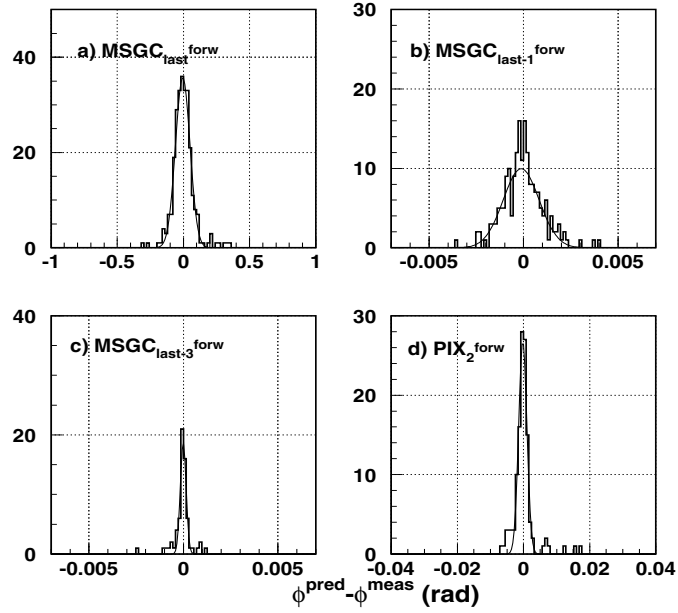
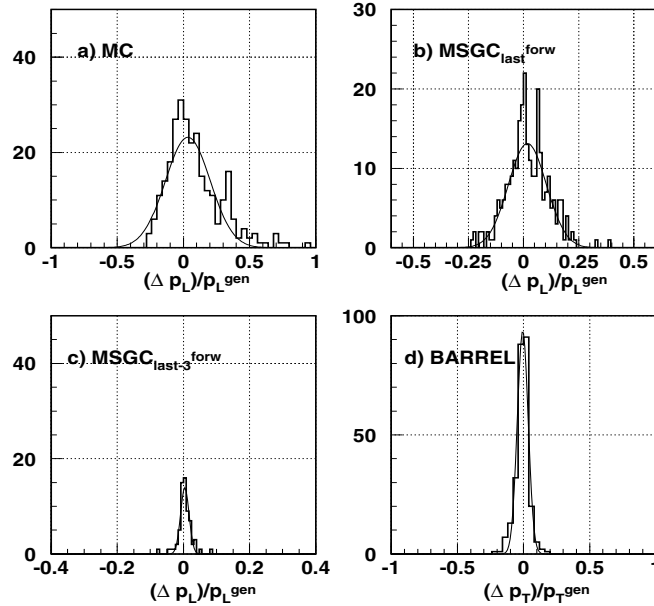**Fig. 5.21.** Distribution of $\delta\phi$ for muons from Υ decay for forward discs (detailed geometry)

Fig. 5.22. p_{L} and p_{T} matching from step-to-step for muons from Υ decay

MSGC counters. One observes a relatively constant efficiency of 90% up to a charged multiplicity $dN^{\pm}/dy = 2500$ and then a decrease to 85% with increasing $dN^{\pm}/dy$ from 2500 to 5000. In Table 5.4 the efficiencies for reconstruction of muon pairs from uncorrelated background are given according to the origin of each muon: both tracks from π/K decays, one track from Υ and the second from π/K decay, etc. In each row there is no difference in efficiency between $dN^{\pm}/dy = 500$, 1500 and 2500 for either signal or background dimuons.

Table 5.4 shows that along the whole multiplicity range the efficiency to reconstruct a dimuon from Υ decay is better a factor 6 than for uncorrelated π/K decays dimuon. Thus the algorithm contributes strongly to the background rejection.
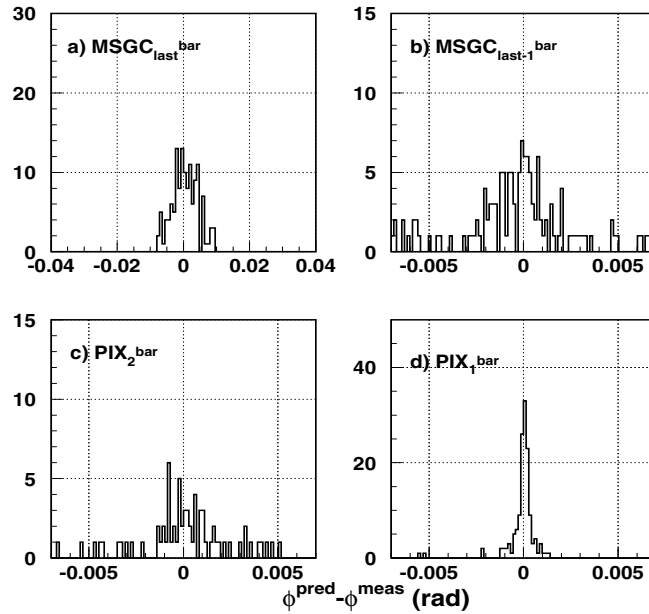
Fig. 5.23. Distribution of $\delta\phi$ from successive barrel cylinders for muons from Υ decay (detailed geometry)
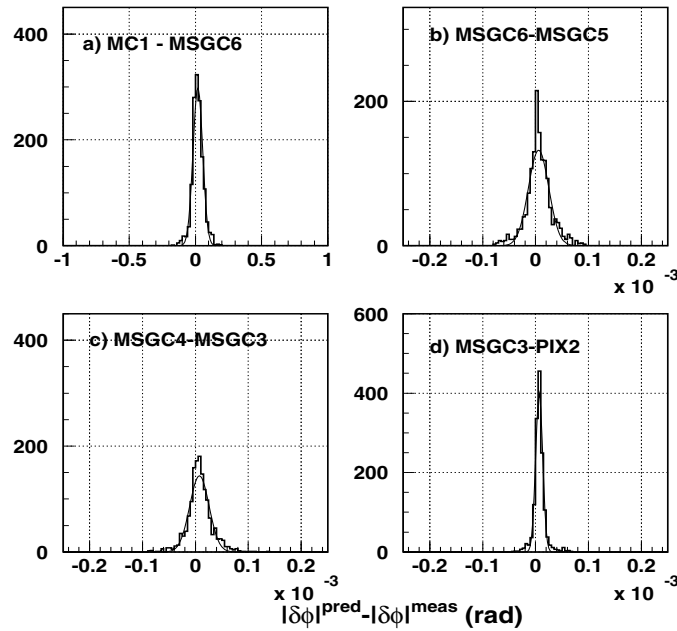

Fig. 5.24. Distribution of $\delta\phi$ for muons from Υ decay using the final estimate of p_{T}

Similar calculations have been made both for dimuons from Υ decays and from uncorrelated background for the cases where one of the tracks traverses the CMS detector in the range $0.8 < |\eta| < 1.3$. A strong reduction of efficiency is observed for $\mathrm{d}N^{\pm}/\mathrm{d}y = 8000$. Figure 5.5 reveals a region where the muon tracks intersect only one or two forward layers after leaving the barrel detectors, corresponding to 3 or 4 hits per track. For these tracks there is no reliable extrapolation into the pixel detectors. This results in a huge number of track candidates. Muons with more than 2000 candidate tracks are rejected. Finally the efficiency to reconstruct the Υ is 2.2 to 3 times greater than the efficiency for the uncorrelated dimuons (Table 5.6).

Including the treatment of lost clusters increases the efficiency by about 10% for $\mathrm{d}N^{\pm}/\mathrm{d}y = 8000$ and less for minimum bias events.
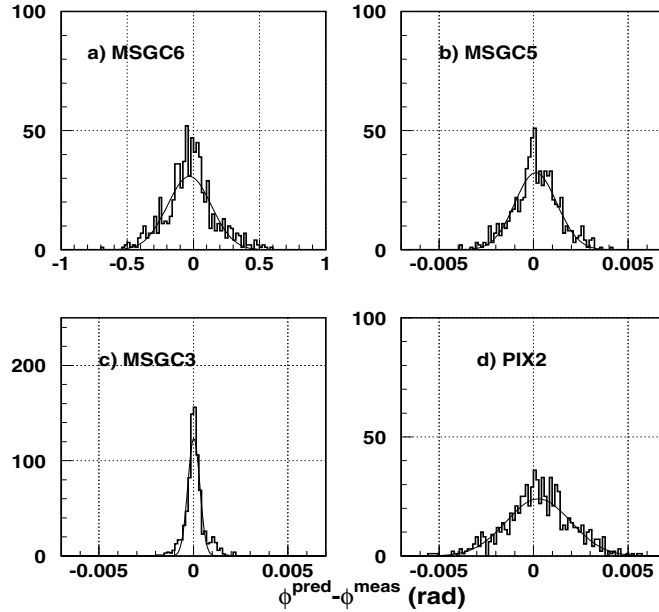
Fig. 5.25. Distribution of $\delta\phi$ for tracks from π/K sample passing through sequential layers through windows determined by the muons from Υ decays (detailed geometry, barrel layers).

Table 5.4. Reconstruction efficiency (%) and purity (%, in parentheses) for different event multiplicities (central barrel region with a MSGC pitch of 240 μm)

$\mathrm{d}N^{\pm}/\mathrm{d}y$	500	1500	2500	5000	8000
Υ	92(100)$\pm$1	92(100)$\pm$1	89(99)$\pm$1	85(99)$\pm$1	64(97)$\pm$1
Υ,b	59$\pm$2	59$\pm$2	57$\pm$2	53$\pm$2	36$\pm$2
$\Upsilon,\pi/K$	34$\pm$3	34$\pm$3	33$\pm$3	33$\pm$3	22$\pm$2
$\pi/K,\pi/K$	14.2$\pm$2	14.4$\pm$2	14.2$\pm$2	15.4$\pm$2	9.7$\pm$1
$\pi/K,b$	24$\pm$3	24$\pm$3	23$\pm$3	24$\pm$3	15$\pm$2
b,b	40$\pm$2	40$\pm$2	38$\pm$2	36$\pm$2	24$\pm$2

Table 5.5. Reconstruction efficiency (%) and purity (%, in parentheses), for the central barrel region with all Silicon tracker design

$\mathrm{d}N^{\pm}/\mathrm{d}y$	500	1500	2500	5000	8000
Υ					76(97)$\pm$1

Table 5.7. Reconstruction efficiency (%) and sample purity (%, in parentheses) in the mass range 9.3-9.6 GeV for $\mathrm{d}N^{\pm}/\mathrm{d}y = 8000$

	central barrel	forward barrel
Υ	64(99)$\pm$2	38(97) $\pm$2

As already mentioned, the reconstruction in the forward barrel is complicated. The purity of the reconstructed sample of dimuons from Υ decays with at least one muon intersecting the forward discs is about 79%. However, the remaining 20% background pairs exhibit a wide mass distribution. This holds also for the central barrel. Only a small fraction is in the Υ mass range (see Table 5.7).

The distribution of the dimuon masses and of the z-coordinates of primary vertices of reconstructed dimuons from Υ decays are shown in Fig. 5.31a,b for the central barrel and Fig. 5.31c,d for the forward barrel.

One finds a mass resolution of 46 MeV for the central barrel and about 60 MeV for the forward barrel, taking into account the background hits corresponding to $\mathrm{d}N^{\pm}/\mathrm{d}y = 8000$.

For the all-silicon tracker design, the efficiency in the central barrel ($|\eta|<0.8$) reaches 76% with purity 97% (Table 5.5) and the same mass resolution as with the MSGCs. Such an improvement is a consequence of a decreasing the number of clusters on the outermost layer in comparison to the MSGC design (Fig. 5.8). The silicon detectors have a smaller thickness than the MSGCs (0.3 mm instead of 3 mm) and thus far fewer split clusters from the
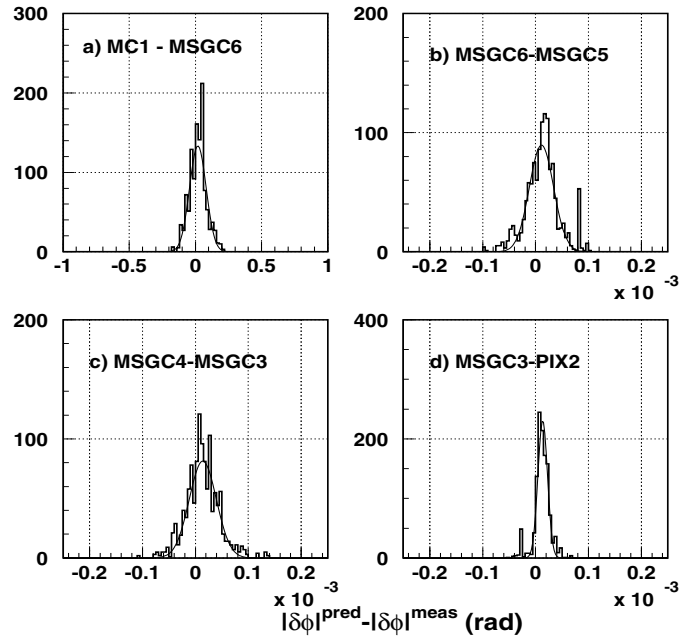
Fig. 5.26. Same as Fig. 5.24 but for π/K sample tracks (detailed geometry – barrel layers)
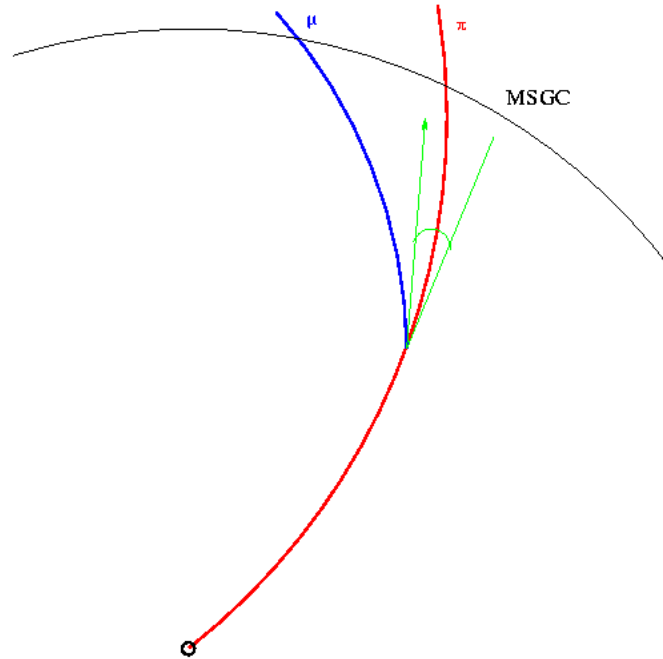
Fig. 5.27. π/K decay track

soft tracks. The smaller strip length of the two outermost layers gives a better prediction of the z-coordinate in the inner layers.

5.4 Summary of muons pairs reconstruction

The dimuon finding and reconstruction algorithm described here has been developed for the detection of

dimuons from Υ decays produced in heavy ion collisions. For this purpose we studied different event multiplicities up to the most difficult situation, *i.e.* a central Pb+Pb collision, with $\mathrm{d}N^{\pm}/\mathrm{d}y = 8000$.

The algorithm needs 2 tracks with $|\eta|<1.3$ in the muon chambers, each track with 2 hits in the first μ-station. It uses both the pixel layers (pixel size of about 150×150 μm^2) and the 4 outermost MSGC layers (strip lengths of

Fig. 5.28. Difference of the azimuthal angle between primary π track and its decay muon (**a**). **b** same as **a**), **but for** π (*white area* and K (*hatched area*)
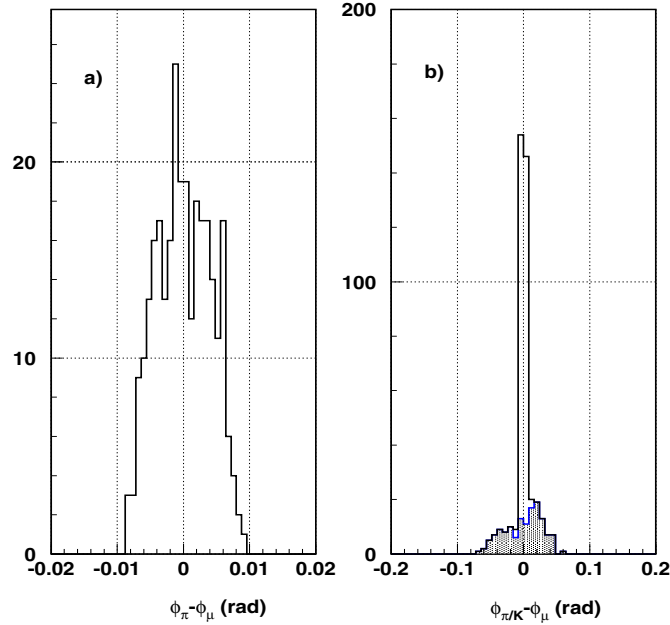
Table 5.6. Reconstruction efficiency (%) and purity (%, in parentheses) for different event multiplicities (forward barrel region with a MSGC pitch of 240 μm)

$\mathrm{d}N^{\pm}/\mathrm{d}y$	500	1500	2500	5000	8000
Υ	54(100)±2	57(99)±2	55(99)±2	64(92)±2	51(81)±2
Υ,b	46±4	46±4	48±4	55±4	41±4
$\Upsilon,\pi/K$	37±4	38±4	42±4	51±4	36±4
$\pi/K,\pi/K$	18±4	19±4	22±4	30±4	23±4
$\pi/K,b$	26±4	27±4	29±4	37±4	28±4
b,b	35±4	36±4	37±4	42±4	34±4

25 cm for the two outermost layers, 12.5 cm for the others). The use of stereo information is not taken into account. The Si-strip detectors and the innermost MSGCs are ignored due to their high occupancy, although it is not excluded to use their information for low charged particle multiplicity, *i.e.* in peripheral collisions or of light ion beams.

The algorithm is based on a full GEANT simulation of the CMS geometry. It uses roads between the layers for various p_T intervals. In addition, circular and linear fits for single muon tracks are performed, and vertex constraints for the dimuons are imposed.

The algorithm has been applied to dimuons from Υ decays as well as from background π/K and b decays. The efficiency to reconstruct dimuons in the central barrel for the all-silicon tracker reaches 76% with purity 97% and the same mass resolution as for the MSGC design.

The z position of the primary vertex is found with a good precision, $\sigma = 140\mu$m by using both pixel layers. The efficiency to reconstruct dimuons from Υ decays in the central barrel is 64% with a purity of about 90-97% depending on the cuts on track quality. This efficiency increases to 89% for collisions with $\mathrm{d}N^{\pm}/\mathrm{d}y=$ 2500. It may increase to 90% for lower multiplicities.

The efficiency to reconstruct the Υs in Pb+Pb central collisions is 64% with MSGC's in the central barrel. This value increase to 76% with the all-Si tracker. The reconstruction algorithm improves the background rejection by a factor 6 with respect to uncorrelated muons pair from π/K decays.

Finally the mass resolution obtained for the reconstructed Υ is 46 MeV.

5.5 Background sources

5.5.1 Soft hadrons

As noted in Section 4.2, soft hadrons (mainly pions and kaons) are one of the most important sources of muon
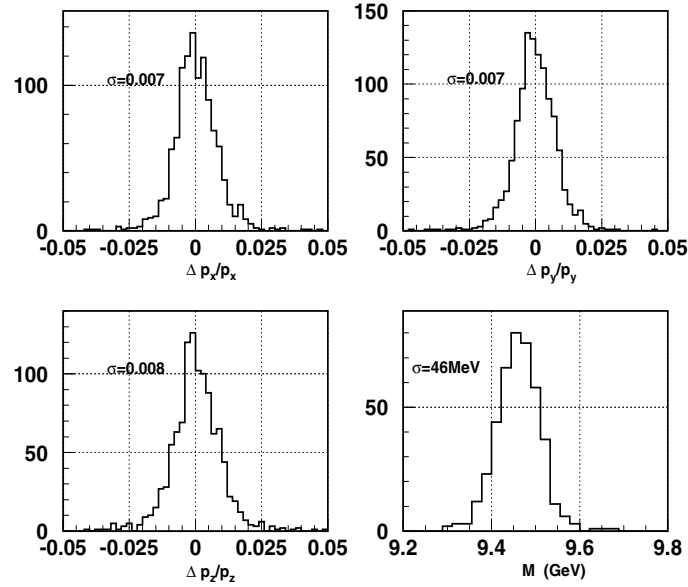
Fig. 5.29. Distribution of momentum components and of dimuon masses for the central barrel
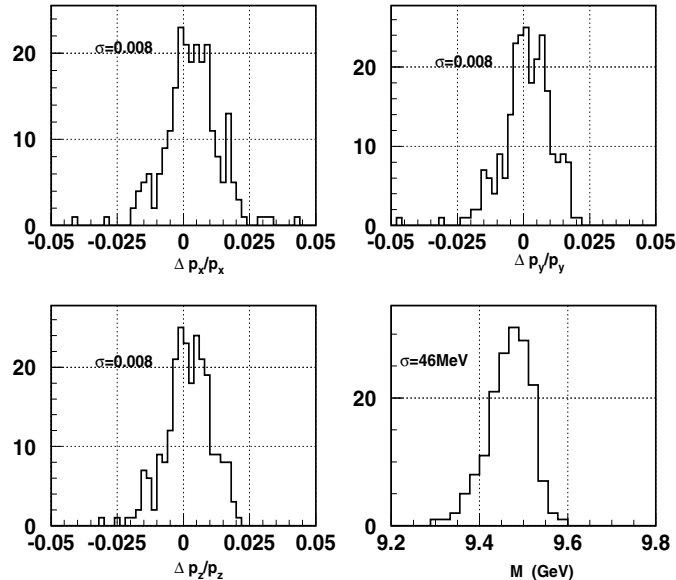
Fig. 5.30. Distribution of momentum components and of dimuon mass for forward barrel

background. In CMS, the dimuon background increases as the multiplicity of particles folded with probability that $p_T > 3.5$ GeV/c. This means that the p_T distributions and the hadronic multiplicities are crucial ingredients in the simulation of dimuon background, because the latter is proportional to the square of the product of the multiplicities and the probability that $p_T > 3.5$ GeV/c. Within reasonable limits we choose the less favourable assumption

In order to simplify our background estimation method, we assume that all the secondary hadrons are pions and kaons. Table 4.2 shows that an average of 1620 charged π and K are emitted in one unit of rapidity at $y=0$, in minimum bias and 7460 in central Pb+Pb collisions

The ratio between the number of pions and kaons is 5:1 independent of impact parameter. This value is much

Fig. 5.31. Spectra of invariant masses and of z-coordinates of primary vertices for reconstructed Υs in the central barrel **a** and **b** and forward barrel **c** and **d**

higher than the ratio given by HIJING (12% kaons in minimum bias and 13.5% in central collisions). The p_T spectra of pions and k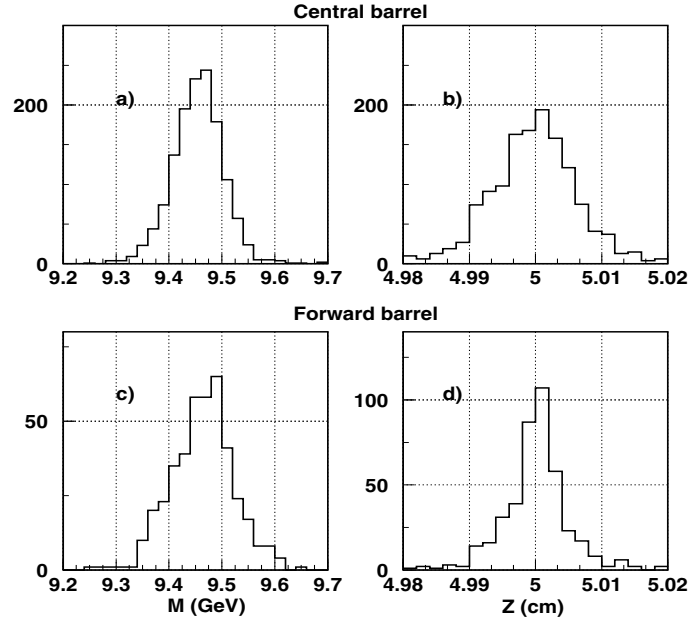aons were obtained from SHAKER [179] and are shown in Fig. 5.32. The average p_T, 0.48 GeV/c for pions and 0.67 GeV/c for kaons, are much higher than those obtained from HIJING. This results from the high p_T tail of the adopted distributions. Figure 5.32 shows the probability as a function of p_T for a particle to have a transverse momentum lower than p_T. One can see that for $p_T = 3.5$ GeV/c, this probability is 0.9987 for a pion and 0.9966 for a kaon. The K/π ratio therefore increases from 0.2 at generation to 0.5 after the p_T cut. In an average Pb+Pb collision, almost 4700 charged π and K are produced at $|\eta| < 1.3$ (corresponding to the barrel) and among them only 9 (0.2%) have a transverse momentum larger than 3.5 GeV/c. For a central Pb+Pb collision the corresponding numbers are 21500 (π,K generated) and 43 ($p_T > 3.5$ GeV/c).

In order to estimate the background, we have built separate acceptance tables for pions and kaons. Because of the processing time needed, we have first generated the particles emitted from the geometrical centre at specific (p_T,η) values, and tracked them through the whole detector with GEANT. The physics processes taken into account in the tracking were the energy loss, the multiple scattering, the decay and the hadronic interactions. The primary particle is flagged as accepted when it (or one of its secondaries) reaches any one of the muon chambers. In a second step, a linear interpolation between two successive points allows the building of the acceptance table with p_T and η bins equal to 0.1 GeV/c and 0.05 respectively. The acceptance tables are given in Fig. 5.33 for pions (top) and for kaons (middle). As can be seen,

Table 5.8. Average number of muons from π and K decays in the CMS-barrel, for minimum bias Pb+Pb collision along with the effects of the p_T cut and acceptance

	at generation	after p_T cut	accepted
pions only	1	0.0014	2×10^{-6}
kaons only	1	0.0035	10^{-5}
$\pi + K$	1	0.0017	3×10^{-6}

the probability for a π or K to be detected is of the order of a few percent at most. Most often, none of the 9 hadrons with $p_T>3.5$ GeV/c emitted in an average Pb+Pb collision are detected.

The effects of the $p_T>3.5$ GeV/c cut and of the acceptance in the barrel muon chambers are shown in Table 5.8 on pions and kaons. The ratio K/π of 20% at the generation level rises to roughly 100% at the acceptance level because kaons have a shorter lifetime and, consequently, a higher probability to decay into muons in the inner tracker before entering the CMS calorimeters. Their transverse momentum distribution is also harder than that of pions. Thus the backgrounds from kaons and pions are of the same magnitude so that the initial ratio $K/\pi = 20\%$ plays a substantial role.

In a minimum bias Pb+Pb collision 4700 π and K are generated with $|\eta| < 1.3$; they yield 0.015 muon detected in the barrel muon chambers. As the dimuon background is proportional to the square of this number, the probability to have a dimuon from π or K decays
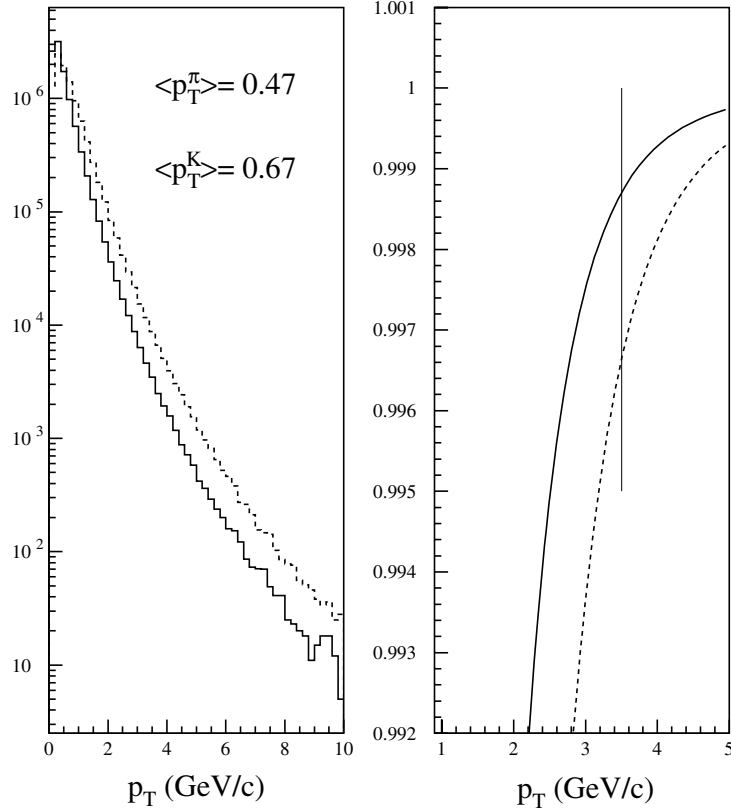
Fig. 5.32. π (solid line) and kaon (dot line) p_T spectra (left) together with the corresponding normalized integral (right). The vertical line indicates the 3.5 GeV/c p_T cut

Table 5.9. Number of $b\bar{b}$ and $c\bar{c}$ pairs produced in minimum bias and central collision

	Pb		Ca	
	min. bias	central	min. bias	central
$N_{b\bar{b}}$	1	4.7	0.1	0.6
$N_{c\bar{c}}$	13.6	68	1.8	8

is $\approx 225 \cdot 10^{-6}$. This is about 40 times higher than the probability to detect a Υ in the same collision. The dimuons from π or K decays have, however, a wide invariant mass distribution; indeed, only 2% of the π and K decay background is found in the Υ mass region ($M_\Upsilon \pm 50$ MeV/c^2).

5.5.2 Open charm and beauty production

In AA collisions the average number $N_{Q\bar{Q}}$ of heavy flavour pairs $(Q\bar{Q})$ is estimated as the number of nucleon-nucleon collisions N_{col} weighted by the ratio of the cross section

$\sigma(pp \rightarrow Q\bar{Q})$ to the proton-proton inelastic cross section $\sigma_{\mathrm{inel}}(pp)$: $N_{Q\bar{Q}} = N_{\mathrm{col}} \, \sigma(pp \rightarrow Q\bar{Q})/\sigma_{\mathrm{inel}}(pp)$. Using: $\sigma(b\bar{b})$=0.35 mb, $\sigma(c\bar{c})$=5 mb and $\sigma_{\mathrm{inel}}(pp)$=100 mb leads to the numbers of $(Q\bar{Q})$ for minimum bias and central collisions shown in Table 5.9.

To simulate the open charm and beauty contributions to the background, the contributions of individual nucleon-nucleon collisions are added. In each NN collision one $c\bar{c}$ pair and one $b\bar{b}$ pair were generated. The pairs decay into muons according to the probabilities given by PYTHIA and listed in Table 5.10. In the final effective background each detected muon has to be weighted by the production cross section of the corresponding process.

The muon p_T and η distributions are extracted from PYTHIA. The big difference between p_T distributions from b or c channels is that $\langle p_T^c \rangle$= 0.51 GeV/c, while $\langle p_T^b \rangle$= 1.2 GeV/c. Among all background sources taken into account in this study, the open beauty channels create muons with the highest average transverse momentum, significantly contributing to the background.

In Table 5.11, the numbers of muons pairs coming from $b\bar{b}$ and $c\bar{c}$ pairs are compared. We have distinguished the correlated opposite-sign dimuon contribution from the single decay muons from different $q\bar{q}$ pairs which can form uncorrelated dimuons. A minimum bias Pb+Pb
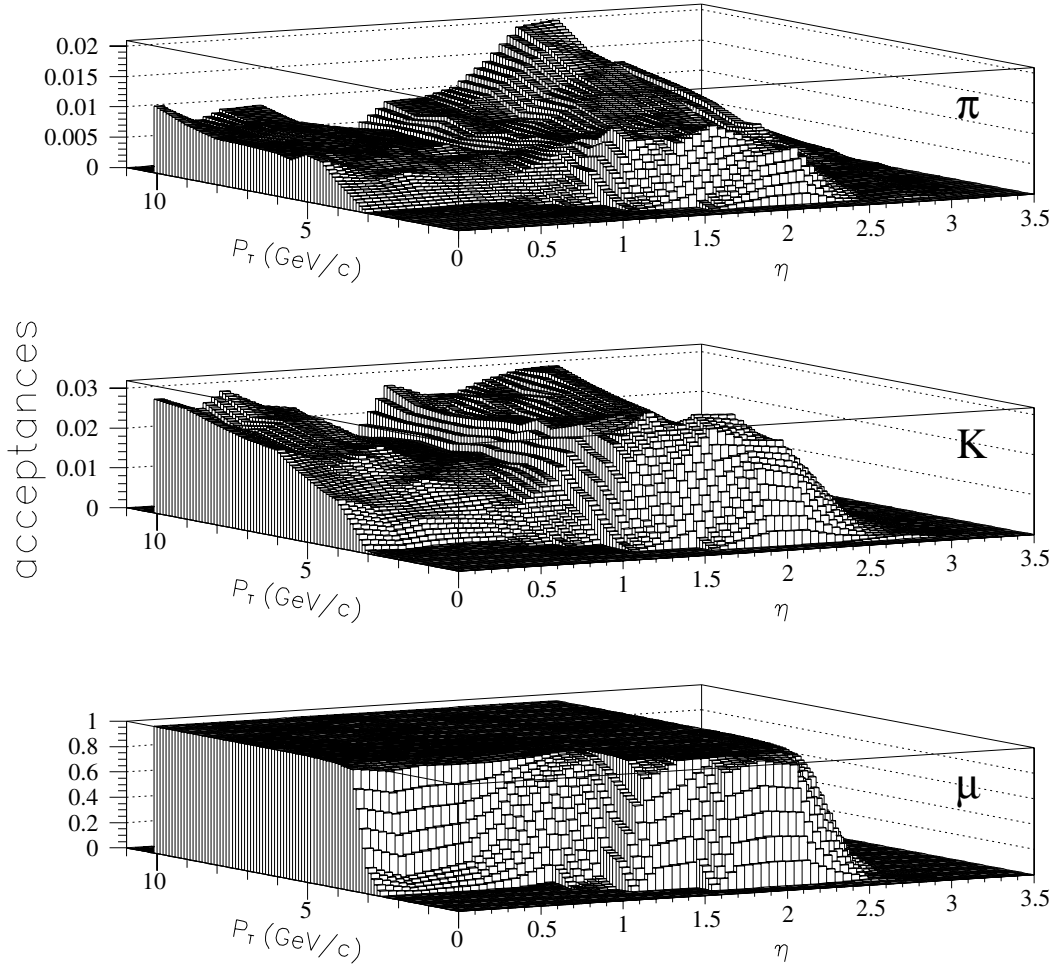
Fig. 5.33. Acceptance tables (p_T,η) for incident charged pion (*top*), incident charged kaon (*middle*) and for incident muon (*bottom*)

Table 5.10. Probability $\mathcal{P}(n)$ that n muons are emitted in pp collisions from $b\bar{b}$, $c\bar{c}$ channels when the corresponding $q\bar{q}$ pair is formed

	$c\bar{c}$	$b\bar{b}$
$\mathcal{P}(0\mu)$	0.819	0.623
$\mathcal{P}(1\mu)$	0.171	0.310
$\mathcal{P}(\geq 2\mu)$	0.010	0.067

interaction with 272 nucleon-nucleon collisions gives, on average, 2.32 single muons and 0.13 correlated opposite-sign dimuons from charm production. The corresponding numbers for $b\bar{b}$ production are 0.29 and 0.06. The p_T cut and the acceptance reduce these numbers to 1.15×10^{-3} and 4.7×10^{-7} for the charm and 4.3×10^{-3} and 3.0×10^{-5}

for beauty. The correlated pair contribution alone is about two orders of magnitude larger for the $b\bar{b}$ production. A comparison between uncorrelated muon pairs from the combination of single muons and correlated pairs is shown in the last column. The correlated pairs represent one quarter of the uncorrelated ones in the case of charm whereas for beauty both contributions are equivalent.

The last row of Table 5.11 includes the π/K contribution to the background. For 7530 π and K generated in the CMS rapidity window, 0.025 muons are detected.

5.5.3 Dimuon event rates

In this section we estimate the multiplicity of muons detected either in the barrel or in the full detector muon chambers. All the p_T, $\Delta\eta$ or $\Delta\phi$ cuts are switched off

Table 5.11. Single muon and muon pair background from $b\bar{b}$ and $c\bar{c}$ channels in a minimum bias Pb+Pb collision, and a comparison with μ from hadrons

	at generation	after p_T cut	detected	dimuon rate
$c\bar{c}$: single muons	2.32	3.6×10^{-3}	1.15×10^{-3}	1.7×10^{-6}
$c\bar{c}$: correlated $\mu^+\mu^-$ pairs	0.13	3.8×10^{-6}	4.7×10^{-7}	4.7×10^{-7}
$b\bar{b}$: single muons	0.29	0.011	4.3×10^{-3}	2.75×10^{-5}
$b\bar{b}$: correlated $\mu^+\mu^-$ pairs	0.064	2.5×10^{-4}	3.0×10^{-5}	3.0×10^{-5}
π/K	7530	13.1	0.025	6.2×10^{-4}

for this study. For each collision, one muon is selected if it hits any of the muon chambers. No trigger condition or muon chamber efficiency is taken into account. The results, including all the muon sources (resonances, soft mesons and open b and c particles), are shown in Table 5.12 for Pb+Pb and Ca+Ca collisions. The single muon rate in the barrel expected for Pb+Pb collisions (*i.e.*7600 (1-0.912)$\approx$670 Hz) is compatible with the estimation obtained in a different way [180] (500 Hz, but taking into account the single muon trigger efficiency). First of all there is a strong difference between the full CMS detector and the barrel, for which more than 90% of Pb+Pb collisions do not give any impact in the muon chambers, and less than 1% of them lead to a multiplicity of 2 or more. The rate for multiplicity M$\geq$2 is quoted in the last column, with the beam luminosity taken from the Table 4.1. For 7600 Pb+Pb minimum bias collisions per second, 2/3 of them generate a dimuon in the full CMS detector, leading to a rate of $\approx$5 kHz, whereas only 61 of them produce 2 muons hitting the barrel muon chambers. This rate is very close to the one obtained in the specific trigger study described in Chapter 8. For Ca+Ca collisions, only 0.01% of the collisions give a dimuon in the barrel region. The very high luminosity leads however to a rate comparable to Pb collisions. Concerning the full detector, although the distribution is shifted towards the low multiplicities, the high luminosity forbids to use the forward and backward parts of the muon chambers unless a further selection is applied at the trigger higher levels. The rates in the barrel indicate that most of the time triggering events have only 2, very rarely 3 hits, showing that when a resonant state is detected it is almost never accompanied by a background muon.

5.6 Dimuon mass spectra in the CMS barrel

5.6.1 Simulation weights

Because Υ production in Pb+Pb collisions is rare, and in order to avoid statistical fluctuations, we adopted a method based on the acceptance tables and weighted simulations for each process. This method allows us to take into account heterogeneous pairs for which the two muons have different origins *e.g.* one muon coming from a π or K decay and another from a b decay.

Our program accounts for a large number of AA collisions, typically several millions, which is impractical to track with a full detector simulation due to CPU time constraints. Each collision is characterized by an impact parameter which defines the charged particle multiplicity and the elementary nucleon-nucleon collision number (Section 4.2).
In each collision, one resonance (J/ψ, ψ', Υ, Υ' or Υ''), is generated in the phase space (p_T,η). The decay muons, provided their p_T is larger than 3.5 GeV/c, are stored with a weight W_res equal to the resonance production cross section relative to the AA inelastic cross section, multiplied by the corresponding acceptance W_acc from the muon acceptance table: $W_\mathrm{res} = [\sigma_\mathrm{prod}(\mathrm{res})/\sigma_\mathrm{int}(AA)]\ W_\mathrm{acc}$. The muon charge, its 3-momentum , pseudorapidity and parent particle are stored.
The same information is kept for pions and kaons with $p_\mathrm{T}^{\pi,K} > 3.5$ GeV/c. In this case, the cross section ratio is set to 1 and W_acc is given by the corresponding acceptance table. The charm and beauty channels are taken into account in each elementary nucleon-nucleon collision. According to the probabilities quoted in Table 5.10, one muon of any charge or 2 muons of opposite charges are generated with a weight equal to $\sigma(Q\bar{Q})/\sigma_\mathrm{inel}(pp)$.
Several tens of muons can be registered in the most central AA collision. They are combined 2 by 2 irrespective of their charge, and the mass of the resulting pair is calculated. The origin of every pair is recorded. The weight is the product of individual weights if the pair is heterogeneous. In addition to the 3.5 GeV/c p_T cut, other kinematical restrictions are imposed on the dimuons, as summarized in Table 5.13.

5.6.2 Dimuon mass reconstruction: resolution and efficiencies

For a given pair, its invariant mass is calculated and altered by a gaussian distribution according to the expected mass resolution discussed in Section 5.3 ($\sigma_\mathrm{M} \approx 46$ MeV if both $|\eta_\mu|$<0.8 and $\sigma_\mathrm{M} \approx 60$ MeV if at least one muon has a pseudorapidity 0.8<$|\eta_\mu|$<1.3). These same mass resolutions are used for the Υ and J/ψ mass regions.
The dimuon reconstruction efficiency [181] is also taken into account. This efficiency is presently known only for $|\eta_\mu|$<1.3. It depends on the origin of each muon as well

Table 5.12. Multiplicity distribution of detected muons and dimuon trigger rate

μ multiplicity		0μ	1μ	2μ	$\geq 2\mu$	$\mu\mu$ rate (Hz)
Pb+Pb	barrel+endcaps	22.0%	12.6%	9.4%	65.5%	4980
	barrel	91.2%	8.2%	0.7%	0.8%	61
Ca+Ca	barrel+endcaps	63.0%	21.7%	9.3%	15.0%	79000
	barrel	99.0%	1.0%	0.01%	0.01%	53

Table 5.13. Additional kinematical cuts between muons

	J/ψ	Υ
p_{T}	$p_{\mathrm{T}}^{\mu_1} > 18.2/p_{\mathrm{T}}^{\mu_2}$	$p_{\mathrm{T}}^{\mu_1} > 18.2/p_{\mathrm{T}}^{\mu_2}$
η	$\left|\Delta\eta(\mu_1,\mu_2)\right| \leq 1.2$	$\left|\Delta\eta(\mu_1,\mu_2)\right| \leq 1.5$
ϕ	$\left|\Delta\phi(\mu_1,\mu_2)\right| \leq 1.4$ or $\left|\Delta\phi(\mu_1,\mu_2)\right| \geq 5$	$1.4 \leq \left|\Delta\phi(\mu_1,\mu_2)\right| \leq 4.8$

Table 5.14. Dimuon reconstruction efficiencies (%) for the case of both μ tracks crossing the barrel MSGCs ($|\eta_\mu| < 0.8$) for various π and K multiplicities

	$\mathrm{d}N^\pm/\mathrm{d}y$				
	500	1500	2500	5000	8000
Υ	88	90	88	83	66
$\pi/K,\pi/K$	16	15	16	15	11
Υ,b	71	69	68	65	49
$\pi/K,b$	31	29	29	28	21
$\Upsilon,\pi/K$	38	38	40	36	28

Table 5.15. Dimuon reconstruction efficiencies (%) when at least one μ crosses a forward MSGC ($0.8<|\eta_\mu|<1.3$)

	$\mathrm{d}N^\pm/\mathrm{d}y$				
	500	1500	2500	5000	8000
Υ	83	82	80	64	34
$\pi/K,\pi/K$	28	19	26	16	15

as on the centrality of the collision. Tables 5.14 and 5.15 give the reconstruction efficiency for each situation. When both muons have $|\eta|<0.8$ the π and K decay background is suppressed by a factor of 6 relative to dimuons from Υ decays. This factor is reduced to 2 when one or both muons cross a forward MSGC disc.

5.6.3 Signal/background for Υ

The ratio between the number of detected Υ(1S) and the number of opposite-sign dimuons below the peak in the mass window $M_\Upsilon\pm50$ MeV is calculated without subtrac-

tion of uncorrelated background. In the following this ratio is noted (Υ/cont). Almost $9.4\ 10^6$ minimum bias Pb+Pb collisions have been studied. Table 5.16 shows the main contributions to the dimuon mass spectrum in this mass interval, according to their origin. The Υ dimuons are by far the dominant component: 61.8% of the total. The background is dominated by π or K decays which contribute to $\approx$65% of the total background when combined with muons from hadronic, b, or c decays. These pairs of muons are uncorrelated and therefore appear also in the like-sign dimuon mass spectra. The pure $c\bar{c}$ contribution is negligible in contrast to the 7.2% $b\bar{b}$ contribution. The 0.35 mb cross section for the production of $b\bar{b}$ pairs is therefore an important parameter in the simulation.

These results have been adapted to a one month run, $1.3\ 10^6$ seconds. The mass spectra in the range [8.5-11 GeV/c^2] at a luminosity of 10^{27}cm^{-2}s^{-1}, are shown in Fig. 5.34 for the opposite-sign (OS) dimuons and Fig. 5.35 for the like-sign pairs (LS++ and LS--). As expected, both like-sign muon pair spectra have the same shape. In the OS spectrum, the various contributions to the background are superimposed. The 3 Υ states stand out clearly with Υ/cont=1.6. The same mass distribution is plotted in Fig. 5.36 for Ca+Ca minimum bias collisions. The hadronic background is one order of magnitude lower than in Pb+Pb collisions and the b-channel provides the dominant contribution to the background. The ratio Υ/cont is 9.4 in this case. Moreover, higher efficiencies might be achieved for dimuon reconstruction as one may use the information from more tracker layers than in the Pb case due to reduced occupancy.

The expected Υ/cont ratios together with the available statistics for one month are summarized in Table 5.17. The statistics of 22000 Υ measured in one month is high enough to study the resonance in different impact parameter bins.

As the background mainly consists of uncorrelated muons, it can be subtracted from the OS spectrum using the LS spectra, as currently done in the SPS NA50

experiment [10]. In this case, the signal is obtained from:

$$\text{Signal}(\mu^+\mu^-) = N^{+-} - 2\sqrt{N^{++} \times N^{--}} \quad (5.12)$$

where N^{+-}, N^{++} and N^{--} are respectively the numbers of combinations in a given mass interval of OS, LS++ and LS-- spectra. Figure 5.37 presents the mass distributions resulting from this subtraction.

As for all experiments studying dimuons in heavy ion collisions, CMS is very sensitive to the hadronic background. Taking 8000 π and K for the multiplicity at midrapidity is certainly pessimistic from this point of view. If the multiplicity is actually only 50% of this, and keeping the same b and c background, a simple calculation shows that the Υ/cont ratio increases by 80% and the $b\bar{b}$ component dominates. In addition, our background calculation is very sensitive to the p_T distributions of pions and kaons. We have adopted the ones given by SHAKER, the average p_T of which are much higher than those given by HIJING. If the physical distributions were closer to those predicted by HIJING, the effect of the 3.5 GeV/c p_T cut (see Fig. 5.32) would increase the Υ/cont ratio by a factor of ≈ 2.

For the 5% most central collisions, the average $\pi + K$ multiplicity at midrapidity is 7460 and the average cross section for the Υ production is 2000 μb, as quoted in Table 4.2. The value Υ/cont=0.9 has been obtained with 4000 resonant states per month. As a consequence, the 5% central Pb+Pb collisions contribute nearly 20% of the detected Υ.

5.6.4 Signal/background for J/ψ

The J/ψ states have been studied in the same way as the Υ family, using the same reconstruction efficiencies and the same p_T cuts. Again, the study was restricted to the barrel. The results are shown on the Table 5.17. The ψ/cont ratio is estimated in the mass interval $M_{J/\psi} \pm 50$ MeV/c^2. Despite the very low acceptance of the barrel, the number of J/ψ expected in one month is very substantial due to the large production cross section. As pointed out in Section 5.1.2, all J/ψs are at $p_\text{T} > 5$ GeV/c. The opposite-sign dimuon mass spectra from Pb+Pb and Ca+Ca collisions are given in Fig. 5.38. These distributions correspond to one month of data taking. The J/ψ resonance is well above the background with a ratio $\psi/cont = 1$ in the case of minimum bias Pb+Pb collisions and nearly 10 for calcium beams. The ψ' is not visible in the spectra, being strongly penalized by its cross section. A more detailed study of the $c\bar{c}$ resonances with appropriate cuts should be done before any definitive conclusion.

5.7 Open beauty and Z^0 production measurements

As indicated in Section 2.4, Z^0 production can be used as a reference for Υ suppression although it is at a much higher mass and its production mechanisms are different. In this section we investigate the CMS detector for the high invariant mass dimuons.

The main sources of dimuons with $M \geq 10$ GeV/c^2 in heavy ion collisions are:

1. production of Υ family bound states;
2. Drell-Yan and Z^0 production;
3. decays of open heavy flavours ($c\bar{c}$, $b\bar{b}$ and $t\bar{t}$);
4. WW, WZ^0 and Z^0Z^0 pair production;
5. decays of π and K mesons;
6. mixed muon pairs from (1-5).

In the following, neither modifications of the parton structure functions in a nucleus relative to a free nucleon nor energy loss of heavy quarks in dense matter have been taken into account. Also no background from cosmic ray muons was considered. We believe that the latter can be suppressed using timing information from the muon chambers and the beam crossing.

5.7.1 Muons from Drell-Yan, heavy flavour, Z^0 and W decays

Heavy flavour, Drell-Yan, Z^0, W, WW, WZ^0 and Z^0Z^0 production cross sections in minimum bias nucleus-nucleus collisions were obtained from those in pp interactions at the same energy ($\sqrt{s} = 5.5$ TeV) using the parameterization $\sigma^i_{AA} = A^{2\alpha} \sigma^i_{pp}$, with α=1.0. The cross sections in pp collisions were evaluated using the PYTHIA Monte Carlo program [79]. In PYTHIA, only leading order processes are simulated. The default CTEQ2L structure functions are used with $K = 1$, the resulting cross sections are significantly smaller than those obtained from next-to-leading order calculations using GRV HO and MRS D parton distribution functions (by a factor of 5-13 for $c\bar{c}$ and 2.5-3.0 for $b\bar{b}$ production [52]). However, for the high p_T region this factor is only of the order of 2 for both processes. The same factor was found between measured open beauty production cross sections (at $p^b_\text{T} \geq 20$ GeV/c) in $p\bar{p}$ collisions at the Tevatron [182,183] and PYTHIA predictions. Therefore PYTHIA simulation results were used with a correction factor $K = 2$ for both $c\bar{c}$ and $b\bar{b}$ production cross sections. For Z^0, W and $t\bar{t}$ production [184, 185] the correction factors are of the order of 1.3-1.5. The cross sections for $t\bar{t}$, WW, WZ^0 and Z^0Z^0 production are so low that their contributions to the dimuon mass distribution are negligible.

Figure 5.39 presents the simulated transverse momentum distributions of muons originating from heavy flavour, Drell-Yan, Z^0 and W production processes in Pb+Pb collisions. Again, only muons with $p_\text{T} \geq 3.5$ GeV/c and $|\eta| \leq 2.5$ were taken into account. In the range 3.5 GeV/c $\leq p_\text{T} \leq 25$ GeV/c the main source of muons is open beauty production. Hence, this range of muon transverse momentum can be used to estimate energy losses of b quarks in heavy ion collisions. For lower p_T values, the contribution from open charm fragmentation is larger; however in this range background from π/K decays becomes dominant. For $p_\text{T} \geq 25$ GeV/c the contributions from W and Z^0 production are important.
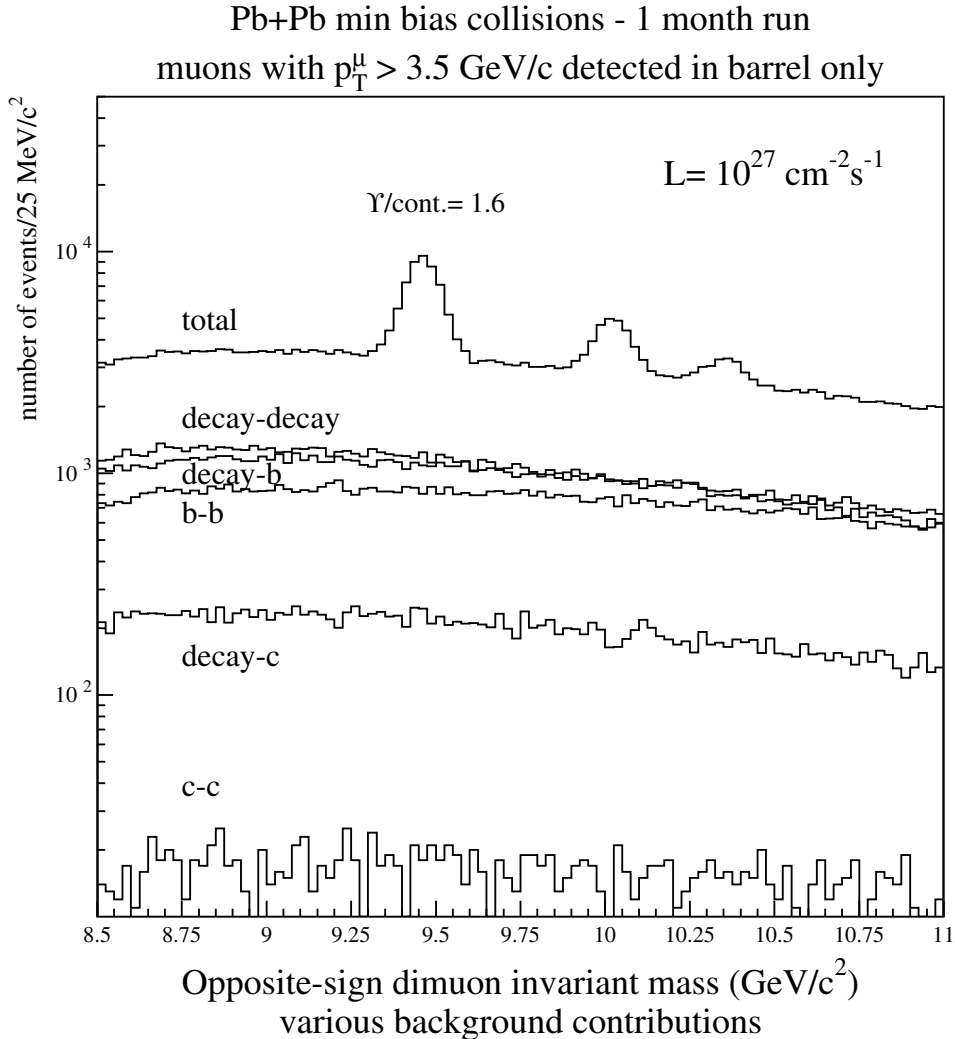
The pseudorapidity distributions of muons from the same set of processes are presented in Fig. 5.40. These

Table 5.16. Main contributions (%) to the dimuon mass spectrum in the mass region $M_\Upsilon \pm 50$ MeV/c^2 for Pb+Pb collisions (left) and Ca+Ca collisions (right)

Pb+Pb	Υ	π, K	$b\bar{b}$	$c\bar{c}$
Υ	61.8	0.0	0.0	0.0
π, K		13.4	12.8	2.6
$b\bar{b}$			7.2	0.0
$c\bar{c}$				0.0

Ca+Ca	Υ	π, K	$b\bar{b}$	$c\bar{c}$
Υ	94.3	0.0	0.0	0.0
π, K		2.7	1.8	0.1
$b\bar{b}$			0.5	0.0
$c\bar{c}$				0.0

Table 5.17. Υ/cont and statistics for Υ(left) and J/ψ (right)

Υ	Pb	Ca
Υ/cont	1.6	9.4
N_Υ/month	22000	340000
$N_{\Upsilon'}$/month	7500	115000

J/ψ	Pb	Ca
ψ/cont	1.0	9.7
$N_{J/\psi}$/month	10600	220000
$N_{\psi'}$/month	350	5800

Fig. 5.34. Opposite-sign dimuon mass spectra obtained for Pb+Pb collisions during one month, together with the different background contributions
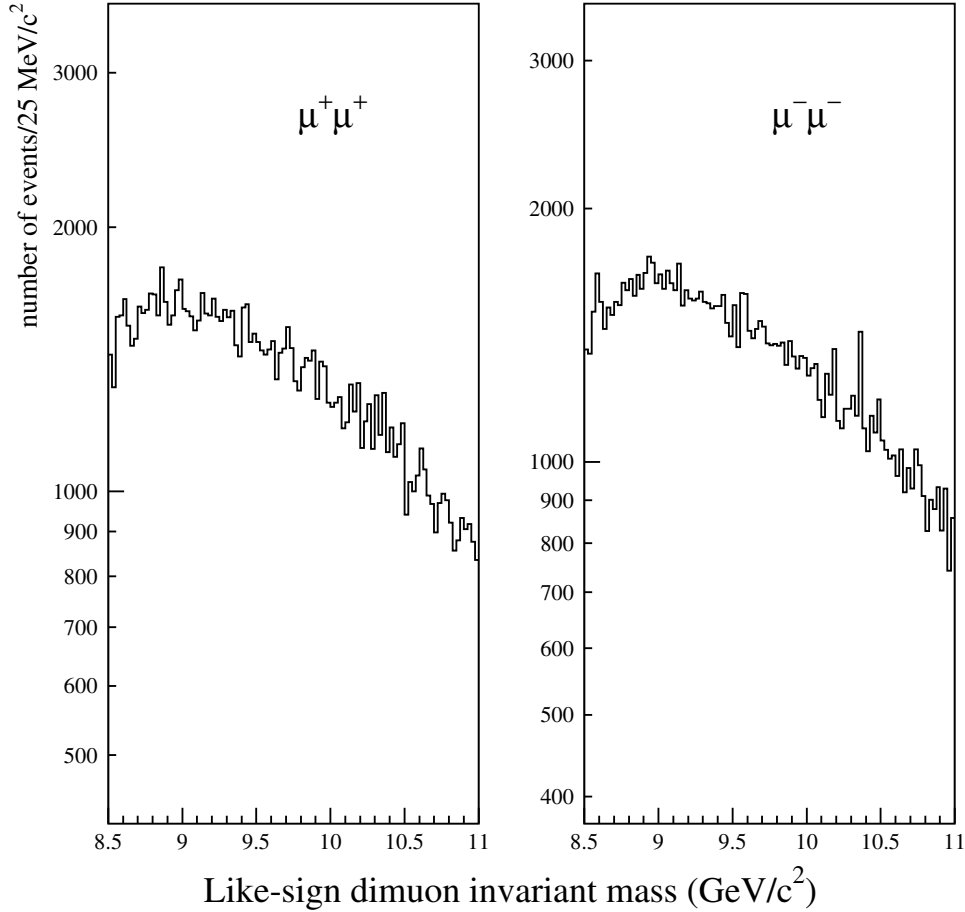
Fig. 5.35. Like-sign dimuon mass spectra obtained for Pb+Pb collisions during one month

distributions are essentially flat within the range of the CMS muon detector acceptance ($|\eta| \leq 2.4$).

5.7.2 Background from π/K decays

Important parameters needed to estimate the background contribution from pion and kaon decays are their multiplicities and transverse momentum distributions (especially the high p_T tails of the spectra). In our simulations we have used the HIJING Monte Carlo program [102]. The values of charged multiplicity density obtained for central and minimum bias Pb+Pb interactions are respectively: $(dN^{\pm}/dy)_{0<y<1} = 8300$ and $(dN^{\pm}/dy)_{0<y<1} = 1600$. As quoted in Section 5.5, the averaged transverse momenta of charged pions and kaons, $\langle p_T^{\pi} \rangle = 0.38$ GeV/c and $\langle p_T^K \rangle = 0.53$ GeV/c, are significantly lower than those obtained with the SHAKER parameterization: $\langle p_T^{\pi} \rangle = 0.48$ GeV/c and $\langle p_T^K \rangle = 0.67$ GeV/c [172,173]. Figure 5.41 presents the p_T and $|\eta|$ distributions of pions and kaons in minimum bias Pb+Pb colli-

sions, obtained from the HIJING event generator, for $p_T \geq 3.5$ GeV/c and $|\eta| \leq 2.5$, where the ratio $N_{K^{\pm}}/N_{\pi^{\pm}} = 0.25$.

The dependence of the number of Pb+Pb interactions as a function of the impact parameter b is shown in Fig. 5.42a. The mean impact parameter is equal to 11.4 fm. The number of nucleon-nucleon collisions and the pion/kaon multiplicity for $p_T \geq 3.5$ GeV/c and $|\eta| \leq 2.5$ strongly depends on b (Fig. 5.42b,c). The mean number of nucleon-nucleon collisions and the average π/K multiplicity are: $N_{col} = 260$ and $N_{\pi/K} = 5.3$.

In order to study dimuons of mixed origin as well as uncorrelated pairs from the same process, different number of events from processes 2 - 4 were superimposed on each Pb+Pb event according to the value of N_{col}. The probabilities ε^i of muon production from these processes per nucleon-nucleon collision, were obtained from the ratios of muon cross sections σ_{μ}^i and the nucleon-nucleon inelastic cross section σ_{pp} at $\sqrt{s} = 5.5$ TeV, $\varepsilon^i = \sigma_{\mu}^i/\sigma_{pp}$, with $\sigma_{pp} = 100$ mb. The simulation parameters were tuned to obtain the expected parameterization

Ca+Ca min bias collisions - 1 month run
muons with $p_T^\mu > 3.5$ GeV/c detected in barrel only

$L = 2.5 \times 10^{29}$ cm^{-2}s^{-1}
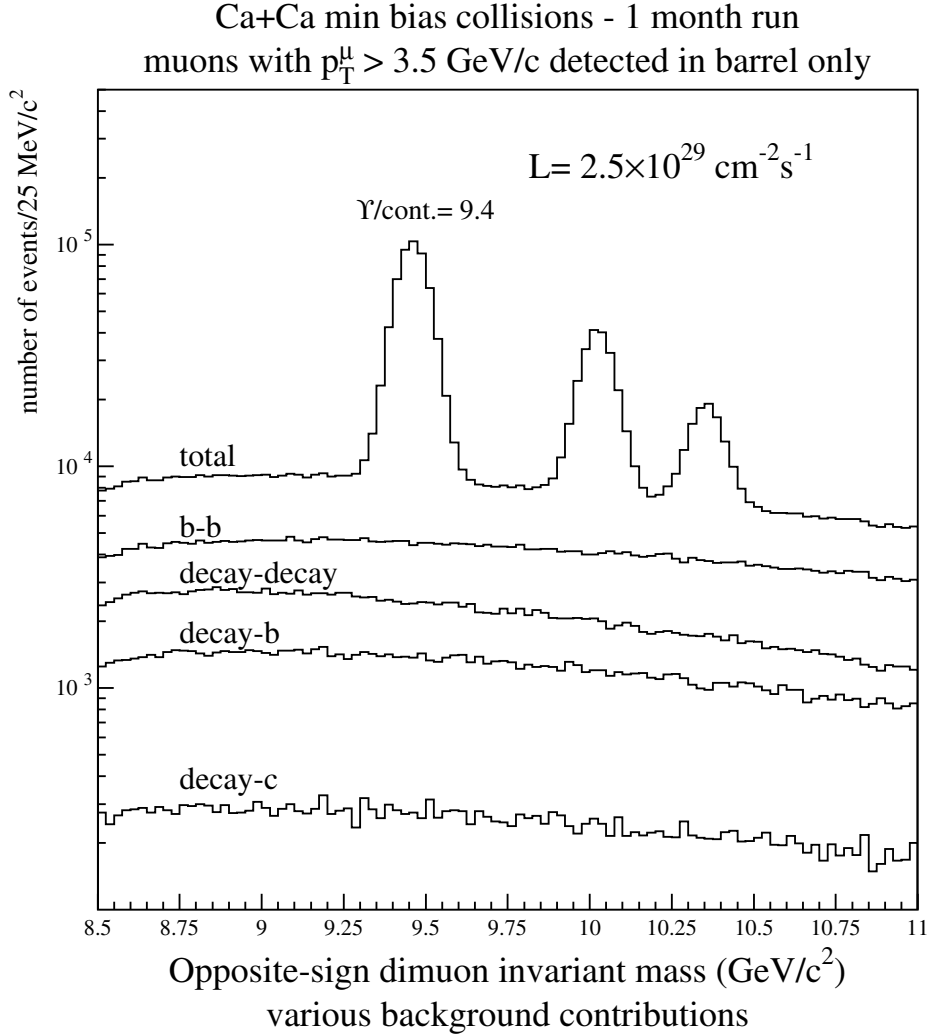
Υ/cont.= 9.4

Fig. 5.36. Opposite-sign dimuon mass spectra obtained for Pb+Pb collisions during one month, together with the different background contributions

$\sigma^i_{AA}(\mu) = A^2 \, \sigma^i_{pp}(\mu)$ for the muon production cross sections.

5.7.3 Invariant mass distributions of $\mu^+\mu^-$ pairs

We have studied invariant mass distributions of dimuons from processes 2 - 6. One month of running time for Pb+Pb interactions at a luminosity of 10^{27} cm^{-2}s^{-1} has been assumed. Table 5.18 presents the expected numbers of detected opposite-sign muon pairs with $M \geq 10$ GeV/c^2 from various background processes for muons with $p_T > 3.5$ GeV/c. Note that these numbers include uncorrelated pairs as well as mixed origin combinations. The contributions listed in the table add up to about 99% of all opposite-sign dimuons. The signal from $Z^0 \to \mu^+\mu^-$ decays was extracted within an interval $M_Z \pm 10$ GeV/c^2. The number of pairs decreases by a factor of 2.5-6.0 for various processes if only the barrel is used for muon detection. For the barrel, the mass distributions of muon pairs

Table 5.18. Number of opposite-sign muon pairs from various sources, in the full CMS detector and in the barrel alone for $p_T > 3.5$ GeV/c

Process	Full CMS	Barrel
Z^0	1.1 10^4	0.43 10^4
Drell-Yan	2.6 10^4	1.1 10^4
$b\bar{b}$	38 10^4	12 10^4
$c\bar{c}$	4.0 10^4	1.3 10^4
π/K decays	7.0 10^4	1.4 10^4
$b, \pi/K$	21 10^4	3.9 10^4
$c, \pi/K$	5.6 10^4	1.0 10^4
b, c	8.9 10^4	1.5 10^4

are concentrated at lower invariant masses compared to the full detector.

Pb+Pb min bias collisions - 1 month run
muons with $p_T^\mu > 3.5$ GeV/c detected in barrel only

L= 10^{27} cm^{-2}s^{-1}

SIGNAL dimuon invariant mass (GeV/c^2)
combinatorial background subtracted

Ca+Ca min bias collisions - 1 month run
muons with $p_T^\mu > 3.5$ GeV/c detected in barrel only

L= 2.5×10^{29} cm^{-2}s^{-1}

SIGNAL dimuon invariant mass (GeV/c^2)
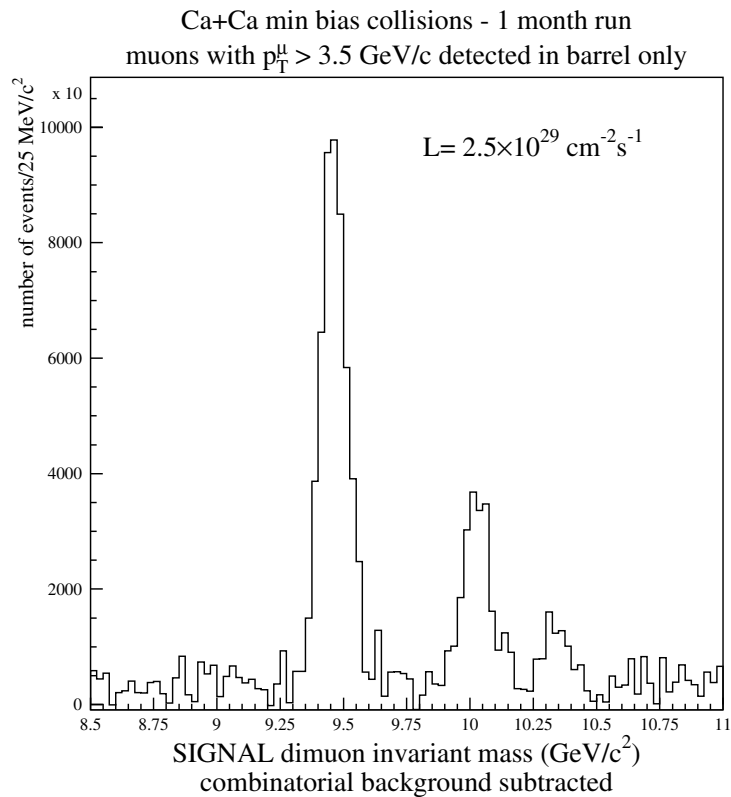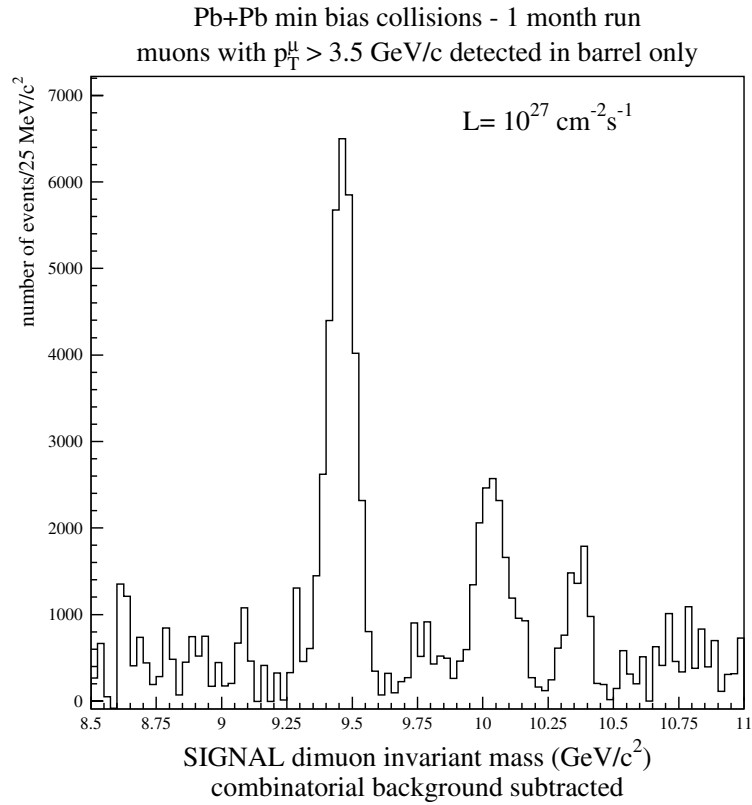combinatorial background subtracted

Fig. 5.37. Dimuon mass spectra after subtraction of uncorrelated background, for Pb+Pb collisions (*top*) and Ca+Ca collisions (*bottom*)
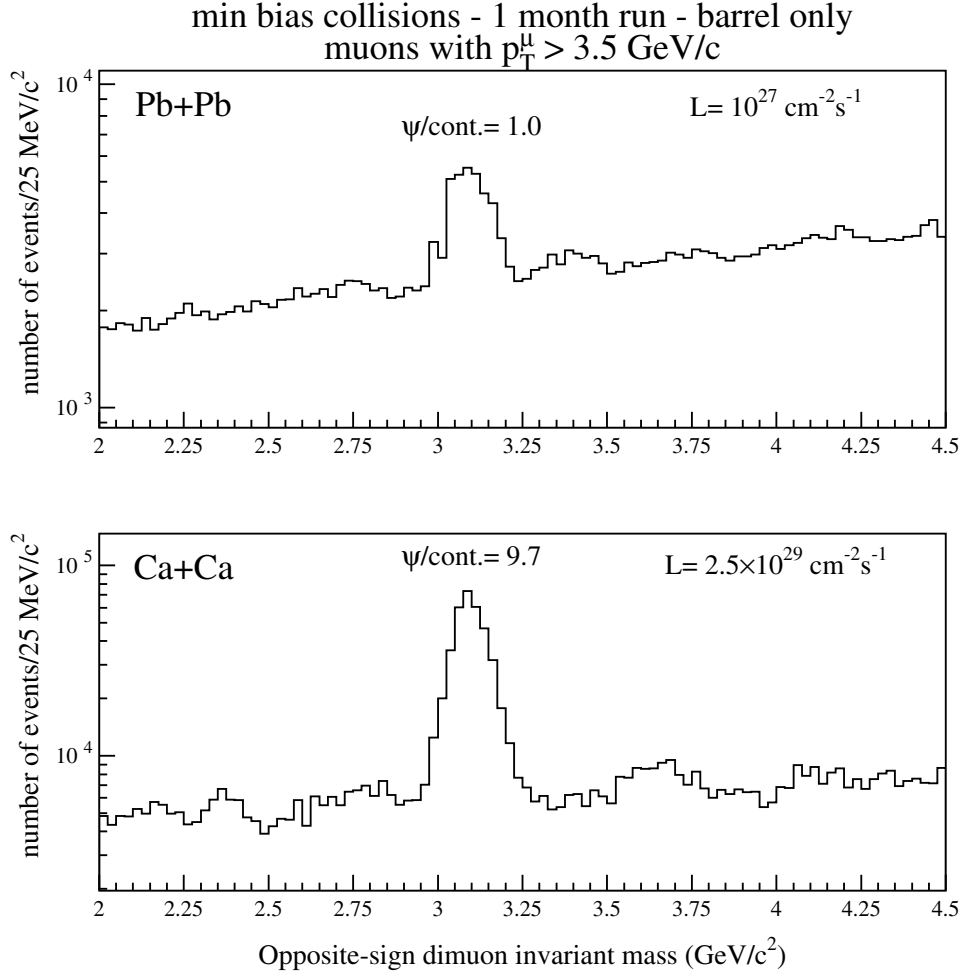
Fig. 5.38. Opposite-sign dimuon mass spectrum in the J/ψ mass range for Pb+Pb collisions (*top*) and Ca+Ca collisions (*bottom*)

Figure 5.43 presents $\mu^+\mu^-$ pair invariant mass spectra for muons with $p_T > 3.5$ GeV/c. A clear signal from decays is seen with a background lower than 5%. In the mass range 10 GeV/$c^2 \leq M \leq 70$ GeV/c^2 the dominant contribution comes from $b\bar{b}$ fragmentation ($\approx 43\%$). About 370000 $\mu^+\mu^-$ pairs from $b\bar{b}$ decays are expected. However, a significant fraction ($\approx 42\%$) of these dimuons come from uncorrelated $b\bar{b}$ pairs produced in different nucleon-nucleon collisions. Another important contribution is from mixed origin pairs, where one muon is from a b or $\bar{b}$ fragmentation and the other from a π/K decay (about 23%). Contributions from π/K decays alone and $c\bar{c}$ semileptonic decay are 8% and 5% respectively.

The background from π/K decays can be subtracted using same-sign dimuons as long as the contributions of opposite-sign and same-sign muon pairs are equal (see Fig. 5.44). The same is true for mixed origin pairs. Using either the subtraction procedures from (5.12) or $dN^{+-}/dM - dN^{++}/dM - dN^{--}/dM$ gives identical results, as the invariant mass distributions for $\mu^+\mu^+$ and

$\mu^-\mu^-$ pairs are equal within statistical errors. Figure 5.45 shows the difference of the invariant mass distributions between opposite-sign and same-sign muon pairs, and contributions of different sources to this difference. Only four processes ($b\bar{b}$, $c\bar{c}$, Drell-Yan and Z^0 production) contribute to the difference. In the mass range 10 GeV/$c^2 \leq M \leq 70$ GeV/c^2 the contribution from $b\bar{b}$ fragmentation is still dominant. The contributions from $c\bar{c}$ and Drell-Yan are nearly equal to each other in this mass interval.

The opposite-sign dimuon invariant mass distribution for muons with $p_T > 5$ GeV/c is presented on Fig. 5.46. The signal from $Z^0 \rightarrow \mu^+\mu^-$ decays is the same as for $p_T > 3.5$ GeV/c. The relative contribution from $b\bar{b}$ fragmentation in the mass range 10 GeV/$c^2 \leq M \leq 70$ GeV/c^2 increases to 54% (about 117000 pairs). The mixed origin contribution from b and π/K decays is reduced to 16% for $p_T > 3.5$ GeV/c relative to 23%. The contribution from π/K decays alone and $c\bar{c}$ semileptonic decays are 5% and 6% respectively.
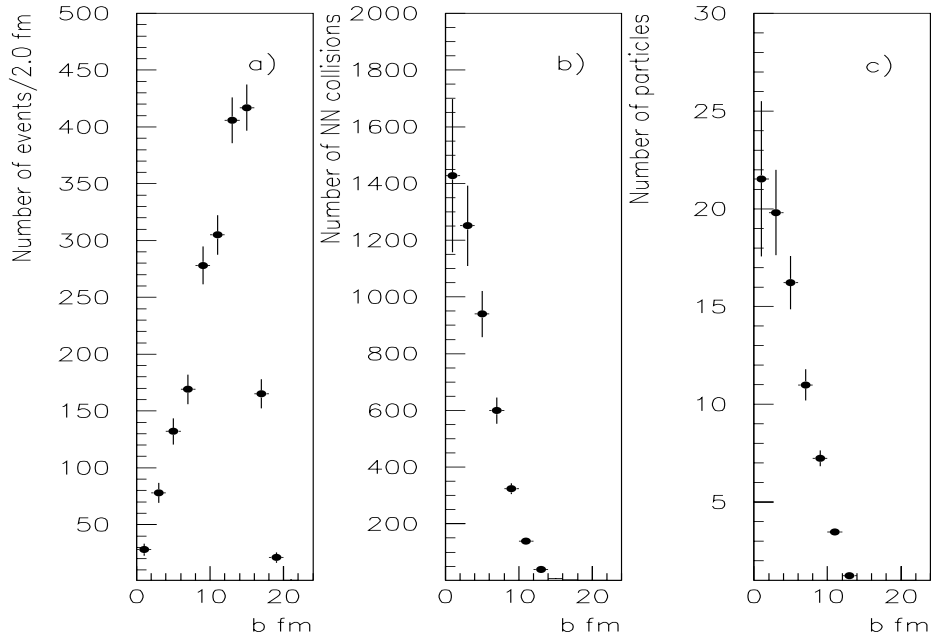
Fig. 5.42. Number of Pb+Pb events (**a**), number of nucleon-nucleon collisions (**b**) and pion/kaon multiplicity (**c**), all as a function of b
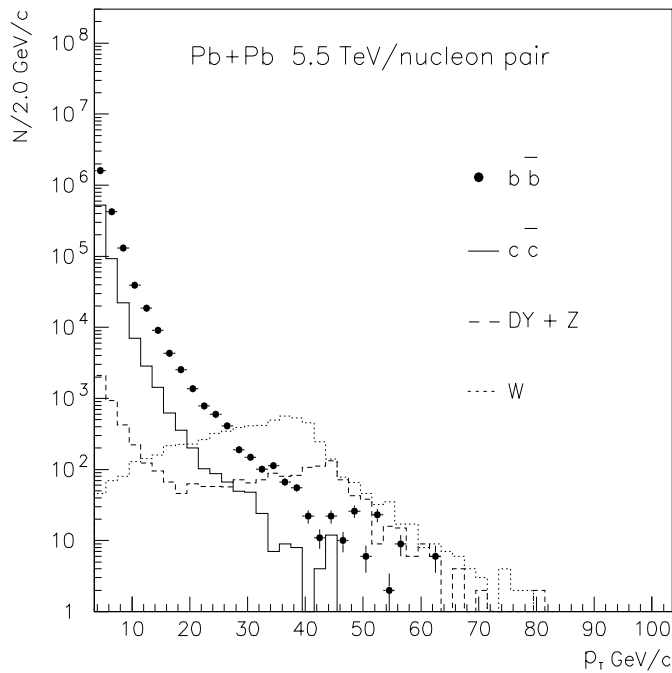

Fig. 5.39. Transverse momentum distribution of muons from various processes
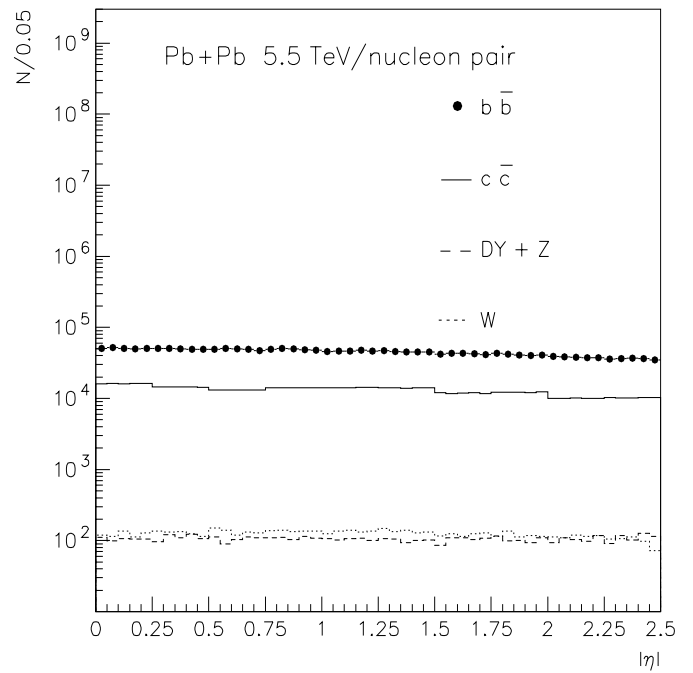
Fig. 5.40. Pseudorapidity distribution of muons

The dominant source of high invariant mass dimuon pairs is $b\bar{b}$ fragmentation. However, while travelling through dense matter, heavy quarks may be subject to significant energy loss resulting in a softening of their muon spectra. Thus, changes in the normalization and in the shape of the dimuon distributions in the 10 to 70 GeV/c^2 mass range as a function of the energy density in nucleus-nucleus collisions could be used to assess heavy quark energy loss.

Fig. 5.41. Transverse momentum and pseudorapidity distributions of pions and kaons in Pb+Pb collisions
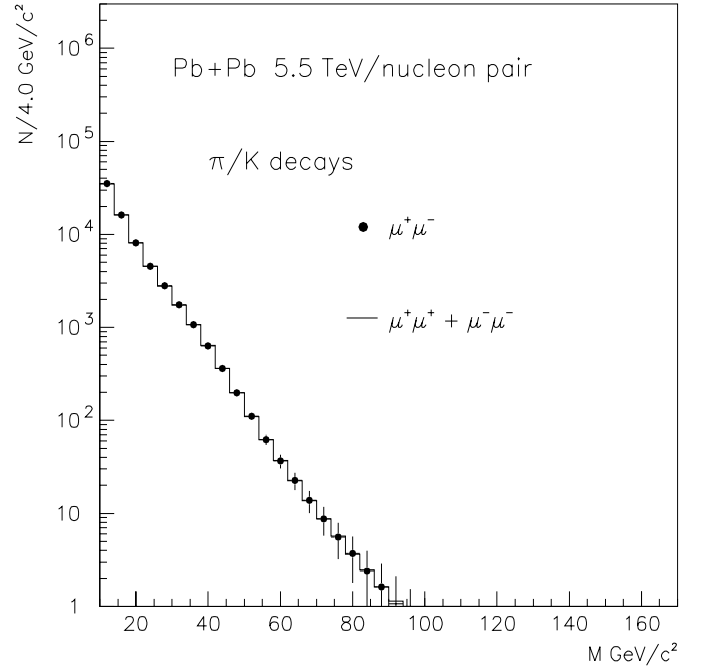
Fig. 5.44. Invariant mass distribution of opposite-sign and same-sign pairs from π/K decays
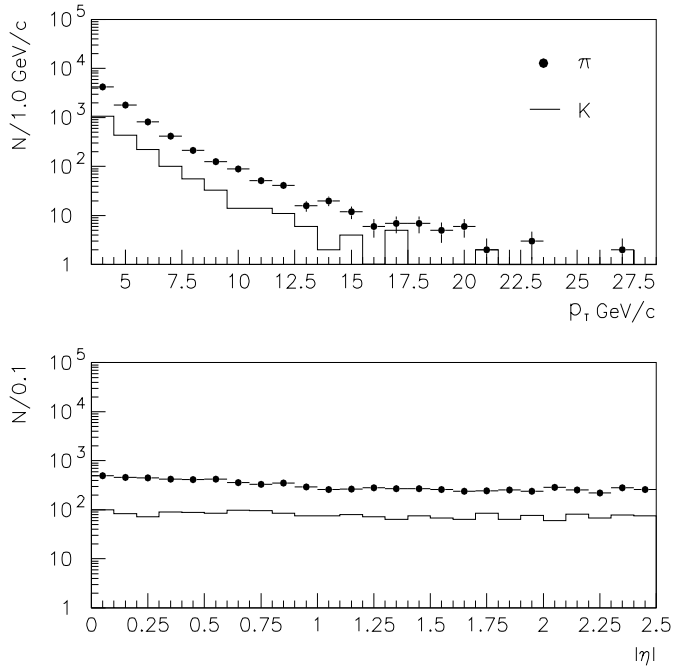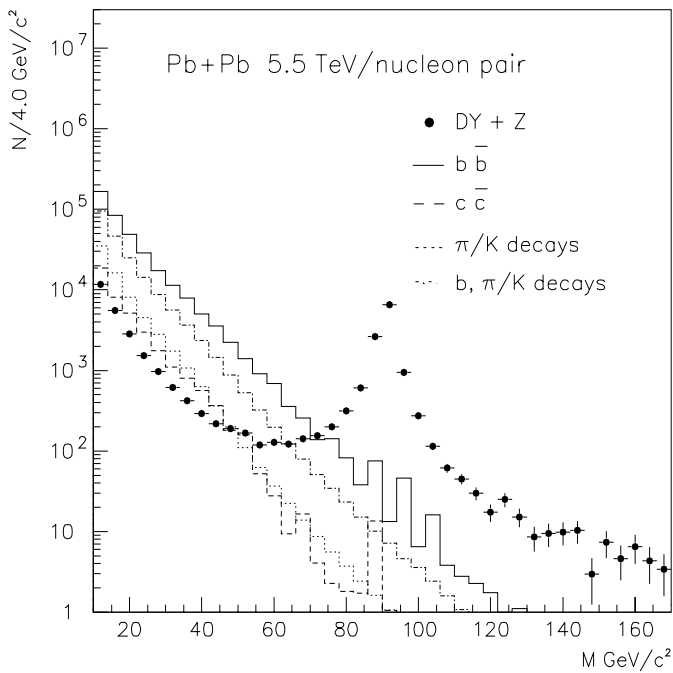

Fig. 5.43. Invariant mass distribution of $\mu^+\mu^-$ pairs for muons with $p_T > 3.5$ GeV/c
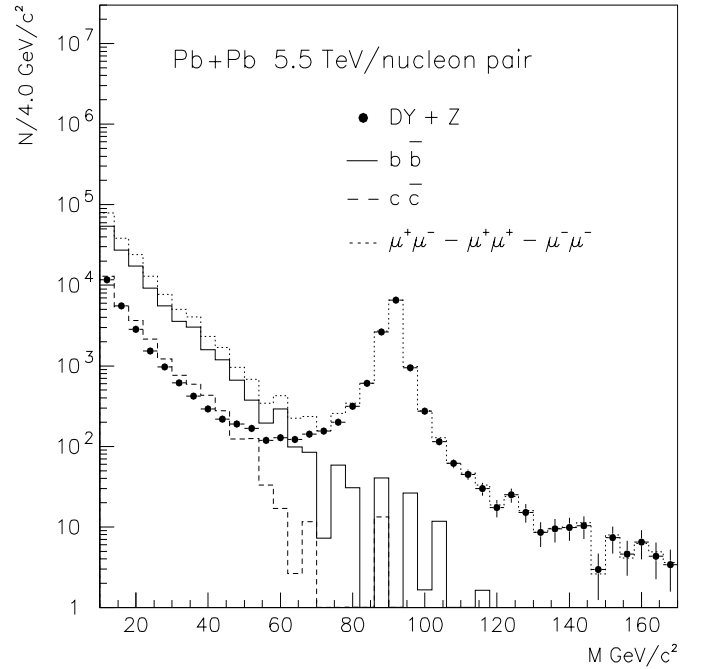
Fig. 5.45. Difference of the invariant mass distributions between opposite-sign and same-sign muon pairs

Our estimates do not take into account trigger efficiencies and data acquisition system capabilities. This will reduce the recorded event rates.

It should be noted that the results presented here differ from previous estimates [186] for the following reasons:

1. The value of α in the nucleus-nucleus cross section parameterization, $\sigma^i_{AA} \propto A^{2\alpha}$, has been changed from 0.95 to 1.0.
2. The K factors for processes 1-5 are now taken into account.
3. Uncorrelated muon pairs are now included in the analysis.

Fig. 5.46. Invariant mass distribution of $\mu^+\mu^-$ pairs for muons with $p_{\mathrm{T}} > 5$ GeV/c

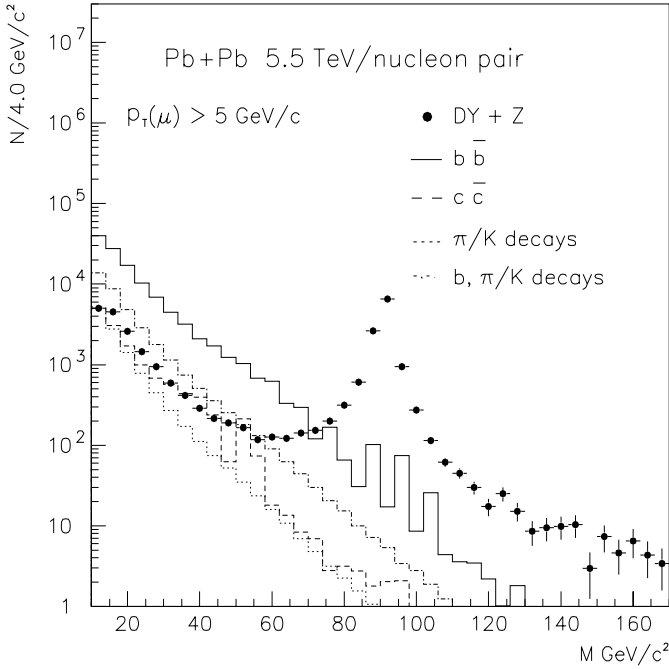4. The parameterization of the π and K transverse momentum distributions are now taken from HIJING.
5. The acceptance tables and reconstruction efficiencies are now calculated in more detail.

5.8 Z^0 reconstruction with the μ-chambers

5.8.1 Introduction

We present an evaluation of the CMS capability to identify and reconstruct Z^0 decays in the case where the track density is too large for the inner tracker to be fully efficient so that only muon chambers can be used. After briefly describing the algorithms to identify muons and reconstruct their trajectories in the barrel region of CMS, results will be given for the process $pp \rightarrow Z^0 + X \rightarrow \mu^+\mu^- + X$ in the framework of two scenarios:

1. $\sqrt{s}$=14 TeV with no background,
2. $\sqrt{s}$=5 TeV with a superposition of 207 pp events.

The second scenario is closer to experimental conditions expected for Pb+Pb collisions in CMS.

5.8.2 Muon identification

In the barrel region, muon identification and reconstruction are based upon four muon stations placed in the magnet return yoke at radial distances from the beam varying between approximately 3.8 m and 7.2 m. Each of the innermost three stations contains 8 planes of staggered drift tubes for the reconstruction of the (r, ϕ) coordinates and 4 planes for the reconstruction of the (r, z) coordinates,

while the outermost station only contains 8 planes in total, all dedicated to the the reconstruction of the (r, ϕ) coordinates. The spatial resolution in each layer is about 200 μm.

Reconstruction of the muon trajectory in the residual magnetic field of the return yoke provides an estimate of the muon momentum independent of the CMS inner tracker. The drift tubes also provide accurate timing information which is used for bunch-crossing identification. To improve the triggering capability, each muon station also contains planes of resistive plate chambers (RPC) which complement the timing information of the drift tubes.

Trajectories of muon candidates traversing the barrel region of CMS are reconstructed off-line by means of a two-step procedure.

1. In a first step muon track segments are formed in each station by searching for sets of hits which are aligned independently in the (r, ϕ) and (r, z) views. Ambiguities due to different track segments having common hits are solved by means of criteria based on hit multiplicity and least-square fits.
2. In a second step a technique based on Kalman filtering is used in order to associate track segments reconstructed in the (r, ϕ) and (r, z) views and/or in different stations to a single muon trajectory. A track is then identified as due to a muon candidate if it contains segments belonging to at least two different muon stations. The primary vertex constraint may be imposed in the track fitting procedure. This improves the momentum resolution for genuine prompt muons but may bias the momentum estimate of muons originating far from the beam interaction region.

The algorithm outlined above has been implemented in the CMS event reconstruction packages CMSIM (in FORTRAN) and ORCA (C++). The analysis described here is based on the CMSIM (version 115) program.

5.8.3 Reconstruction of $Z^0 \rightarrow \mu^+\mu^-$

The CMS capability to reconstruct $Z^0 \rightarrow \mu^+\mu^-$ with the barrel muon system was initially evaluated by generating events corresponding to the process $pp \rightarrow Z^0 + X$ at $\sqrt{s}$ =14 TeV followed by the decay $Z^0 \rightarrow \mu^+\mu^-$. Generation was based on PYTHIA while detector effects and event reconstruction were simulated by the CMSIM package. To identify muon candidates, it was required that muon tracks were formed in at least two muon stations (necessary for muon identification), implying an effective minimum momentum cut of about 3-5 GeV/c, taking into account the energy loss in the calorimeters and in the first layers of the iron return yoke. A primary vertex constraint was used to calculate the momentum of the muon candidate.

The Z^0 reconstruction efficiency and mass resolution were estimated by considering only events in which both muons were generated in the pseudorapidity region -0.8 < η < 0.8, covered by all four muon stations, and with invariant mass $M_{\mu\mu}$ >30 GeV/c^2. The results obtained are shown in Figs. 5.47 and 5.48. A reconstruction
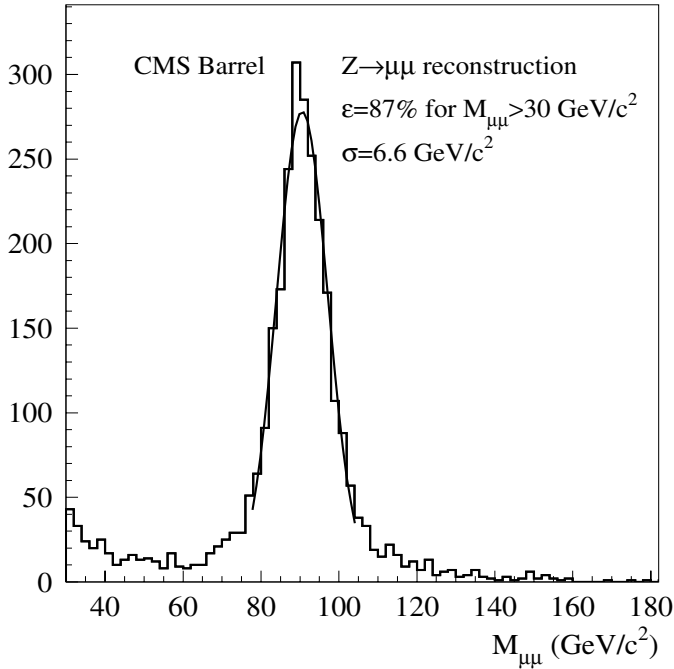
Fig. 5.47. Invariant mass distribution of the reconstructed $Z^0 \rightarrow \mu^+\mu^-$ in $pp \rightarrow Z^0 + X$ events at $\sqrt{s} = 14$ TeV. Both muons come from the pseudorapidity region $-0.8 < \eta < 0.8$. Only invariant masses $M_{\mu\mu} > 30$ GeV/c^2 are considered

efficiency of 87% was observed for $Z^0 \rightarrow \mu^+\mu^-$ while the invariant mass resolution at the Z^0 mass was found to be 5.0 GeV/c^2. The average momentum resolution for muon candidates from Z^0 decays and is 8.4%. These results are slightly better than those reported in the muon TDR [2] due to some software improvements.

In a modified approach for Pb+Pb collisions, the centre-of-mass energy for pp interactions was reduced to 5 TeV and a background of 207 minimum bias pp events was added to the primary process $pp \rightarrow Z^0 + X$. The acceptance for muon candidates was extended in pseudorapidity up to $|\eta| = 1.1$, corresponding to the region covered by at least two barrel muon stations. To clean up the sample of muon candidates from the minimum bias contribution, only muons with reconstructed transverse momentum above 5 GeV/c were considered. In addition, only muons of opposite charges were retained. The overall efficiency for Z^0 reconstruction in the considered angular region was found to be to 88.5% in this case.

Some results obtained in this second analysis are displayed in Figs. 5.50 and 5.51. The comparison with Figs. 5.47 and 5.48 shows that the CMS reconstruction capability for $Z^0 \rightarrow \mu^+\mu^-$ in the barrel region is not significantly affected by the presence of minimum bias events and by the lower centre-of-mass energy.

5.8.4 Summary

We have performed a Monte Carlo simulation of the processes contributing to dimuon continuum with $M \geq 10$ GeV/c^2 in Pb+Pb collisions at the LHC.

For $M \geq 80$ GeV/c^2, the dominant source is Z^0 production. Its production should not be affected by hadronic media, and could be used as a reference process for Υ studies [95,43] though there are some drawbacks:

1. The Z^0 mass is much larger than that of Υ resonances, and shadowing in the range $x \sim M/\sqrt{s}$, as well as other nuclear effects, can be different at $Q^2 = M_Z^2$ and $Q^2 = M_\Upsilon^2$.
2. Z^0 production is dominated by $q\bar{q}$ annihilation since the qg channel is only important for Z^0's with high transverse momentum, while Υ states are mainly produced via gluon-gluon fusion.

The study of transverse momentum distribution of the Z^0 and of Z^0+ jet events may turn out to be an important tool for understanding nuclear shadowing and energy loss of hard partons in dense matter (see Section 6.1.4). For this purpose it will be necessary to measure Z^0 and Z^0+ jet production in Pb+Pb and pp collisions at the same energy: 5.5 TeV.

For a one month of run at a luminosity 10^{27} cm^{-2}s^{-1}, the CMS detector will be able to detect about 11000 events of $Z^0 \rightarrow \mu^+\mu^-$ decays with less than 5% background. If only the barrel is used for the analysis, the detected number of Z^0 decays will be reduced to 4300 events.

When energy loss of heavy quarks is not taken into account, the transverse momentum distribution of single muons in the range 3.5 GeV/$c \leq p_T \leq 25$ GeV/c is dominated by open beauty production. In the invariant mass range 10 GeV/$c^2 \leq M \leq 70$ GeV/c^2 the main source of opposite-sign muon pairs is $b\bar{b}$ fragmentation. For muons with $p_T > 3.5$ GeV/c the expected number of $\mu^+\mu^-$ pairs is about 370000. Approximately 42% of these pairs come from uncorrelated $b\bar{b}$ production.

Since the muons from $b\bar{b}$ fragmentation are produced within jets, the background from Drell-Yan and π/K decay can be reduced using additional information from the hadronic and electromagnetic calorimeters [186]. Hence, the measurement of muon transverse momentum spectra and dimuon invariant mass distributions can be used to study energy loss of $b\bar{b}$ quarks in heavy ion collisions.

Reconstruction of $Z^0 \rightarrow \mu^+\mu^-$ without input from the inner tracker, has been studied in the case of pure pp collisions at $\sqrt{s} = 14$ TeV and Pb+Pb interactions. The reconstruction efficiency and Z^0 mass resolution were found to be similar in both cases.

6 Jet physics

6.1 Jet Physics in CMS heavy ion program

As discussed in Section 2.5, the energy lost by a fast parton traversing a dense medium can reveal certain characteristics of the medium. The amount of energy lost by a

Fig. 5.48. Distribution of difference between generated and measured invariant mass of reconstructed $Z^0 \to \mu^+\mu^-$ in $pp \to Z^0+ X$ events at $\sqrt{s} = 14$ TeV. Both muons are generated in the pseudorapidity region $|\eta| < 0.8$. Only masses $M_{\mu\mu} > 30$ GeV/c^2 are considered
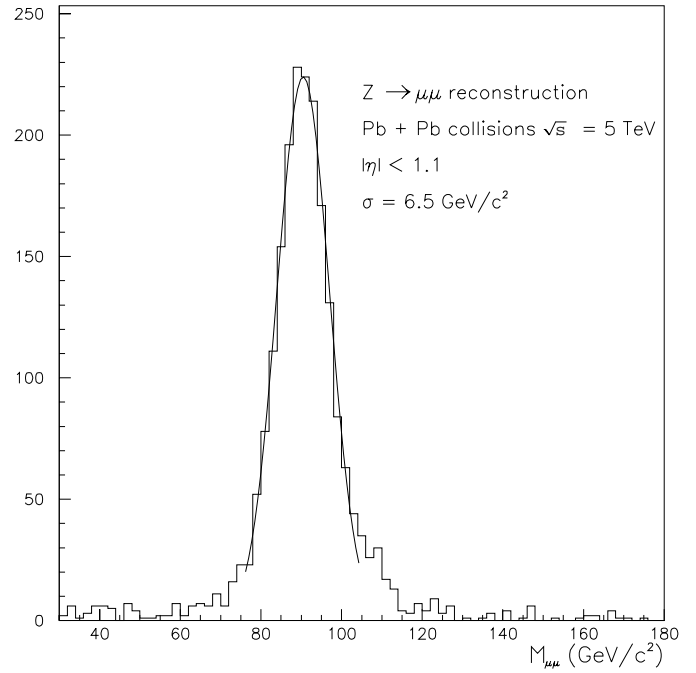
Fig. 5.50. Invariant mass distribution of reconstructed $Z^0 \to \mu^+\mu^-$ in the reaction Pb+Pb $\to Z^0+ X$ events at $\sqrt{s} = 5$ TeV simulated using a superposition of 207 minimum bias pp events
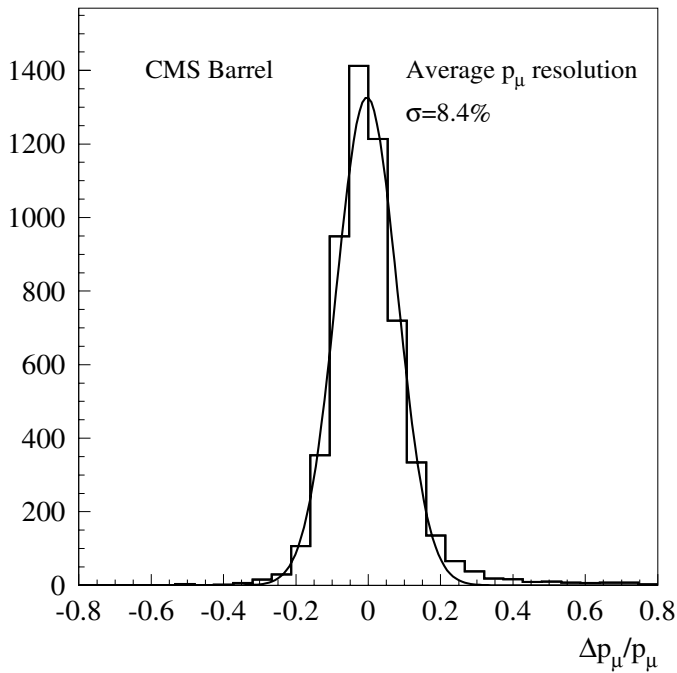
Fig. 5.49. Average muon momentum resolution obtained in $Z^0 \to \mu^+\mu^-$ decays in $pp \to Z^0+ X$ events at $\sqrt{s} = 14$ TeV. Both muons are generated in the pseudorapidity region $|\eta| < 0.8$. Only masses $M_{\mu\mu} > 30$ GeV/c^2 are considered
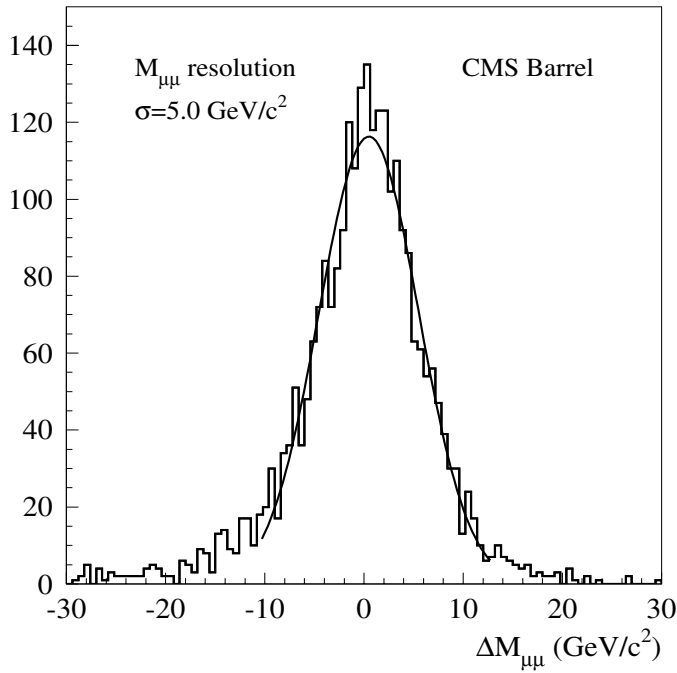

Fig. 5.51. Distribution of difference between generated and measured invariant mass of reconstructed $Z^0 \to \mu^+\mu^-$ in the reaction Pb+Pb $\to Z^0+ X$ events at $\sqrt{s} = 5$ TeV, simulated using a superposition of 207 minimum bias pp events

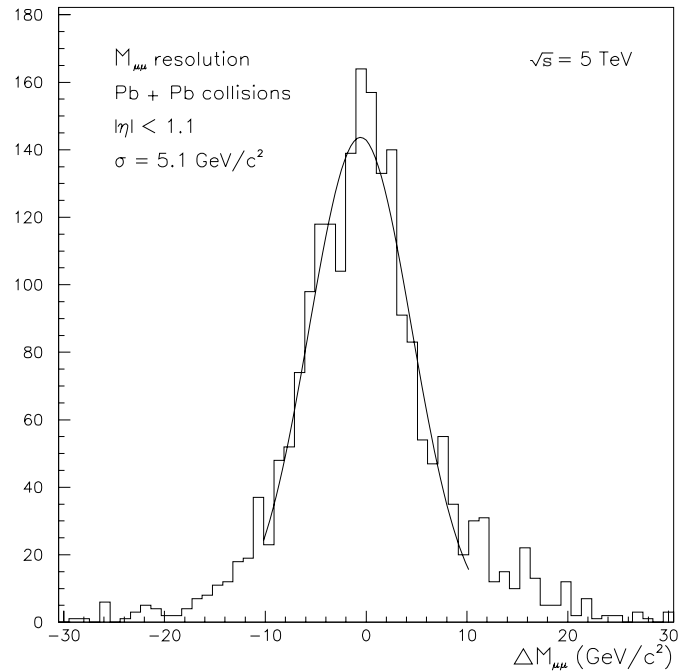jet, known as jet quenching, is different in a quark-gluon plasma than in normal nuclear matter.

In the search for experimental evidence of this medium-induced energy loss, a significant dijet quenching [92] and a corresponding enhancement of the monojet-to-dijet ratio [93] were proposed as possible signals of dense matter formation in ultrarelativistic nuclear collisions. The monojet-to-dijet ratio obtained for high E_T jets in CMS was described in Section 2.5.

Other possible ways to directly measure the energy loss involves tagging the hard jet opposite a particle that does not interact strongly such as a Z^0 [95] or a photon [96], both produced in the reactions $qg \to qV$ and $q\bar{q} \to gV$ where $V = Z^0$ or γ. For Z^0 production, we only consider the cases where the Z^0 is detected through its $\mu^+\mu^-$ decay. The advantage of this triggering is that one can determine the initial transverse momentum of the hard jet since $p_\mathrm{T}^\mathrm{jet} \approx p_\mathrm{T}^{\gamma, Z^0}$. In particular, one can study coherent effects in the QCD-medium since the dependence of $\mathrm{d}E/\mathrm{d}x$ on the initial jet energy or distance traversed can be studied by varying the energy of the tagged photon or Z^0 in the collisions of different nuclei.

All the above measurements will be needed to extract information about the properties of super-dense matter which will created in ultrarelativistic heavy ion collisions at the LHC.

6.1.1 Production rates as a function of the impact parameter of the collision

We study the dependence of jet + jet, γ + jet and Z^0+ jet rates on impact parameter in Pb+Pb collisions at $\sqrt{s} = 5.5A$ TeV.

The average number of hard processes h with one or two jets in the final state in an AA collision at impact parameter b with energy greater than E_T is a generalization of Eqs. (2.3) and (2.7) with p_0 replaced by E_T [32],

$$\bar{N}_{AA}^h(b, \sqrt{s}, E_\mathrm{T}) = T_{AA}(b)\sigma_{NN}^h(\sqrt{s}, E_\mathrm{T}) . \quad (6.1)$$

In this case, σ_{NN}^h is the hard production cross section in NN collisions calculated with PYTHIA [79]. When h is very rare, $\bar{N}_{AA}^h \ll 1$, (6.1) is a strongly increasing function of centrality, as shown in Fig. 6.1a for the differential probability of dijet production with $E_\mathrm{T}^\mathrm{jet} > 100$ GeV in the CMS acceptances, $|\eta| < 1.5$ and $|\eta| < 2.6$. However, the most interesting central collisions with $b \ll 2R_A$ represent only a few percent of the total inelastic AA cross section. The integrated and differential total inelastic cross sections are calculated from

$$\sigma_{AA}^\mathrm{in}(< b) = \int_0^b \mathrm{d}^2b \left[1 - \left(1 - \frac{1}{A^2} T_{AA}(b)\sigma_{NN}^\mathrm{in} \right)^{A^2} \right] (6.2)$$

$$\sigma_{AA}^\mathrm{in}(b \pm \Delta b) = \int_{b-\Delta b}^{b+\Delta b} \mathrm{d}^2b \left[1 - \left(1 - \frac{1}{A^2} T_{AA}(b)\sigma_{NN}^\mathrm{in} \right)^{A^2} \right] (6.3)$$

where the integrated cross section, (6.3), is in the interval from 0 to b, while the differential cross section is

the integral of the cross section within an interval $|\Delta b|$ of b. At 5.5 TeV, the inelastic non-diffractive nucleon-nucleon cross section is $\sigma_{NN}^\mathrm{in} \simeq 60$ mb. Figure 6.1b represents the integral Pb+Pb rate assuming luminosity $\mathcal{L} \simeq 10^{27}$ cm^{-2}s^{-1}. The total number of inelastic Pb+Pb interactions is about 8 kHz, but only $\sim 2.5\%$ of the events, ≈ 200 Hz, are at $b < 2.5$ fm.

The differential and integral dijet rates, $\sigma_{AA}^\mathrm{in}\bar{N}_{AA}^h\mathcal{L}$ over a one month Pb+Pb run, 1.3×10^6 s, are shown as functions of b in Fig. 6.1c,d respectively. The total number of dijets with $E_\mathrm{T}^\mathrm{jet} > 100$ GeV is 1.1×10^7 for $|\eta| < 2.6$. The number is reduced by a factor ~ 2 if only the barrel is considered, $|\eta| < 1.5$. Collisions with $b < 6$ fm contribute $\approx 50\%$ of the total dijet rate while only 15% of the dijets are produced in collisions with $b < 2.5$ fm.

If the luminosity has to be shared between two experiments, the integrated luminosity of each experiment will be about one third or one quarter of the design one. In this case, the expected statistics will still be large enough to study the dijet rates as a function of b. Note that increased transverse energy deposition in the barrel, endcap and very forward parts of the CMS calorimeters is expected to be correlated with decreasing impact parameter in nucleus-nucleus collisions, thus giving us a tool for measuring the centrality of the collision and select the most central events with the off-line E_T trigger [166]. The suppression of dijet rates (jet quenching) due to energy loss by hard partons can be much stronger in very central relative to peripheral collisions. The experimental observation of a dramatic change in the impact parameter dependence and absolute values of the dijet rates in heavy ion collisions compared to independent nucleon-nucleon interactions could indicate the existence of medium-induced multiple parton scattering.

Figure 6.2 shows the differential and integral rates of γ+ jet (a,b) and Z^0+ jet (c,d) production obtained by the dijet method. The curves in Fig. 6.2c,d are rescaled to the corresponding cross section. We find 7800 (3900) γ+ jet events and 180 (120) Z^0+ jet events with $E_\mathrm{T}^{\mathrm{jet},\gamma}, p_\mathrm{T}^{Z^0} > 100$ GeV at $|\eta| < 2.6$ (1.5) respectively. Such statistics are rather low compared to dijet production, especially for the Z^0+ jet channel. When only a small number of events are produced, the energy loss effect may be enhanced in these processes by measuring the distribution of differences in transverse energy between the γ and jet or between the transverse momentum of the Z^0 and the transverse energy of the jet in the most central heavy ion collisions.

6.1.2 Triggering on dijet and γ + jet events

An estimate of the Level 1 single jet and electron/photon trigger rates in Pb+Pb collisions has been made [187] using the CMS Technical Proposal Trigger algorithms developed for pp collisions in the CMS detector. A parameterization of HIJING estimates of the soft particle background has been used for different multiplicities. The dominant contribution to the trigger rate comes from the single jet trigger, which uses the transverse energy sums, electromagnetic and hadronic, computed in the fixed calorimeter
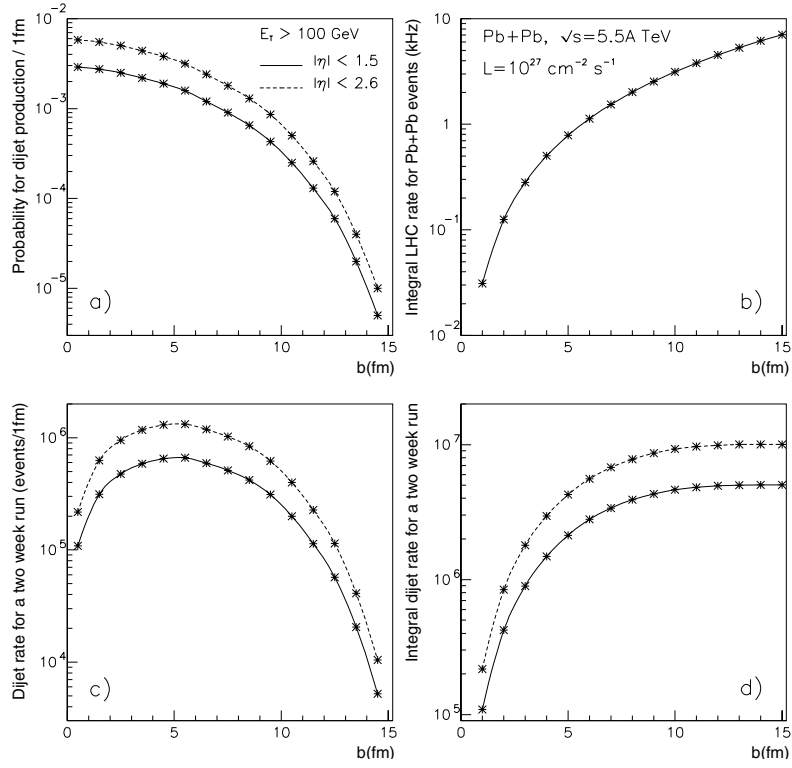
Fig. 6.1. Predictions of dijet production with $E_T^{\text{jet}} > 100$ GeV, $|\eta| < 1.5$ and $|\eta| < 2.6$ in Pb+Pb collisions at $\sqrt{s} = 5.5$ TeV as a function of impact parameter. **a** Probability of dijet production at b, **b** integral LHC rate for Pb+Pb collisions at luminosity $\mathcal{L} = 10^{27}\text{cm}^{-2}\text{s}^{-1}$, **c** and **d** differential and integral dijet rates expected in a two week run

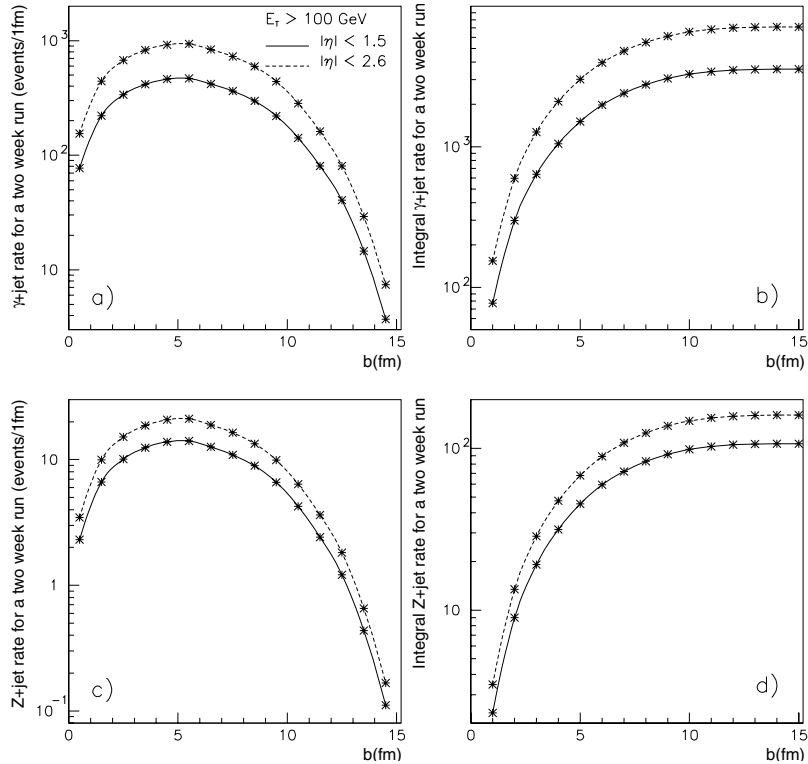**Fig. 6.2.** The differential and integral rates of initially produced $\gamma+$ jet **a**–**b** and Z^0+ jet **c-d** pairs with $E_T^{\text{jet},\gamma}, p_T^{Z^0} > 100$ GeV, $|\eta| < 1.5$ and $|\eta| < 2.6$ in Pb+Pb collisions at $\sqrt{s} = 5.5$ TeV and $\mathcal{L} = 10^{27}\text{cm}^{-2}\text{s}^{-1}$ as a function of impact parameter

region $\Delta\eta \times \Delta\phi = 0.348 \times 0.348$ with 4×4 trigger cells. For a threshold of 40 - 50 GeV it gives an acceptable output rate of about 400 - 200 Hz and is fully efficient for jets with transverse energy greater than 50 GeV produced in the most central collisions. For events with large impact parameter it is fully efficient for jets above $\simeq 100$ GeV. Assuming that with the higher level trigger, the full jet reconstruction is possible with the algorithms developed in [94,188,189] and the rate can be further reduced to a level lower than 10 Hz for jets with reconstructed transverse energy larger than 100 GeV.

A new scheme for the L1 jet triggers recently proposed uses a sliding window of 12×12 trigger towers, equivalent to cone size $\simeq 0.6$. It may be possible to perform a simple jet shape analysis in this scheme. In this case we do not expect degradation of the jet trigger performance for heavy ion collisions. The rate evaluation for this new jet trigger scheme is under study.

The CMS electron/photon trigger algorithm [190] is suitable for triggering highly energetic photons produced in heavy ion collisions. Programmable thresholds on cluster variables used in the algorithm may be tuned to make the trigger efficient even with 100% occupancy of the trigger cells, as expected in central Pb+Pb collisions. The rate of the single photon trigger is estimated to be less than 1 Hz for a 50 GeV threshold. With such a threshold, the trigger efficiency is close to 100% for the $\gamma+$ jet events useful for off-line analysis. More details on the tuning of the e/γ trigger for heavy ion collisions can be found in [187] and in Section 6.2.

6.1.3 Jet recognition and resolution in central Pb+Pb collisions

The study of jet characteristics in heavy ion collisions is difficult because of the "false" jet background – fluctuations of the transverse energy flow arising from a large multiplicity of "soft" secondary particles. Various estimates give from 3000 to 8000 charged particles per rapidity unit in a central Pb+Pb collision. Under these conditions, the reconstruction of "true" QCD jets resulting from hard parton-parton scattering is difficult. The optimization of the jet-finding algorithm in heavy ion collisions with CMS conditions has been investigated in [94,98, 188,189,191]. The interaction cross section for Pb+Pb collisions is about 7.6 b, leading to an event rate of 7.6 kHz. In the following, only central Pb+Pb collisions with reduced impact parameter $b_r = b/b_{\max} < 0.3$ are considered.

In order to study the recognition of different transverse energy jets in central Pb+Pb collisions, the production cross section of high transverse momentum jets in minimum bias nucleus-nucleus collisions was extrapolated from that in pp interactions at $\sqrt{s} = 5.5$ TeV using the parameterization $\sigma_{AA} = \sigma_{pp}A^{2\alpha}$ with $\alpha = 1$. The QCD jet production cross section in pp collisions was obtained using PYTHIA [79] with default structure functions CTEQ2L and a k factor of 1.

To estimate the influence of the large number of secondary particles on jet recognition in central Pb+Pb colli-

sions, the high transverse momentum QCD jet events were superimposed on the soft background. It is then necessary to know the multiplicity of soft particles, mainly pions and kaons, and their transverse momentum distributions, especially in the high p_T tail of the spectra. We assume that the number of charged particles emitted per unit of rapidity with $b_r = 0$ and at $y = 0$ is $dN^{\pm}/dy = 8000$, the upper limit of most theoretical expectations. The ratios $N_{\pi^0}/N_{\pi^\pm} = 0.5$ and $N_{K^\pm}/N_{\pi^\pm} = 0.2$ were used independent of impact parameter. The pseudorapidity distributions of π and K mesons were obtained from HIJING [102] and can be described by the sum of two Gaussian functions.

The transverse momentum distributions of particles produced in heavy ion collisions obtained from HIJING is softer than in pp interactions due to jet quenching. However, we took harder spectra to be conservative in our estimates. The pion p_T distribution was parameterized as [192,193]

$$\frac{dN_\pi}{dp_T^2} = \begin{cases} A\exp(-\sqrt{M_\pi^2 + p_T^2}/T) & \text{for } p_T < p_T^{\lim} \\ B(1 + p_T/p_T^0)^{-n} & \text{for } p_T > p_T^{\lim} \end{cases} \quad (6.4)$$

where $B = A(1 + p_T^{\lim}/p_T^0)^n \exp(-\sqrt{M_\pi^2 + (p_T^{\lim})^2}/T)$. The K transverse momentum spectra are obtained from the pion distribution

$$\frac{dN_K}{dp_T^2} = \left(\frac{\sqrt{M_\pi^2 + p_T^2} + 2)}{\sqrt{M_K^2 + p_T^2} + 2}\right)^m \frac{dN_\pi}{dp_T^2} . \quad (6.5)$$

The parameters are extracted from a fit to the pion and kaon transverse momentum distributions in pp interactions from PYTHIA. We find $T = 0.16$ GeV, $p_T^0 = 0.74$ GeV/c, $p_T^{\lim} = 0.5$ GeV/c, $n = 7.2$ and $m = 12.3$.

The jet recognition efficiency and expected production rates were studied for the barrel calorimeters, $|\eta| \leq 1.5$, with the detector response modelled using the CMSJET program [163]. The modified UA1-type [194] jet finding algorithm was used in $\eta - \phi$ space. After finding a preliminary set of clusters, the merging/splitting procedure was applied for overlapping clusters. Two clusters were merged into one jet if more than 75% of the transverse energy of the cluster with smaller E_T was contained in the overlap region. The direction and the energy of the new jet was then recalculated. If less than 75% of the E_T was contained in the overlap region, the clusters were split into two separate jets.

The jet finding procedure was applied at three different stages of the simulation: at the parton level; at the particle level with all final state particles except neutrinos taken into account without momentum smearing; and at the calorimeter level for the same QCD jet event superimposed on the soft particle background. Results from the first two steps were used for the estimate of jet characteristics at the generator level and for the optimization of the jet finding algorithm for heavy ion collision simulation (the third step). In order to reduce the contribution from false jets originating from fluctuations in the large transverse energy flow of non-jet particles in central Pb+Pb
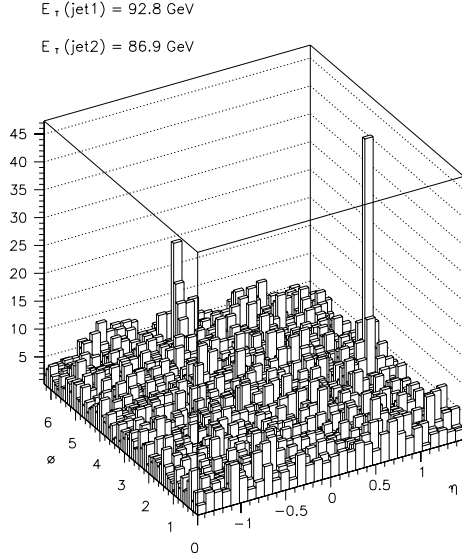
E_T (jet1) = 92.8 GeV

E_T (jet2) = 86.9 GeV

Fig. 6.3. The sum of the transverse energy deposition in the electromagnetic and hadronic calorimeter cells for a high E_T dijet event

Fig. 6.4. Distributions of differences in transverse energy, pseudorapidity and azimuthal angle between the simulated and reconstructed jets with $R_{\mathrm{jet}} = 0.3$ and $E_T^{\mathrm{jet}} \geq 100$ GeV (P_1, P_2 and P_3 are the constant, mean and standard deviation respectively of a Gaussian fit)

Table 6.1. Ratio of reconstructed to simulated jet numbers, ϵ_1, contribution of "false" jets, ϵ_2, and transverse energy resolution of jets with E_T larger than $E_{T,\min}$

$E_{T,\min}$ (GeV)	ϵ_1	ϵ_2	$\sigma(E_T)/E_T(\%)$
50	0.94 ± 0.03	0.120 ± 0.030	16.7
100	1.03 ± 0.02	0.010 ± 0.004	11.6
150	0.98 ± 0.02	0.004 ± 0.003	9.2
200	0.99 ± 0.02	0.004 ± 0.003	8.6

collisions, it is necessary to use a narrow jet cone radius, $R = \sqrt{(\Delta\eta)^2 + (\Delta\phi)^2} = 0.3 - 0.5$, in the jet finding algorithm. We note that in pp interactions about 80% of the high E_T, ≈ 100 GeV, jets are contained within the radius $R \sim 0.3$ [195,196].

For heavy ion collisions, before applying the jet finding algorithm, a simple iterative procedure was used to determine the average transverse energy of electromagnetic and hadronic calorimeter cells. All cells with transverse energy greater than $E_T^{\mathrm{cell}} > 3\langle E_T^{\mathrm{cell}}\rangle$ were excluded from the calculation of the average transverse energy and the resulting value of $\langle E_T^{\mathrm{cell}}\rangle$, multiplied by a factor κ, was subtracted from each cell. We find $\kappa \sim 1$ to be a good match between the generated and the reconstructed jet characteristics.

Figure 6.3 presents the sum of the transverse energy depositions in electromagnetic and hadronic calorimeter cells for two high E_T jets in a central Pb+Pb collision. Although the fluctuations of the transverse energy flow are rather large, jets are still clearly visible over the background. The distributions of the difference in the transverse energy, pseudorapidity and azimuthal angle between the simulated and the reconstructed jets are shown in Fig. 6.4 for jets with cone radius $R = 0.3$ and transverse energy $E_T \geq 100$ GeV. The precision of the reconstruction of the η and ϕ position of the jets, $\sigma(\eta)/R \approx 10\%$ and $\sigma(\phi)/R \approx 6\%$, is slightly better than for the transverse energy, $\sigma(E_T)/E_T \approx 12\%$.

Table 6.1 presents the ratios of reconstructed to simulated jet numbers, the relative contribution of "false" jets and the transverse energy resolution for jets with different transverse energies. The ratio, ϵ_1, of reconstructed to simulated jets is very close to unity. Note that due to the finite jet energy resolution and the sharp decrease of the initial dijet spectrum with energy, ϵ_1 can be greater or

less than 1. The probability, ϵ_2, of "false" jet detection is $12 \pm 3\%$ for $E_T \geq 50$ GeV and becomes negligible for higher transverse energies. The resolution in jet transverse energy improves from 16.7% for $E_T \geq 50$ GeV to 8.6% for $E_T \geq 200$ GeV. For jet transverse energies lower than 50 GeV, the background contribution increases rapidly and the energy resolution is worse.

Another (window-type) jet finding algorithm was also developed in [98,189] to search for "jet-like" clusters above the average energy. This algorithm is used in the study of the $\gamma+$ jet channel and described in Section 6.2.

6.1.4 Z^0 + jet and γ + jet channels

The dominant channels for high transverse momentum Z^0+ jet and $\gamma +$ jet production are $q + g \rightarrow q + Z^0(\gamma)$. Thus the bulk of detected jets have at least one initial quark, allowing the study of quark energy loss, contrary to gluon-dominated dijet production. However, it is important to note that due to initial state gluon radiation and finite energy resolution of the calorimeters, the transverse

momenta of the Z^0 or γ and the jet are exactly equal and opposite only on average, without energy loss, but not for each given event. The relatively broad symmetric distribution of differences in transverse momentum between the Z^0 or γ and the jet emerges already at the parton level, but the average value of this distribution is zero without energy loss. An asymmetric shape appears if a jet loses energy since the average value of the distribution is equal to the average energy loss of the quark-initiated jet at a given energy detection threshold, $\langle p_{\mathrm{T}}^{Z^0,\,\gamma} - p_{\mathrm{T}}^{\mathrm{jet}} \rangle = \langle \Delta E_q^{\mathrm{jet}} \rangle$. Note that we do not measure the energy loss of a leading quark by this method, but rather obtain the total loss by quark-initiated jets outside the given jet cone.

The detection of Z^0+ jet events was studied for jets with $E_{\mathrm{T}} > 50$ GeV in the pseudorapidity range $|\eta| < 3.0$. We expect about 900 events in a two week run with a background of less than 10%. In contrast, we expect 12000 Z^0+ jet events in Ca+Ca collisions over the same period even for an order of magnitude less than design luminosity.

The possibility of observing energy loss by quark-initiated jets in dense QCD-matter using the $\gamma+$ jet channel in heavy ion collisions have been investigated [189]. The details are presented in the next section.

6.2 Observation of energy loss in the $\gamma+$ jet channel

As pointed out in the previous section, one may perform a direct jet energy loss measurement in processes where a hard parton jet is tagged by an "unquenched" (*i.e.* not strongly interacting) particle such as a Z^0 or γ. Since the dominant channel for high p_{T} $\gamma+$ jet production is $q+g \rightarrow q+\gamma$, the bulk of the detected jets are quark-induced.

6.2.1 Signal and background cross sections in Pb+Pb collisions

The background for the $\gamma+$ jet channel is hard dijet production when one of the jets in an event is misidentified as a photon. The leading π^0 in the jet is the main source of misidentification. Cross sections for jet + jet and $\gamma+$ jet production in Pb+Pb collisions were obtained from those in pp interactions at $\sqrt{s} = 5.5$ TeV using PYTHIA 5.7 [79] assuming

$$\sigma_{AA} = \sigma_{pp} A^{2\alpha}, \quad \alpha = 1 . \tag{6.6}$$

Cross sections for the signal and background are plotted in Fig. 6.6 as a function of the lower limit on transverse momentum $\hat{p}_\perp$ defined in the rest frame of the hard interaction, CKIN(3) in PYTHIA. The pseudorapidity interval is $|\eta| < 2.6$.

In previous studies it was found that jets with transverse energies greater than 100 - 120 GeV can be effectively reconstructed in Pb+Pb collisions [94,188]. Figure 6.7 shows the transverse energy spectra of the photon signal and the leading pion from the jet + jet background for events with $\hat{p}_\perp > 100$ GeV and $|\eta| < 2.6$. The histograms are normalized to the expected number of events

from a two week Pb+Pb run at $\mathcal{L} = 10^{27} \mathrm{cm}^{-2} \mathrm{s}^{-1}$ assuming one experiment. There are 7800 signal events and 1.1×10^7 background events. One can see that for events with $E_{\mathrm{T}} > 100$ GeV the background is still dominant.

One indication of jet energy loss in the dense matter created in heavy ion collisions is the difference between the transverse energy of the photon and the recoiling jet in the event

$$\Delta E_{\gamma-\mathrm{jet}} = E_{\mathrm{T}}^\gamma - E_{\mathrm{T}}^{\mathrm{jet}} . \tag{6.7}$$

The difference between a γ or leading π^0 and a recoiling parton, p, $\Delta E_{\gamma/\pi^0-p}$ is shown in Fig. 6.8 at the parton level and without jet quenching for the signal and background with $E_{\mathrm{T}}^{\mathrm{parton}} > 120$ GeV and $|\eta^{\mathrm{parton}}| < 1.5$. The histograms are normalized to the expected number of events: 1854 signal and 5927 background. We only consider the barrel calorimeter here.

In the next sections we discuss the detector aspects of the measurement such as a jet and photon identification and measurement in Pb+Pb collisions as well as background suppression criteria.

6.2.2 Photon triggering, identification and measurement

The results presented in this section were obtained with a full GEANT simulation of the CMS calorimetry using the CMS114 package [5]. We consider Pb+Pb collisions with $\mathrm{d}N^\pm/\mathrm{d}y = 8000$.

The CMS electron/photon Trigger Algorithm, [190] and Fig. 6.9, is suitable for triggering on energetic photons produced in heavy ion collisions. Programmable thresholds on cluster variables used in the algorithm have to be tuned to make it efficient even for the case of 100% occupancy of the trigger cells. We have estimated the thresholds of the two Algorithm Vetoes: Hadronic Veto and Neighbour E_{T} Veto (see Fig. 6.9). Figure 6.10a,b shows the distribution of variables $\sum_5$ Neighbours E_{T} (a) and H/E (b) used in these Vetoes. Thresholds optimized for pp collisions (1-2 GeV on $\sum_5$ Neighbours E_{T} and 5% on H/E) have to be increased up to 22-25 GeV and 40-50% respectively to retain a high efficiency algorithm.

Apart from the trigger selection, we have considered possible photon identification based on the calorimeter isolation or zero suppression criteria. The energy of the photon may be measured in a cell of 5×5 crystals (size of the trigger cell) centred on the highest response [197]. Such a cell contains about 97% of the photon energy [198]. Identification may be based on the cut on transverse energy E_T^{isol} deposited in a larger area of 3×3 or 5×5 such cells not including the central one. Distributions of $E_T^{\mathrm{isol}}(5 \times 5)$ and $E_T^{\mathrm{isol}}(3 \times 3)$ are shown in Fig. 6.11a,b. The distributions are shown for the energy deposited in the electromagnetic calorimeter only and in the total ECAL + HCAL system. One can see that only about 6% of the transverse energy in the isolation area is measured by the hadron calorimeter, reflecting the softness of the charged particle spectrum.

The zero suppression criterion is another method of photon identification which has been applied for this study. It requires no energy deposited in every cell of the
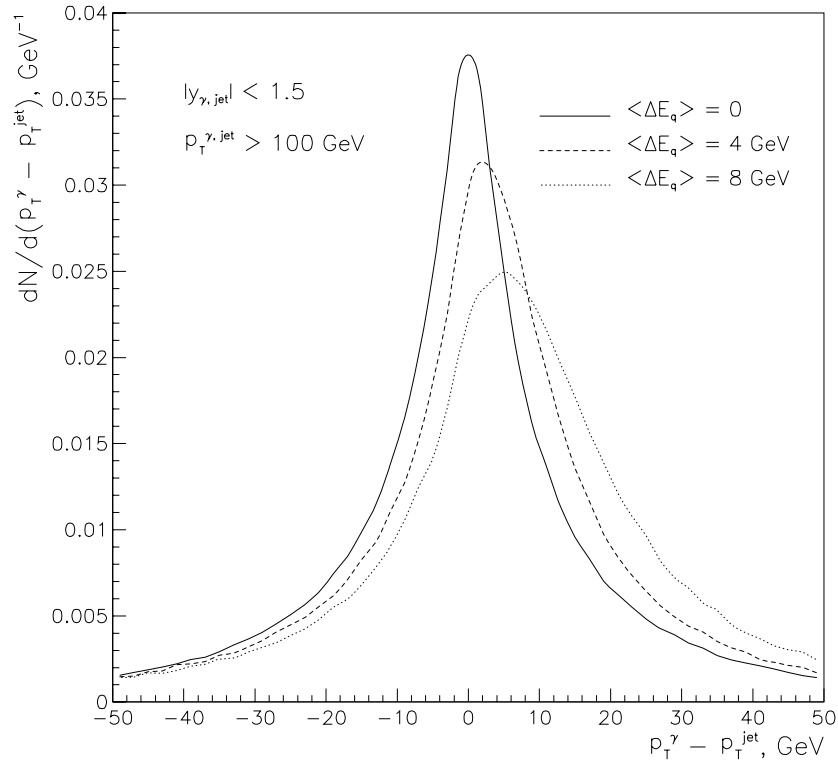
Fig. 6.5. The distribution of differences in transverse momentum between the γ and jet with $p_T^\gamma, p_T^{jet} > 100$ GeV in the rapidity region $\mid y_\gamma, y_{jet} \mid < 1.5$ for different values of jet energy loss. (Initial state gluon radiation is taken into account in PYTHIA)
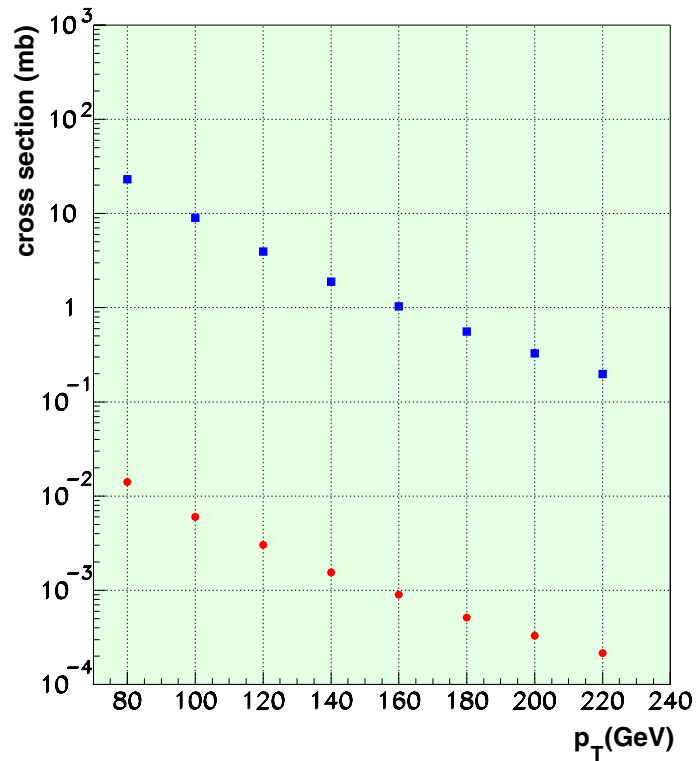
Fig. 6.6. Cross sections for γ + jet (*circles*) and jet + jet (*squares*) production in Pb+Pb collisions as a function of the lower limit of transverse momentum $\hat{p}_\perp$ defined in the rest frame of the hard interaction with $|\eta| < 2.6$. The results are calculated with (6.6)
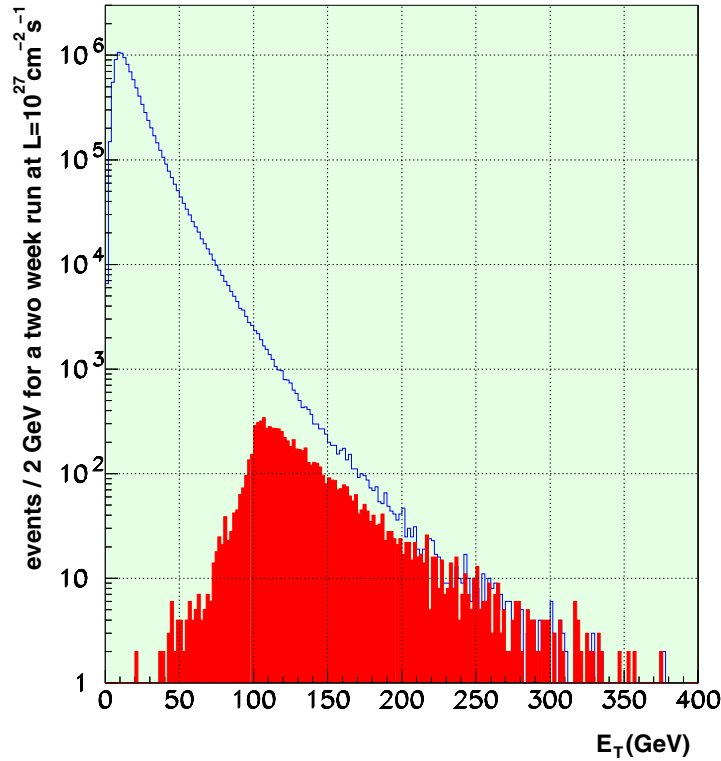
Fig. 6.7. Transverse energy of the photon from γ + jet events (*shaded histogram*) and the leading pion from jet + jet events (*solid line*) for events generated with $\hat{p}_\perp > 100$ GeV and $|\eta| < 2.6$. Histograms are normalized to the expected number of events produced in Pb+Pb collisions in a two week running at $\mathcal{L} = 10^{27}$cm^{-2}s^{-1} assuming one experiment. There are 7800 signal events and 1.1×10^7 background events

area around the central cell in the cluster above a given threshold. The transverse energy distribution in the cell is shown in Fig. 6.11 (c). A threshold of $E_T = 6.5$ GeV has been chosen from Fig. 6.11 (c). With this threshold the zero suppression criterion has been applied in the 7×7 cells not including the central 3×3 trigger matrix. The E_T of the hottest cell in the area is shown for the signal and background in Fig. 6.12. Zero suppression gives us a rejection factor of 2.66 against the background and reduces the signal by 14%.

The photon energy resolution is degraded by large "pile up" noise in heavy ion collisions. In a 5×5 crystal matrix we have about 1 GeV "pile up" noise as seen in Fig. 6.11 (d). This means that, for *e.g.* 120 GeV photons, the 0.64% resolution measured in the test beam [197] will degrade to 0.80%. Nevertheless, this photon resolution is much better than the jet energy resolution, as discussed in the next section.

6.2.3 Jet finding and jet energy resolution

Investigating QGP production in heavy ion collisions may be difficult because of the "false" jet background – fluctuations of the transverse energy flux arising from a huge multiplicity of soft secondary particles in the event. In such events the cells of the calorimeter are typically filled completely and the response of the calorimeter from these soft particles hitting the cell can imitate a signal from a single

high-p_T particle. Under these conditions the reconstruction of true QCD jets resulting from hard parton-parton scattering is important for the CMS heavy ion physics programme [72]. A number of studies of jet finding algorithm optimization in heavy ion collisions under CMS conditions have been made [94,188].

We have simulated the soft particle production in central Pb+Pb events at the LHC energy using a simple hydrodynamical model [94] with maximum particle density $\mathrm{d}N^\pm/\mathrm{d}y = 8000$. The average hadron transverse momentum is $\langle p_T^\pi \rangle = 0.5$ GeV and $\langle p_T^K \rangle = 0.7$ GeV. and $K/\pi = 0.2$. The "hard" central Pb+Pb event is the superposition of the soft particles and a hard PYTHIA pp event.

In order to investigate the hadronic jet resolution under CMS conditions, the CMS calorimeter response was modelled using CMSIM-008 adapted for heavy ion collisions with a shower parameterization for the barrel hadron calorimeter, $|\eta| < 1.5$.

The modified window-type jet-finding algorithm was applied to search for "jet-like" clusters above the average energy. First, all possible rectangular windows of size $2R$ with $R = \sqrt{(\Delta\eta)^2 + (\Delta\phi)^2}$ in the calorimeter map of η-ϕ space are constructed and sorted over window energy. The average transverse energy in a cell, $\overline{E_c}(\eta)$, and its dispersion $D(\eta) = \sqrt{\overline{(E_c^2}(\eta) - \overline{E_c}(\eta)^2)}$ are calculated as functions of η. The window energy is then calculated
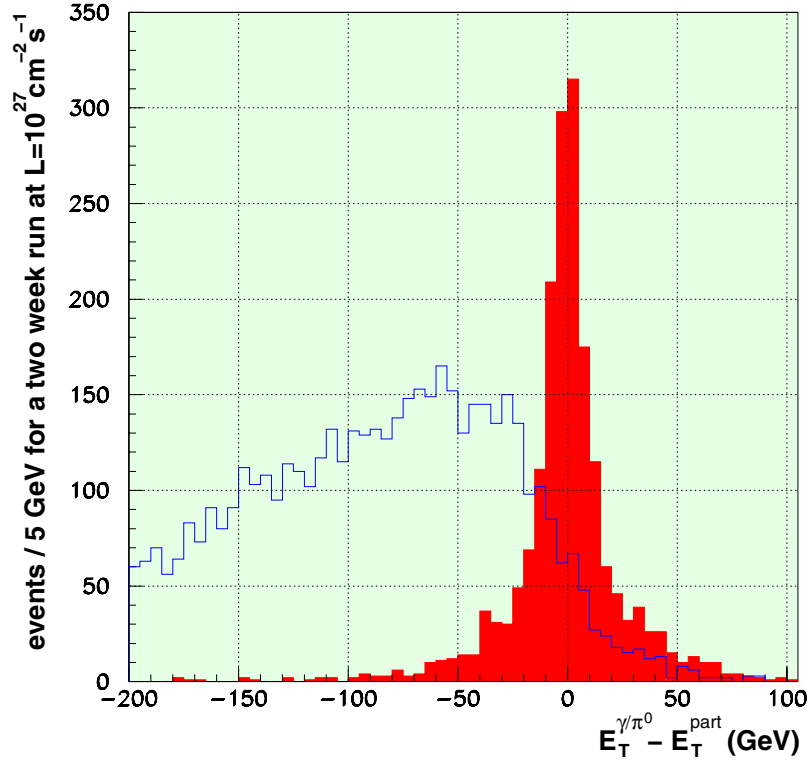
Fig. 6.8. Distribution of the variable $\Delta E_{\gamma/\pi^0 - p}$ (see text) for the signal (*shaded histogram*) and background (*solid line*) for the pseudorapidity region $|\eta^{\mathrm{parton}}| < 1.5$ and $E_{\mathrm{T}}^{\mathrm{parton}} > 120$ GeV. Histograms are normalized to the expected number of events produced in Pb+Pb collisions in a two week run at $\mathcal{L} = 10^{27} \mathrm{cm}^{-2} \mathrm{s}^{-1}$ and assuming one experiment. There are 1854 signal events and 5927 background events.

as the sum over all cells, n_c, included in this window, $E_w = \sum (E_c - \overline{E_c}(\eta))$. Then the loop on windows starts from the window with the maximum transverse energy. The non-overlapping windows with energy greater than $E_{\min} = 3 \sqrt{\sum D^2(\eta)}$ are considered as jet candidates and cells within a radius R from the centre of the window are collected. The values of $\overline{E_c}(\eta)$ and $D(\eta)$ are recalculated using cells which are not included in the jets. The jet energy is then the sum of the energies in the collected cells minus the background: $E_{\mathrm{jet}} = \sum (E_c - \overline{E_c}(\eta))$

We have found two criteria which allow the further optimization of jet finding algorithms exploiting different intrinsic structure of false and true hard QCD-jets, the average radius of a jet and the energy density in the centre of a jet. We describe each in turn.

The average radius of a jet can be defined as

$$\langle R \rangle = \sum_i R_{i0} \frac{E_i - \overline{E_i}}{E_{\mathrm{jet}}}, \quad E_{\mathrm{jet}} = \sum_i E_i - \overline{E_i}, \quad (6.8)$$

where R_{i0} is the distance between cell i covered by the jet and the centre of the jet in $\eta - \phi$ space, E_i and E_{jet} are the transverse energy of the cell and the jet respectively, and $\overline{E_i}$ is the average transverse energy in the cell. Figure 6.13a presents the average radius of false jets, calculated in the thermal model, and true hard jets, calculated with PYTHIA [79], versus jet energy $E_{\mathrm{T}}^{\mathrm{jet}}$ at $\mathrm{d}N^{\pm}/\mathrm{d}y = 8000$ assuming no energy loss. Note that in

this case the window-type jet finding algorithm was used with a cone radius of $R = 0.5$. The selection criterion $\langle R \rangle / R \ 0.5$ allows the major part of the false jets to be removed ($\approx 95\%$ for $E_{\mathrm{T}}^{\mathrm{jet}} > 100$ GeV) while the signal is almost insensitive to this cut (5% at the same E_{T}).

The energy density in the centre of a jet is the ratio of the sum of transverse energy of cells covered by the jet within radius $r = 0.7R$ to the total jet energy. Figure 6.13b shows the energy density of false and true hard jets versus jet energy $E_{\mathrm{T}}^{\mathrm{jet}}$ for the window-type jet finding algorithm with cone radius $R = 0.5$. We can see that the selection criterion $E_{\mathrm{T}} \ (r < 0.7R)/E_{\mathrm{T}}^{\mathrm{jet}} \gtrsim 0.7$ allows the bulk of the false jets to be removed.

Figure 6.14 shows the jet energy resolution at $y = 0$ as a function of jet energy in pp collisions and in Pb+Pb collisions with $\mathrm{d}N^{\pm}/\mathrm{d}y = 8000$.

6.3 Results

We have used the jet energy resolution at mid-rapidity obtained for Pb+Pb collisions, Fig. 6.14, to smear the energy of the recoiling parton (the slight improvement of the resolution with increasing $|\eta|$ [1] is not taken into account). The distribution of the variable $\Delta E_{\gamma - \mathrm{jet}}$ (see Section 6.2) is shown in Fig. 6.15 for the signal and background, taking into account smearing as well as the jet rejection factor and signal efficiency obtained in the pre-
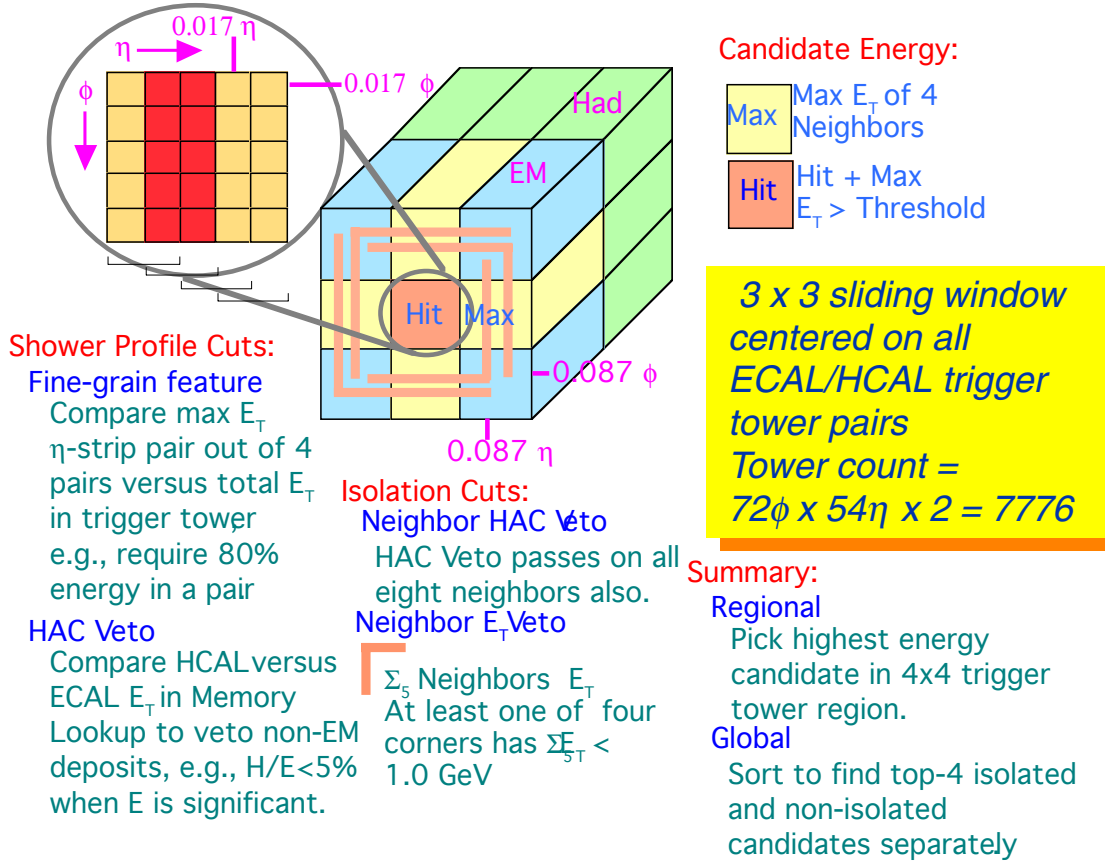
Fig. 6.9. The CMS electron/photon trigger algorithm
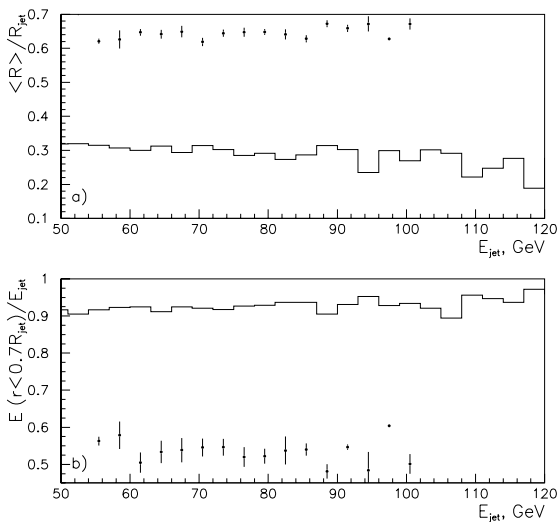
Fig. 6.13. The average jet radius $\langle R \rangle$ **a** and the transverse energy density E_T $(r < 0.7R_{\text{jet}})/E_T^{\text{jet}}$ **b** of true hard jets (histogram) and false jets (points) versus jet energy E_T^{jet} for $R_{\text{jet}} = 0.5$

vious sections. No energy loss of parton-initiated jets are included in this figure. Using (6.6), we expect about 1600 signal and 2200 background events after a two week run at $\mathcal{L} = 10^{27}\text{cm}^{-2}\text{s}^{-1}$ assuming one experiment.

We test the measurement of energy loss by quark-initiated jets in dense QCD-matter using the $\gamma +$ jet channel. To do so, we consider three different jet quenching scenarios, similar to those discussed for gluons in Section 2.5 [94]: (i) no jet quenching, (ii) jet quenching in a perfect quark-gluon plasma with $\langle \Delta E_q \rangle \simeq 4$ GeV and $\langle \Delta E_g \rangle = 9/4 \langle \Delta E_q \rangle$, and (iii) jet quenching in a maximally viscous quark-gluon fluid, resulting in $\langle \Delta E_q \rangle \simeq 8$ GeV.

We have calculated the distributions transverse energy differences between the γ and jet with $E_T^{\gamma/\text{jet}} > 120$ GeV for a two week run in the rapidity region $| y_\gamma, y_{\text{jet}} | < 1.5$ in our three scenarios. Figure 6.16(a) shows the result without $\pi^0 +$ jet background counting while this background counting is included in Fig. 6.16(b). Note that the shape of the background distribution is not very sensitive to the jet energy loss because the leading π^0 carries only part of the total hadronic jet energy and only a small fraction of the loss influences the final energy of the isolated pion.

The mean values of the distributions in Fig. 6.16 (a) without background are $\langle E_T^\gamma - E_T^{\text{jet}} \rangle \simeq 0.0 \pm 0.7, 2.9 \pm 0.7$
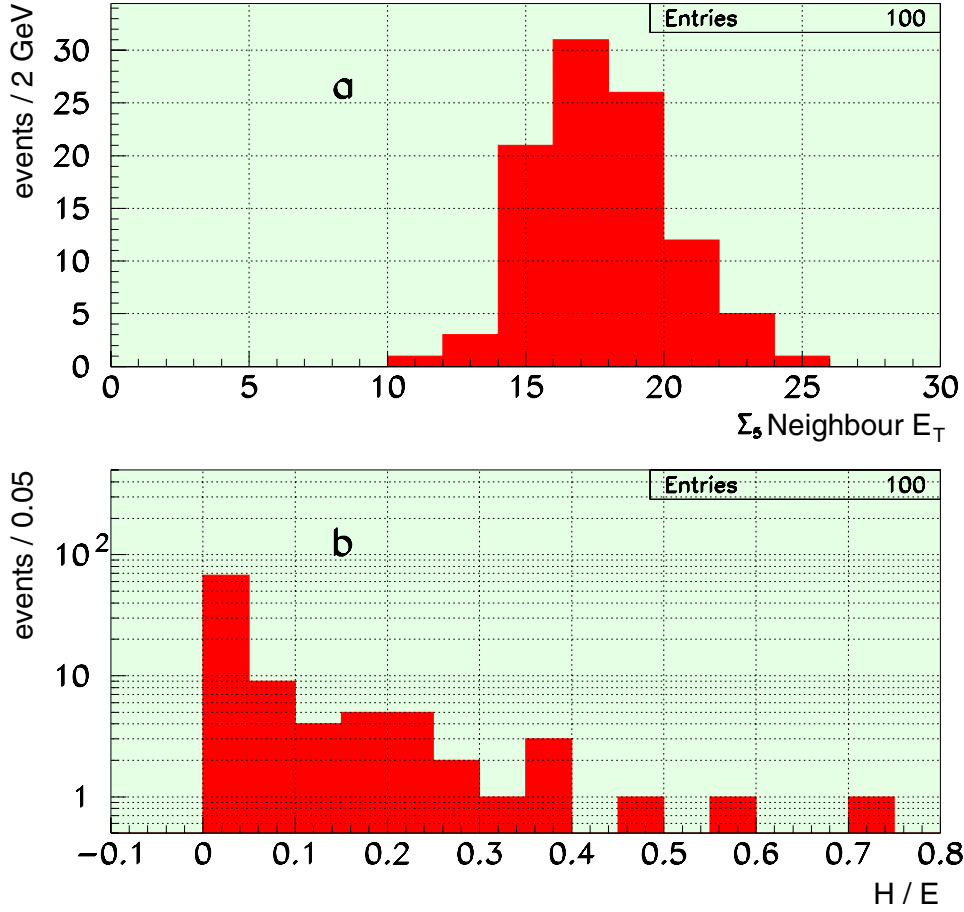
Fig. 6.10. Distribution of variables $\sum_5$ Neighbours E_{T} **a** and H/E **b** used in the Hadronic Veto and Neighbour E_{T} Veto of the CMS $e\gamma$ algorithm.

and 6.6 ± 0.7 GeV for $\langle \Delta E_q \rangle = 0$, 4 and 8 GeV respectively. The jet energy resolution leads to differences between the input values $\langle \Delta E_q \rangle$ and those obtained from the spectra. The π^0-contamination results in negative values in the final distributions of differences in Fig. 6.16 (b) already without energy loss. In a real experiment, however, it will be possible to estimate the number of background events using the region without the signal, $E_{\mathrm{T}}^\gamma - E_{\mathrm{T}}^{\mathrm{jet}} <$ -100 GeV, (see Fig. 6.15) and the background shape from Monte-Carlo simulation and/or from pp data. Thus it may be possible to subtract the background events from the experimental spectra.

One can see from Figs. 6.16 (a)-(b) that the shapes of the distributions are well distinguished for the three scenarios. In the region $E_{\mathrm{T}}^\gamma - E_{\mathrm{T}}^{\mathrm{jet}} > 0$ there is a greater than 1σ difference between the results for almost every bin with the 4 GeV energy loss and even for the 8 GeV loss. The predicted number of events in this region is 830 for case i, 920 for case ii and 1200 for case iii. Thus all three scenarios are distinguishable from each other. We find

$$N_{ii} - N_i/\sqrt{N_{ii}} = 3, \quad N_{iii} - N_i/\sqrt{N_{iii}} = 10,$$
$$N_{iii} - N_{ii}/\sqrt{N_{iii}} = 8 \qquad (6.9)$$

for $E_{\mathrm{T}}^\gamma - E_{\mathrm{T}}^{\mathrm{jet}} > 0$.

The previous data were obtained assuming a two week run at luminosity $\mathcal{L} = 10^{27} \mathrm{cm}^{-2}\mathrm{s}^{-1}$ and one Pb+Pb experiment. If we assume a more realistic case with two experiments with luminosity $\mathcal{L} = 6 \times 10^{26} \mathrm{cm}^{-2}\mathrm{s}^{-1}$ the scenarios can still be distinguished by the number of events expected with $E_{\mathrm{T}}^\gamma - E_{\mathrm{T}}^{\mathrm{jet}} > 0$

$$N_{ii} - N_i/\sqrt{N_{ii}} = 2.3, \quad N_{iii} - N_i/\sqrt{N_{iii}} = 8.3 \quad \text{and}$$
$$N_{iii} - N_{ii}/\sqrt{N_{iii}} = 6.3. \qquad (6.10)$$

Figures 6.17 (a)-(b) show the distribution of $\Delta E_{\gamma-\mathrm{jet}}$ for scenarios iii and i normalized to the expected number of events for a two week run with $\mathcal{L} = 6 \times 10^{26} \mathrm{cm}^{-2}\mathrm{s}^{-1}$.

We conclude that the $\gamma+$ jet channel allows us to determine the energy loss of quark-initiated jets in dense QCD-matter in Pb+Pb collisions.

6.4 Summary

To summarize, we have considered the capability of the CMS detector to observe the medium-induced energy loss of quarks and gluons by measuring the characteristics of hadronic jets in heavy ion collisions. The resolution in jet transverse energy has been found to be 16.7% at
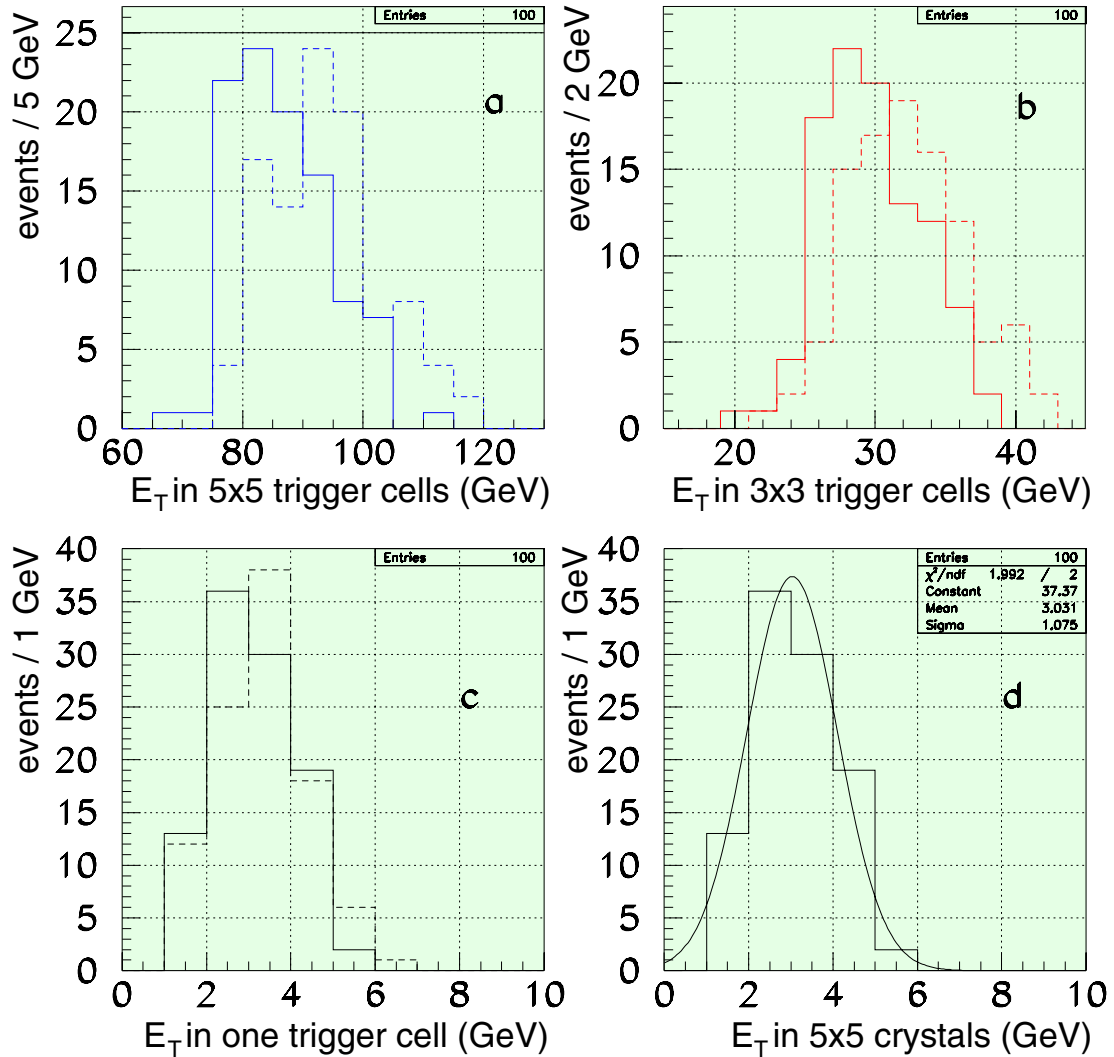
Fig. 6.11. Distribution of the measured transverse energy in the area of 5×5 (**a**) and 3×3 (**b**) trigger cells not including the central one. (c) Transverse energy measured in one trigger cell. The solid line in **a–c** is the energy in the electromagnetic calorimeter while the dashed line is the energy in the ECAL + HCAL system. **d** A fit to the distribution of the transverse energy measured in the electromagnetic part of one trigger cell.

$E_T \geq 50$ GeV for the CMS barrel calorimeters, decreasing to 8.6% for $E_T \geq 200$ GeV. Using the selection criterion of the jet internal structure allows us to obtain the maximum efficiency for true hard jet recognition as well as maximum suppression of the false jet background. For an energy threshold of 40-50 GeV the Level 1 single jet trigger gives an acceptable output rate of about 400-200 Hz and is fully efficient for most central collisions. With the high level trigger the rate can be further reduced to less than 10 Hz for the jets with reconstructed transverse energy larger than 100 GeV.

The expected statistics for dijet production will be large enough to study dijet rates as a function of impact parameter and the jet transverse energy. Dijet production is more sensitive to multiple scattering of partons in dense matter than the monojet yield which suffers strongly from finite resolution and background effects. The suppression of dijet rates due to energy loss by hard partons is ex-

pected to be much stronger for very central collisions compared to peripheral collisions.

Other possible signatures that could enable us to directly observe energy loss involve tagging the hard jet opposite a particle that does not interact strongly, such as γ or Z^0. The jet energy loss should result in an asymmetric shape of the distribution of differences in transverse momentum between the Z^0/γ and the jet. The estimated statistics are rather low for the Z^0+ jet channel. On the other hand, using $\gamma+$ jet production is complicated due to large background from jet + jet production when one of the jets in an event is misidentified as a photon (the leading π^0). However the shape of the distribution of differences in transverse energy between the γ and jet is sensitive to the jet quenching effect. It seems possible to extract the background $\gamma+$ jet events from the experimental spectra using the region without the signal,
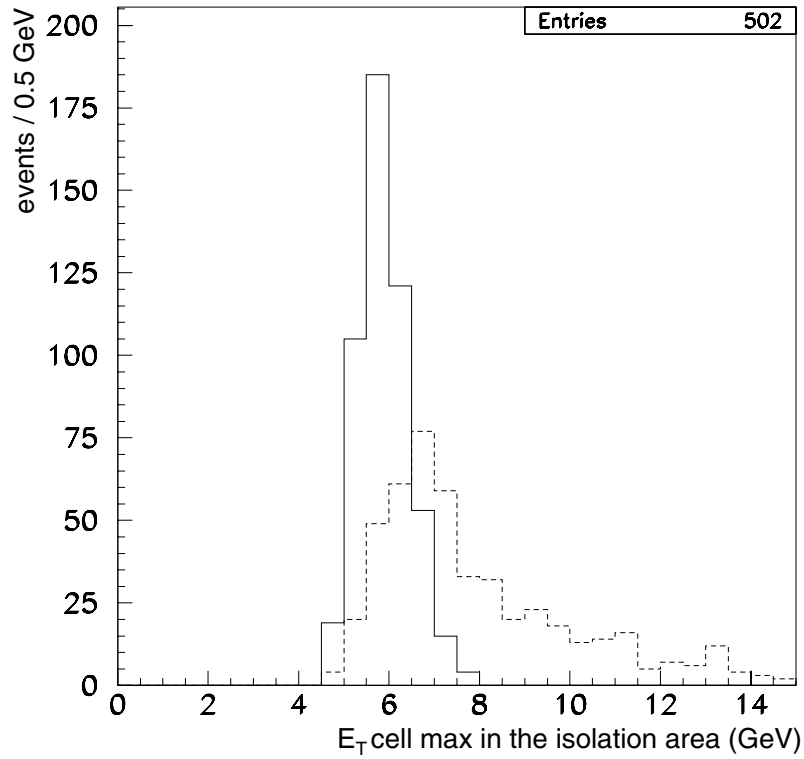
Fig. 6.12. Transverse energy of the hottest cell in the isolation area where zero suppression is applied (see text)

Fig. 6.14. The squares show the jet resolution in the *pp* mode with cone size 0.7 [1]; the grey circles the jet resolution in *pp* with window algorithm optimized for heavy ion collisions and the black circles show the jet resolution in Pb+Pb collisions with the window algorithm for $\mathrm{d}N^{\pm}/\mathrm{d}y = 8000$

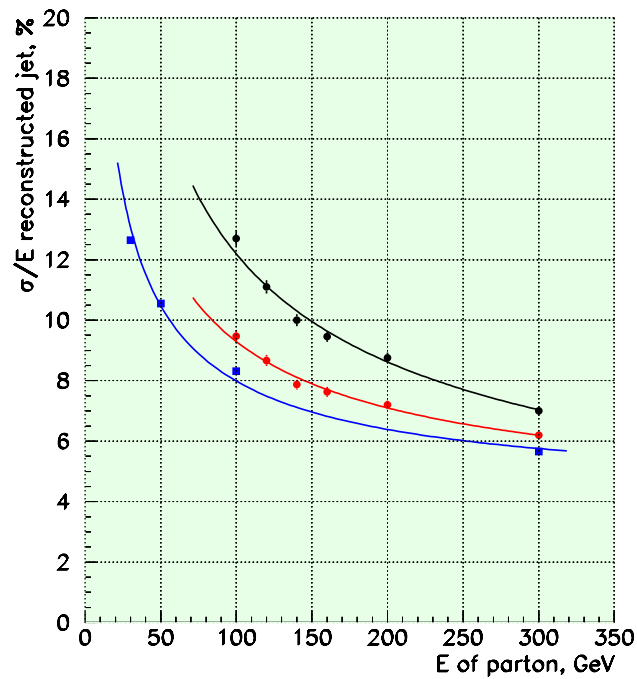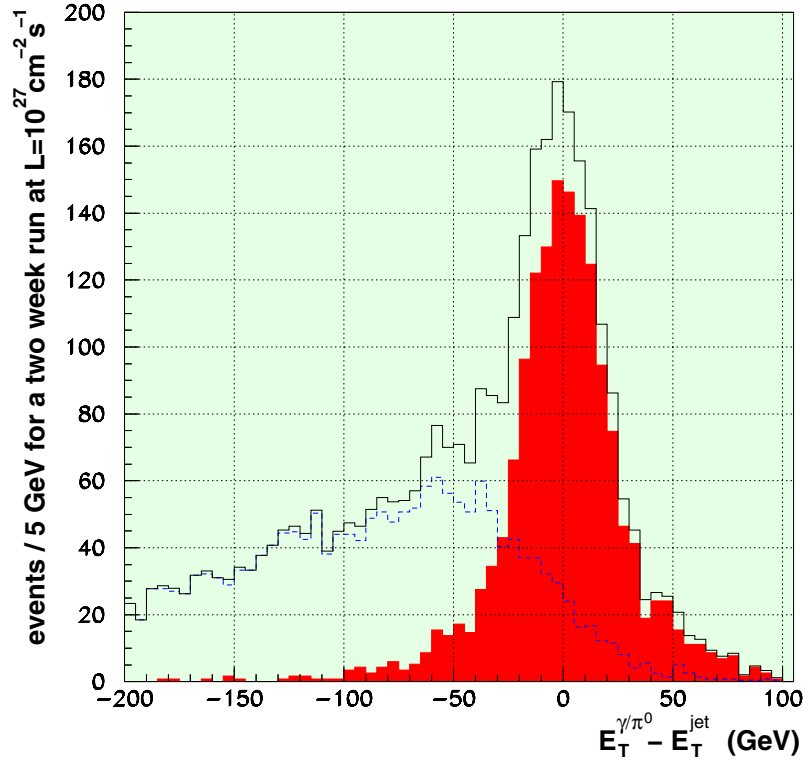**Fig. 6.15.** Distribution of the variable $\Delta E_{\gamma/\pi^0-\text{jet}}$ for the signal (shaded histogram), background (dashed line) and their sum (solid line) for the pseudorapidity region $|\eta^{\text{parton}}| < 1.5$ and $E_T^\gamma, E_T^{\text{jet}} > 120$ GeV. The histograms are normalized to the expected number of events in Pb+Pb collisions in a two week run at $\mathcal{L} = 10^{27} \text{cm}^{-2}\text{s}^{-1}$ assuming one experiment and taking into account efficiency of the event selection. There are 1600 signal events and 2200 background events

$E_T^\gamma - E_T^{\text{jet}} < -100$ GeV, with the background shape from Monte-Carlo simulations and/or from pp data.

Monte-Carlo studies show that the CMS detector is well suited to the investigation of high transverse energy jets. Dijet production, Z^0+ jet and $\gamma+$ jet channels are important for extracting information about the properties of super-dense matter which will be created in heavy ion collisions at the LHC.

7 $\gamma\gamma$ Physics

7.1 General introduction

The physics of central collisions is the physics of the Quark Gluon Plasma. Apart from projects like the search for new physics at very high rapidities (see the CASTOR subproject at ALICE for a search for Centauro events at the LHC), "Non QGP Physics" may be defined as the physics of peripheral collisions, which includes the effects of coherent photons and diffraction effects (Pomeron exchange). It is our aim to show that CMS can address very interesting physics topics in a rather clean way.

Central collision events are characterized by a very high multiplicity. Conversely, the multiplicity in peripheral collisions is comparatively low. The ions do not interact directly with each other and move on essentially undisturbed in the beam direction. The only possible interaction are therefore due to the long range electromagnetic

interaction and diffractive processes. Due to the coherent action of all the protons in the nucleus, the electromagnetic field is very strong and the resulting flux of equivalent photons is large, proportional to Z^2, where Z is the nuclear charge. Due to the very short interaction times the spectrum of these photons extends up to about 100 GeV in the laboratory system. The coherence condition limits the virtuality of the photon to very low values of $Q^2 < 1/R^2$, where $R = 1.2\ A^{1/3}$fm is the nuclear radius.

Hard diffractive processes in heavy ion collisions have also been studied. These are interesting processes on their own, but they are also a possible background to photon-photon and photon-hadron interactions. The physics potential of such kind of collisions is discussed in Section 7.2, in an extension of CMS note1998/009. It ranges from studies in QCD and strong field QED to the search for new particles like a light Higgs. This kind of physics is strongly related to $\gamma\gamma$ physics at e^+e^- colliders with increased luminosity. In view of the strong interaction background, experimental conditions will be somewhat different from the $\gamma\gamma$ physics at e^+e^- colliders. A limitation of the heavy ions is that only quasireal but no highly virtual photons will be available in the AA collisions.

Another interesting possibility is the study of photon-hadron interactions, extending the γp interaction studies at HERA/DESY to γA interactions, and reaching higher invariant masses than those possible at HERA.
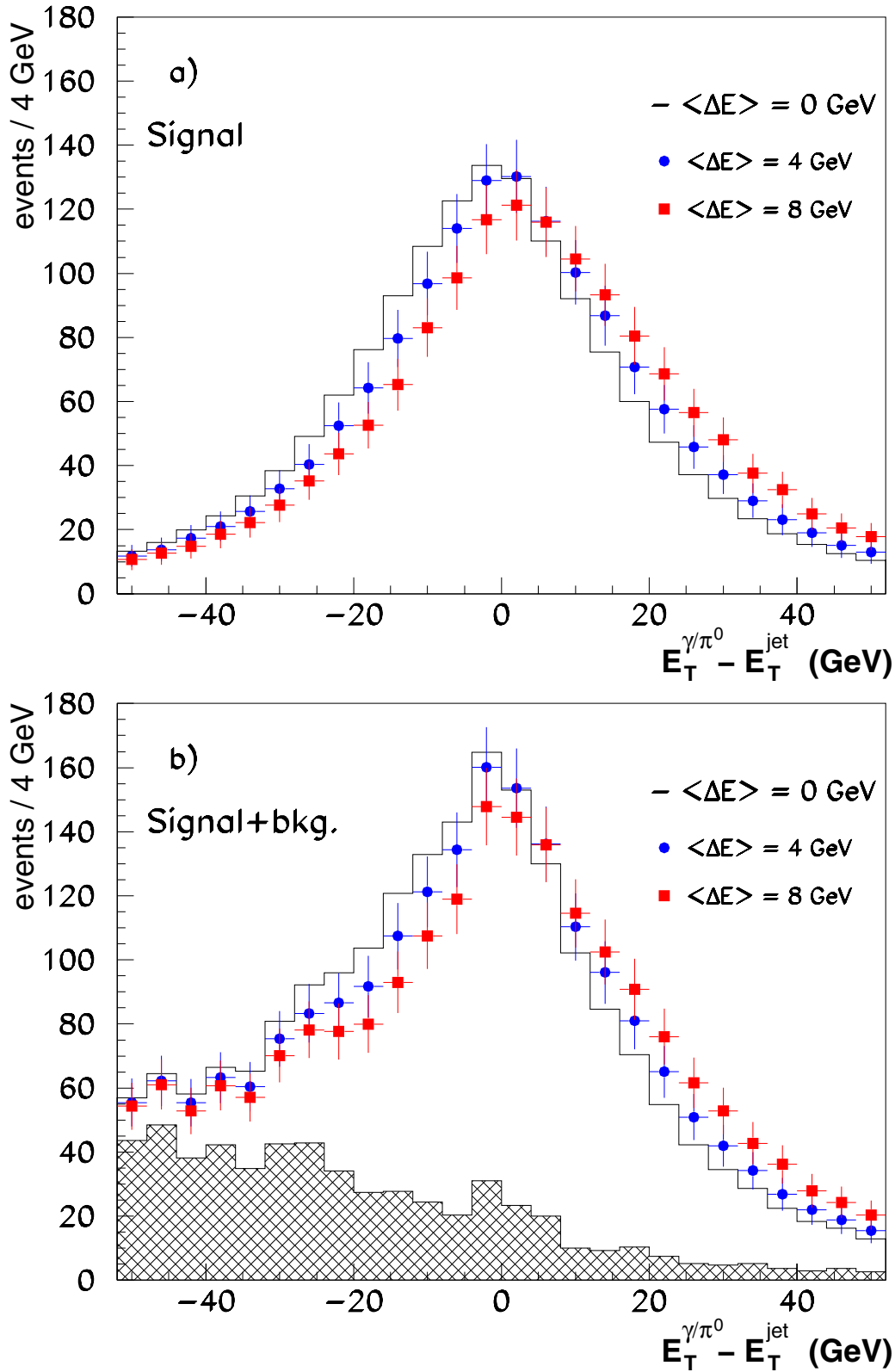
Fig. 6.16. The distributions of differences in transverse energy between the γ and jet with $E_T^\gamma, E_T^{\text{jet}} > 120$ GeV for a two week run at $\mathcal{L} = 10^{27}\text{cm}^{-2}\text{s}^{-1}$ and assuming one experiment **a** without π^0 + jet background counting, and **b** with π^0 + jet background counting, in the rapidity region $| y_\gamma, y_{\text{jet}} |< 1.5$ for different values of jet energy loss. Initial state gluon radiation and finite jet energy resolution are taken into account
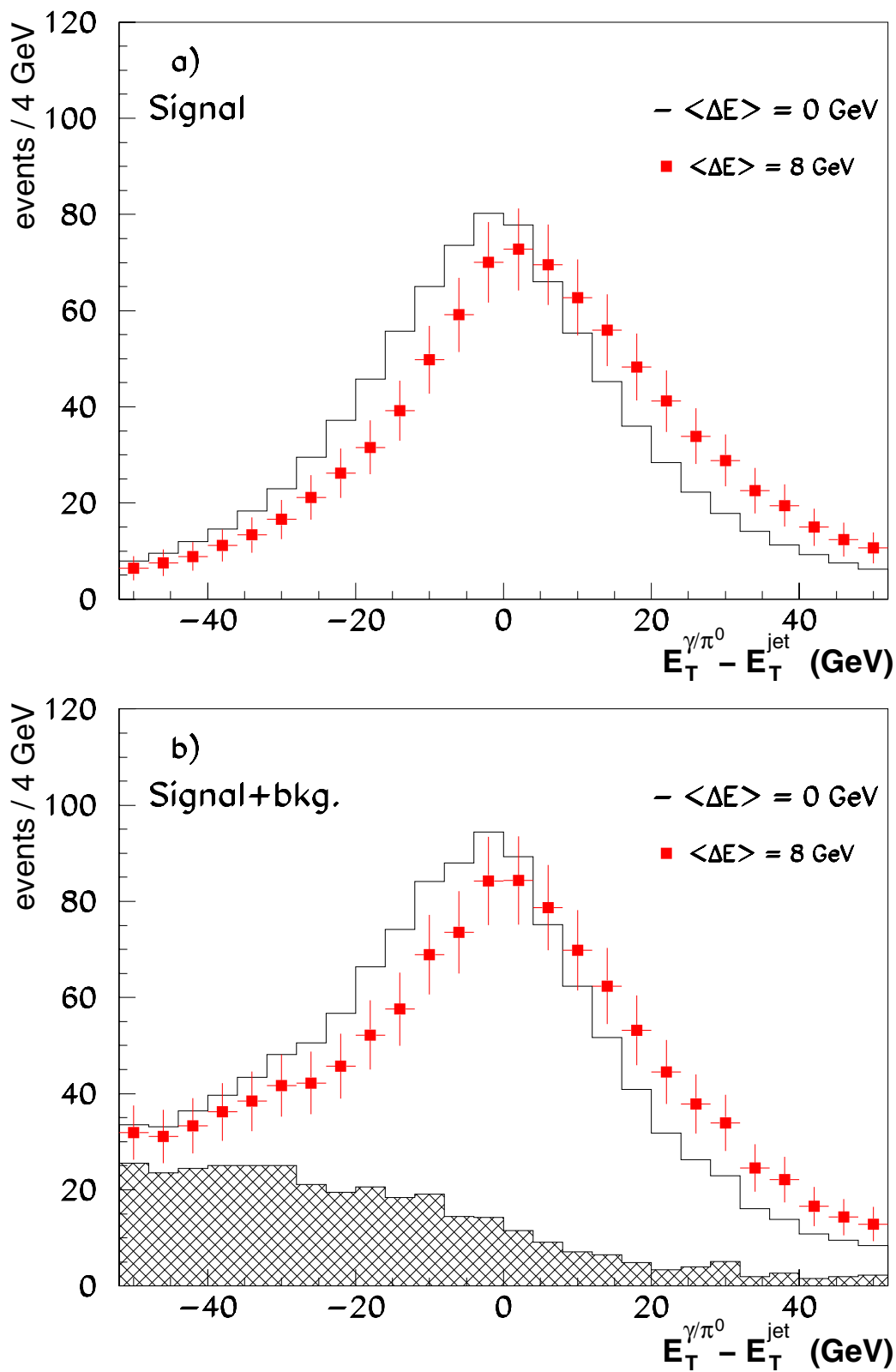
Fig. 6.17. The distributions of differences in transverse energy between the γ and jet with E_{T}^{γ}, $E_{\mathrm{T}}^{\mathrm{jet}} > 120$ GeV for a two week run at $\mathcal{L} = 6 \times 10^{26} \mathrm{cm}^{-2}\mathrm{s}^{-1}$ **a** without π^0 + jet background counting, and **b** with π^0 + jet background counting, in the rapidity region $\mid y_{\gamma}, y_{\mathrm{jet}} \mid < 1.5$ for different values of jet energy loss. Initial state gluon radiation and finite jet energy resolution are taken into account.

At the STAR (Solenoidal Tracker At RHIC) detector – which began operations in June 2000 – a similar program of photon and Pomeron interaction studies exists. At RHIC the photon flux will be of the same order of magnitude but the spectrum is limited to about 3 GeV.

7.2 Photon-photon and photon-hadron physics

The parton model is very useful to study scattering processes at very high energies. The scattering is described as an incoherent superposition of the scattering of the various constituents. For example, nuclei consist of nucleons which in turn consist of quarks and gluons, photons consist of lepton pairs, electrons consist of photons, etc.. We note that relativistic nuclei have photons as an important constituent, especially for low enough virtuality $Q^2 = -q^2 > 0$ of the photon. This is due to the coherent action of all the charges in the nucleus. The virtuality of the photon is related to the size R of the nucleus by

$$Q^2 \lesssim 1/R^2 \qquad (7.1)$$

the condition for coherence. From the kinematics of the process one has

$$Q^2 = \frac{\omega^2}{\gamma^2} + q_\perp^2 \qquad (7.2)$$

which limits the maximum energy of the quasireal photon to

$$\omega_{\max} \approx \frac{\gamma}{R}. \qquad (7.3)$$

where γ is the Lorentz factor of the projectile and the perpendicular component of its momentum is

$$q_\perp \lesssim \frac{1}{R} \qquad (7.4)$$

We define the ratio $x = \omega/E$, where E denotes the energy of the nucleus $E = M_N \gamma A$ and M_N is the nucleon mass. It is therefore smaller than

$$x < x_{\max} = \frac{1}{RM_N A} = \frac{\lambda_C(A)}{R} \qquad (7.5)$$

where $\lambda_C(A)$ is the Compton wave length of the ion. Here and throughout the rest of this chapter we use natural units, setting $\hbar = c = 1$.

The collisions of e^+ and e^- have been the traditional way to study $\gamma\gamma$ collisions. Similarly photon-photon collisions can also be observed in hadron-hadron collisions. Since the photon number scales with Z^2 such effects can be particularly large. Of course, the strong interaction of the two nuclei has to be taken into consideration.

The equivalent photon flux present in medium and high energy nuclear collisions is very high. Recent reviews of this topic can be found in [199, 200, 201]. This high equivalent photon flux has already found many useful applications in nuclear physics [202], nuclear astrophysics [203, 204], particle physics [205] (sometimes called the "Primakoff effect"), as well as atomic physics [206].
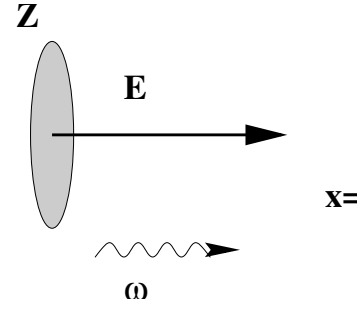

Fig. 7.1. A fast moving nucleus with charge Ze is surrounded by a strong electromagnetic field. This can be viewed as a cloud of virtual photons. These photons can often be considered as real. They are called equivalent or quasireal photons. The ratio of the photon energy ω and the incident ion energy E is denoted by $x = \omega/E$. Its maximal value is restricted by the coherence condition to $x < \lambda_C(A)/R \approx 0.175/A^{4/3}$, that is, $x \lesssim 10^{-3}$ for Ca ions and $x \lesssim 10^{-4}$ for Pb ions
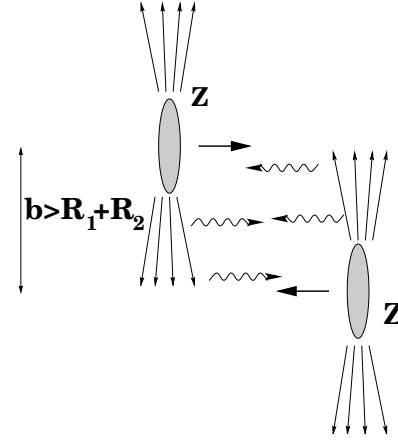
Fig. 7.2. Two fast moving electrically charged objects are an abundant source of (quasireal) photons. They can collide with each other and with the other nucleus. For peripheral collisions with impact parameters $b > 2R$, this is useful for photon-photon as well as photon-nucleus collisions

Here our main purpose is to discuss the physics of photon-photon and photon-hadron (nucleus) collisions in high energy heavy ion collisions. The RHIC program includes such investigation. The equivalent photon spectrum there extends up to several GeV ($\gamma \approx 100$). Therefore the available invariant mass range is up to about the mass of the η_c. At the 1999 RHIC/INT Winter Workshop in Berkeley, the physics of peripheral collisions was discussed by S.K. Klein and S.J. Brodsky [207]. When the LHC begins operation in 2005/2008, the study of these reactions can be extended to both higher luminosities and much higher invariant masses.

Relativistic heavy ion collisions were suggested as a general tool for two photon physics about a decade ago. Yet the study of a special case, the production of e^+e^- pairs in nucleus-nucleus collisions, goes back to the work of Landau and Lifschitz in 1934 [208]. (In those days, of course, one thought more about high energy cosmic ray nuclei than relativistic heavy ion colliders.) The gen-

eral possibilities and characteristic features of two-photon physics in relativistic heavy ion collisions have been discussed [209]. The possibility to produce a Higgs boson via $\gamma\gamma$ fusion was also suggested [210, 211]. In these papers the effect of strong absorption in heavy ion collisions was not taken into account. This absorption is a feature which is quite different from the two-photon physics at e^+e^- colliders. The problem of taking strong interactions into account was solved by using impact parameter space methods [212–214]. Thus the calculation of $\gamma\gamma$ luminosities in heavy ion collisions is put on a firm basis and rather definite conclusions were reached by many groups working in the field, as described, e.g., in [215, 200, 199]. This opens the way for many interesting applications. Up to now hadron-hadron collisions have not been used for two-photon physics. An exception can be found in [216] where the production of $\mu^+\mu^-$ pairs at the ISR was studied. The special class of events was selected where no hadrons are seen associated with the muon pair in a large solid angle vertex detector. In this way one makes sure that the hadrons do not interact strongly with each other, i.e., one is dealing with peripheral collisions with impact parameters $b > 2R$. The photon-photon collisions thus manifest themselves as "silent events". Dimuons with a very low sum of transverse momenta are also considered as a luminosity monitor for the ATLAS detector at the LHC [217].

Experiments are planned at RHIC [218, 219, 220, 221, 222] and are discussed at the LHC [223, 224, 225]. We quote J. D. Bjorken [226]: "It is an important portion (of the FELIX program at the LHC [119]) to tag on Weizsaecker Williams photons (via the non observation of completely undissociated forward ions) in ion-ion running, creating a high luminosity $\gamma\gamma$ collider".

7.2.1 From impact-parameter dependent equivalent photon spectra to $\gamma\gamma$ Luminosities

Photon-photon collisions have been studied extensively at e^+e^- colliders. The theoretical framework is reviewed, e.g. in [227]. The basic graph for the two-photon process in ion-ion collisions is shown in Fig. 7.3. Two virtual (spacelike) photons collide to form a final state f. In the equivalent photon approximation (EPA), it is assumed that the square of the 4-momentum of the virtual photons is small, i.e., $q_1^2 \approx q_2^2 \approx 0$ and the photons can be treated as quasireal. In this case, $\gamma\gamma$ production is factorized into an elementary cross section for the process $\gamma + \gamma \to f$ (with real photons, i.e., $q^2 = 0$) and a $\gamma\gamma$ luminosity function. In contrast to the point-like elementary electrons and positrons, nuclei are extended, strongly interacting objects with internal structure. This gives rise to modifications in the theoretical treatment of two photon processes. The emission of a photon depends on the (elastic) form factor. Often a Gaussian form factor or a homogeneous charged sphere is used. The typical behaviour of a form factor is

$$f(q^2) \approx \begin{cases} Z & \text{for } |q^2| < 1/R^2 \\ 0 & \text{for } |q^2| \gg 1/R^2 \end{cases} \quad (7.6)$$
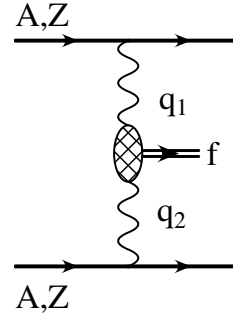
Fig. 7.3. The general Feynman diagram of photon-photon processes in heavy ion collisions: Two (virtual) photons fuse in a charged particle collision into a final system f

For low $|q^2|$ all the protons inside the nucleus act coherently, whereas for $|q^2| \gg 1/R^2$ the form factor is very small, close to 0. For a medium size nucleus with, say, $R = 5$ fm, the limiting $Q^2 = -q^2 = 1/R^2$ is given by $Q^2 = (40 \text{ MeV})^2 = 1.6 \times 10^{-3} \text{ GeV}^2$. Apart from e^+e^- (and to a certain extent also $\mu^+\mu^-$) pair production, this scale is much smaller than typical scales in the two-photon processes. Therefore the virtual photons in relativistic heavy ion collisions can be treated as quasireal. This is a limitation as compared to e^+e^- collisions where the two-photon processes can also be studied as a function of the corresponding masses q_1^2 and q_2^2 of the exchanged photon ("tagged mode").

As was discussed already in the previous section, relativistic heavy ions interact strongly when the impact parameter is smaller than the sum of the radii of the two nuclei. In such cases $\gamma\gamma$ processes are still present as a background that has to be considered in central collisions. In order to study "clean" photon-photon events however, central collisions must be eliminated in the calculation of photon-photon luminosities as the particle production due to the strong interaction dominates. In the usual treatment of photon-photon processes in e^+e^- collisions, plane waves are used and there is no direct information on the impact parameter. For heavy ion collisions on the other hand it is very appropriate to introduce impact parameter dependent equivalent photon numbers. They have been widely discussed in the literature, see, e.g., [202, 228, 229].

The equivalent photon spectrum corresponding to a point charge Ze moving with a velocity v at impact parameter b is given by

$$N(\omega, b) = \frac{Z^2\alpha}{\pi^2} \frac{1}{b^2} \left(\frac{c}{v}\right)^2 x^2 \left[K_1^2(x) + \frac{1}{\gamma^2}K_0^2(x)\right] \quad (7.7)$$

where $K_n(x)$ are the modified Bessel Functions (MacDonald Functions) and $x = \omega b/\gamma v$. Then one obtains the probability for a certain electromagnetic process to occur in terms of the same process generated by an equivalent pulse of light as

$$P(b) = \int \frac{d\omega}{\omega} N(\omega, b)\sigma_\gamma(\omega). \quad (7.8)$$

Possible modifications of $N(\omega, b)$ due to an extended spherically symmetric charge distribution are given in [230]. It should be noted that (7.7) also describes the equivalent photon spectrum of an extended charge distribution, such as a nucleus, as long as b is larger than the extension of the object. This is due to the fact that the electric field of a spherically symmetric system depends only on the total charge inside it.

As the x-dependent term in (7.7) can be roughly approximated as 1 for $x < 1$ and 0 for $x > 1$, the equivalent photon number $N(\omega, b)$ is almost a constant up to a maximum $\omega_{\max} = \gamma/b$ ($x = 1$). By integrating the photon spectrum over b from a minimum value of $R_{\min}$ up to infinity (where essentially only impact parameters up to $b_{\max} \approx \gamma/\omega$ contribute, compared with (7.3)), one can define an equivalent photon number $n(\omega)$. This integral can be carried out analytically and is given by [202, 228]

$$n(\omega) = \int d^2 b N(\omega, b)$$
$$= \frac{2}{\pi} Z_1^2 \alpha \left(\frac{c}{v}\right)^2 \left[\xi K_0 K_1 - \frac{v^2 \xi^2}{2c^2}\left(K_1^2 - K_0^2\right)\right]$$
$$(7.9)$$

where the argument of the modified Bessel functions is $\xi = \omega R_{\min}/\gamma v$. The cross section for a certain electromagnetic process is then

$$\sigma = \int \frac{d\omega}{\omega} n(\omega) \sigma_\gamma(\omega) \qquad (7.10)$$

Using the approximation above for the MacDonald functions, we get an approximated form, which is quite reasonable and is useful for estimates:

$$n(\omega) \approx \frac{2 Z^2 \alpha}{\pi} \ln \frac{\gamma}{\omega R_{\min}} \qquad \omega < \frac{\gamma}{R_{\min}} \qquad (7.11)$$

The photon-photon production cross section is obtained from a similar factorized form by folding the corresponding equivalent photon spectra of the two colliding heavy ions [213, 214] (for polarization effects see [213])

$$\sigma_c = \int \frac{d\omega_1}{\omega_1} \int \frac{d\omega_2}{\omega_2} F(\omega_1, \omega_2) \sigma_{\gamma\gamma}(W_{\gamma\gamma}) \qquad (7.12)$$

with

$$F(\omega_1, \omega_2) = 2\pi \int_{R_1}^{\infty} b_1 db_1 \int_{R_2}^{\infty} b_2 db_2 \int_0^{2\pi} d\phi$$
$$\times N(\omega_1, b_1) N(\omega_2, b_2) \Theta\left(b_1^2 + b_2^2 - 2 b_1 b_2 \cos\phi - R_{\mathrm{cutoff}}^2\right) \qquad (7.13)$$

where $W_{\gamma\gamma} = \sqrt{4\omega_1\omega_2}$ is the invariant mass of the $\gamma\gamma$ system and $R_{\mathrm{cutoff}} = R_1 + R_2$. (In [222] the effect of replacing the simple sharp cutoff (Θ function) by a more realistic probability of the nucleus to survive was studied. Apart from the very high end of the spectrum, modifications are rather small.) This cross section can also be rewritten in terms of the invariant mass $W_{\gamma\gamma}$ and the rapidity
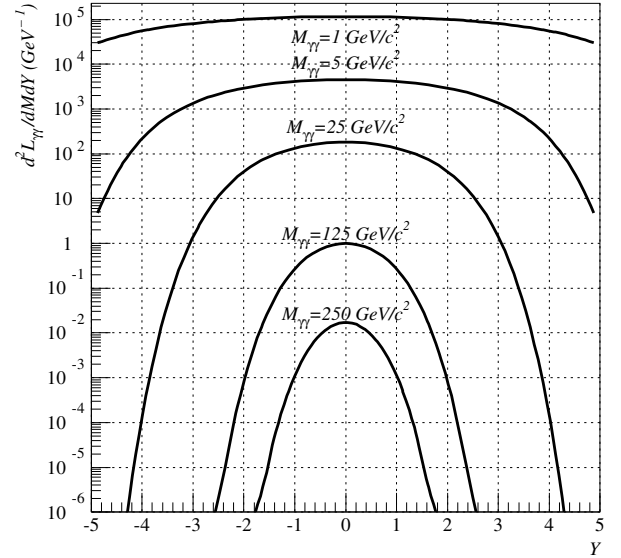
Fig. 7.4. The luminosity function $d^2\mathcal{L}_{\gamma\gamma}/dMdY$ for Pb+Pb collisions with $\gamma = 2950$ as a function of Y for different values of M

$Y = 1/2\ln[(p_0 + P_z)/(p_0 - p_z)] = 1/2\ln(\omega_1/\omega_2)$ as:

$$\sigma_c = \int dW_{\gamma\gamma} dY \frac{d^2\mathcal{L}}{dW_{\gamma\gamma}dY} \sigma_{\gamma\gamma}(W_{\gamma\gamma}) \qquad (7.14)$$

with

$$\frac{d^2\mathcal{L}_{\gamma\gamma}}{dW_{\gamma\gamma}dY} = \frac{2}{W_{\gamma\gamma}} F\left(\frac{W_{\gamma\gamma}}{2}e^Y, \frac{W_{\gamma\gamma}}{2}e^{-Y}\right) \qquad (7.15)$$

Here the energy and momentum of the $\gamma\gamma$ system in the beam direction are denoted by p_0 and p_z. The transverse momentum is of the order of $p_\perp \leq 1/R$ and is neglected. The transverse momentum distribution is calculated in [231].

In [231] and [232] the intuitively plausible formula (7.13) is derived *ab initio*, starting from the assumption that the two ions move on a straight line with impact parameter b. The advantage of heavy nuclei is seen in the coherence factor $Z_1^2 Z_2^2$ contained in $N(\omega, b)$ in (7.13).

As a function of Y, the luminosity $d^2\mathcal{L}/dW_{\gamma\gamma}dY$ for symmetrical ion collisions has a Gaussian shape with the maximum at $Y = 0$. The width is approximately given by $\Delta Y = 2\ln\left[(2\gamma)/(RW_{\gamma\gamma})\right]$, see also Fig. 7.4. Depending on the experimental situation, additional cuts in the allowed Y range are needed.

Additional effects due to the nuclear structure have been also studied. For inelastic vertices a photon number $N(\omega, b)$ can also be defined, see, *e.g.*, [199]. Its effect was found to be small. The dominant correction comes from the electromagnetic excitation of one of the ions in addition to the photon emission. See [199] for further details.

In Fig. 7.5 we give a comparison of effective $\gamma\gamma$ luminosities, that is the product of the beam luminosity and the two-photon luminosity for various collider scenarios. We use the following collider parameters:
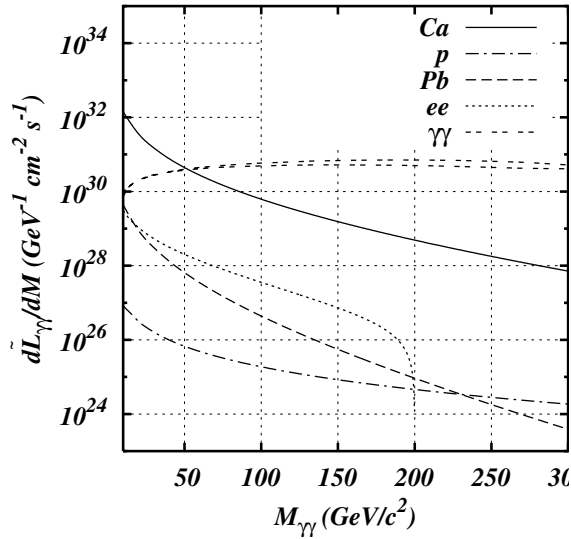
Fig. 7.5. Comparison of the effective $\gamma\gamma$ luminosities $(\mathrm{d}\tilde{\mathcal{L}}_{\gamma\gamma}/\mathrm{d}M = \mathcal{L}_{AA}\mathrm{d}\mathcal{L}_{\gamma\gamma}/\mathrm{d}M)$ for different ion species. For comparison the same quantity is shown for LEP200 and a future NLC/PLC (next linear collider/photon linear collider), where photons are obtained by laser backscattering; the results for two different polarizations are shown

- LEP200: $E_e = 100$ GeV, $\mathcal{L} = 10^{32}\mathrm{cm}^{-2}\mathrm{s}^{-1}$,
- NLC/PLC: $E_e = 500$ GeV, $\mathcal{L} = 2 \ 10^{33}\mathrm{cm}^{-2}\mathrm{s}^{-1}$,
- Pb+Pb heavy-ion mode at the LHC: $\gamma = 2950$, $\mathcal{L} = 10^{26}\mathrm{cm}^{-2}\mathrm{s}^{-1}$,
- Ca+Ca : $\gamma = 3750$, $\mathcal{L} = 4 \ 10^{30}\mathrm{cm}^{-2}\mathrm{s}^{-1}$,
- pp: $\gamma = 7450$, $\mathcal{L} = 10^{30}\mathrm{cm}^{-2}\mathrm{s}^{-1}$.

In Ca+Ca collisions, higher effective luminosities (defined as collider luminosity times $\gamma\gamma$ luminosity) can be achieved than in the Pb+Pb mode since higher AA luminosities can be reached. Since the event rates are proportional to the luminosities, and interesting events are rare (see also below), we think that it is important to aim at rather high luminosities in the ion-ion runs. This should be possible,especially for the medium heavy ions like Ca. For further details see [103, 233, 148].

7.2.2 γA interactions

There are many interesting phenomena that can be investigated in γA interactions ranging from the excitation of discrete nuclear states, giant multipole resonances (especially the giant dipole resonance), quasideuteron absorption, nucleon resonance excitation to the nucleon continuum.

The interaction of quasireal photons with protons has been studied extensively at the e^+e^- collider HERA, with $\sqrt{s} = 300$ GeV ($E_e = 27.5$ GeV and $E_p = 820$ GeV). This is made possible by the large flux of quasi-real photons from the electron (positron) beam. The obtained γp centre-of-mass energies ($W_{\gamma p} \leq 200$ GeV) are an order

of magnitude larger than those reached by fixed target experiments.

Similar and more detailed studies will be possible at the relativistic heavy ion colliders RHIC and LHC due to the larger flux of quasireal photons from one of the colliding nuclei. In the photon-nucleon subsystem, one can reach invariant masses $W_{\gamma N}$ up to $W_{\gamma N,\mathrm{max}} = \sqrt{4W_{\mathrm{max}}E_N} \approx 0.8\gamma A^{-1/6}$ GeV. For Pb at the LHC ($\gamma = 2950$) $W_{\gamma N,\mathrm{max}} = 950$ GeV while even higher values are possible for Ca. Thus one can study processes quite similar to those at HERA, with nuclei instead of protons. Photon-nucleon physics includes topics, such as the energy dependence of total cross sections, diffractive, and non-diffractive processes.

One important subject is the elastic vector meson production, $\gamma p \rightarrow Vp$, with $V = \rho, \omega, \phi, J/\psi, \ldots$. A review of exclusive neutral vector meson production is given in [234]. The diffractive production of vector mesons allows one to gain insight into the interface between perturbative QCD and hadronic physics. Elastic processes where the proton remains in the ground state have to be described within nonperturbative (and therefore phenomenological) models. It was shown in [235] that diffractive "elastic" J/ψ photoproduction is a probe of the gluon density at $x \approx M_\psi^2/W_{\gamma N}^2$ (for quasi-real photons). Inelastic J/ψ photoproduction has also been studied recently at HERA [236].

Going to hard exclusive photoproduction of heavy mesons on the other hand, perturbative QCD is applicable. Recent data from HERA on J/ψ photoproduction have shown a rapid increase of the total cross section with $W_{\gamma N}$, as predicted by perturbative QCD. Such studies could be extended to photon-nucleus interactions at RHIC, thus complementing the HERA studies. Equivalent photon flux factors are large for the heavy ions due to coherence. On the other hand, the AA luminosities are quite low compared to HERA. Of special interest is the coupling of the photon of one nucleus to the Pomeron-field of the other nucleus. Such studies are envisaged for RHIC, see [218,219,220,221] where experimental feasibility studies were also performed.

Estimates of the order of magnitude of vector meson production in photon-nucleon processes at RHIC and LHC are given in [199]. In AA collisions there is incoherent photoproduction on the individual A nucleons. There is also the coherent contribution where the nucleus remains in the ground state. Due to the large momentum transfer, the total (angle integrated) coherent scattering shows an $A^{4/3}$ dependence. This is in contrast to, *e.g.*, low energy νA elastic scattering where coherence effects lead to an A^2 dependence. For a general pedagogical discussion of the coherence effects see, *e.g.*, [237]. The coherent exclusive vector meson production at RHIC was studied recently [238]. The increase of the cross section with A was found to be between the two extremes ($A^{4/3}$ and A^2) mentioned above. In this context, RHIC and LHC can be considered as vector meson factories [238]. In addition there are inelastic contributions, where the proton (nucleon) is transformed into some final state X during the interac-

tion (see [236]). Nuclear shadowing effects can influence all these processes.

At the LHC one can extend these processes to much higher invariant masses W, therefore much smaller values of x will be probed. Whereas J/ψ production at HERA was measured up to invariant masses of $W \approx 160$ GeV, the energies at the LHC allow for studies up to ≈ 1 TeV.

At the LHC hard diffractive vector meson photoproduction can be investigated especially well in AA collisions. In comparison to previous experiments, the very large photon luminosity should allow observation of processes with quite small γp cross sections, such as Υ production. For more details see [119].

Photo-induced processes are also of practical importance since they are a serious source of beam loss as they lead to a change of the charge-to-mass ratio of the nuclei. The cross section for the excitation of the giant dipole resonance, a collective mode of the nucleus, is rather large for the heavy systems (of the order of 100 b). The cross section scales approximately with $Z^{10/3}$. The contribution from nucleon resonances (especially the Δ resonance) has also been confirmed experimentally in fixed target experiments with 60 and 200 GeV/A [239, 240, 241]. For details of these aspects, see [200, 242, 243, 244] where scaling laws as well as detailed calculations are given.

7.2.3 Photon-photon physics at various invariant mass scales

Up to now photon-photon scattering has been mainly studied at e^+e^- colliders. Many reviews [227, 245, 246] as well as conference reports [247, 248, 249, 250] exist. Typical two photon invariant meson masses studied range from m_{π^0} to about m_{η_c}. Recently the total $\gamma\gamma \to$ hadron cross section has been studied at LEP2 up to invariant masses of about 70 GeV [251]. We are concerned here mainly with the invariant mass region relevant for the LHC (see the $\gamma\gamma$ luminosity figures below). Apart from the production of e^+e^- (and $\mu^+\mu^-$) pairs, the photons can always be considered as quasi-real. The cross section for virtual photons deviates from that for real photons only for Q^2 values much larger than the coherence limit $Q^2 \lesssim 1/R^2$ (see also the discussion in [227]). For real photons general symmetry requirements restrict the possible final states, as is well known from the Landau-Yang theorem. Especially it is impossible to produce spin 1 final states. In e^+e^- annihilation only states with $J^{PC} = 1^{--}$ can be produced directly. Two photon collisions give access to most of the $C = +1$ mesons.

In principle $C = -1$ vector mesons can be produced by the fusion of three (or, less important, five, seven, ...) equivalent photons. This cross section scales with Z^6. But it is smaller than the contribution coming from γA collisions, as discussed above, even for nuclei with large Z (see [199]).

The cross section for $\gamma\gamma$ production in a heavy ion collision factorizes into a $\gamma\gamma$ luminosity function and a cross section $\sigma_{\gamma\gamma}(W_{\gamma\gamma})$ for the reaction of the quasi-real photons $\gamma\gamma \to f$ where f is any final state of interest
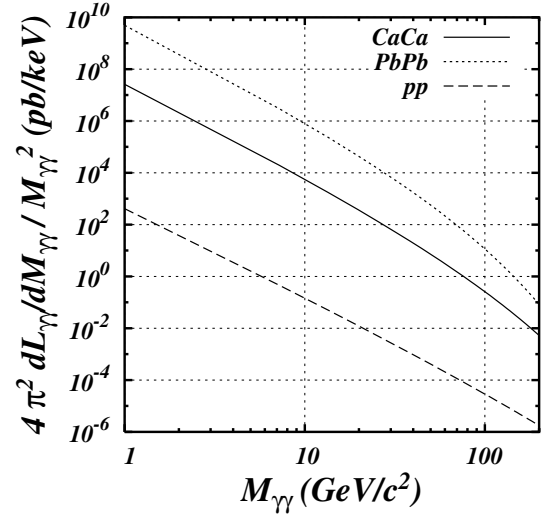
Fig. 7.6. The universal function $4\pi^2 M_{\gamma\gamma}^{-2} d\mathcal{L}_{\gamma\gamma}/dM_{\gamma\gamma}$ is plotted for different ion species at the LHC. We use $R = 1.2A^{1/3}$ fm and $\gamma = 2950$, 3750 and 7000 for Pb+Pb, Ca+Ca and pp respectively

(see 7.12). When the final state is a narrow resonance, its production cross section in two-photon collisions is given by

$$\sigma_{\gamma\gamma \to R}(M^2) = 8\pi^2(2J_R + 1)\Gamma_{\gamma\gamma}(R)\delta(M^2 - M_R^2)/M_R \quad (7.16)$$

where J_R, M_R and $\Gamma_{\gamma\gamma}(R)$ are the spin, mass and two-photon width of the resonance R. This makes it easy to calculate the production cross section $\sigma_{AA \to AA+R}$ of a particle in terms of its basic properties.

In Fig. 7.6 the function $4(\pi^2 d\mathcal{L}_{\gamma\gamma}/dM)/M^2$ is plotted for various systems. It can be directly used to calculate the cross section for the production of a resonance R from

$$\sigma_{AA \to AA+R}(M) = (2J_R + 1)\Gamma_{\gamma\gamma}\frac{4\pi^2 d\mathcal{L}_{\gamma\gamma}/dM}{M^2}. \quad (7.17)$$

We will now give a general discussion of possible photon-photon physics at relativistic heavy ion colliders. Invariant masses up to several GeV can be reached at RHIC and up to about 100 GeV at the LHC.

We can divide our discussion into the following two main subsections: Basic QCD phenomena in $\gamma\gamma$ collisions and $\gamma\gamma$ collisions as a tool for new physics, especially at very high invariant masses. An interesting topic is e^+e^- pair production. The fields are strong enough to produce multiple pairs in single collisions. A discussion of this subject together with calculations within the semiclassical approximation can be found in [252, 253, 254, 255].

7.2.4 Basic QCD phenomena in $\gamma\gamma$ collisions

Hadron spectroscopy: Light quark spectroscopy

One may say that photon-photon collisions provide an independent view of meson and baryon spectroscopy. They

provide powerful information on both the flavour and spin/angular momentum internal structure of the mesons. Much has already been done at e^+e^- colliders. Light quark spectroscopy is possible at RHIC, benefiting from the high $\gamma\gamma$ luminosities. Detailed feasibility studies exist [218,219, 220, 221]. In these studies, $\gamma\gamma$ signals and backgrounds from grazing nuclear and beam gas collisions were simulated with both the FRITIOF and VENUS Monte Carlo codes. The narrow $p_\perp$-spectra of the $\gamma\gamma$ signals provide a good discrimination against the background (see also the discussion of a possible trigger in 7.2.8 below). The possibilities at the LHC are given in the FELIX Letter of Intend [119].

The absence of meson production via $\gamma\gamma$ fusion is also of great interest for a glueball search. The two-photon width of a resonance is a probe of the charge of its constituents. Thus the magnitude of the two-photon coupling can serve to distinguish quark dominated resonances from glue-dominated resonances "glueballs". In $\gamma\gamma$ collisions, a glueball can only be produced via the annihilation of a $q\bar{q}$ pair into a pair of gluons whereas a normal $q\bar{q}$-meson can be produced directly. The "stickiness" of a mesonic state X is defined as

$$S_X = \frac{\Gamma(J/\psi \to \gamma X)}{\Gamma(X \to \gamma\gamma)} \qquad (7.18)$$

We expect the stickiness of all mesons to be comparable, while for glueballs it should be enhanced by a factor of about $1/\alpha_s^4 \sim 20$. In a recent reference, results of the search for $f_J(2220)$ production in two-photon interactions were presented [256]. A very small upper limit for the product of $\Gamma_{\gamma\gamma}B_{K_sK_s}$ was given where $B_{K_sK_s}$ denotes the branching fraction of its decay into K_sK_s. From this it was concluded that there is strong evidence that the $f_J(2220)$ is a glueball.

Heavy quark spectroscopy

Only the two-photon width $\Gamma_{\gamma\gamma}$ of η_c (2960 MeV, $J^{PC} = 0^{-+}$) is known from experiment. But the two-photon widths of P-wave charmonium states have been measured with only modest accuracy. For RHIC the study of η_c is a real challenge [219]; the luminosities are falling and the branching ratios to experimentally interesting channels are small.

In Table 7.1 (adapted from Table 2.6 of [119]) the two-photon production cross sections for $c\bar{c}$ and $b\bar{b}$ mesons in the rapidity range $|y| < 7$ are given. Also given are the number of events in a 10^6 s run with the ion luminosities of 4×10^{30}cm^{-2}s^{-1} for Ca+Ca and 10^{26}cm^{-2}s^{-1} for Pb+Pb. Millions of C-even charmonium states will be produced in coherent two-photon processes during a standard 10^6 s heavy ion run at the LHC. The detection efficiency of charmonium events is estimated $\approx 5\%$ for the forward-backward FELIX geometry [119], *i.e.*, one can expect detection of about 5×10^3 charmonium events in Pb+Pb and about 10^6 events in Ca+Ca collisions. This is two to three orders of magnitude higher than what is expected
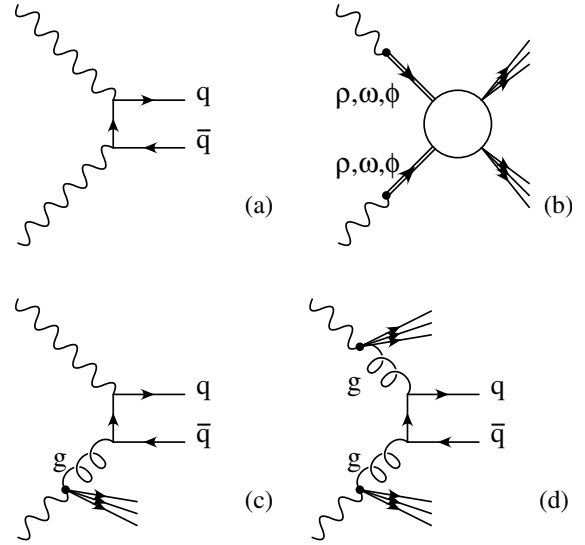
Fig. 7.7. Diagrams showing the contribution to the $\gamma\gamma \to$hadron reaction: direct mechanism (**a**), vector meson dominance (**b**), single (**c**) and double (**d**) resolved photons

during five years of LEP200 operation. Further details, including experimental cuts, backgrounds and the possibilities for the study of C-even bottomonium states are given in [119].

Vector-meson pair production. Total hadronic cross section

There are various mechanisms to produce hadrons in photon-photon collisions. Photons can interact as point particles which produce quark-antiquark pairs (jets), which subsequently hadronize. Often a quantum fluctuation transforms the photon into a vector meson (ρ, ω, ϕ, ...) opening up all the possibilities of hadronic interactions. In hard scattering, the structure of the photon can be resolved into quarks and gluons. Leaving a spectator jet, the quarks and gluon contained in the photon will take part in the interaction. It is of great interest to study the relative importance of these components and their properties.

The L3 collaboration recently made a measurement of the total hadron cross section for photon-photon collisions in the interval 5 GeV $< W_{\gamma\gamma} < 75$ GeV [251]. It was found that the $\gamma\gamma \to$ hadrons cross section is consistent with the universal Regge behaviour of total hadronic cross sections. The production of vector meson pairs can be studied at RHIC with high statistics in the GeV region [218]. For the possibilities at the LHC, we refer the reader to [119] and [225] where also experimental details and simulations are described.

7.2.5 $\gamma\gamma$ collisions as a tool for new physics

The high flux of photons at relativistic heavy ion colliders offers possibilities for the search of new physics. This in-

Table 7.1. Mass, and $\gamma\gamma$ widths used to calculate the cross section for meson production for Pb+Pb and Ca+Ca collisions at CMS. Masses and widths are taken from [156] and [119]

State	Mass (MeV)	$\Gamma_{\gamma\gamma}$ (keV)	$\sigma(AA \to AA + X)$ Pb+Pb	Ca+Ca
π_0	134	8×10^{-3}	46 mb	210 μb
η	547	0.46	20 mb	100 μb
η'	958	4.2	25 mb	130 μb
$f_2(1270)$	1275	2.4	25 mb	133 μb
$a_2(1320)$	1318	1.0	9.2 mb	49 μb
$f_2'(1525)$	1525	0.1	540 μb	2.9 μb
η_c	2981	7.5	360 μb	2.1 μb
χ_{0c}	3415	3.3	180 μb	1.0 μb
χ_{2c}	3556	0.8	74 μb	0.44 μb
η_b	9366	0.43	450 nb	3.1 nb
η_{0b}	9860	2.5×10^{-2}	21 nb	0.15 nb
η_{2b}	9913	6.7×10^{-3}	28 nb	0.20 nb

cludes the discovery of the Higgs boson in the $\gamma\gamma$ production channel or new physics beyond the standard model such as supersymmetry or compositeness.

Let us mention here the plans to build an e^+e^- linear collider. Such future linear colliders will be used for e^+e^-, $e\gamma$ and $\gamma\gamma$ collisions (PLC, photon linear collider). The photons will be obtained by scattering of laser photons (of eV energy) on high energy electrons ($\approx$ TeV region) (see [257]). Such photons in the TeV energy range will be monochromatic and polarized. The physics program at such future machines includes Higgs boson and gauge boson physics and the discovery of new particles [258].

While the $\gamma\gamma$ invariant masses which will be reached at RHIC will mainly be useful to explore QCD at lower energies, the $\gamma\gamma$ invariant mass range at the LHC — up to about 100 GeV — will open up new possibilities.

A number of calculations have been made for a medium heavy standard model Higgs [259,260,261,262]. For masses $m_H < 2m_{W^\pm}$ the Higgs boson decays dominantly into $b\bar{b}$. Chances of finding the standard model Higgs in this case are marginal [225].

An alternative scenario with a light Higgs boson was, e.g., given in [263] in the framework of the "general two Higgs doublet model". Such a model allows for a very light particle in the few GeV region. With a mass of 10 GeV, the $\gamma\gamma$ width is about 0.1 keV. The authors of [263] proposed to look for such a light neutral Higgs boson at the proposed low energy $\gamma\gamma$ collider. We want to point out that the LHC Ca+Ca heavy ion mode would also be very suitable for such a search.

One can also speculate about new particles with strong coupling to the $\gamma\gamma$ channel. Large 2 photon widths, $\Gamma_{\gamma\gamma}$, will directly lead to large $\gamma\gamma$ production cross sections [264,265]. Since the $\gamma\gamma$ width of a resonance is mainly proportional to the wave function at the origin, huge values can be obtained for very tightly bound systems. Composite scalar bosons at $W_{\gamma\gamma} \approx 50$ GeV are expected to have $\gamma\gamma$ widths of several MeV [264,265]. The

search for these kind of resonances in the $\gamma\gamma$ production channel will be possible at the LHC.

In [266,267] $\gamma\gamma$ processes at pp colliders are studied. It is observed there that non-strongly interacting supersymmetric particles (sleptons, charginos, neutralinos, and charged Higgs bosons) are difficult to detect in hadronic collisions at the LHC. The Drell-Yan and gg fusion mechanisms yield low production rates for such particles. Therefore the possibility of producing such particles in $\gamma\gamma$ interactions at hadron colliders is examined. Since photons can be emitted from protons which do not break up in the radiation process, clean events can be generated which should compensate for the small number. In Reference [266] it was pointed out that at the high pp luminosity of $\mathcal{L} = 10^{34}\text{cm}^{-2}\text{s}^{-1}$ at the LHC, one expects about 16 minimum bias events per bunch crossing. Even the elastic $\gamma\gamma$ events will therefore not be free of hadronic debris. Clean elastic events will be detectable at luminosities below $10^{33}\text{cm}^{-2}\text{s}^{-1}$. This danger of "overlapping events" has also to be checked for the heavy ion runs but it will be much reduced due to the lower luminosities.

Similar considerations for new physics were also made in connection with the planned eA collider at DESY. Again, the coherent field of a nucleus gives rise to a Z^2 factor in the cross section for photon-photon processes in eA collisions [268].

7.2.6 Dilepton production

Electrons (positrons) and to some extent also muons have a special status due to their small mass. They are therefore produced more easily than heavier particles and in the case of e^+e^- pair production also lead to new phenomena like multiple pair production. Their large Compton wave length relative to the nuclear radius means that the equivalent photon approximation has to be modified when applied to them. For the muon, with a Compton wavelength of about 2 fm, we expect the standard equiv-

alent photon approximation to be applicable, with only small corrections. Both electrons and muons can be produced not only as free particles but also into an atomic state bound to one of the ions, or even as a bound state, positronium or muonium.

The special situation of the electron pairs can already be seen from the formula for the impact parameter dependent probability in lowest order. Using the equivalent photon approximation one obtains [202]

$$P^{(1)}(b) \approx \frac{14}{9\pi^2} \left(Z\alpha\right)^4 \frac{1}{m_e^2 b^2} \ln^2\left(\frac{\gamma\delta}{2m_e b}\right) \qquad (7.19)$$

where $\delta \approx 0.681$ and $\gamma = 2\gamma_{\rm cm}^2 - 1$ the Lorentz factor in the target frame, one can see that at RHIC and LHC energies and for impact parameters of the order of the Compton wave length $b \approx 1/m_e$, this probability exceeds one. Unitarity is restored by considering the production of multiple pairs [252, 253, 269, 270, 271]. To a good approximation the multiple pair production can be described by a Poisson distribution. The impact parameter dependent probability needed in this Poisson distribution was calculated in lowest order [254, 272], the total cross section for single pair production [273], and for single and multiple pair production [255]. Of course the total cross section is dominated by the single pair production since the main contribution to the cross section comes from very large impact parameters b. On the other hand one can see that for $b \approx 2R$ the number of electron-positron pairs produced in each ion collision is about 5 (2) for the LHC with $Z = 82$ (RHIC with $Z = 79$). This means that each photon-photon event — especially those at a high invariant mass — which occur predominantly at impact parameters close to $b \gtrsim 2R$ — is accompanied by the production of several low-energy e^+e^- pairs.

Because the total cross section for this process is huge (about 200 kb for Pb+Pb at the LHC), one has to take this into account as a possible background process. Most of the particles are produced invariant masses below 10 MeV and in the very forward direction (see Fig. 7.9). Energetic electrons and positrons are even more concentrated along the beam pipe so that most of them are unobserved. On the other hand, a substantial amount of them are still left at high energies, $e.g.$, above 1 GeV. These QED pairs therefore constitute a potential hazard for the detectors, see Section 7.2.8. On the other hand, they can also be useful as a possible luminosity monitor [119, 217].

Differential production probabilities for $\gamma\gamma$ dileptons in central relativistic heavy ion collisions are calculated using the equivalent photon approximation and an impact parameter formulation and compared to Drell-Yan and thermal dileptons [232, 274, 275]. The very low $p_\perp$ and the angular distribution of the pairs provide a handle for their discrimination.

Higher order corrections, $e.g.$, Coulomb corrections, have to be taken into account for certain regions in the phase space. A classical result for these higher-order effects can be found in the Bethe–Heitler formula for the
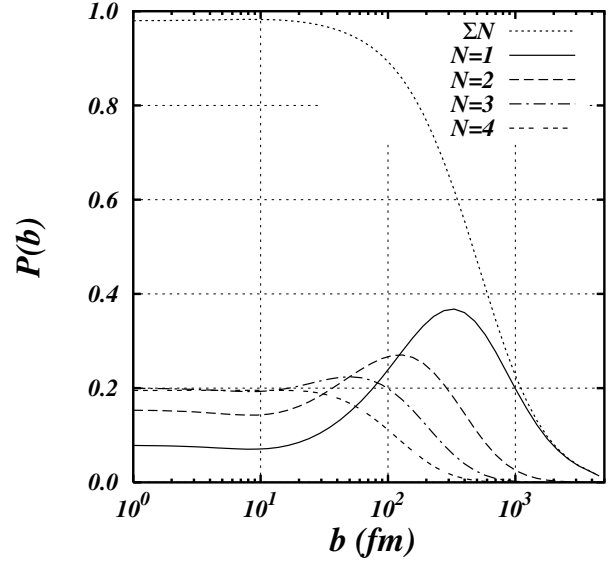
Fig. 7.8. The impact parameter dependent probability to produce N e^+e^- pairs ($N = 1, 2, 3, 4$) in one collision is shown for the LHC ($\gamma = 2950$, Pb+Pb). Also shown is the total probability to produce at least one e^+e^- pair. One sees that at small impact parameters multiple pair production dominates over single pair production

process $Z + \gamma \to Z + e^+ + e^-$

$$\sigma = \frac{28}{9} Z^2 \alpha r_e^2 \left[\ln \frac{2\omega}{m_e} - \frac{109}{42} - f(Z\alpha) \right], \qquad (7.20)$$

with the higher-order term given by

$$f(Z\alpha) = (Z\alpha)^2 \sum_{n=1}^{\infty} \frac{1}{n(n^2 + (Z\alpha)^2)} \qquad (7.21)$$

where $r_e = \alpha/m_e$ is the classical electron radius. As far as total cross sections are concerned, the higher-order contributions tend to a constant for $\omega \to \infty$. A systematic way to take leading terms of higher order effects into account in e^+e^- pair production is pursued in [276, 277] using Sudakov variables and the impact-factor representation. They find a reduction of the single-pair production cross section of the order of 10%. In contrast to this some papers have recently discussed nonperturbative results using a light-cone approach [278, 279, 280]. There it is found that the single-pair production cross section is identical to the lowest order result. A calculation of the change of multiple pair production cross section due to such higher order effects can be found in [281].

Equivalent muons

Up to now only the production of dileptons was considered, for which the four-momentum Q^2 of the photons was less than about $1/R^2$ (coherent interactions). There is another class of processes where one of the interactions is coherent ($Q^2 \leq 1/R^2$) and the other one involves a
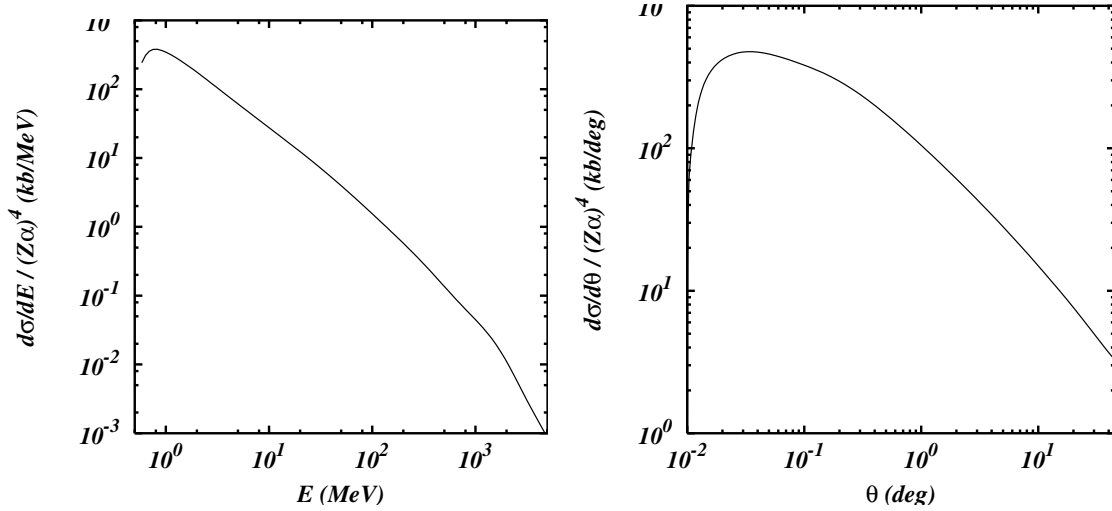
Fig. 7.9. Cross section for the e^+e^- pair production as a function of the energy (**A**) of either electron or positron and as a function of the angle of the electron or positron with the beam axis (**B**). Most pairs are produced with energies between 2–5 MeV and in the very forward or backward direction

deep inelastic interaction ($Q^2 \gg 1/R^2$). These processes are readily described using the equivalent electron— (or muon—, or tau—) approximation, as given, *e.g.*, in [282, 283]. The equivalent photon can be considered as containing muons as partons, that is, consisting in part of an equivalent muon beam. The equivalent muon number is given by [282]

$$f_{\mu/\gamma}(\omega, x) = \frac{\alpha}{\pi} \ln\left(\frac{\omega}{m_\mu}\right)\left(x^2 + (1-x)^2\right) \qquad (7.22)$$

where m_μ denotes the muon mass. The muon energy E_μ is given by $E_\mu = x\omega$, where ω is the energy of the equivalent photon. This spectrum has to be folded with the equivalent photon spectrum given by

$$f_{\gamma/Z}(u) = \frac{2\alpha}{\pi}\frac{Z^2}{u}\ln\left(\frac{1}{um_A R}\right) \qquad (7.23)$$

for $u < u_{\max} = 1/Rm_A$. The deep inelastic lepton-nucleon scattering can now be calculated in terms of the structure functions F_1 and F_2 of the nucleon. The inclusive cross section for the deep-inelastic scattering of the equivalent muons is therefore given by

$$\frac{\mathrm{d}^2\sigma}{\mathrm{d}E'\mathrm{d}\Omega} = \int \mathrm{d}x_1 f_{\mu/Z}(x_1)\frac{\mathrm{d}^2\sigma}{\mathrm{d}E'\mathrm{d}\Omega}(x_1) \qquad (7.24)$$

where $\mathrm{d}^2\sigma(x_1)/\mathrm{d}E'\mathrm{d}\Omega$ can be calculated from the usual invariant variables in deep inelastic lepton scattering (see, *e.g.*, (35.2) of [68]) The lepton is scattered to an angle θ with an energy E'. The equivalent muon spectrum of the heavy ion is

$$f_{\mu/Z}(x_1) = \int_{x_1}^{u_{\max}} \mathrm{d}u f_{\gamma/Z}(u)f_{\mu/\gamma}(x_1/u). \qquad (7.25)$$

This expression can be calculated analytically and work on this is in progress [284].

Such events are characterized by a single muon with an energy E' and scattering angle θ. The accompanying muon of opposite charge, as well as the remnants of the struck nucleus, will scatter to small angles and remain unobserved. The hadrons scattered to large angles can be observed with total energy E_h and momentum in the beam direction of p_{zh}. Using the Jacquet–Blondel variable y_{JB} the energy of the equivalent muon can in principle be reconstructed as

$$E_\mu = \frac{1}{2}\left(E_h - p_{zh} + E'(1 - \cos\theta)\right) \qquad (7.26)$$

This is quite similar to the situation at HERA with the difference that the energy of the lepton beam is continuous, and its energy has to be reconstructed from the kinematics. How well this can be done in practice remains to be seen.

Radiation from e^+e^- pairs

The bremsstrahlung in peripheral relativistic heavy ion collisions was found to be small, both for real [202] and virtual [285] bremsstrahlung photons. This is due to the large mass of the heavy ions. Since the cross section for e^+e^- pair production is so large, one can expect to see sizeable effects from the radiation of these light mass particles. In the soft photon limit (see, *e.g.* [286]) one can calculate the cross section for soft photon emission of the process

$$Z + Z \rightarrow Z + Z + e^+ + e^- + \gamma \qquad (7.27)$$

as

$$\mathrm{d}\sigma(k, p_-, p_+) = -e^2\left[\frac{p_-}{p_-k} - \frac{p_+}{p_+k}\right]^2\frac{\mathrm{d}^3k}{4\pi^2\omega}\mathrm{d}\sigma_0(p_+, p_-) \qquad (7.28)$$

where $d\sigma_0$ denotes the cross section for the e^+e^- pair production in heavy ion collisions. An alternative approach is

Fig. 7.10. The energy dependence of bremsstrahlung photons from e^+e^- pair production is shown for different angles. We show results for Pb+Pb collisions at the LHC

done by using the equivalent photon approximation (EPA) and calculating the exact lowest order matrix element for the process

$$\gamma + \gamma \rightarrow e^+ + e^- + \gamma.$$

In Fig. 7.10 we show results of calculations for low energy photons where the exact lowest order QED process in the equivalent photon approximation has been used [287].

These low energy photons constitute a background for the detectors. Unlike the low energy electrons and positrons, they are of course not bent away by the magnets. The angular distribution of the photons also peak at small angles but again a substantial amount is still left at larger angles, even at 90°.
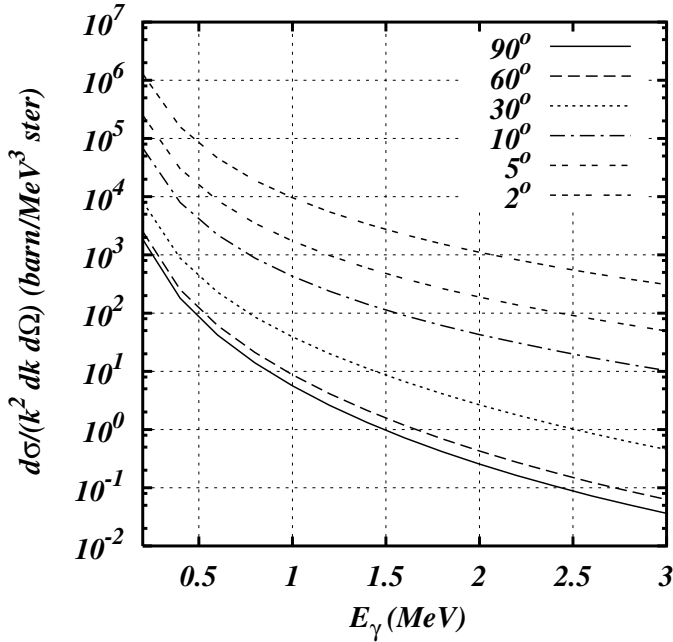
Bound-free pair production

The bound-free pair production, also known as electron-pair production with capture is a process which is also of practical importance in the collider. In this process, a pair is produced but the electron is in an atomic bound state of one of the nuclei. As this changes the charge state of the nucleus, it is lost from the beam. Together with the electromagnetic dissociation of the nuclei (see Section 7.2.2) these two processes are the dominant loss mechanisms for heavy ion colliders.

In [202] an approximate value for this cross section is

$$\sigma_{\text{capt}}^K \approx \frac{33\pi}{10} Z_1^2 Z_2^6 \alpha^6 r_e^2 \frac{1}{\exp(2\pi Z_2 \alpha) - 1} \left[\ln\left(\gamma\delta/2\right) - \frac{5}{3} \right] \tag{7.29}$$

where only capture to the K-shell is included. The cross section for all higher shells is expected to be of the order of

Table 7.2. Parameters A and B (see (7.30)) and the resulting total cross sections for the bound-free pair production for RHIC and LHC. The parameters are taken from [291]

Ion	A	B	$\sigma(\gamma = 106)$	$\sigma(\gamma = 2950)$
Pb	15.4b	−39.0b	115 b	222 b
Au	12.1b	−30.7b	90 b	173 b
Ca	1.95mb	−5.19mb	14 mb	27.8 mb
O	4.50μb	−12.0μb	32 μb	64.3 μb

20% of this cross section (see Eqs. (7.6.23) and (7.6.24) in [202]). The cross section in (7.29) may be parameterized as

$$\sigma = A \ln \gamma + B. \tag{7.30}$$

This form is universal at sufficiently high γ. The constants A and B only depend on the type of the target. The above cross section was found making use of the EPA and also using approximate wave functions for the bound state and continuum. More precise calculations exist in the literature [288, 289, 290, 291, 292, 293]. Recent calculations within DWBA for high values of γ have shown that the exact first order results do not differ significantly from EPA results [294, 295]. Values of the parameters A and B [289, 291] for typical cases are given in Table 7.2.

For a long time the effect of higher order and non-perturbative processes have been under investigation. At lower beam energies, in the region of few GeV per nucleon, coupled channel calculations have indicated that these give large contributions, especially at small impact parameters. Newer calculation tend to predict considerably smaller values, of the order of the first order result and in a recent article. Baltz finds that in the limit $\gamma \rightarrow \infty$ contributions from higher orders are even slightly smaller than the first order results [296].

Bound-free pair production was measured in two recent fixed target experiments at the SPS, with $\gamma = 168$ [297] and $\gamma \approx 2$ [298, 299]. Both experiments found good agreement between measurement and calculations.

We note that the electron and positron can also form a bound state, positronium. This is in analogy to the $\gamma\gamma$ production of mesons discussed in Section 7.2.3. With the known width of the parapositronium $\Gamma((e^+e^-)_{n=1}{}^1S_0 \rightarrow \gamma\gamma) = mc^2\alpha^5/2$, the photon-photon production of this bound state was calculated [300]. The production of orthopositronium, $n = 1^3S_1$ was also calculated recently [301]. As discussed in Section 7.2.3 the production of orthopositronium is only suppressed by the factor $(Z\alpha)^2$ which is not very small. Therefore one expects that both kind of positronium are produced in similar numbers. Detailed calculation show that the three-photon process is indeed not much smaller than the two-photon process [301, 302].

7.2.7 Event rates at CMS

An overview of the expected event rate for a number of different photon-photon reactions to either discrete states
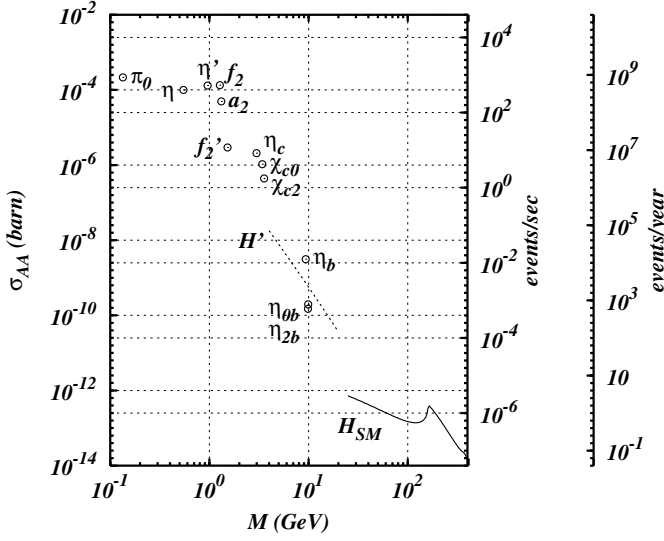
Fig. 7.11. Overview of the total cross section and production rates (both per second and per 10^6 s) of different resonances in Ca+Ca collisions at CMS. We have used the parameters as given in the text and in Table 7.1

Fig. 7.12. Overview of the total cross section and production rates (both per second and per 10^6 s) per GeV for different dilepton and $Q\bar{Q}$ production for Ca+Ca collisions at CMS. Also shown is the total hadronic cross section. The parameters used are given in the text

or continuum states is given in the following figures. The y axis on the right hand sides show both the number of events per second and per 10^6 s. We use beam luminosities of $10^{26}\mathrm{cm}^{-2}\mathrm{s}^{-1}$ for Pb+Pb and $4 \times 10^{30}\mathrm{cm}^{-2}\mathrm{s}^{-1}$ for Ca+Ca. The resonances have been calculated using the masses and photon-decay widths given in Table 7.1. For the calculation of the rate for a standard model Higgs boson, we use the approach discussed in [259]. H' denotes a nonstandard Higgs as given in the "general two-Higgs doublet model" [263]. Because its photon-photon decay width is rather weakly dependent on its mass in the relevant mass region, we have used a constant value of 0.1 keV in our calculations.

The total hadronic cross section $\sigma_{\gamma\gamma}(\mathrm{hadron})$ is parameterized as [251]

$$\sigma_{\gamma\gamma}(\mathrm{hadron}) = A(s/s_0)^\epsilon + B(s/s_0)^{-\eta} \qquad (7.31)$$

with $s_0 = 1$ GeV^2, $\epsilon = 0.079$, $\eta = 0.4678$, $A = 173$ nb and $B = 519$ nb. For dilepton and $q\bar{q}$ production via $\gamma\gamma$, we have used the lowest order QED expression for point-like fermions. The heavy quark masses are $m_c = 1.1$ GeV and $m_b = 4.1$ GeV.

7.2.8 Selecting $\gamma\gamma$ events

The $\gamma\gamma$ luminosities are rather large but the $\gamma\gamma \to X$ cross sections are small compared to their hadronic counterparts, therefore, *e.g.*, the total hadronic production cross section for all events is still dominated by hadronic events. This makes it necessary to have an efficient trigger to distinguish photon-photon events from hadronic ones.

There are some characteristic features that make such a trigger possible. $\gamma\gamma$ events are characterized by the fact that both nuclei remain intact after the interaction. Therefore a $\gamma\gamma$ event will be characterized by a low multiplicity
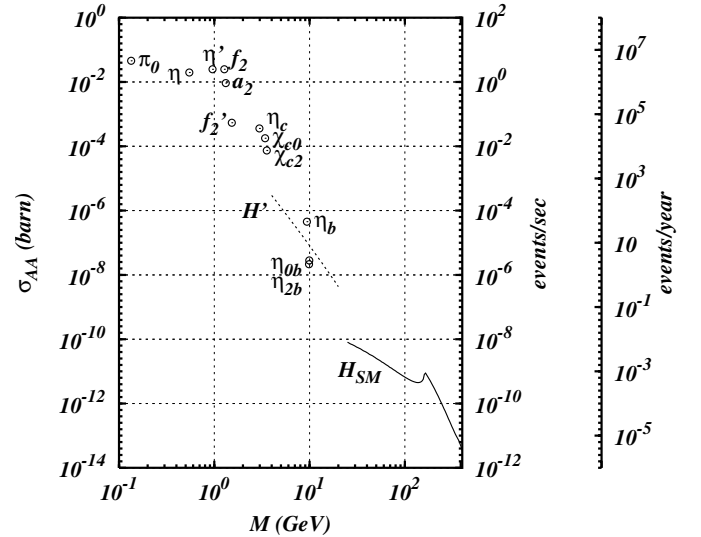
Fig. 7.13. Overview of the total cross section and production rates (both per second and per 10^6 s) of different resonances in Pb+Pb collisions at CMS. We have used the parameters as given in the text and in Table 7.1

in the central region and no event in the very forward or backward directions (corresponding to fragments of the ions). The momentum transfer and energy loss for each ion are too small for the ion to leave the beam. It should be noted that in a $\gamma\gamma$ interaction with an invariant mass of several GeV leading to hadronic final states, quite a few particles will be produced, see, *e.g.*, [251]

A second characteristic is the small transverse momenta of the produced system due to the coherence condition $q_\perp < 1/R \approx 50$ MeV. If one is able to make a complete reconstruction of the momenta of all produced par-
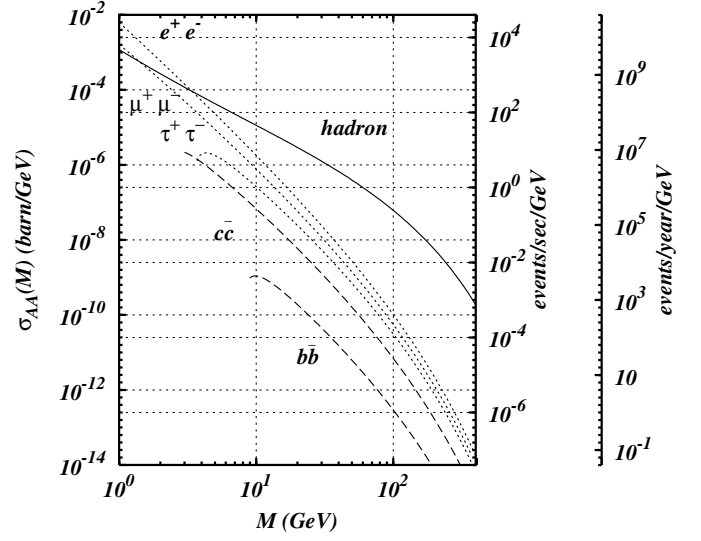
Fig. 7.14. Overview of the total cross section and production rates (both per second and per 10^6 s) per GeV for different dilepton and $Q\bar{Q}$ production for Pb+Pb collisions at CMS. Also shown is the total hadronic cross section. The parameters used are given in the text
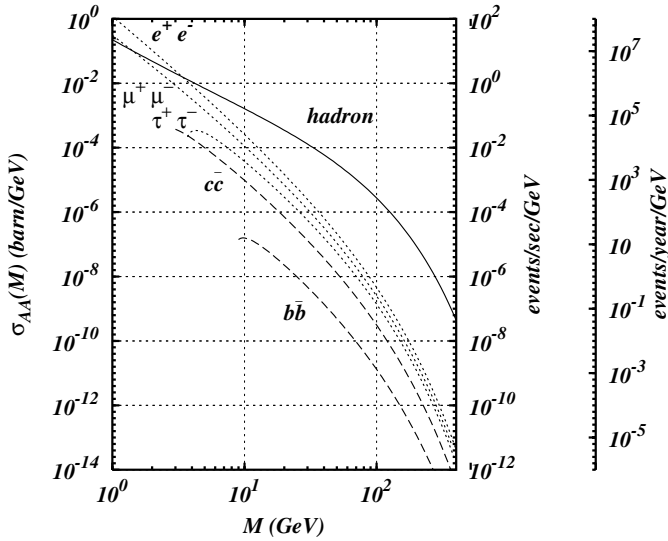
ticles with sufficient accuracy, this can be used as a very good suppression at grazing collisions. As the strong interaction is short ranged, it has normally a much broader distribution in the transverse momenta. A calculation using the PHOJET event generator [303] to study processes in central and grazing collisions by Pomeron-exchange found an average transverse momentum of ~ 450 MeV, about a factor of 10 larger than the $\gamma\gamma$ events. In a study for the STAR experiment [304] it was also found that triggering for small transverse momenta is an efficient method to reduce the background coming from grazing collisions.

Another question that has to be addressed is the importance of diffractive events, that is, *e.g.* photon-Pomeron and Pomeron-Pomeron processes in ion collisions. From experiments at HERA one knows that the proton has a large probability to survive intact after these collisions. The theoretical situation unfortunately is not very clear for these high energies and especially for nuclei as compared to nucleons. Some calculations within the dual parton model have been made and were interpreted as an indication that photon-Pomeron and Pomeron-Pomeron events are of the same size or even larger than photon-photon events [303]. But these calculations were done without requiring the condition to have intact nuclei in the final state. As the nuclei are bound only rather weakly and as mentioned above the average momentum transfer to the nucleus is of the order of 200 MeV, it is very likely that the nucleus will break up in such a collision. First estimates based on this model indicate that this leads to a substantial suppression of diffractive events, favouring again the photon-photon events.

The cross section ratio of photon-photon to Pomeron-Pomeron processes depends on the ion species. Roughly it can be approximated by $Z^4/A^{1/3}$ [119]. Thus for heavy ions like Pb we may expect dominance of the photon-

photon processes whereas, say in pp collisions, Pomeron-Pomeron processes will dominate the coherent collisions.

Nevertheless, diffractive events are of interest in ion collisions too. As one is triggering on an intact nucleus, one expects that the coherent Pomeron emission from the whole nucleus will lead to a total transverse momentum of the produced system similar to the $\gamma\gamma$ events. Therefore one expects that part of the events are coming from diffractive processes. It is of interest to study how these could be further distinguished from the photon-photon events.

Another class of background events are additional electromagnetic processes. One of the dominant events here is the electromagnetic excitation of the ions due to an additional single photon exchange. As mentioned above, this is one of the dominant beam loss processes for Pb+Pb collisions. The probability to excite at least one of the ions for Pb+Pb collisions is about 65% and about 2% for Ca+Ca for an impact parameter of $2R$. Especially at large invariant masses, $\gamma\gamma$ events occur at impact parameter close to $2R$. Therefore in the case of Pb+Pb collisions one has to expect that most collisions are accompanied by the excitation or dissociation of one of the ions [148,305]. Most of the excitations lead into the giant dipole resonance (GDR), which has almost all of the dipole strength. As it decays predominantly via the emission of a neutron, this leads to a relativistic neutron with an energy of about 3 TeV in the forward direction. Similarly, all other low energy breakup reactions in the rest frame of one of the ions are boosted to high energy particles in the laboratory. In order to increase the $\gamma\gamma$ luminosity it would be interesting to include these events also in the $\gamma\gamma$ trigger. On the other hand one has to make sure that this does not obscure the interpretation of these events as photon-photon events.

Another background process is the production of electron-positron pairs, see Section 7.2.6. Due to their small mass, they are produced rather copiously. They are predominantly produced at low invariant masses and energies and in the forward and backward direction. Figure 7.15 shows cross section as a function of energy and angle for different experimental cuts. On the other hand, since the total cross section for this process is enormous, ≈ 230 kb for Pb+Pb collisions, 800 b for Ca+Ca collisions, a significant cross section remains even at high energies in the forward direction. This has to be taken into account when designing forward detectors. Table 7.3 shows the cross section for e^+e^- production where the energy of both particles is above a certain threshold value.

7.2.9 Summary

In this chapter the basic properties of peripheral hadron-hadron collisions are described. Electromagnetic processes, that is, photon-photon and photon-hadron collisions, are an interesting option, complementing the program for central collisions. It is the study of "silent events" with relatively small multiplicities and a small background. These are good conditions to search for new physics. The method of equivalent photons is a well es-
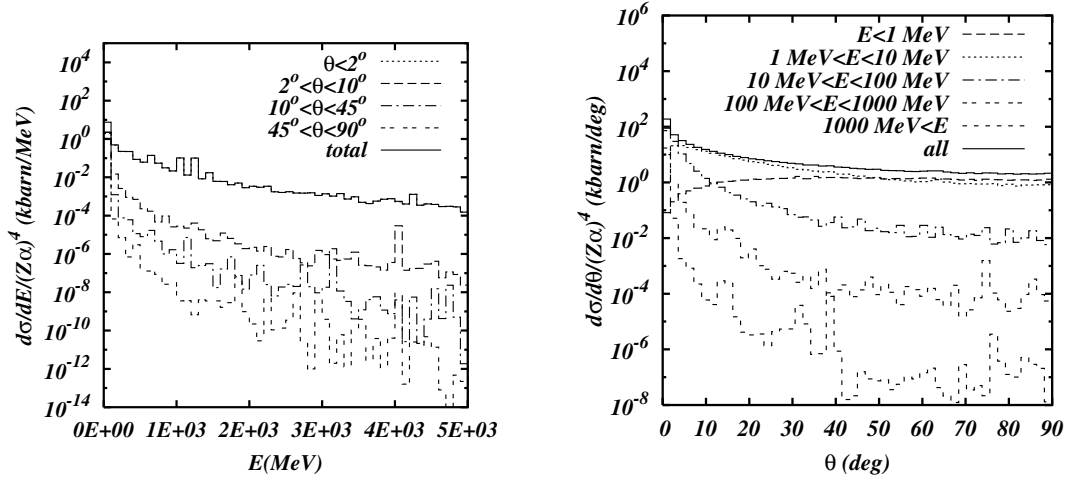
Fig. 7.15. The single differential cross section for a number of experimental constraints. **a** for different angular ranges as a function of energy, **b** for different energies as a function of the angle with the beam axis θ

Table 7.3. Cross sections of e^+e^- pair production when both electron and positron have an energy above the threshold value E_{thr}

E_{thr} (GeV)	σ(Pb+Pb)	σ(Ca+Ca)
0.25	3.5 kb	12 b
0.50	1.5 kb	5.5 b
1.0	0.5 kb	1.8 b
2.5	0.08 kb	0.3 b
5.0	0.03 kb	0.1 b

tablished tool to describe these kinds of reactions. Reliable results of quasireal photon fluxes and $\gamma\gamma$ luminosities are available. Unlike electrons and positrons heavy ions and protons are particles with an internal structure. Effects arising from this structure are well under control and minor uncertainties coming from the exclusion of central collisions and triggering can be eliminated by using a luminosity monitor from muon — or electron — pairs. A trigger for peripheral collisions is essential in order to select photon-photon events. Such a trigger seems to be possible based on the survival of the nuclei after the collision and the use of the small transverse momenta of the produced system. A problem which is difficult to judge quantitatively at the moment is the influence of strong interactions in grazing collisions, *i.e.*, effects arising from the nuclear stratosphere and Pomeron interactions.

The high photon fluxes open up possibilities for photon-photon as well as photon-nucleus interaction studies up to energies hitherto unexplored at the forthcoming colliders RHIC and LHC. Interesting physics can be explored at the high invariant $\gamma\gamma$ masses where detecting new particles could be within range. Also very interesting studies within the standard model, *i.e.*, QCD studies will be possible. This ranges from the study of the total $\gamma\gamma$ cross section into hadronic final states up to invariant masses of about 100 GeV to the spectroscopy of light and heavy mesons. The production via photon-photon fu-

sion complements the production from single photons in an e^+e^- collider and hadronic collisions via other partonic processes.

Peripheral collisions using photon-Pomeron and Pomeron-Pomeron collisions, diffractive processes, are an additional application. They use essentially the same triggering conditions and therefore one should be able to record them at the same time as photon-photon events.

8 Muon trigger and DAQ performances

8.1 Introduction

The muons from heavy quark resonances decay, from J/ψ to Υs have rather low p_{T}. Therefore it is extremely important to have low threshold for muon trigger and reconstruction. This is illustrated in Fig. 8.1, where the number of collected $\Upsilon \rightarrow \mu^+\mu^-$ events is presented as a function of trigger threshold $p_{\mathrm{T}}^{\mathrm{cut}}$. The very strong dependence of available statistics on the $p_{\mathrm{T}}^{\mathrm{cut}}$ is clearly visible. For this reason among the requirements for the CMS muon trigger one finds [306]: low p_{T} reach should be limited only by muon energy loss in the calorimeters. In the next section we discuss what is the low p_{T} reach of the CMS muon system according to the current design.

Although the present geometry of the barrel extends up to $\eta = 1.3$, the trigger estimations presented in this chapter where done with a former geometry with a barrel up to $\eta = 1.5$.

8.2 Acceptance for low p_{T} muons

In this section we study the performance of the Pattern Comparator Trigger (PACT) based on Resistive Plate Chambers (RPC). This trigger searches for a patterns of hits in 4 RPC planes along a possible muon track. In the endcaps the RPC planes are placed in 4 muon stations, one plane per station. In the barrel two algorithms are
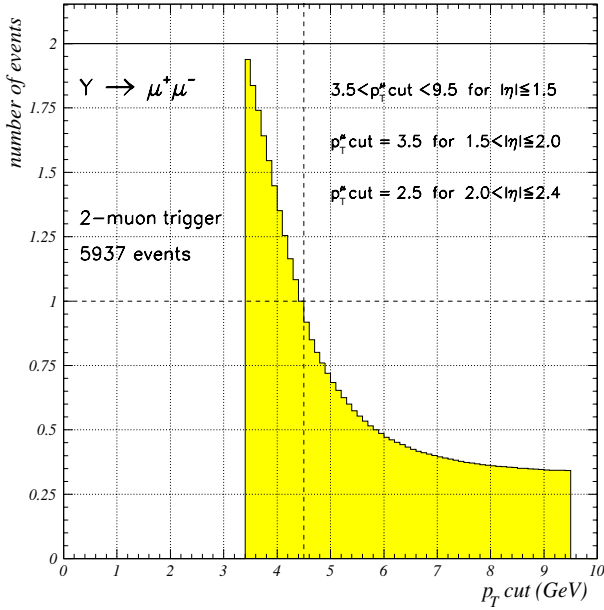
Fig. 8.1. Expected number of $\Upsilon \rightarrow \mu^+\mu^-$ events as a function of trigger threshold p_T^{cut} normalized to $p_T^{\mathrm{cut}} = 4.5$ GeV/c

Fig. 8.3. Muon trigger acceptance (coincidence of 3 out of 4 RPC planes required) for muons with $4.5 < p_T < 5.0$ GeV/c for a central gap of 20 cm, plus dead RPC edges of 4 cm on each side of the gap

used. High p_T muons ($p_T > 5$ GeV/c) are required to give hits in 4 RPC planes (denoted as MS1, MS2, MS3, MS4) placed in different muon stations. Low p_T muons ($p_T \leq 5$ GeV/c) also need to give hits in 4 RPC planes, but this time placed only in the first two muon stations (MS1, MS1', MS2, MS2'). In order to account for chamber inefficiency and dead areas, a coincidence of 3 out of 4 planes is enough to give a trigger. The range-limited minimal value of the trigger threshold p_T^{min} which can be obtained in CMS is plotted in Fig. 8.2 (left) as a function of $|\eta|$. Because of Landau fluctuations of the energy lost by muons, different p_T^{min} values are obtained for different required efficiencies. Because the detector design is not yet completely frozen, one can expect some minor changes in the amount of absorber (for example due to cables and services just behind the coil cryostat), however these should not be bigger than one nuclear interaction length λ. The effects of a $+1\lambda$ increment in depth is indicated in the figure as a kind of error bar. For comparison the total momentum p^{min} is also plotted in Fig. 8.2 (right).

There is a region at $|\eta| \approx 0.3$ with particularly low efficiency. This is due to the gap between the central and next neighbouring wheels of the CMS barrel. The gap is needed mainly for cables and services of inner detectors and calorimeters. In the current design it is 20 cm wide. On top of that, one should add 2×4 cm of dead RPC edge. There are efforts at present to reduce these numbers, but it seems that the absolute lower limit is 14+2×2 cm. The effect of this gap on the muon trigger acceptance is better seen in Fig. 8.3. The trigger acceptance (coincidence of 3 out of 4 planes required) for muons with $4.5 < p_T < 5.0$ GeV/c is plotted for low and high p_T algorithms separately as well as for the logical OR of the two. The full acceptance table is given in Fig. 8.4.
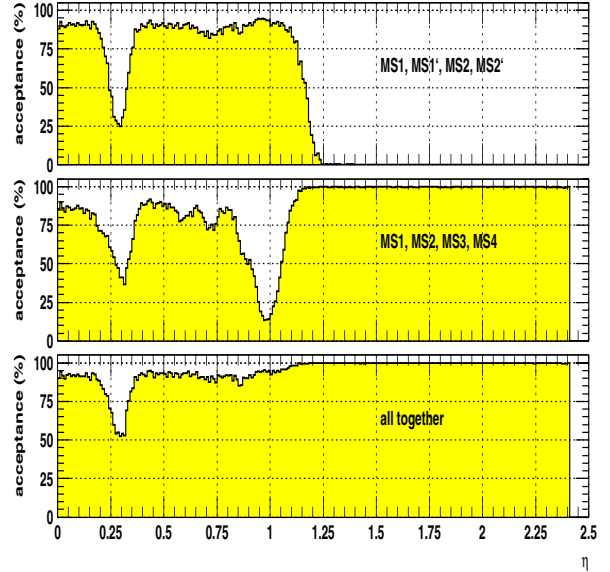
Keeping in mind all the above mentioned uncertainties one can conclude that the lowest "triggerable" muon p_T is about 4 GeV/c in the barrel and it decreases down to 2 GeV/c in the endcaps, if an efficiency of 90% for muon is required. One can, however, reduce p_T^{min} in the barrel down to 3.5 GeV/c relaxing the requirement on the efficiency down to 80 %. Relaxing it further down to 50% allows us to trigger on muons with $p_T > 3.2$ GeV/c. This can be better seen from Fig. 8.5 (left).

In the case of heavy ion physics we are interested in two-muon events. Requirement of 2 muons at the first level trigger squares the single muon trigger efficiency. The result is shown as the lower curve in Fig. 8.5 (right). In such a case the trigger is rather inefficient, especially at low p_T, so crucial for heavy ion physics. If one can, however, trigger on anyone of the two muons then the inefficiency gets squared, and the trigger performance becomes very good, as seen from the upper curve in Fig. 8.5 (right).

A single muon trigger is however subject to various backgrounds. Among them are prompt muons form c- and b-quark decays, muons from π and K decays, punchthrough of hadronic showers. The crucial question is then whether the first level trigger rate due to background is tolerable in view of higher levels. We are going to address this question in the following sections.

8.3 Calculation of muon trigger rates

The question of the trigger rate due to background should be addressed through rather detailed simulation. One cannot, however, simulate full events, because getting reasonable statistics would require enormous amount of CPU time. Therefore it is important to identify various contri-
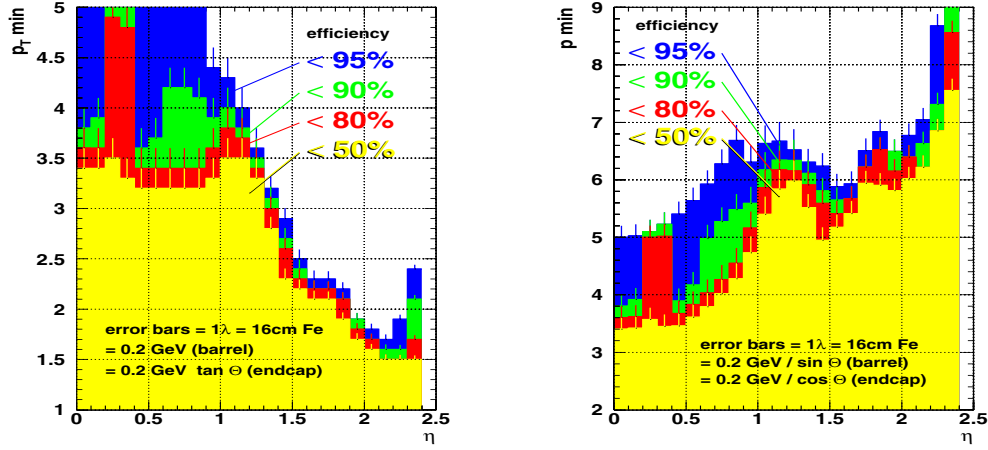
Fig. 8.2. Minimal muon trigger threshold p_T^{min} for various required efficiencies as a function of muon pseudorapidity (*left*). Total momentum corresponding to the minimal muon trigger threshold as a function of muon pseudorapidity (*right*)

butions to the trigger rate and find an optimal simulation strategy for each of them. A muon trigger can be caused by:

– prompt muons from c- and b-quark decays (in the case of heavy ion collisions, heavier particles can be neglected),
– muons from hadron decays (mainly π and K),
– charged particles (electrons, hadrons, muons) emerging from hadronic showers (this component is often called punchthrough),
– hadrons non-interacting in the calorimeters,
– beam halo muons,
– uncorrelated hits due to electrons produced by photons following a thermal neutron capture,
– detector noise.

The first three sources clearly dominate over the others and only those are considered in this chapter. In order to achieve reasonable statistics we simulate single hadrons and muons. Hadrons are allowed to develop showers and decay into muons. All charged particles can produce hits in RPC detectors and thus cause a trigger. Obtained trigger rates should be weighted by the expected p_T spectra. In order to do that one needs to know the shape of the hadron and muon p_T spectra.

8.4 Hadron and muon p_T spectra

Typically the p_T spectrum of hadrons in proton-proton (pp) or heavy ion (AA) collisions is parameterized in the following way

$$\frac{dR}{dp_T}\left(\frac{Hz}{GeV.\eta-unit}\right)$$

$$= A \exp\left(-\frac{\sqrt{m_\pi^2 + p_T^2}}{T}\right) \quad \text{for} \quad p_T \leq p_T^{lim}$$

$$= \frac{B}{(1 + \frac{p_T}{p_T^0})^n} \quad \text{for} \quad p_T > p_T^{lim}$$

Table 8.1. Parameters of fits to measured and simulated hadron p_T spectra

	CDF pp	PYTHIA	HIJING
T	0.16 GeV	0.16 GeV	0.16 GeV
p_T^0	1.30 GeV/c	0.74 GeV	0.16 GeV
n	8.28	7.2	5.1
p_T^{min}	0.5 GeV/c	0.5 GeV	1.1 GeV
B	8.120×10^8	8.804×10^8	9.355×10^8

where

$$A = B \left(1 + \frac{p_T^{lim}}{p_T^0}\right)^n \exp\left(-\frac{\sqrt{m_\pi^2 + p_T^{lim\,2}}}{T}\right)$$

Recent experimental data, closest to the LHC conditions, are from the CDF experiment [307]. Parameters of the above formula fitted to these data are listed in Table 8.1. Pb+Pb collisions at $\sqrt{s} = 5.5$ TeV have been simulated by the ALICE collaboration [9] using PYTHIA and HIJING Monte Carlo. Results of fits to obtained hadron p_T distributions are also given in Table 8.1. The parameter B in the table is normalized to give an expected number of charged particles per rapidity unit. In the case of minimum bias Pb+Pb collision at $\sqrt{s} = 5.5$ TeV a conservative estimate is 2500 particles per η unit.

An interesting question is how much different could be the hadron p_T spectra in Pb+Pb collisions at $\sqrt{s} = 5.5$ TeV and in pp collisions at $\sqrt{s} = 14$ TeV. The former one was simulated with PYTHIA and parameterized by the following formula [308]

$$\frac{dR}{dp_T}\left(\frac{Hz}{GeV.\eta-unit}\right) = f(p_T)$$

$$= C \times 1.1429$$

$$\times 10^{10} (p_T^{1.306} + 0.8251)^{-3.781}$$

Fig. 8.4. Acceptance table of the muon trigger in present CMS setup (central gap of 20 cm, plus dead RPC edges of 4 cm on each side of the gap

Axes: vertical p_T min (GeV), from 1.5 (bottom) to 5 (top); horizontal η, from 0 to 2.5. Each cell value is the acceptance (%) in the corresponding η (columns, 0.1 wide) and p_T min (rows, 0.1 wide) bin.

p_T min	0.0	0.1	0.2	0.3	0.4	0.5	0.6	0.7	0.8	0.9	1.0	1.1	1.2	1.3	1.4	1.5	1.6	1.7	1.8	1.9	2.0	2.1	2.2	2.3	2.4
5.0	92	92	80	82	94	93	92	91	87	92	94	99	100	99	100	100	99	100	99	100	100	100	99	100	100
4.9	91	90	74	81	93	93	92	90	89	93	95	99	99	99	99	100	99	100	100	100	100	100	100	99	100
4.8	92	91	69	78	93	92	92	90	90	93	94	99	100	99	99	100	99	100	99	100	99	99	100	99	100
4.7	91	90	66	77	92	91	90	89	90	94	95	99	99	99	100	99	99	100	99	99	100	100	100	99	100
4.6	91	90	56	73	91	91	91	90	88	93	95	99	99	100	99	99	99	99	99	100	99	99	99	99	100
4.5	89	90	55	71	91	92	90	87	89	95	95	99	99	99	99	100	100	99	99	100	99	100	100	99	
4.4	90	89	53	69	91	90	88	88	88	93	95	98	99	99	100	100	100	100	100	99	100	99	100	100	100
4.3	91	89	54	74	91	92	90	90	90	94	94	98	99	99	99	100	100	99	99	99	99	99	99	99	100
4.2	92	88	49	72	90	92	88	88	90	92	93	98	99	99	99	100	99	99	99	99	99	99	99	99	100
4.1	91	88	50	72	90	91	88	89	89	91	91	96	99	99	100	99	99	99	100	99	100	100	99	99	100
4.0	90	90	50	72	92	90	88	87	88	90	89	93	99	99	99	99	99	99	99	99	99	99	99	99	100
3.9	92	87	52	75	91	92	87	86	88	88	84	91	99	99	99	100	100	99	99	99	99	99	99	99	90
3.8	89	86	53	75	89	91	89	88	87	85	78	83	97	99	99	99	99	99	99	99	99	99	99	99	100
3.7	86	82	54	76	90	89	87	88	86	80	71	73	95	99	99	100	99	99	100	99	100	99	99	99	91
3.6	77	74	54	78	89	87	84	86	84	72	58	60	91	99	99	99	99	99	99	99	99	99	99	99	100
3.5	66	57	47	71	83	80	80	82	81	64	42	40	83	98	99	100	99	99	99	99	99	99	99	99	100
3.4	47	34	33	65	73	73	69	75	72	53	29	25	69	97	99	100	99	99	99	99	99	99	99	98	100
3.3	28	14	19	44	53	55	51	62	59	39	19	12	49	96	99	99	99	99	99	99	99	99	99	98	91
3.2	15	2	8	23	29	29	30	41	43	28	11	4	33	94	99	99	99	99	99	99	99	99	99	98	95
3.1	7		1	6	9	10	14	23	24	17	6	2	17	88	98	99	99	99	99	99	99	99	99	98	87
3.0	1				2	2	3	8	10	8	3	1	8	77	97	99	99	99	99	99	99	99	99	97	90
2.9								1	3	2	1		3	64	94	99	99	99	99	99	99	99	99	97	83
2.8										1			1	47	91	99	99	99	99	99	99	99	99	97	90
2.7														28	84	99	99	99	99	99	99	99	99	97	90
2.6														16	76	98	99	99	99	99	99	99	99	95	100
2.5														11	66	94	98	98	99	99	99	99	99	95	87
2.4														8	53	88	96	96	98	99	99	99	99	94	55
2.3														5	36	70	90	91	97	99	99	99	98	93	66
2.2														2	22	44	72	74	94	99	99	99	98	90	81
2.1															10	17	38	42	79	98	99	99	97	89	69
2.0															3	4	10	9	57	95	98	98	96	85	75
1.9															1	1			23	83	97	98	94	84	85
1.8																			3	53	92	96	93	81	50
1.7																				16	74	91	90	76	25
1.6																				1	37	82	83	70	37

Fig. 8.5. Trigger efficiency for $|\eta| < 1.5$ for low and high p_T algorithms (*left*). Trigger efficiency in the case of 1- and 2-muon events ($|\eta| < 1.5$) (*right*)

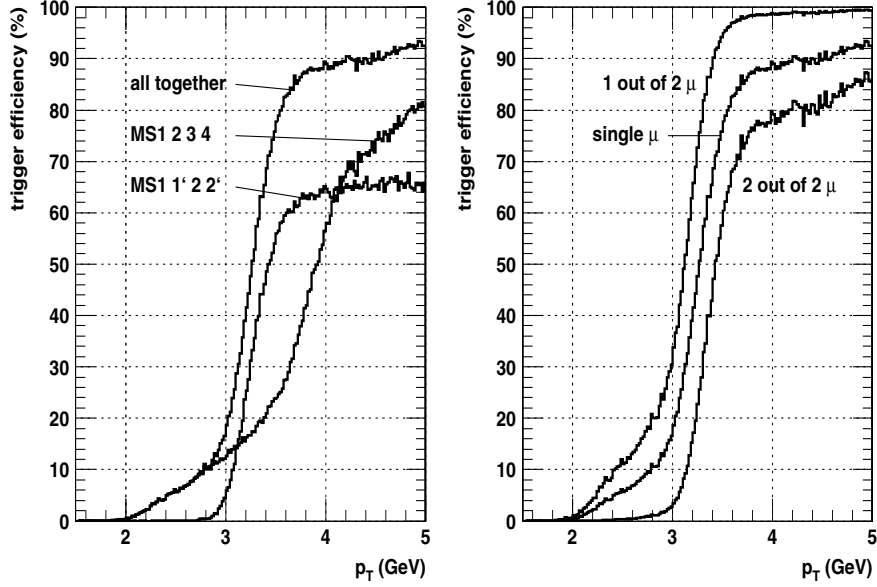The normalisation factor was chosen such that the parameter C is equal to 1 for pp collisions at $\sqrt{s} = 14$ TeV and $\mathcal{L} = 10^{34}$ cm^{-2}s^{-1}. In order to apply this spectrum to heavy ion collisions we used a simple scaling law

$$\sigma_{AA}^{\text{hard}} = A^{2\alpha} \times \sigma_{pp}^{\text{hard}}$$

where $\alpha = 0.95$.

The cross sections in the above formula are marked "hard", because this scaling law can be applied for relatively hard object only. This is our case because we are interested in hadrons with $p_T > 1$ GeV/c. Softer hadrons cannot penetrate calorimeters and therefore they cannot contribute to the muon trigger background.

The parameter C one can calculate as a ratio of particle rates in AA and pp cases. Values obtained are given in Table 8.2.

$$C = \frac{R_{AA}(p_T)}{R_{pp}(p_T)} = \frac{\sigma_{AA}^{\text{hard}} \mathcal{L}_{AA}}{\sigma_{pp}^{\text{hard}} \mathcal{L}_{pp}} = A^{2 \times 0.95} \frac{\mathcal{L}_{AA}}{\mathcal{L}_{pp}}$$

All parameterizations discussed above are plotted in Fig. 8.6 (left). The HIJING spectrum is the hardest, but the overall rate is the smallest. It can be seen however that these distributions do not differ significantly in the region of 3-6 GeV/c which gives the main contribution to the background (as it will be shown in next Section, Fig. 8.9). The rescaled pp spectrum is a rather conservative estimate and therefore it is used hereafter. Consequently we applied the same scaling law also to the p_T spectrum of prompt muons (from c- and b-quark decays). We used the parameterization proposed in [308]. The result is shown in Fig. 8.6 (right).

Table 8.4. Statistics of simulated hadrons

simulation time	events simulated	triggered	fraction
5.5 CPU days	215000	803	0.37 %

8.5 Simulation of hadrons

In order to simulate particle passage and detection in CMS we used CMSIM/GEANT/FLUKA software. FLUKA was chosen to simulate hadronic showers because it was shown [309] that it reproduces the RD5 data on punchthrough significantly better than GHEISHA. The CMS detector was described by the CMSIM 101 package. The RPC trigger was simulated in detail using the MRPC software [310]. The approximate time needed to simulate one particle or one event in given in Table 8.3.

Trying to simulate hadrons according to this spectrum one would immediately have the same problems with CPU time as in the case of full minimum bias events. Therefore we have generated hadrons of p_T between 1 and 100 with a flat distribution of $\log_{10}(p_T)$. One event took on average 2.2 s, which allowed us to simulate 215000 hadrons using "only" 5.5 CPU days. 803 among the simulated hadrons caused a trigger (see Table 8.4). The hadrons were generated with $\phi \in (0, 2\pi)$ and $\eta \in (-0.25, 0.25)$. The following mixture was generated: 31.62% of π^+ and π^-, 5.32% of K^+, K^-, K_L^0 and K_S^0, 3.87% of p, $\bar{p}$, n, $\bar{n}$. The sample contains also those events where the hadron decayed into μ before the calorimeter.

Momentum (p_T^{hadron}) distributions of hadrons causing a muon trigger (for whatever reason) and distribution of momentum given by the trigger (p_T^{trigger}) are shown in Fig. 8.7, left and right respectively. As expected,

Table 8.2. Parameter C for various species

	pp	O+O	Ca+Ca	Nb+Nb	Pb+Pb
A	1	16	40	93	207
$\mathcal{L}(\mathrm{cm}^{-2}\mathrm{s}^{-1})$	10^{34}	3.2×10^{31}	2.5×10^{30}	9×10^{28}	10^{27}
C	1	0.621	0.277	0.0495	0.00251

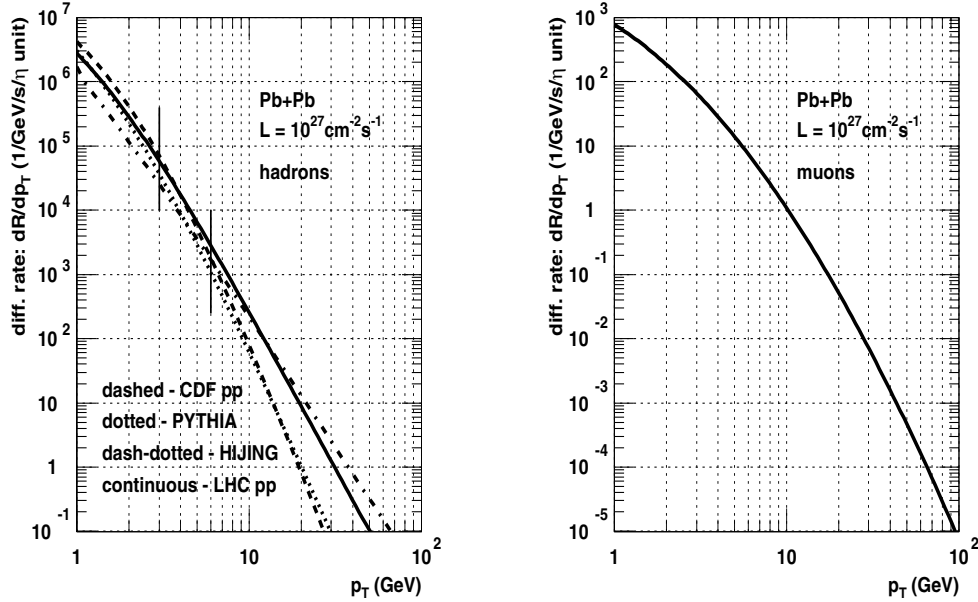**Fig. 8.6.** Expected hadron rate in minimum bias Pb+Pb events at $\mathcal{L} = 10^{27}$ cm^{-2}s^{-1}, compared to present CDF data and rescaled expectation for pp collisions at the LHC (*left*). Expected muon rate in minimum bias Pb+Pb events at $\mathcal{L} = 10^{27}$ cm^{-2}s^{-1}, obtained by rescaling expectation for pp collisions (*right*)

Table 8.3. Simulation time at SHIFTCMS

μ	$< \pi >$ [1-100 GeV]	π = 100 GeV	π = 1 TeV	min.bias event
0.04 s	2.2 s	1 min.	5 min.	1 min.

higher p_T hadrons have a higher probability to produce punchthrough. However the trigger response p_T^{trigger} distribution is rather flat, with a peak at 5 GeV/c. This is because the trigger algorithm is based on 4 muon stations for $p_T > 5$ GeV/c whereas only the first two stations are used below this threshold. Thus any punchthrough event which has no hits in station 3 or 4 cannot have $p_T > 5$ GeV/c assigned by the trigger. Since most of the punchthrough events cannot reach station 3 (which is too deep) they are "suppressed" below 5 GeV/c. This is well illustrated by Fig 8.8 (left). The probability that a hadron of a given p_T causes a trigger can be calculated normalising the distribution from Fig. 8.7 (left) to the number of generated hadrons. The result is shown in Fig. 8.8 (right).

Let us denote the expected p_T spectrum of hadrons by

$$\frac{\mathrm{d}R_{\mathrm{expected}}}{\mathrm{d}p_T}\left(\frac{\mathrm{Hz}}{\mathrm{GeV}.\eta - \mathrm{unit}}\right) = f(p_T)$$

We have simulated a flat distribution in $\log_{10}(p_T)$:

$$\frac{\mathrm{d}N}{\mathrm{d}\log_{10}(p_T)} = \frac{N}{\Delta_l} = \mathrm{const.}$$

where N is the total number of generated hadrons and $\Delta_l = \log_{10}(100\ \mathrm{GeV}) - \log_{10}(1\ \mathrm{GeV}) = 2$.
This can be transformed into:

$$\frac{\mathrm{d}N}{\mathrm{d}p_T} = \frac{\mathrm{d}N}{\mathrm{d}\log_{10}(p_T)}\frac{\mathrm{d}\log_{10}(p_T)}{\mathrm{d}p_T} = \frac{N}{\Delta_l}\frac{1}{p_T\ \ln(10)}$$

The number of particles can be converted into a rate by a weight function $w(p_T)$:

$$\frac{\mathrm{d}R}{\mathrm{d}p_T} = w(p_T)\frac{\mathrm{d}N}{\mathrm{d}p_T}$$

In the case of the generated hadron distribution this reads:

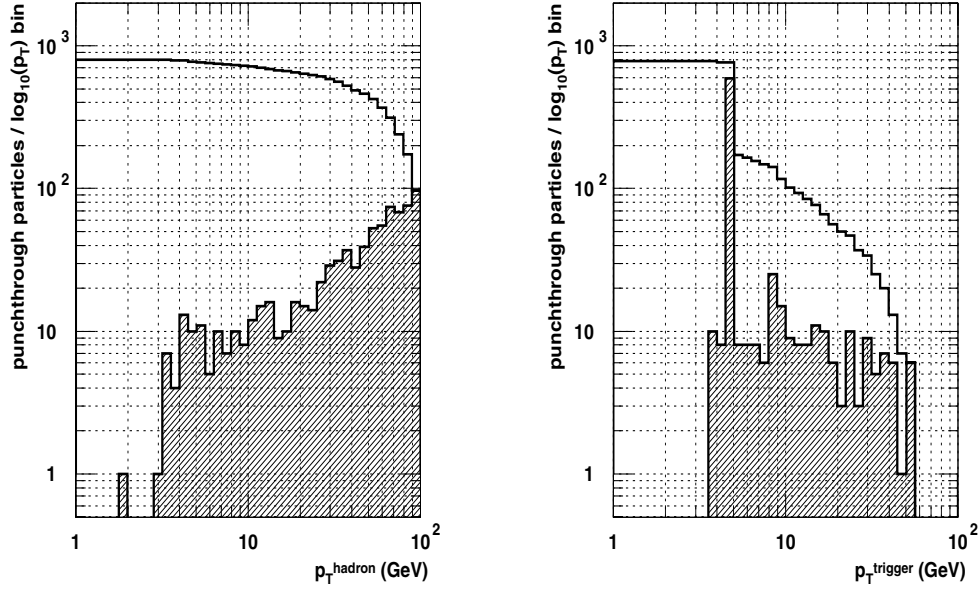$$f(p_T) = w(p_T)\frac{N}{\Delta_l\ p_T\ \ln(10)}$$

Fig. 8.7. *Left:* Differential (*hatched histogram*) and integral (*solid line*) p_T spectra of hadrons causing a trigger. *Right:* Differential (*hatched histogram*) and integral (*solid line*) spectra of trigger responses p_T^{trigger}
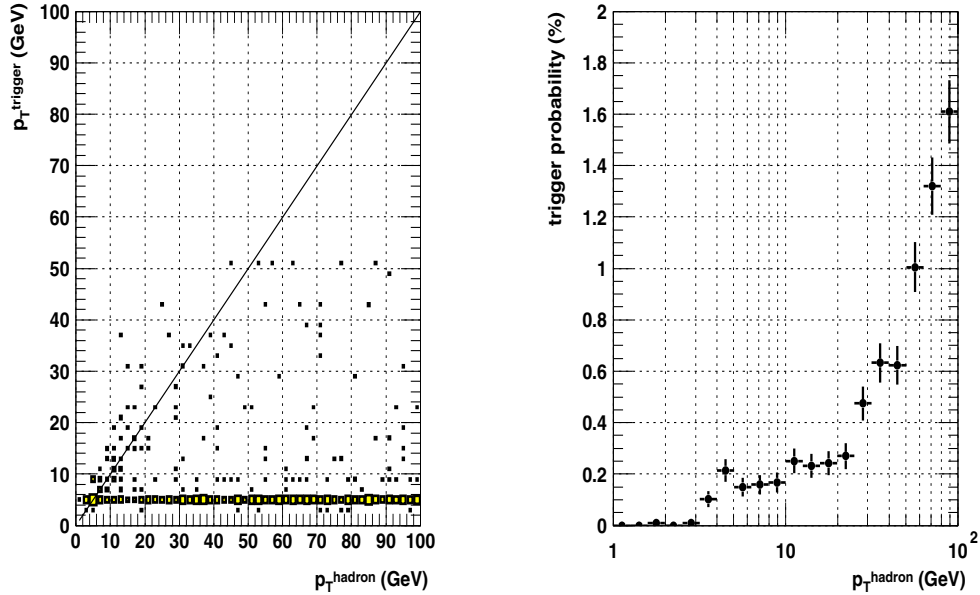

Fig. 8.8. Correlation between hadron momentum p_T^{hadron} and trigger response p_T^{trigger} (*left*). Trigger probability as a function of hadron momentum p_T^{hadron} (*right*)

From here we can calculate the weight function $w(p_T)$:

$$w(p_T) = f(p_T) \, \frac{\Delta_l}{N} \, p_T \, \ln(10)$$

This weight function has been applied to the distributions in Fig. 8.7. The results are shown in Fig. 8.9 left and right for both distributions respectively. It is seen that the contribution from low p_T (3-6 GeV/c) hadrons dominates. The punchthrough probability is higher for high hadron momenta, but the rate of low p_T hadrons is high enough to overcompensate this effect.

In order to obtain the trigger rate as a function of the p_T^{cut} threshold, the distribution from Fig. 8.8 left, has been integrated. The result is shown in Fig. 8.9 (left). The rate due to prompt muons (those from c- and b-quark decays) is shown for comparison. The two rates contribute almost equally to the total trigger rate at the lowest p_T, appropriate for heavy ion physics. They are summed up and normalized to $|\eta| < 1.5$ in Fig. 8.10 (right). It can be seen that the total single muon trigger for this η range at the lowest accessible p_T^{cut} is about 500 Hz.
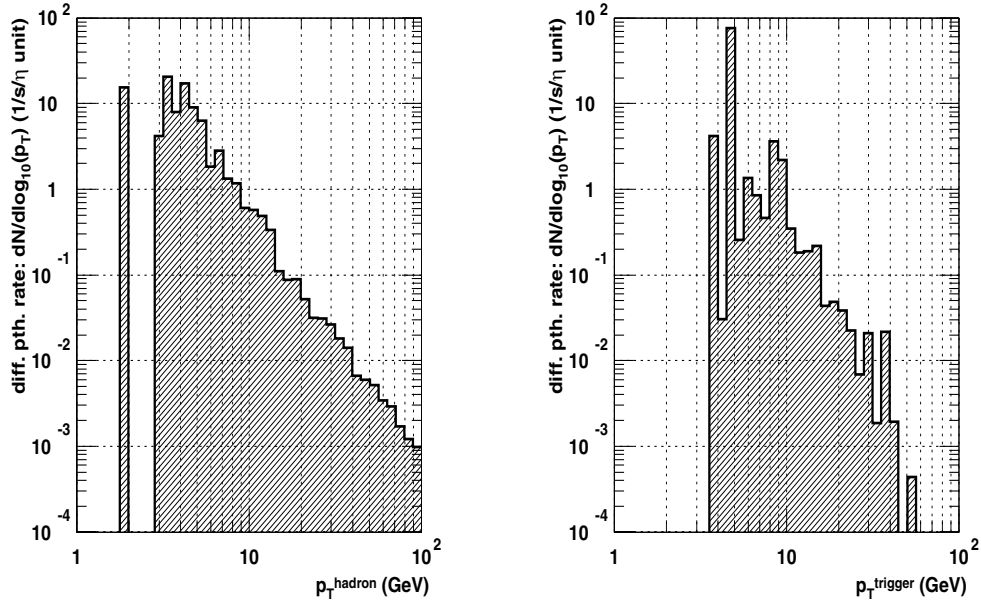
Fig. 8.9. Weighted spectrum of hadrons causing a trigger (in the barrel) (*left*). Weighted distribution of trigger responses (in the barrel) (*right*)
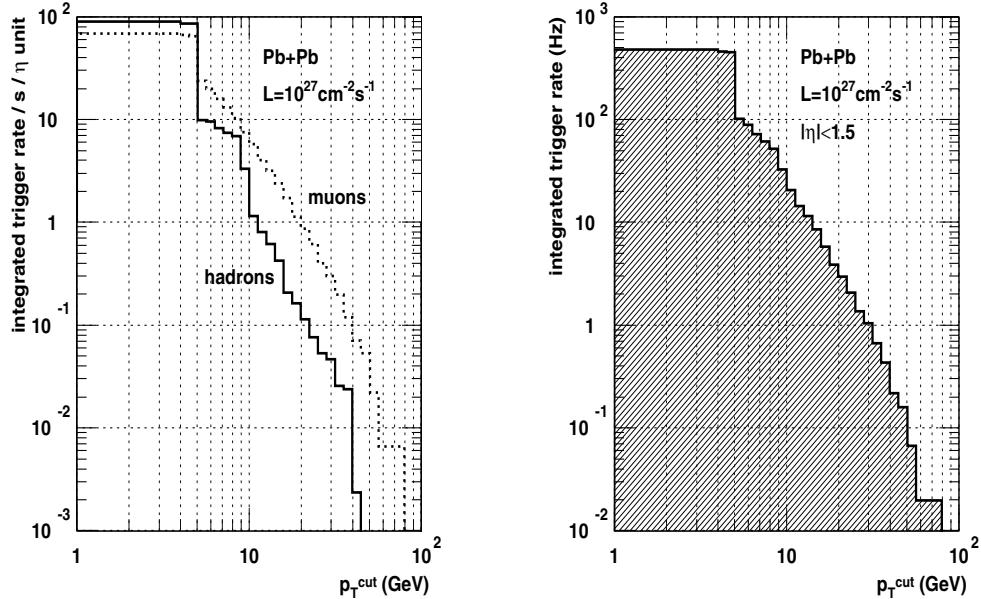

Fig. 8.10. Single muon trigger rate due to prompt muons and punchthrough (including π and K decays) in the barrel (*left*). Total single muon trigger rate (*right*)

8.6 Luminosity considerations

The rate obtained for Pb+Pb collisions can be rescaled to other ion species assuming luminosities given in the ALICE Technical Proposal [9]. The results are shown in Table 8.5. The luminosities given in the Table are initial ones, assuming 125 ns bunch spacing and only one experiment running at a time. There are several factors influencing the nominal luminosity:

– after 10 hours of a run the luminosity is about 2 times lower;

– reducing bunch spacing to 25 ns can increase the luminosity by factor 4-5 (this option is impossible for Pb+Pb collisions);
– running 2 experiments at the same time reduces the luminosity by a factor 3-4;
– running 3 experiments at the same time reduces the luminosity by a factor 6-9.

Trigger rates for the last two cases are given in Table 8.6. The two-muon trigger rates according to [311] are also given.

Table 8.5. Single muon trigger rates for $|\eta| < 1.5$

	pp	O+O	Ca+Ca	Nb+Nb	Pb+Pb
$\mathcal{L}(\text{cm}^{-2}\text{s}^{-1})$	10^{34}	3.2×10^{31}	2.5×10^{30}	9×10^{28}	10^{27}
average collision rate (kHz)	550000	32000	5200	400	7.6
trigger rate (kHz)	190	120	53	10	0.5

Table 8.6. Muon trigger rates for $|\eta| < 1.5$

Pb+Pb: experiments	1	2	3
$\mathcal{L}(\text{cm}^{-2}\text{s}^{-1})$	10^{27}	3.3×10^{26}	1.7×10^{26}
average collision rate (Hz)	7600	2500	1300
1 μ trigger rate (Hz)	500	165	85
2 μ trigger rate (Hz)	60	20	10

Luminosities and trigger rates given above should be taken with care when used to estimate available statistics. They show possibilities of the LHC machine, but it is not obvious that the experiments can stand them. For example a luminosity of 3.2×10^{31} cm^{-2}s^{-1} quoted for O+O collisions with the cross section of 1 barn gives an average collision rate of 30 MHz. This is to be compared with the bunch crossing frequency of 8 MHz corresponding to a bunch spacing of 125 ns. In such a case one should expect in average 4 O+O collisions per bunch crossing which makes absolutely impossible most of the study planned for heavy ion collisions!

8.7 Trigger strategy for Pb+Pb collisions

Let us assume the following:

- $\mathcal{L} = 10^{27}$ cm^{-2}s^{-1} (1 experiment running at a time) for Pb+Pb
- mass storage capacity: 60 events/s (see [312]), equally divided between dimuon and "calorimetric" physics
- equal rates for muon and calorimeter triggers
- pseudorapidity range of interest for dimuon physics: $|\eta| < 1.5$

For these conditions we propose the following trigger strategy:

- require single muon trigger in $|\eta| < 1.5$ at the first level $\rightarrow$ 500 Hz
- search for a second muon in muon chambers in $|\eta| < 1.5$ at the second level $\rightarrow$ < 60 Hz

Since one can write to tape $\approx$ 30 dimuon events/s we are already in the right ball park. In fact the estimate of 60 Hz for the two-muon trigger was based on a very soft requirement on the second muon - at least one hit in any muon station. Slightly more restrictive requirement may easily reduce the rate. Presumably a factor two can be gained by rejecting same sign muon pairs. In any case, if there

is a mismatch between the second level trigger rate and the mass storage capacity there are several possibilities to solve it:

- have a bigger mass storage
- reduce the luminosity
- reconstruct $\Upsilon \rightarrow \mu\mu$ at the virtual third level and cut on a $\mu\mu$ mass range

The first two possibilities are trivial, so let us consider the third one. Assume a farm of 500 processors, divided equally for 2nd and 3rd level, and for muon and calorimeter events. Hence available processing time per event is 500 / 2 / 2 / 60 Hz = 2 s. Is it feasible? It is difficult to conclude today. At least it does not look impossible. In fact this solution will probably not be needed for Pb+Pb collisions, but might be very useful for lighter ions where we expect higher luminosities and thus higher rates. The strategy described above works well for Pb+Pb collisions and it may work (with some modifications) in the Nb+Nb case. For lighter ions, however one has to require two muons already at the first level. This is necessary in order to maintain an acceptable trigger rate. The price for this is an efficiency for low p_T muon pairs of 80% or even lower. Fortunately this is not a problem, because in the case of light ions we expect much higher luminosities which ensure to collect high enough statistics in spite of low efficiency.

8.8 DAQ performances

The CMS Data Acquisition System (DAQ) was designed for pp collisions at the highest design luminosity. In this case one can expect the following conditions:

- bunch spacing = 25 ns
- luminosity $\mathcal{L} = 10^{34}$ cm^{-2}s^{-1}
- number of pp interactions per bunch crossing $\approx$ 20
- number of charged particles per η-unit $\approx$ 5
- First Level Trigger rate < 100 kHz

This has led to the design of a DAQ with the following parameters:

- Readout Dual Port Memory (RDPM) input < 200 Mbytes/s continuous rate (400 Mbytes/s peak rate).
- number of RDPM's = 512
- nominal Switch bandwidth = 500 Gbits/s
- mass storage capacity = 100 Mbytes/s

Conditions in heavy ion collisions are very different. Let us consider an extreme case of Pb+Pb collisions:

– bunch spacing = 125 ns
– luminosity $\mathcal{L} = 10^{27}$ cm^{-2}s^{-1}
– average interaction rate $\approx$ 7.6 kHz
– number of charged particles per η-unit $\approx$ 2500 (min. bias) — $\approx$ 8000 (central)
– First Level Trigger rate $\approx$ 1 kHz [180]

One expects much higher occupancy but with relatively low event rate. Is the CMS DAQ system suitable for such conditions? Where are possible bottle-necks? These are the questions we are going to address in this chapter.

8.9 Requirements for dimuon physics

Probably the most demanding physics are the dimuon channels used to study formation of bound states of heavy quarks in dense matter [311]. They require data from the muon detector to recognise muons, from the central tracker to measure precisely their momenta, and from calorimeters to estimate the centrality of collisions. Recent study has shown that occupancies in the Pixel Detector [313] and in Outer Silicon Tracker layers (see [181] and Sec. 5.2.4) are low enough to perform an effective pattern recognition up to $|\eta| = 1.5$. They are quoted in the table below for the Phase II, high luminosity all-silicon Tracker. They have been obtained assuming 8000 charged particles per η unit, which is an upper limit. We assume to read only one side of double-sided silicon detectors, because at these high occupancies the stereo information is unlikely to be useful.

detector	width	length	radius	occupancy
	μm	mm	cm	%
Pixel layer 1	125	0.150	7	0.53
Pixel layer 2	125	0.150	11	0.28
Silicon layer 1	143	160	75	16.28
Silicon layer 2	143	160	85	11.85
Silicon layer 3	143	160	95	7.85
Silicon layer 4	143	160	105	5.21
Silicon layer 5	143	160	115	3.39

The occupancies are calculated for $|\eta| < 0.8$. One can extrapolate the data volume to $|\eta| < 1.5$ assuming constant number of tracks per η unit. Going beyond this region would require careful, dedicated study. Therefore for the purpose of this chapter we restrict ourselves to the region of $|\eta| < 1.5$. Thus, the forward Pixel discs are not required. This restriction, however, is not valid for calorimeters. Full η coverage ($|\eta| < 5$, including Forward Calorimeter HF) is needed to estimate the centrality of the collisions.

Finally, we would like to read out the following detectors:

– Pixel barrel detector
– 5 Outer Silicon Tracker layers
– all calorimeters (ECAL + HCAL)
– muon system (RPC + Drift Tubes + CSC)

This configuration is a baseline, which is rather conservative. If the occupancies will be significantly lower, especially for lighter ions, one can think of using additional Silicon layers.

8.10 Scope of the study

In the following sections we are going to examine the CMS DAQ according to the following plan:

– calculate the data volume for each subdetector
– calculate the data flow
  – from detector Front Ends to Front End Drivers (FED)
  – from FED's to RDPM's
  – through the Switch

The aim of the exercise is not to give precise numbers. It is just a very first attempt at a rough estimation. All the numbers given below should be taken with care, because they are subject to change due to many reasons.

– The CMS Tracker is still under optimization and some moderate changes in the detector layout and thus in the number of channels are possible.
– The development of the DAQ system is in the design phase. Parameters assumed here result from an extrapolation of technological trends. They may change significantly depending *e.g.* on technology which will be finally chosen.
– There is a lot of flexibility built into the system. The system can be configured in many ways and it can work in many different modes. Concrete solutions will be adopted to running conditions and physics needs. Therefore they cannot be determined precisely today.

8.11 Data volumes for DAQ

8.11.1 Pixel barrel

1 module = 2 rows $\times$8 chips $\times$(53$\times$52) pixels = 44 k pixels
Layer 1
(30$\times$8) modules $\times$44 k pixels = 10.6 M channels
$\times$0.53% occupancy = 56 k hits
Layer 2
(46$\times$8) modules $\times$44 k pixels = 16.2 M channels
$\times$0.28% occupancy = 45 k hits.

The full readout option, without zero suppression, is not provided by hardware.

Zero suppressed readout
Let us assume that the readout is arranged in blocks corresponding to 1 module. Thus 2 bytes are needed for an address within a module. Analog information about the signal on 1 pixel is equivalent to 4-6 bits. Taking a more conservative value of 6 bits for the analog pixel information and taking into account some overhead due to module headers one can assume 3 bytes per pixel in total.

$$(56 + 45) \text{ k hits} \times 3 \text{ bytes} = 300 \text{ kbytes}$$

The zero suppressed readout is clearly more economic than the full readout. One can, however, try to reduce further the data volume making use of the fact that a single particle usually creates a cluster of 2-4 hits. Thus one can apply some clusterization algorithm. Let us consider a simple example.

A single module (physical detector) is a matrix of 106 rows ×416 columns of pixels. Let us introduce the following notation.

M – module number (1-608), 10 bits
X_i – column number (1-416), 9 bits
Y_{ij} – row number of the first pixel in the cluster (1-106), 7 bits
N_{ij} – cluster size, 3 bits
$A(k)$ – amplitude of the k-th pixel in the cluster, 6 bits
EOC – End Of Cluster marker (7 bits, to be distinguished from the next Y_{ij})
EOM – End Of Module marker (9 bits, to be distinguished from the next X_i)

The data format for one module can look as follows:

$M, X_1, Y_{11}, N_{11}, A(1), \ldots,$
$A(N_{11}), Y_{12}, N_{12}, A(1), \ldots,$
$A(N_{12}), \ldots,$
EOC
$\vdots$
$X_i, Y_{i1}, N_{i1}, A(1), \ldots,$
$A(N_{i1}), Y_{i2}, N_{i2}, A(1), \ldots,$
$A(N_{i2}), \ldots,$
EOM

The clusters are characterized by the following average values.

	layer 1	layer 2
clusters (particles) per module	150	80
pixels per module	470	250
pixels per cluster	3.1	3.1
columns per cluster	2.1	2.1

Thus an average cluster will contain 3 pixels in 2 rows and 2 columns:

$X,\ Y_1,\ N_1,\ A_1,\ A_2,\ Y_2,\ N_2,\ A_1,\ EOC$
$9 + 7 + 3 + 6 + 6 + 7 + 3 + 6 + 7 \qquad = 54$ bits

Hence, in total we need roughly
Layer 1: (30×8) modules ×54 bits ×150 clusters = 250 kbytes
Layer 2: (46×8) modules ×54 bits ×80 clusters = 200 kbytes

The total data volume is ∼ 450 kbytes, which is higher than in the case of single pixels. This means that the average cluster size is too small to compensate the overhead of the format.

8.11.2 Outer silicon tracker

	modules	channels	hits
layer 1	45×13 = 585	×768 = 448 k	×16.3% = 73 k
layer 2	51×13 = 663	×768 = 509 k	×11.9% = 60 k
layer 3	57×13 = 741	×768 = 569 k	×7.8% = 44 k
layer 4	63×13 = 819	×768 = 629 k	×5.2% = 33 k
layer 5	69×13 = 897	×768 = 689 k	×3.4% = 23 k
TOTAL		2.8 M	233 k

Full readout
Not feasible.

Zero suppressed readout
8 bits for the address and 8 bits for the amplitude are needed for each hit.
233 k hits ×(8+8) bits = 466 kbytes

We can extrapolate the data volume for $|\eta| < 1.5$ simply multiplying by 2 and we get about 930 kbytes.

8.11.3 ECAL

100% occupancy
Almost 2 bytes per crystal per time sample are needed — 12 bits for the amplitude + 4 bits for the range.
In addition one needs 4 bytes of header per crystal, but in Pb+Pb runs all the crystals are read out and the headers are not needed. They can be stripped out in the Filter Farm.

Full precise information readout
This solution leads to very large data volume, but probably 10 time slices are not needed. Without the pileup 1 time slice gives a precision of 1-2 %, which is enough for heavy ions. The possibility of recording e.g. 3 slices for lighter ions (O+O, Ca+Ca) is being considered. Currently it is not foreseen to implement a digital filter reducing the number of time slices at the Front End, but one can apply a filter at the Online Farm.

Full granularity, 1 time slice readout
≈83000 crystals ×2 bytes = 166 kbytes
This is already feasible, but in the case of heavy ions one can consider a reduction of the readout granularity to that of the trigger.

Full trigger information readout
towers of 25 crystals, only one time slice
3456 towers ×2 bytes = 7 kbytes
This is very low value, but this granularity is probably not adequate for studying electrons. Therefore, in case of a possible future need we consider further the full granularity, 1 time slice option.

Calculating the data volume to be transferred through the Switch one has to take into account 4 bytes header for each crystal. This increases the volumes calculated above by ≈83000 crystals ×4 bytes = 332 kbytes

8.11.4 HCAL (HB+HE+HF)

100% occupancy

Full readout
It is assumed to readout the energy calculated online by local DSPs. 2 bytes are needed for the amplitude.
14 k channels $\times 2$ bytes = 28 kbytes.

8.11.5 Muon stations

Muon RPC
< 1 kbyte.

Muon drift tubes
5 kbytes.

Muon cathode strip chambers
6 kbytes per muon segment in one station are needed. Conservative assumption of 2 muons crossing 4 endcap stations gives
8 $\times 6$ kbytes = 48 kbytes

8.11.6 Total

	kbytes
Pixel barrel	300
MSGC barrel	930
ECAL - 1 time slice	166
HCAL full	28
Muon RPC	1
Muon Drift Tubes	5
Muon CSC	48
in total	$\sim$1478

The total event size $\approx$ 1.5 Mbytes is only 1.5 time higher than for pp collisions at $\mathcal{L} = 10^{34}$ cm^{-2}s^{-1}.
Assuming mass storage of 100 Mbytes/s we can write to tape about 70 central Pb+Pb events/second.

8.12 Data flow

8.12.1 Pixel barrel – front end

A single Pixel Front End chip covers an array of 52 columns, 53 pixels each. If at least one hit occurred in a column the time-stamp is recorded and the full information (amplitude and position) from the hit pixel is stored in a buffer. In the case of very high rate some data might be lost due to buffer overflow. Let us consider the most demanding case of layer 1 at $\eta = 0$.

Pixels in 1 module	470
Pixels in one chip	30
Pixels in a hit column	2.1
Hit columns in one chip	14
Pixel hit rate	60 Hz
Column rate	3.5 kHz
Chip rate	8 kHz

The rates mentioned above are based on physics simulation and do not include any noise contribution. The readout error rate depends on the buffer size.

Buffer size	8	16	24	32
Error rate	4.7 10^{-5}	1.0 10^{-5}	5.2 10^{-6}	1.8 10^{-7}

For the pp collisons the pixel buffer size was chosen to be 24. This also seems sufficient for Pb+Pb collisions.
Another possible mechanism of spoiling the data is an overlap of clusters created by different particles. Again the simulation shows the values which are tolerable.

Pixel overlaps	0.75 %
Cluster overlaps	1.7 %

8.12.2 Pixel barrel – from front end to FED

For 1 pixel channel one needs to read the analog amplitude and the position information consisting of the chip, column and row addresses. This information is sent from the Front End to the FED using an analog link, with the digital information being octal coded as analog signals (see Tracker TDR). Overall about 8-10 analog samples per pixel are transferred.

Layer 1: 1 link = 4 chips $\times(53\times52)$ pixels = 11 k channels
Layer 2: 1 link = 8 chips $\times(53\times52)$ pixels = 22 k channels
14-15 bits are needed for the address — 2-3 for the chip number + 6 for the column number + 6 for the row number
A full readout is not possible.
Zero suppressed readout:
Layer 1: 11 k channels $\times 0.53\%$ occupancy $\times(8\text{-}10)$ samples $\times 1000$ Hz = 0.58 M samples/s
Layer 2: 22 k channels $\times 0.28\%$ occupancy $\times(8\text{-}10)$ samples $\times 1000$ Hz = 0.62 M samples/s

8.12.3 Pixel barrel – from FED to RDPM

Layer 1: 3 $\times 16$ modules $\to$ 3 FED's $\to$ 1 RDPM
3 $\times 16$ $\times 44$ k = 2.1 M channels
Zero suppressed readout: 2.1 M channels $\times 0.53\%$ occupancy $\times 3$ bytes $\times 1000$ Hz = 34 Mbytes/s
Layer 2: 3 $\times 32$ modules $\to$ 3 FED's $\to$ 1 RDPM
3 $\times 32$ $\times 44$ k = 4.2 M channels
Zero suppressed readout: 4.2 M channels $\times 0.28\%$ occupancy $\times 3$ bytes $\times 1000$ Hz = 36 Mbytes/s

Thus the zero suppressed readout is feasible.

8.12.4 Outer silicon barrel

64 links $\times 2$ chips $\times 128$ channels = 16 k channels $\to$ 1 FED
2 FED's $\to$ 1 RDPM

Zero suppressed readout
We consider the worst case of the innermost layer.
2 ×16 k channels ×16.3% occupancy ×(8+8) bits = 10 kbytes
×1000 Hz = 10 Mbytes/s
    2.1 M channels ×0.53% occupancy ×3 bytes ×1000 Hz = 34 Mbytes/s
    The conditions are comfortable for both options.

8.12.5 ECAL

Full precise information readout
2 bytes amplitude ×10 times slices + 4 bytes header = 24 bytes per crystal
68 towers ×25 crystals ×24 bytes = 41 kbytes
×1000 Hz = 51 Mbytes/s
    Optional – full, 1 time slice readout (currently not considered at the Front End level)
2 bytes amplitude ×1 times slices + 4 bytes header = 6 bytes per crystal
68 towers ×25 crystals ×6 bytes = 10 kbytes
×1000 Hz = 10 Mbytes/s
    Full trigger information readout
towers of 25 crystals, only one time slice
68 towers ×3 bytes = 204 bytes
×1000 Hz = 0.2 Mbytes/s
    Thus all the options would be feasible.

8.12.6 Miscellaneous

HCAL, Muons
Very low bandwidth required.
Switch
event size = 1.5 Mbytes + 0.35 Mbytes of ECAL headers = 1.85 Mbytes
trigger rate = 1000 Hz
⇒ required bandwidth = 1.85 Gbytes/s.
    nominal bandwidth = 500 Gbits/s = 62 Gbytes/s
In practice only 50% of the nominal bandwidth can be used due to traffic problems.
Hence the effective bandwidth is ∼ 30 Gbytes/s. This ensures a large safety margin (factor 16).

8.13 Conclusions

The expected p_T spectra above 1 GeV in AA collisions at $\sqrt{s} = 5\text{-}7$ TeV are not much different from those in pp collisions at $\sqrt{s} = 14$ TeV. A simple scaling by $A^{2\times0.95}$ works well. This has a big practical importance, as a lot of study was done in CMS for the pp case and this can be easily extrapolated to heavy ion collisions. For example, one gets Pb+Pb rates at $\mathcal{L} = 10^{27}\text{cm}^{-2}\text{s}^{-1}$ multiplying pp rates at $\mathcal{L} = 10^{34}\text{cm}^{-2}\text{s}^{-1}$ by 0.0025. For Pb+Pb collisions at $\mathcal{L} = 10^{27}\text{cm}^{-2}\text{s}^{-1}$ one can expect a single muon trigger rate of ≈ 500 Hz in $|\eta| < 1.5$ with almost equal contributions from prompt muons (c- and b-quark decays) and from hadronic punchthrough + decays (mainly π and K). This allows us to run requesting a single muon at the first level trigger, which ensure high efficiency for $\Upsilon \to \mu^+\mu^-$. The muon trigger threshold is determined by the energy loss in calorimeters and it is equal to ≈ 3.2 GeV in the barrel region. This allows to explore central Υ, Υ', $\Upsilon'' \to \mu^+\mu^-$ production with good statistics at all $p_T(\Upsilon)$, down to $p_T(\Upsilon)=0$, with nuclei from pp to Pb+Pb. The exploitation of the forward region of $1.5 < |\eta| < 2.4$, either for still lower $p_T(\mu)$ detection of Υ, Υ', $\Upsilon'' \to \mu^+\mu^-$, or for observation of J/ψ, $\psi' \to \mu^+\mu^-$ requires a separate study.

There is no problem with the data volume and the data flow for any of the subdetectors. The system is able to work in conditions which are very different from those for which it was designed, which is a good demonstration of its flexibility.

The expected event size for Pb+Pb collisions is ∼ 1.5 Mbytes without any digital compression. With the First Level Trigger rate of 1 kHz and a mass storage of 100 Mbytes/s one can write to tape ∼ 70 central Pb+Pb events per second. This seems to be adequate for heavy ion physics.

9 General Conclusions

The CMS detector has been conceived as a general-purpose detector for pp physics at the LHC optimized for Higgs and SUSY searches. However, from the very beginning it was realized that the CMS detector, with its $\approx 4\pi$ muon acceptance and calorimetric coverage, could, with appropriate triggers and adaptations of its data acquisition system, make very significant and in some respect unique contributions in the domain of heavy ion collisions and investigations of the quark gluon plasma. Subsequent evaluations and studies have indeed confirmed that CMS, with emphasis on "hard probes", quarkonium production, high mass dimuons, high p_T photons and jets, will to a large extent be complementary to ALICE in the investigations of the QGP. The study of the production of the Υ family, from pp through Ar+Ar to Pb+Pb and from peripheral to central collisions, is likely to be of central interest in the LHC era, just as the J/$\psi \to \mu^+\mu^-$ has been for the SPS period. The key issue for CMS is the muon reconstruction efficiency in the tracker in conditions of extreme congestion and occupancy expected in Pb+Pb collisions. It is particularly satisfying that the final adoption of the all-silicon tracker resulting in reduced effective occupancies has brought a significant improvement in the reconstruction efficiencies (and purities), from 64% to 76% for dimuons in $\eta < 0.8$ for the extreme charged particle densities considered $\mathrm{d}N^{\pm}/\mathrm{d}y= 8000$. In the rapidity region from 0.8 to 1.3 the efficiency is reduced to 50% due to the change in tracker layer geometry from cylinders to disks increasing, thus, the pattern recognition difficulties. It is of prime importance to extend the study to the endcaps regions. Motivations are several: i) to increase statistics of Υ's (especially of Υ'' which is limited), ii) to lower the gap in rapidity between CMS and ALICE muon acceptances thus allowing continuous physics coverage and possibly

some overlap for cross-checks, and iii) as for $1.6 < \eta < 2.4$ the muon p_T detection threshold decreases from 3.5 to 2.0 GeV/c, muon detection in endcaps would allow CMS to study $J/\psi \to \mu^+\mu^-$ over the full range of production $p_T{}^\psi$.

The pixel detector layers in the CMS tracker play a very important role in muon filtering and reconstruction efficiency and especially for $\Upsilon \to \mu^+\mu^-$ sample purity by suppressing π/K decay muons when combined with a beam-line vertex constraint. Up to now muon reconstruction has been evaluated with pixel layers at radii of 7 and 11 cm (occupancies are below the percent). The initial running in 2006 and 2007 for pp and heavy ions will rather be with pixel layers at 4 and 7 cm, thus a reevaluation is needed in these conditions. More generally, it would be important to evaluate what would be the possible advantages/gains for heavy ions of running with all three barrel pixel layers. Furthermore, as occupancies in the all Si tracker are somewhat lower compared to the previous Si+MSGC tracker, possibilities to include in the muon reconstruction deeper tracker Si-layers - not only the outermost four - should be considered. This could bring improvements in the muon reconstruction efficiency in the 0.8 - 1.3 rapidity range and also in dimuon effective mass resolution (at present 50 MeV), not of negligible importance to separate Υ' and Υ''. These aspects should be investigated with the large Monte Carlo samples now in preparation for detailed detector response simulations (CMSIM) and using object oriented reconstruction software (ORCA).

For dimuons beyond the Υ region the expected large rate of $Z^0 \to \mu\mu$ will be a unique feature of CMS. The observation of the Z^0 independently in the outer muon system and in the muon+tracker systems will obviously provide means to calibrate the tracker muon reconstruction efficiency over an extended ptm range. The extent of the physics significance, as distinct from the instrumental one, of observing the point-like Z^0 in heavy ion collisions is not yet fully understood. CMS could probably also have a large sample of W $\to \mu\nu$ events, although the exact selection procedure based on the Jacobian peak in p_T^μ and the achievable sample purity has still to be investigated. If the W $\to \mu\nu$ would turn out to be an interesting physics probe in heavy ions, then the issue of triggering on single muons in HI collisions must be addressed. In any case there is a need to better understand the trigger cocktail for HI running.

The other likely major field of activity in heavy ions physics in CMS will be the search for evidence for jet quenching from the propagation of hard partons through the dense QGP medium. The study of the monojet to dijet ratio as well as the direct study of hard partons (jets) tagged by the recoil hard photon or high transverse momentum Z^0 ($\to \mu\mu$) were already considered. Much more work is still needed to understand what can be learned and what sensitivity to the fractional energy loss can be achieved from calorimetric transverse jet profile measurements taking advantage of the CMS granularity. How are large mass dimuons originating from $b\bar{b}$ production followed by b$\to \mu$ affected by (b-)jet quenching and what

information they would provide on this mechanism has still to be understood. Jet quenching could also measurably affect the b $\to J/\psi \to \mu\mu$ dimuon rate and p_T^ψ differential cross section. These muon-based measurements should benefit from the large muon acceptance of CMS, as well as from the 4π calorimetry allowing to select the collision centrality on basis of measured transverse energy flows, but a phenomenological analysis of these issues is also needed. An issue to be addressed in the future is the possible detection of muons within jets and possibly also of a jet multiplicity count using the outer parts of the tracker. Even more ambitious would be track pt measurements within jets in the 50 to 100 GeV E_T range. This has been studied in great detail for pp collisions (even for jets of 500 GeV), but what is possible in heavy ion collisions is unknown at present. Such measurements could be more sensitive probes of jet quenching than just calorimetric profiles. Better understanding is also needed of what could be learned on quenching from the global (scalar) transverse energy flow as measured in the barrel, endcap and very forward electromagnetic plus hadronic calorimetric systems of CMS with essentially complete azimuthal coverage over the full rapidity range $-5 < \eta < 5$, varying and comparing the various nuclei and the centrality of collisions. Measurements of ECAL to HCAL responses in the endcap (1.5 - 3.0) and very forward (3.0 - 5.0) rapidity ranges should give information directly related to the $\pi^0/\pi^\pm$ (or charged particle) ratio. We have also to learn how to better exploit this information in a search for Centauro type events for example. A related issue which should also be addressed is what additional physics potential would CMS gain from a zero-degree calorimeter. Heavy ions running in CMS will also allow investigating a range of non-QGP-related physics topics as $\gamma\gamma$ physics and diffractive physics with possible windows of opportunity even in the domain of Higgs searches. Phenomenological studies exist, what is needed as the next step is to understand better how to avoid the possibly overwhelming strong interaction background by selecting highly peripheral collisions and find ways to trigger on the interesting final states, and then evaluate what is the CMS physics reach. The domain of pA interactions discussed in this study is another field where no physics reach with detector response simulation studies has yet been done. There is little doubt that pA interactions will be interesting on their own, and it is most likely that understanding these would be an extremely helpful, perhaps even necessary, intermediate step on the way to understand QGP. So the detailed experimental aspects will have to be addressed at some point.

References

1. CMS HCAL Design Report, CERN/LHCC 97-31
2. CMS MUON Design Report, CERN/LHCC 97-32
3. CMS ECAL Design Report, CERN/LHCC 97-33
4. CMS Tracker Design Report, CERN/LHCC 98-6
5. C.Charlot et al.: CMS Simulation Facilities, CERN/CMS TN 1993/063

6. F. Karsch: Nucl. Phys. A **590**, 367c (1995)
7. For the latest data on heavy ion collisions at the AGS and the SPS, see the Proceedings of the 13th International Conference on Ultra-Relativistic Nucleus-Nucleus Collisions, Tsukuba, Japan, 1997, Nucl. Phys. A **638**, (1998) and the Proceedings of the 14th International Conference on Ultra-Relativistic Nucleus-Nucleus Collisions, Torino, Italy, 1999, Nucl. Phys. A **661**, (1999)
8. *Conceptual Design for the Relativistic Heavy Ion Collider*, BNL-52195, May, 1989, Brookhaven National Laboratory
9. ALICE Technical Proposal, CERN/LHCC 95-71; ALICE Addendum to the Technical Proposal, CERN/LHCC 96-32; A. Morsch et al. (ALICE Collab.): Nucl. Phys. A **638**, 571c (1998)
10. M.C. Abreu et al. (NA50 Collab.): Phys. Lett. B **450**, 456 (1999); M.C. Abreu et al. (NA50 Collab.): Phys. Lett. B **477**, 28 (2000)
11. R. Vogt: Phys. Rep. **310**, 197 (1999)
12. D.M. Alde et al.: Phys. Rev. Lett. **66**, 2285 (1991)
13. T.K. Gaisser and F. Halzen: Phys. Rev. Lett. **54**, 1754 (1985); L. Durand and H. Pi: Phys. Rev. Lett. **58**, 303 (1987); G. Pancheri and Y.N. Srivastava: Phys. Lett. B **182**, 199 (1986)
14. C. Albajar et al. (UA1 Collab.): Nucl. Phys. B **309**, 405 (1988)
15. K.J. Eskola and M. Gyulassy: Phys. Rev. C **47**, 2329 (1993)
16. K.J. Eskola and K. Kajantie: Z. Phys. C **75**, 515 (1997); K.J. Eskola, K. Kajantie and J. Lindfors: Nucl. Phys. B **323**, 37 (1989)
17. I. Abt et al. (H1 Collab.): Nucl. Phys. B **407**, 515 (1993); M. Derrick et al. (ZEUS Collab.): Phys. Lett. B **316**, 412 (1993)
18. M. Glück, E. Reya, and A. Vogt: Z. Phys. C **67**, 433 (1995)
19. A.D. Martin, R.G. Roberts, W.J. Stirling, and R.S. Thorne: Eur. Phys. J. C **4**, 463 (1998); Phys. Lett. B **443**, 301 (1998)
20. H. Satz and X.-N. Wang: Int. J. Mod. Phys. A **10**, 2881 (1995)
21. J.J. Aubert et al. (European Muon Collab.): Nucl. Phys. B **293**, 740 (1987)
22. M. Arneodo: Phys. Rep. **240**, 301 (1994)
23. S. Gavin, P.L. McGaughey, P.V. Ruuskanen and R. Vogt: Phys. Rev. C **54**, 2606 (1996)
24. K.J. Eskola, V.J. Kolhinen and P.V. Ruuskanen: Nucl. Phys. B **535**, 351 (1998)
25. K.J. Eskola, V.J. Kolhinen and C.A. Salgado: Eur. Phys. J. C **9**, 61 (1999)
26. K.J. Eskola, J. Qiu, and J. Czyzewski, private communication
27. K.J. Eskola: Nucl. Phys. B **400**, 240 (1993)
28. D.W. Duke and J.F. Owens: Phys. Rev. D **30**, 49 (1984)
29. M. Glück, E. Reya, and A. Vogt: Z. Phys. C **53**, 127 (1992)
30. V. Emel'yanov, A. Khodinov, S.R. Klein and R. Vogt: Phys. Rev. C **56**, 2726 (1997); V. Emel'yanov, A. Khodinov, S.R. Klein and R. Vogt: Phys. Rev. Lett. **81**, 1801 (1998)
31. V. Emel'yanov, A. Khodinov, S.R. Klein and R. Vogt: Phys. Rev. C **61**, 044904 (2000)
32. K.J. Eskola, R. Vogt, and X.-N. Wang: Int. J. Mod. Phys. A **10**, 3087 (1995)
33. R. Vogt: Heavy Ion Phys. **9**, 339 (1999)
34. C.W. deJager, H. deVries, and C. deVries: Atomic Data and Nuclear Data Tables **14**, 485 (1974)
35. L.V. Gribov, E.M. Levin, and M.G. Ryskin: Phys. Rep. **100**, 1 (1983)
36. J. Breitweg et al. (ZEUS Collab.): Eur. Phys. J. C **7**, 609 (1999)
37. J.D. Bjorken: Phys. Rev. D **27**, 140 (1983)
38. K.J. Eskola, K. Kajantie and P.V. Ruuskanen: Phys. Lett. B **332**, 191 (1994)
39. H. Satz: Nucl. Phys. A **544**, 371c (1992)
40. T. Matsui and H. Satz: Phys. Lett. B **178**, 416 (1986)
41. F. Karsch, M.T. Mehr, and H. Satz: Z. Phys. C **37**, 617 (1988)
42. F. Karsch and H. Satz: Z. Phys. C **51**, 209 (1991)
43. J.F. Gunion and R. Vogt: Nucl. Phys. B **492**, 301 (1997)
44. D.J. Gross, R.D. Pisarski, and L.G. Yaffe: Rev. Mod. Phys. **53**, 43 (1981)
45. P. Levai and U. Heinz: Phys. Rev. C **57**, 1879 (1998)
46. G. Boyd et al.: Nucl. Phys. B **469**, 419 (1996)
47. J. Fingberg, U.M. Heller and F. Karsch: Nucl. Phys. B **392**, 493 (1993)
48. U.M. Heller, F. Karsch and J. Rank: Phys. Lett. B **355**, 511 (1995)
49. B. Petersson: Nucl. Phys. A **525**, 237c (1991)
50. For a review, see G. Schuler: CERN-TH-7170-94, February 1994 and references therein
51. M.L. Mangano, P. Nason and G. Ridolfi: Nucl. Phys. B **405**, 507 (1993)
52. R.V. Gavai et al.: Int. J. Mod. Phys. A **10**, 3043 (1995)
53. G.A. Schuler and R. Vogt: Phys. Lett. B **387**, 181 (1996)
54. E. Braaten, M.A. Doncheski, S. Fleming and M.L. Mangano: Phys. Lett. B **333**, 548 (1994)
55. A. Sansoni (CDF Collab.): Nucl. Phys. A **610**, 373c (1996)
56. L. Antoniazzi et al. (E705 Collab.): Phys. Rev. Lett. **70**, 383 (1993)
57. L. Antoniazzi et al. (E705 Collab.): Phys. Rev. D **46**, 4828 (1992)
58. B. Ronceux et al. (NA38 Collab.): Nucl. Phys. A **566**, 371c (1994)
59. J.K. Yoh et al.: Phys. Rev. Lett. **41**, 684 (1978), erratum ibid **41**, 1083 (1978); K. Ueno et al.: Phys. Rev. Lett. **42**, 486 (1979)
60. T. Yoshida et al.: Phys. Rev. D **39**, 3516 (1989)
61. G. Moreno et al.: Phys. Rev. D **43**, 2815 (1991)
62. F. Abe et al. (CDF Collab.): Phys. Rev. Lett. **75**, 4358 (1995)
63. S.J. Brodsky, C. Peterson and N. Sakai: Phys. Rev. D **23**, 2745 (1981); S.J. Brodsky, P. Hoyer, C. Peterson and N. Sakai: Phys. Lett. B **93**, 451 (1980)
64. J. Badier et al.: Phys. Lett. B **86**, 98 (1979); S. Childress et al.: Phys. Rev. Lett. **55**, 1962 (1985)
65. D. Antreasyan et al.: Phys. Rev. Lett. **45**, 863 (1980); C. Kourkoumelis et al.: Phys. Lett. B **91**, 481 (1980); A.L.S. Angelis et al.: Phys. Lett. B **87**, 398 (1979)
66. A.D. Martin, W.J. Stirling and R.G. Roberts: Phys. Lett. B **354**, 155 (1995)

67. C. Albajar et al. (UA1 Collab.): Phys. Lett. B **186**, 237 (1987)
68. R.M. Barnett et al. (Particle Data Group): Phys. Rev. D **54**, 1 (1996)
69. X.-M. Xu, D. Kharzeev, H. Satz and X.-N. Wang: Phys. Rev. C **53**, 3051 (1996)
70. D. Kharzeev and H. Satz: Phys. Lett. B **366**, 316 (1996)
71. J. Ftaćnik, P. Lichard and J. Pišút: Phys. Lett. B **207**, 194 (1988);
    S. Gavin, M. Gyulassy and A. Jackson: Phys. Lett. B **207**, 257 (1988);
    R. Vogt, M. Prakash, P. Koch and T.H. Hansson: Phys. Lett. B **207**, 263 (1988);
    J. Ftaćnik, P. Lichard, N. Pišútova and J. Pišút: Z. Phys. C **42**, 132 (1989)
72. CMS Technical Proposal, CERN/LHCC 94-38
73. S. Ramos et al., (NA38 Collab.): Nucl. Phys. A **590**, 117c (1995), and references therein
74. These statements are based on the calculations of [23] for the LHC (using the acceptances of the ALICE experiment)
75. X.-N. Wang and M. Gyulassy: Phys. Rev. Lett. **68**, 1480 (1992)
76. Z. Lin, R. Vogt and X.-N. Wang: Phys. Rev. C **57**, 899 (1998)
77. Z. Lin and R. Vogt: Nucl. Phys. B **544**, 339 (1999)
78. M.G. Mustafa, D. Pal, D.K. Srivastava and M.H. Thoma: Phys. Lett. B **428**, 234 (1998)
79. T. Sjöstrand: Comput. Phys. Commun. **82**, 74 (1994). Further program updates and documentation can be found at http://www.thep.lu.se/tf2/staff/torbjorn/Pythia.html
80. A.D. Martin, W.J. Stirling and R.G. Roberts: Phys. Lett. B **306**, 145 (1993), erratum ibid B **309**, 492 (1993)
81. R. Vogt, S.J. Brodsky and P. Hoyer: Nucl. Phys. B **383**, 643 (1992)
82. G.A. Alves et al. (E769 Collab.): Phys. Rev. Lett. **77**, 2392 (1996)
83. C. Peterson, D. Schlatter, I. Schmitt, and P. Zerwas: Phys. Rev. D **27**, 105 (1983)
84. J. Chirn, in *Proc. Int. Symp. on Production and Decay of Heavy Flavors*, Stanford, California, 1987, edited by E. Bloom and A. Fridman, p. 131
85. R.M. Baltrusaitis et al. (MARK-III Collab.): Phys. Rev. Lett. **54**, 1976 (1985), erratum ibid **55**, 638 (1985)
86. S. Behrends et al. (CLEO Collab.): Phys. Rev. Lett. **59**, 407 (1987);
    B. Barish et al. (CLEO Collab.): Phys. Rev. Lett. **76**, 1570 (1996)
87. M. Tannenbaum: Heavy Ion Phys. **4**, 139 (1996)
88. M. Gyulassy and X.-N. Wang: Nucl. Phys. B **420**, 583 (1994);
    X.-N. Wang, M. Gyulassy and M. Plumer: Phys. Rev. D **51**, 3436 (1995)
89. R. Baier, Y.L. Dokshitser, S. Peigne and D. Schiff: Phys. Lett. B **345**, 277 (1995)
90. R. Baier, Y.L. Dokshitser, A.H. Mueller, S. Peigne and D. Schiff: Nucl. Phys. B **478**, 577 (1996)
91. R. Baier, Y.L. Dokshitser, A.H. Mueller, S. Peigne and D. Schiff: Nucl. Phys. B **483**, 291 (1997);
    R. Baier, Y.L. Dokshitser, A.H. Mueller, S. Peigne and D. Schiff: Nucl. Phys. B **484**, 265 (1997)

92. M. Gyulassy and M. Plumer: Phys. Lett. B **243**, 432 (1990)
93. M. Plumer, M. Gyulassy and X.-N. Wang: Nucl. Phys. A **590**, 511c (1995)
94. I.P. Lokhtin, L.I. Sarycheva, A.M. Snigirev and I.N. Vardanyan, CERN/CMS Note 1998/025
95. V. Kartvelishvili, R. Kvatadze and R. Shanidze: Phys. Lett. B **356**, 589 (1995)
96. X.-N. Wang, Z. Huang, and I. Sarcevic: Phys. Rev. Lett. **77**, 231 (1996)
97. I.P. Lokhtin and A.M. Snigirev: Phys. At. Nucl. **60**, 295 (1997);
    Z. Phys C **73**, 315 (1997)
98. N.A. Kruglov et al.: CERN/CMS TN 1996/083; CERN/CMS TN 1996/084
99. N.A. Kruglov, I.P. Lokhtin, L.I. Sarycheva, A.M. Snigirev: Z. Phys. C **76**, 99 (1997)
100. V.L. Korotkikh et al.: CERN/CMS TN 1994/244
101. M.V. Savina, S.V. Shmatov, N.V. Slavin, and P.I. Zarubin, private communication
102. X.-N. Wang and M. Gyulassy: Phys. Rev. D **44**, 3501 (1991);
    X.-N. Wang and M. Gyulassy: Phys. Rev. D **45**, 844 (1992);
    M. Gyulassy and X.-N. Wang: Comput.Phys.Commun. **83**, 307 (1994)
103. D. Brandt, K. Eggert, and A. Morsch, CERN/AT 94-05 DI
104. J. Baechler et al. (NA35 Collab.): Phys. Rev. Lett. **72**, 1419 (1994);
    T. Wienold et al. (NA49 Collab.): Nucl. Phys. A **610**, 76c (1996)
105. K. Werner: Phys. Rep. **232**, 87 (1993)
106. V. Genchev, N.V. Slavin, V.V. Uzhinskii, and P.I. Zarubin, CERN/CMS IN 1997/010
107. R. Gomez et al. (E557 and E672 Collabs.): Phys. Rev. D **35**, 2736 (1987)
108. A.S. Sambamurti et al. (E557 and E672 Collabs.): Phys. Rev. D **41**, 1371 (1990)
109. W. Bell et al.: Z. Phys. A **324**, 67 (1986);
    W. Bell et al.: Z. Phys. C **30**, 513 (1986);
    W. Bell et al.: Nucl. Phys. B **254**, 475 (1985);
    W. Bell et al.: Phys. Lett. B **128**, 349 (1983) and refs. therein;
    A. Breakstone et al.: Z. Phys. C **30**, 507 (1986) and refs. therein;
    T. Akesson et al.: Nucl. Phys. B **209**, 309 (1982);
    T. Akesson et al.: Phys. Lett. B **119**, 464 (1982) and refs. therein;
    M. Faessler: Phys. Rep. **115**, 1 (1984)
110. W. Busza and R. Ledoux: Ann. Rev. Nucl. Part. Sci. **38**, 119 (1988)
111. W.M. Geist: Nucl. Phys. A **525**, 149c (1991)
112. A. Morsch, CERN/ALICE 97-13 (PHY)
113. R.J. Glauber, *Lectures in Theoretical Physics*, W.E. Brittin and L. Dunham, eds. (New-York, Interscience 1959), **1**, p. 315;
    Ch.-Y. Wong, *Introduction to High Energy Heavy-Ion Collisions*, (World Scientific, Singapore 1994)
114. V.Kartvelishvili et al.: CERN/CMS Note 1999/015
115. D. Heck et al.: Karlsruhe preprint FZKA6019 (1998)
116. J.W. Cronin et al.: Phys. Rev. D **11**, 3105 (1975)
117. C. Stewart et al.: Phys. Rev. D **42**, 1385 (1990)

118. T. Ochiai et al.: Progr. Theor. Phys. **75**, 288 (1986) and refs. therein
119. FELIX, Letter of Intent, CERN/LHCC 97-45
120. G. Alberi et al.: Phys. Rep. **74**, 1 (1981)
121. A. Donnachie et al.: Phys. Lett. B **296**, 227 (1992)
122. R. Castaldi et al.: Ann. Rev. Nucl. Part. Sci. **35**, 351 (1985)
123. J.E. Elias et al.: Phys. Rev. D **22**, 13 (1980)
124. T.F. Hoang et al.: Z. Phys. C **29**, 611 (1985)
125. D.H. Brick et al.: Phys. Rev. D **39**, 2484 (1989)
126. J.L. Bailly et al.: Z. Phys. C **35**, 301 (1987), erratum ibid C **36**, 512 (1987)
127. S. Afanasiev et al. (NA49 Collab.): Nucl. Instr. Meth. A **430**, 210 (1999)
128. A. Rybicki et al. (NA49 Collab.), Contribution to Quark Matter '99, Torino, Italy;
     C.E. Cooper et al. (NA49 Collab.): Nucl. Phys. A **661**, 362c (1999);
     F. Sikler et al. (NA49 Collab.): Nucl. Phys. A **661**, 45c (1999);
     C. Hoehne et al. (NA49 Collab.): Nucl. Phys. A **661** 485c (1999);
     G.I. Veres et al. (NA49 Collab.): Nucl. Phys. A **661**, 383c (1999);
     R. Ganz et al. (NA49 Collab.): Nucl. Phys. A **661**, 448c (1999)
129. C. De Marzo et al.: Phys. Rev. D **26**, 1019 (1982)
130. C. Gale et al.: Phys. Rev. Lett. **82**, 1636 (1999)
131. E.L. Feinberg and I. Pomerančuk: Suppl. Nuovo Cim. **3**, 652 (1956) ;
     Yu.L. Dokshitzer et al.: *Basics of Perturbative QCD* (Editions Frontières, France 1991)
132. N.A. Pavel, Proceedings of the Conference on "Perspectives in Hadronic Physics", Trieste, May 1997
133. H.L. Bradt, B. Peters: Phys. Rev. **77**, 54 (1950)
134. D. Brandt, 5th CMS heavy ion meeting, Saint-Petersburg, June 2000
135. A. Capella et al.: Heavy Ion Phys. **9**, 169 (1999), and refs. therein
136. TOTEM, Letter of Intent, CERN/LHCC 97-49
137. C. Avila et al. (E811 Collab.): Phys. Lett. B **445**, 419 (1999)
138. A.M. Hillas: Ann. Rev. Astr. Astrophys. **22**, 425 (1984)
139. G. Bellettini et al.: Nucl. Phys. **79**, 609 (1966);
     S.P. Denisov et al.: Nucl. Phys. B **61**, 62 (1973);
     A.S. Carroll et al.: Phys. Lett. B **80**, 319 (1979)
140. F. Pauss et al. (ACCMOR Collab.): Z. Phys. C **27**, 211 (1985)
141. K. Geiger, BNL-63632, hep-ph/9701226
142. Proceedings of "Quark Gluon Plasma Signatures" (Editions Frontières, France 1991);
     R.A. Salmeron: Nucl. Phys. B **389**, 301 (1993);
     see also ref. [111]
143. H. Wilczynski (JACEE Collab.): Proceedings of the IX International Symposium on Very High Energy Cosmic Ray Interactions, Karlsruhe, 1996, Nucl. Phys. Proc. Suppl. B **52**, 81 (1997)
144. L. Kluberg et al.: Phys. Rev. Lett. **38**, 670 (1977)
145. F. Abe et al. (CDF Collab.): Phys. Rev. Lett. **80**, 2773 (1998)
146. J. Ellis et al.: Eur. Phys. J. C **10**, 443 (1999)
147. A. Breakstone et al.: Z. Phys. C **42**, 387 (1989), erratum ibid C **43**, 522 (1989);
     A. Breakstone et al.: Z. Phys. C **48**, 569 (1990);
     A. Breakstone et al.: Z. Phys. C **58**, 251 (1993) and refs. therein;
     T. Akesson et al.: Nucl. Phys. B **264**, 154 (1986) and refs. therein
148. K. Hencken et al.: Z. Phys. C **68**, 473 (1995)
149. S. Klein et al.: STAR Note 347
150. A.S. Goldhaber: Phys. Lett. B **53**, 306 (1974)
151. A.H. Mueller: Nucl. Phys. B **558**, 285 (1999)
152. J. Blumlein: hep-ph/9909449
153. S. Gavin et al.: Phys. Lett. B **214**, 241 (1988)
154. M. Strickman et al.: in [119]
155. W.M. Geist et al.: Phys. Rep. **197**, 263 (1990)
156. C. Caso et al. (Particle Data Group): Eur. Phys. J. C **3**, 1 (1998)
157. M.A. Vasiliev et al. (E866 Collab.): Phys. Rev. Lett. **83**, 2304 (1999);
     X.N. Wang: Phys. Rev. Lett. **81**, 2655 (1998)
158. C.G.S. Costa et al.: Phys. Rev. D **52**, 3890 (1995);
     C.G.S. Costa et al.: Phys. Rev. D **54**, 5558 (1996);
     Z. Wlodarczyk: J. Phys. G. Nucl. Part. Phys. **19**, L133 (1993);
     Z. Wlodarczyk: J. Phys. G. Nucl. Part. Phys. **21**, 281 (1995)
159. CosmoLep Report 1 (available at http://cosmolep.web.cern.ch/CosmoLep/), and H. Wachsmuth: private communication
160. O. Carrel and M. Martin: Phys. Lett. B **325**, 526 (1994);
     T. Kitamura et al.: Astropart. Phys. **6**, 279 (1997);
     W. Unno et al.: Europhys. Lett. **39**, 465 (1997)
161. The LHC Study Group: CERN/AC 95-05-LHC
162. N. Armesto and C. Pajares: hep-ph/0002163
163. S. Abdullin, A. Khanov and N. Stepanov: CERN/CMS TN 1994/180
164. D. Denegri and V. Genchev: CERN/CMS Note 1996/020
165. D. Litvintsev: CERN/CMS IN 1996/003
166. R. Kvatadze: CERN/CMS CR 1997/015
167. The CDF Collaboration: Fermilab-Conf-94/136-E, hep-ex/9412013
168. C. Baglin et al. (NA38 Collab.): Phys. Lett. B **270**, 105 (1991)
169. D.M. Alde et al. (E772 Collab.): Phys. Rev. Lett. **66**, 133 (1991)
170. GEANT: CERN program library, long writeup W5013
171. O. Kodolova and M. Bedjidian: CERN/CMS TN 1995/124
172. M. Bedjidian: CERN/CMS TN 1995/188
173. M. Bedjidian and O.Drapier: CERN/CMS Note 1999/052
174. O. Kodolova and M. Bedjidian: CERN/CMS Note 1997/095
175. A.Caner et al.: Nucl. Instr. Meth. A **435**, 118 (1999)
176. V. Innocente, M. Maire and E. Nagy: preprint / cern / IT-ASDW5013
177. V. Karimaki: Nucl. Instr. Meth. A **305**, 187 (1991)
178. V. Karimaki: Comput. Phys. Com. **69**, 133 (1992)
179. F. Antinori: CERN/ALICE 93-09 (MC)
180. G. Wrochna: CERN/CMS Note 1997/089
181. O. Kodolova et al.: CERN/CMS Note 1999/004
182. F. Abe et al. (CDF Collab.): Phys. Rev. Lett. **68**, 3403 (1992);
     F. Abe et al. (CDF Collab.): Phys. Rev. Lett. **69**, 3704

(1992);
F. Abe et al. (CDF Collab.): Phys. Rev. Lett. **71**, 500 (1993);
F. Abe et al. (CDF Collab.): Phys. Rev. Lett. **71**, 2396 (1993);
F. Abe et al. (CDF Collab.): Phys. Rev. Lett. **71**, 2537 (1993);
F. Abe et al. (CDF Collab.): Phys. Rev. D **50**, 4252 (1994)
183. S. Abachi et al. (D0 Collab.): Phys. Rev. Lett. **74**, 3548 (1995)
184. C.E. Gerber (D0 and CDF Collabs.): hep-ex/9806005
185. P.C. Bhat, H.B. Prosper and S.S. Snyder: Int. J. Mod. Phys. A **13**, 5113 (1998)
186. M. Bedjidian et al.: CERN/CMS TN 1996/086
187. O. Kodolova et al.: CERN/CMS Note 1998/078
188. M. Bedjidian, R. Kvatadze and V. Kartvelishvili: CERN/CMS Note 1997/082
189. O. Kodolova et al.: CERN/CMS Note 1998/063
190. J. Varela et al.: CERN/CMS TN 1996/010
191. R. Kvatadze and R. Shanidze: CERN/CMS TN 1994/270
192. M. Bourquin and M. Gaillard: Nucl. Phys. B **114**, 334 (1976)
193. K. Eggert, A. Morsch: CERN/ALICE 95-05 (PHY)
194. B. Flaugher and K. Meier: Proc. of the Snowmass Summer Studies (1990), FERMILAB-CONF-90/248-E
195. F. Abe et al. (CDF Collab.): Phys. Rev. Lett. **70**, 713 (1993)
196. T.C. Heuring et al. (D0 Collab.): FERMILAB-CONF-96/162-E, hep-ex/9607001
197. C. Seez: CERN/CMS Note 1998/030
198. A. Givernaud: CERN/CMS TN 1996/119
199. G. Baur, K. Hencken, and D. Trautmann: Topical Review, J. Phys. G **24**, 1657 (1998)
200. F. Krauss, M. Greiner, and G. Soff: Prog. Part. Nucl. Phys. **39**, 503 (1997)
201. G. Baur, K. Hencken, and D. Trautmann, in *Proceedings of the Lund Workshop on Photon Interactions and the Photon Structure, Lund, September 10-13, 1998*, G. Jarlskog and T. Sjostrand, eds. (Lund University, Lund, 1998), hep-ph/9810418
202. C.A. Bertulani and G. Baur: Phys. Rep. **163**, 299 (1988)
203. G. Baur and H. Rebel, Topical Review: J. Phys. G **20**, 1 (1994)
204. G. Baur and H. Rebel: Annu. Rev. Nucl. Part. Sci. **46**, 321 (1996)
205. H. Primakoff: Phys. Rev. **81**, 899 (1951)
206. R. Moshammer et al.: Phys. Rev. Lett. **79**, 3621 (1997)
207. Transparencies of the RHIC/INT workshop, Berkeley, 7–9th Jan. 1999, are available at http://www-rnc.lbl.gov/~nxu/oldstuff/workshop/rww99.html
208. L.D. Landau and E.M. Lifshitz: Phys. Z. Sowjet. **6**, 244 (1934)
209. G. Baur and C.A. Bertulani: Z. Phys. A **330**, 77 (1988)
210. M. Grabiak, B. Müller, W. Greiner, and P. Koch: J. Phys. G **15**, L25 (1989)
211. E. Papageorgiu: Phys. Rev. D **40**, 92 (1989)
212. G. Baur: in *CBPF Int. Workshop on Relativistic Aspects of Nuclear Physics, Rio de Janeiro, Brazil 1989*, T. Kodama et al., eds. (World Scientific, Singapore, 1990), p. 127
213. G. Baur and L.G. Ferreira Filho: Nucl. Phys. A **518**, 786 (1990)
214. N. Cahn and J.D. Jackson: Phys. Rev. D **42**, 3690 (1990)

215. M. Vidović, M. Greiner, C. Best, and G. Soff: Phys. Rev. C **47**, 2308 (1993)
216. F. Vannucci, in γγ *Collisions, Proceedings, Amiens 1980*, Vol. 134 of *Lecture Notes in Physics*, G. Cochard and P. Kessler, eds. (Springer, Berlin 1980), CERN-EP/80-82
217. A.G. Shamov and V.I. Telnov: talk by A. Maslennikov, in *Proceedings of the Lund Workshop on Photon Interactions and the Photon Structure, Lund, September 10-13, 1998*, G. Jarlskog and T. Sjostrand, eds. (Lund University, Lund 1998)
218. S. Klein and E. Scannapieco: in [250] (p. 369), hep-ph/9706358
219. S. Klein and E. Scannapieco: Coherent Photons and Pomerons in Heavy Ion Collisions, presented at 6th Conference on the Intersections of Particle and Nuclear Physics, May 1997, Big Sky, Montana, STAR Note 298, LBNL-40495, 1997, nucl-th/9707008
220. S. Klein and E. Scannapieco: STAR Note 243 (1995)
221. S. Klein: in *Photon '95, Sheffield*, D.J. Miller, S.L. Cartwright, and V. Khoze, eds. (World Scientific, Singapore 1995), p. 417, LBL-37295
222. J. Nystrand, in *Proceedings of the Lund Workshop on Photon Interactions and the Photon Structure, Lund, September 10-13, 1998*, G. Jarlskog and T. Sjostrand, eds. (Lund University, Lund, 1998), nucl-ex/9811007
223. K. Hencken, Y.V. Kharlov, G.V. Khaustov, S.A. Sadovsky, and V.D. Samoylenko: TPHIC, event generator of two photon interactions in heavy ion collisions, IHEP-96-38, 1996
224. S. Sadovsky: CERN/ ALICE 93-07 (PHY)
225. G. Baur, K. Hencken, D. Trautmann, S. Sadovsky, and Y. Kharlov: Photon-Photon Physics with heavy ions at CMS, CERN/CMS Note 1998/009
226. J.D. Bjorken: Nucl. Phys. Proc. Suppl. **71**, 484 (1999)
227. V.M. Budnev, I.F. Ginzburg, G.V. Meledin, and V.G. Serbo: Phys. Rep. **15**, 181 (1975)
228. J.D. Jackson, *Classical Electrodynamics* (John Wiley, New York, 1975)
229. A. Winther and K. Alder: Nucl. Phys. A **319**, 518 (1979)
230. G. Baur and L.G. Ferreira Filho: Phys. Lett. B **254**, 30 (1991)
231. G. Baur and N. Baron: Nucl. Phys. A **561**, 628 (1993)
232. G. Baur: Z. Phys. C **54**, 419 (1992)
233. O. Brüning: Talk at the CMS heavy ion physics meeting, 11–12 june 1998, CERN, Geneva
234. J.A. Crittenden, *Exclusive production of neutral vector mesons at the electron-proton collider HERA*, Vol. 140 of *Springer tracts in modern physics* (Springer, Heidelberg, 1997), hep-ex/9704009
235. M.G. Ryskin, R.G. Roberts, A.D. Martin, and E.M. Levin: Z. Phys. C **76**, 231 (1997)
236. J. Breitweg et al. (ZEUS Collab.): Z. Phys. C **76**, 599 (1997)
237. D.Z. Freedman, D.N. Schramm, and D.L. Tubbs: Annu. Rev. Nucl. Part. Sci. **27**, 167 (1977)
238. S. Klein and J. Nystrand: Phys. Rev. C **60**, 014903 (1999)
239. C. Brechtmann and W. Heinrich: Z. Phys. A **330**, 407 (1988)
240. C. Brechtmann and W. Heinrich: Z. Phys. A **331**, 463 (1988)
241. P.B. Price, R. Guoxiao, and W.T. Williams: Phys. Rev. Lett. **61**, 2193 (1988)

242. M. Vidović, M. Greiner, and G. Soff: Phys. Rev. C **48**, 2011 (1993)
243. A.J. Baltz, M.J. Rhoades-Brown, and J. Weneser: Phys. Rev. E **54**, 4233 (1996)
244. G. Baur and C.A. Bertulani: Nucl. Phys. A **505**, 835 (1989)
245. H. Kolanoski and P. Zerwas: in *High Energy Electron-Positron Physics*, A. Ali and P. Söding, eds. (World Scientific, Singapore 1988)
246. Ch. Berger and W. Wagner: Phys. Rep. **146**, 1 (1987)
247. *γγ Collisions, Proceedings, Amiens 1980*, Vol. 134 of *Lecture Notes in Physics*, G. Cochard and P. Kessler, eds. (Springer, Berlin 1980)
248. *Proc. 9th International Workshop on Photon-Photon Collisions, San Diego (1992)* (World Scientific, Singapore 1992)
249. *Photon'95, Xth International Workshop on Gamma-Gamma Collisions and related Processes*, D.J. Miller, S.L. Cartwright, and V. Khoze, eds. (World Scientific, Singapore 1995)
250. *Photon'97, XIth International Workshop on Gamma-Gamma Collisions and related Processes, Egmond aan Zee*, A. Buijs, ed. (World Scientific, Singapore 1997)
251. M. Acciarri et al. (L3 Collab.): Phys. Lett. B **408**, 450 (1997)
252. G. Baur: Phys. Rev. A **42**, 5736 (1990)
253. K. Hencken, D. Trautmann, and G. Baur: Phys. Rev. A **51**, 998 (1995)
254. K. Hencken, D. Trautmann, and G. Baur: Phys. Rev. A **51**, 1874 (1995)
255. A. Alscher, K. Hencken, D. Trautmann, and G. Baur: Phys. Rev. A **55**, 396 (1997)
256. R. Godang et al. (CLEO Collab.): Phys. Rev. Lett. **79**, 3829 (1997)
257. V. Telnov, in *Photon '95, Sheffield*, D.J. Miller, S.L. Cartwright, and V. Khoze, eds. (World Scientific, Singapore 1995), p. 369
258. I.F. Ginzburg: in *Photon '95, Sheffield*, D.J. Miller, S.L. Cartwright, and V. Khoze, eds. (World Scientific, Singapore 1995), p. 399, hep-ph/9507233
259. M. Drees, H. Ellis, and D. Zeppenfeld: Phys. Lett. B **223**, 454 (1989)
260. B. Müller and A.J. Schramm: Phys. Rev. D **42**, 3699 (1990)
261. E. Papageorgiu: Phys. Lett. B **352**, 394 (1995)
262. J. Norbury: Phys. Rev. D **42**, 3696 (1990)
263. D. Choudhury and M. Krawczyk: Phys. Rev. D **55**, 2774 (1997)
264. F.M. Renard: Phys. Lett. B **126**, 59 (1983)
265. U. Baur, H. Fritzsch, and H. Faissner: Phys. Lett. B **135**, 313 (1984)
266. M. Drees, R.M. Godbole, N. Nowakowski, and S.D. Rindami: Phys. Rev. D **50**, 2335 (1994)
267. J. Ohnemus, T.F. Walsh, and P.M. Zerwas: Phys. Lett. B **328**, 369 (1994)
268. M. Krawczyk and B.B. Levchenko: in *Proc. Future Physics at HERA 1995-1996*, G. Ingelmann, A. de Roeck, and R. Klanner, eds.
269. G. Baur: Phys. Rev. D **41**, 3535 (1990)
270. C. Best, W. Greiner, and G. Soff: Phys. Rev. A **46**, 261 (1992)
271. M.J. Rhoades-Brown and J. Weneser: Phys. Rev. A **44**, 330 (1991)
272. M.C. Güçlü et al.: Phys. Rev. A **51**, 1836 (1995)
273. C. Bottcher and M.R. Strayer: Phys. Rev. D **39**, 1330 (1989)
274. N. Baron and G. Baur: Z. Phys. C **60**, 95 (1993)
275. G. Baur: Nucl. Phys. A **538**, 187c (1992)
276. D. Ivanov and K. Melnikov: Phys. Rev. D **57**, 4025 (1998)
277. D. Ivanov, A. Schiller, and V.G. Serbo: Phys. Lett. B **454**, 155 (1999)
278. B. Segev and J.C. Wells: Phys. Rev. A **57**, 1849 (1998)
279. U. Eichmann, J. Reinhardt, S. Schramm, and W. Greiner: nucl-th/9804064
280. A.J. Baltz and L. McLerran: Phys. Rev. C **58**, 1679 (1998)
281. K. Hencken, D. Trautmann, and G. Baur: Phys. Rev. C **59**, 841 (1999)
282. M. Chen and P. Zerwas: Phys. Rev. D **12**, 187 (1975)
283. V.N. Baier, V.S. Fadin, and V.H. Khoze: Nucl. Phys. B **65**, 381 (1973)
284. G. Baur, K. Hencken, and D. Trautmann: work in progress, 1999
285. H. Meier et al.: Eur. Phys. J. C **2**, 741 (1998)
286. S. Weinberg, *The Quantum Theory of Fields* (Cambridge University Press, Cambridge 1997), Vol. 1
287. K. Hencken, D. Trautmann, and G. Baur: Phys. Rev. C **60**, 014901 (1999)
288. A.J. Baltz, M.J. Rhoades-Brown, and J. Weneser: Phys. Rev. A **44**, 5569 (1992)
289. A.J. Baltz, M.J. Rhoades-Brown, and J. Weneser: Phys. Rev. A **48**, 2002 (1993)
290. U. Becker: J. Phys. B **20**, 6563 (1987)
291. A. Aste, K. Hencken, D. Trautmann, and G. Baur: Phys. Rev. A **50**, 3980 (1994)
292. C.K. Agger and A.H. Sørensen: Phys. Rev. A **55**, 402 (1997)
293. M.J. Rhoades-Brown, C. Bottcher, and M.R. Strayer: Phys. Rev. A **40**, 2831 (1089)
294. H. Meier et al.: Eur. Phys. J. C **5**, 287 (1998)
295. C.A. Bertulani and G. Baur: Phys. Rev. D **58**, 034005 (1998)
296. A. Baltz: Phys. Rev. Lett. **78**, 1231 (1997)
297. H.F. Krause et al.: Phys. Rev. Lett. **80**, 1190 (1998)
298. A. Belkacem et al.: Phys. Rev. Lett. **71**, 1514 (1993)
299. A. Belkacem et al.: Phys. Rev. Lett. **73**, 2432 (1994)
300. G. Baur: in *Perspectives on Photon Interactions with Hadrons and Nuclei, Lecture Notes in Physics*, M. Schumacher and G. Tamas, eds. (Springer Verlag, Berlin, Heidelberg, New York 1990), p. 111
301. I.F. Ginzburg: private communication
302. S.R. Gevorkyan et al.: Phys. Rev. A **58**, 4556 (1998)
303. R. Engel et al.: Z. Phys. C **74**, 687 (1997)
304. J. Nystrand and S. Klein: Two Photons Physics at RHIC: Separating Signals from Backgrounds, talk presented at "Hadron'97", Brookhaven National Laboratory, August 1997, STAR Note 315, LBNL-41111 Nov. 1977
305. A.J. Baltz and M. Strikman: Phys. Rev. D **57**, 548 (1998)
306. CMS Muon Trigger Group: CERN/CMS TN 1996/060
307. F. Abe et al. (CDF Collab.): Phys. Rev. Lett. **61**, 1819 (1988)
308. M. Cwiok and G. Wrochna: CERN/CMS TN 1995/150
309. C. Albajar et al.: Z. Phys C **69**, 415 (1996)
310. M. Konecki, J. Królikowski, G. Wrochna, RPC Muon Trigger Software MRPC 100-102, draft, http://cmsdoc.cern.ch/ wrochna/mrpc/mrpc.ps

311. M. Bedjidian, *Status of Dimuon Reconstruction*, presented at *CMS Heavy Ion Meeting*, 4–6 February 97, Dubna
312. G. Wrochna: CERN/CMS IN 1999/07
313. O. L. Kodolova, D. Kotliński: http://www1.psi.ch/∼kotlinski/cms_pix_hi.html